INFORMATION TO USERS

This manuscript has been reproduced from the microfilm master. UMI films the text directly from the original or copy submitted. Thus, some thesis and dissertation copies are in typewriter face, while others may be from any type of computer printer.

The quality of this reproduction is dependent upon the quality of the copy submitted. Broken or indistinct print, colored or poor quality illustrations and photographs, print bleedthrough, substandard margins, and improper alignment can adversely affect reproduction.

In the unlikely event that the author did not send UMI a complete manuscript and there are missing pages, these will be noted. Also, if unauthorized copyright material had to be removed, a note will indicate the deletion.

Oversize materials (e.g., maps, drawings, charts) are reproduced by sectioning the original, beginning at the upper left-hand corner and continuing from left to right in equal sections with small overlaps.

Photographs included in the original manuscript have been reproduced xerographically in this copy. Higher quality 6" x 9" black and white photographic prints are available for any photographs or illustrations appearing in this copy for an additional charge. Contact UMI directly to order.

ProQuest Information and Learning
300 North Zeeb Road, Ann Arbor, MI 48106-1346 USA
800-521-0600

PHOTOFRAGMENTATION SPECTROSCOPY OF THE ZIRCONIUM AND NIOBIUM CLUSTER CATIONS AND AB INITIO STUDIES

by

METIN AYDIN

A dissertation submitted to the Graduate Faculty in Chemistry in partial fulfillment of the requirements for the degree of Doctor of Philosophy, The City University of New York.

2001

UMI Number: 3008807

Bell & Howell Information and Learning Company
300 North Zeeb Road
P.O. Box 1346
Ann Arbor, MI 48106-1346

This manuscript has been read and accepted for the Graduate Faculty in Chemistry in satisfaction of the dissertation requirement for the degree of Doctor of Philosophy.

1-10-01

Date

Chair of Examining Committee

Jan. 25, 2001

Date

Executive Officer

Dr. John R. Lombardi

Dr. Lawrence W. Johnson

Dr. Ronald Birke

Supervisory Committee

THE CITY UNIVERSITY OF NEW YORK

ABSTRACT

LASER SPECTROSCOPY OF TRANSITION METAL CLUSTER CATIONS AND AB INITIO CALCULATION ON THE NEUTRAL AND IONIC TRANSITION METAL CLUSTERS.

by

Metin Aydin

Adviser: Professor John R. Lombardi

This thesis describes research done in the field of cluster chemistry. It is virtually divided into three parts. Virtual part I describes experimental studies of metal cluster cations in gas phase, and virtual part II describes the ab initio methods; experimental and theoretical results are presented in virtual part III.

A metal cluster is a group of metal atoms consisting of two to several thousand metal atoms in gas, liquid, solid, and plasma phase. Chemical physicists studying the spectra of transition metal clusters produced in supersonic nozzle beams and detected by either resonant two-photon ionization or photofragmentation allude in their discussions to the metal-metal multiple bonding. In the field of cluster chemistry and physics the aim is to understand how a chemical process depends on cluster size, how the chemistry of a metal changes with its state of aggregation, and how structural, electronic, optical, and magnetic properties vary with cluster size, eventually reaching those of the bulk metal.

Even for small transition metal (ionic) clusters, their electronic structures are complexes and remain questions. For theory, too, the future holds its challenges. Even cluster as small as diatomics may prove difficult species to get right answers for because of the partially occupied d orbitals. Therefore, it is difficult to calculate the exchange-correlation energy contribution to the system in an accurate manner.

Virtual part I consists of three chapter. Chapter I is an introduction, Chapter II and III describe the instrument and experimental conditions, respectively. Virtual part II consists of two chapters. In Chapter IV, the theoretical methods are discussed. In Chapter V, spin-orbit interaction is discussed. Virtual part III covers chapters VI to XI. Chapter VI shows the experimental and theoretical results for Zr_2^-. In chapters VII to IX, the experimental and theoretical result for Nb_2^+, Nb_3^+, and Nb_4^+ are given. In Chapter X, the electronic spectra of the Nb_2^+ and possible assignments are given. Chapter XI is the conclusion.

ACKNOWLEDGEMENTS

THANKS YOU TO ALL THE INDIVIDUALS LISTED HEREIN

I owe a wealth of gratitude to all these wonderful people who I am proud to number among my friends.

Professor John R. Lombardi

Professor Larry Johnson

Professor Ronald Birke

Professor Joseph G. Eaton

Professor Daniel Akins

Professor Michael E. Green

Dr. Abdullah Cavus

Dr. Shelley B. Deosaran

Dr. Wumin Wang

Dr. Ron Brown

Dr. Fang

Mrs. Sandra Smith

Mr. Derek Quinlan

A special thanks to Professor Derek M. Lindsay. You had a great personality as well as you were an outstanding scientist. You always gave me good advice and financial support.

These are the people whose support and love helped me to survive the ordeal.

A very special thanks to my family!

- Parents Mulkinaz and Cemal
- Sisters in Law Nilufer (rest in peace), Nuran, Leyla, Derya, Melahat, and Sevim
- Brothers Guven, Dogan, Kenan, Cetin, and Akin.

My dear Sherri thank you for your "understanding", "love", and "support", it meant a lot to me. I will always remember you and being in my heart wherever you are now, rest in peace.

My good friends, Lori and Abdullah thank you, I will never forget your kindness and great help when I first arrived in New York and always welcoming me into your home.

TABLE OF CONTENTS

Abstract		iii
Acknowledgment		v
Table of Contents		vii
List of tables		xiii
List of Figures		xv
	CHAPTER I	
I.	Introduction	1
	CHAPTER II	
II.1	Metal Cluster Ion Photofragmentation	10
II.2	Experimental	14
II. 2.1	Laser Vaporization Source	17
II.2.2	Pulsd Supersonic Valve	19
II.2.3	Cluster Source Nozzle	21
II.2.4	Target Assembly	24
II.2.5	The Skimmer	24
II.3	The Primary Mass Spectra: Linear Time-Of-Flight (TOF)	29
II.3.1	Wiley McLaren Lens	30
II.3.2	Ion Lens and Deflectors	41
II.4	Mass selection, Fragmentation and Detection	43
11.4 .1	Mass-Gate	43
II.4.2	Secondary Mass Separation	47

II.4.3	Fragmentation Laser	52
II.4.4	Ion Detection	53
II.4.5	Instrument Control and Data Acquisition	54
	Chapter II. References	61

CHAPTER III

Photofragmentation Spectroscopy of the Niobium and Zirconium Cation Clusters

III.1	Ion Photofragmentation Spectroscopy	63
III.2	Photofragmentation of Nb_2^+, Nb_3^+, Nb_4^+, and Zr_2^+	67
III.2.1	Introduction	67
III.2.2	Experimental	67
	Chapter III References	72

CHAPTER IV

IV.1	Introduction	75
IV.2	The Many-Particle System	77
IV.3	Hartree and Hartree-Fock Theory	79
IV3.1	The Born-Oppenheimer Approximation	86
IV3.2	The MO-LCAO Approximation	87
IV.3.3	The Hartree-Fock Equations	88
IV.4	Semi-Empirical Hartree-Fock	92
IV.5	Density Functional Theory	98

III.5.1	Kohn-Sham Theory	99
IV.5.2	The Local Density Approximation	103
IV.5.3.	Nonlocal Density Functionals for the Exchange-Correlation Energy	104
IV.5.4.	Correct Asymptotic Behavior Approximation to Density Functional Energy and Becke Type One Parameter Exchange Functional (B).	105
IV.5.4.1.	Development of the Colle-Salvetti Correlation-Energy Formula Into a Functional of the Electron Density.	109
IV.5.4.2.	Formula Involving Local Kinetic-Energy Density	110
IV.5.4.3.	Gradient Expansion Formulas	112
IV.5.4.4.	Correlation Potential	114
IV.5.5.1.	The Exchange Term in VWN Approximation	114
IV.5.5.2.	The Correlation Term	115
IV.5.6.	The Correlation Term in PW91 Approximation	117
IV.5.7.	The Correlation Term in BP86 Approximation	117
IV 6.	Vibrational Frequency	119
IV 6.1.	Mass Weighted the Hessian and Diagonalize:	119
IV 6.2	Generate Coordinates in the Rotating and Translating Frame.	120
	Chapter III References	123

CHAPTER V

V.1	Introduction	126
V.2	Interaction of Electron Spin	126
V.2.1	Case a	131

V.2.2	Case b	133
V.2.3	Case c	140
	Chapter V References	141
	CHAPTER VI	
	Determination of the Bond Strength of the Metal Cluster (Ions)	142
VI.1	Photofragmentation Spectroscopy of Zirconium Dimer Cation	
	Molecule and Ab Initio Study on Zr_2, Zr_2^+	147
	Abstract	147
VI 2.	Introduction	147
VI 2.1.	Experimental Study on Zirconium Dimer Cation	150
VI 2.1.1	Fluence Study.	150
VI 2.1.2	Multiphoton Fragmentation Spectrum of Zr_2^+	156
VI 2.2.	Methods of Calculations	157
VI 2.2.2.	Result of Calculations	158
VI 3.	Discussion	172
	Chapter VI References	174
	CHAPTER VII	
	Photon Fragmentation Spectroscopy of Niobium Dimer Cation	
	Molecule and Ab Initio Studies on Nb_2, Nb^+_2	179
	Abstract	179
VII	Introduction	179
VII.1	Experimental Study on Niobium Dimer Cation	180
VII 2.1	Fluence Study	180

VII 2.1.1	Determination of the Lowest Dissociation Energy Limit and Threshold Energy Spectrum of the Nb_2^+	182
VII 2.2	Result of Calculations	184
VII 2.3	Discussion	191
	Chapter VII References	192

CHAPTER VIII

Photofragmentation Spectroscopy of Niobium Trimer Cation and Ab Initio Study

	Abstract	195
VIII. 1.	Introduction	196
VIII. 2.	Calculations	197
VIII. 3.	Multiphoton Fragmentation of Nb_3^+	201
VIII. 4.	Conclusion	204
	Chapter VIII References	207

CHAPTER IX

Photofragmentation spectroscopy of niobium tetramer cation molecule and ab inito study on Nb_4, Nb_4^+

	Abstract	213
IX.1	Introduction	213

IX 2.	Multiphoton Fragmentation Spectrum and Determination of Dissociation Energy Limit of $Nb_4^+ \rightarrow Nb_3^+ + Nb$	215
IX 3	Methods of Calculations	218
IX 3.1	Computing Detail	218
IX 3.2	Result of Calculations	219
IX 3.2.3	Conclusions	223
IX 4	Bond Energy of the Nb_2	224
	Chapter IX References	226
	CHAPTER X.	
	Electronic structure of the Nb_2^+	
	Abstract	229
X. 1.	Introduction	229
X. 2.	One-Color Multiphoton Fragmentation	233
X. 3.	Discussion	242
X. 4.	First- and Second-Order Spin-Orbit Coupling	245
	Chapter X References	250
	CHAPTER XI	
XI	Conclusion	254
BIBLIOGRAPHY		267

LIST OF TABLES

Table		
Table 2.1	Calculated Wiley-McLaren Time-Of-Flight (TOF) arrival times for the Nb_2^+	39
Table 2.2	Calculated Reflectron TOF arrival times for Nb^+ and Nb_2^+	40
Table 3.1	The experimental conditions	69
Table 6.1	Summary of the pervious studies on Zr_2	149
Table 6.2	Calculated spectroscopic constants of the Zr_2 ($^3\Delta_g$)	161
Table 6.3	Calculated spectroscopic constants of the Zr_2 ($^7\Sigma^+_u$)	162
Table 6.4	Calculated spectroscopic constants of the Zr_2 ($^1\Gamma_g$)	163
Table 6.5	Calculated orbital-orbital transitions (T_e) of triplet states of the Zr_2	164
Table 6.6	Calculated orbital-orbital transitions (T_e) of septet states of the Zr_2	165
Table 6.7	Calculated spectroscopic constants of the Zr_2^+	169
Table 6.8	Calculated orbital-orbital transitions (T_e) of doublet states of the Zr_2^+	170
Table 7.1	Calculated spectroscopic constants of Nb_2	185
Table 7.2	Calculated orbital-orbital transitions (T_e) of the triplet states of the Nb_2	185
Table 7.3	Calculated spectroscopic constants of the Nb_2^+	188
Table 7.4	Calculated orbital-orbital transitions (T_e) of the quartet states of the Nb_2^+	189

Table 8.1	Calculated spectroscopic constants of Nb_3^+	199
Table 8.2	Calculated orbital-orbital transitions (T_e) of the triplet states of the Nb_3^+	200
Table 9.1	Calculated spectroscopic constants of the Nb_4	221
Table 9.2	Calculated spectroscopic constants of the Nb_4^+	222
Table 10.1	Assigned multiple bands of the Nb_2^+	239
Table 10.2	The spectroscopicaly determined parameters of Nb_2^+	241
Table 10.3	The selected first- and second-order spin-orbit couplings for various electronic states of the Nb_2^+	249
Table 11.1	Calculated spectroscopic properties of the second-row transition metal neutral, cationic, and anionic dimer molecules	261

LIST OF FIGURES

Figure		
Figure 2.1	Figure 2.1 Diagram highlighting the main parts of the instrument, viewed from the top looking down.	16
Figure 2.2	Diagram illustrating how the vaporization laser is focused on the target disk.	18
Figure 2.3	Photograph blow up to show the interior of the source chamber	20
Figure 2.4	Diagram of the Teflon nozzle inserts	22
Figure 2.5	Diagram of the nozzle support	23
Figure 2.6A	Photograph indicating the side view of the target holder, gear assembly	25
Figure 2.6B	Photograph indicating the "head on" view of the target holder, gear assembly	26
Figure 2.6C	Photograph of a close up view of the target holder and gear assembly	27
Figure 2.7A	Simulation of the laser burn pattern.	28
Figure 2.7B	Photograph of an actual target after using for 100 hours	28
Figure 2.8	Photograph of the Wiley-McLaren TOF lens	31
Figure 2.9	Schematic of the Wiley-McLaren TOF lens showing an ion packet being focused at the detector	34
Figure 2.10	Plot of ion intensity versus the relative lowering of three apertures of	

	differing diameters	35
Figure 2.11	Plot of the arrival times of the Nb_2^+ ions versus their distance away from the backing plate	36
Figure 2.12A	Mass spectrum of niobium cluster cations and niobium oxide clusters cations	37
Figure 2.12B	Plot of the relative mass of the cluster ions versus the arrival time of ions	42
Figure 2.13A	Mass spectrum of Nb_n^+, n = 1 to 10, in the absence of the mass gate	44
Figure 2.13B	Mass spectrum of Nb_n^+, n = 3, 5, and 6, in the presence of the mass gate	45
Figure 2.14	Photograph of the reflectron TOF mounted on a 12" flange	48
Figure 2.15	Schematic of the reflectron TOF showing what occurs when an ion fragments to produce a daughter ion and then both traverse the reflectron	49
Figure 2.16	Diagram illustrating experimental outline	55
Figure 2.17A	Mass spectrum of Nb_4^+, Nb_3^+, Nb_2^+, Nb^+ formed from the metastable decomposition of Nb_4^+	5 9
Figure 2.17B	Mass spectrum of Nb_n^+, n = 1 to 4, formed from photofragmentation	60
Figure 3.1	Conceptual diagram illustrating photodissociation and predissociation.	65
Figure 5.1	A vector model of Hund's case a	135

Figure 5.2	A vector model of Hund's case b	135
Figure 5.3	A vector diagram of the kth electron orbiting around the nuclei	139
Figure 5.4	A vector model of Hund's case c	139
Figure 6.1	Fluence dependence studies of Zr_2^+ at 595.4 nm	151
Figure 6.2A	Fluence dependence studies of Zr_2^+ at 590 nm	152
Figure 6.2B	Fluence dependence studies of Zr_2^+ at 560 nm	152
Figure 6.3	Observed threshold spectrum of Zr_2^+	154
Figure 6.4	Multiphoton fragmentation spectrum of Zr_2^+	155
Figure 6.5	Calculated potential energy curves of $^3\Delta_g$, $^1\Gamma_g$, and $^7\Sigma^+_u$ states Zr_2.	166
Figure 6.6	Calculated potential energy curves of $^2\Sigma^+_g$ and $^2\Delta_g$ states Zr_2^+.	171
Figure 7.1	Fluence dependence studies of Nb_2^+ at 560.24 nm	181
Figure 7.2	Fluence dependence studies of Nb_2^+ at 560.0 nm	181
Figure 7.3	Observed threshold spectrum of Nb_2^+	183
Figure 7.4	Calculated potential energy curves of $^3\Sigma^-_g$, $^1\Gamma_g$, and $^5\Delta_u$ states of Nb_2	186
Figure 7.5	Calculated potential energy curves of $^4\Sigma^-_g$ and $^2\Gamma_g$ states of Nb_2^+	190
Figure 8.1	Observed threshold spectrum of the Nb_3^+	203
Figure 8.2	Conceptual diagram illustrating two possible mechanism which of one may be responsible for the observed threshold in the multiphoton fragmentation spectrum of the Nb_3^+	204

Figure 9.1	Observed threshold spectrum of the Nb_4^+	217
Figure 10.1a	Resonant multiphoton fragmentation spectrum of the Nb_4^+ in the range 16,000-17,300 cm^{-1}	237
Figure 10.1b	Resonant multiphoton fragmentation spectrum of the Nb_4^+ in the range 17,100-18,450 cm^{-1}	238
Figure 11.1	Plot of the calculated force constants of the first-row transition metal neutral dimer with their known experimental values for comparison	263
Figure 11.2a	Plot of the calculated force constants of the second-row transition metal neutral dimer with their known experimental values for comparison	264
Figure 11.2b	Plot of the calculated force constants of the second-row transition metal dimer cations and anions	265
Figure 11.3	Plot of the calculated force constants of the second-row transition metal neutral dimer with their known experimental values for comparison	266

CHAPTER I

I. INTRODUCTION

From the time of John Dalton, when the atomic theory became generally accepted, the study of how matter behaves has divided into two streams. In the 1930's, one stream led to nuclear physics and then to particle physics. The other stream has emphasized the properties of very many atoms or molecules together, so many that the aggregates they make can be treated as infinite. The realm between these limits concerned only a few independent souls until about the late 1970's. Since then, interest has grown almost explosively in the study of what have come to be called clusters.[1-3]

Clusters are aggregates of atoms or molecules, generally intermediate in size between individual atoms and aggregates large enough to be called bulk matter. A mole particle of anything has far too many particles to be a cluster; that much material is certainly bulk matter. Even a hundred billion particles stuck together, far fewer than a mole, behave in most ways like bulk matter. When we talk of small clusters, we mean something containing no more than a few hundred or possibly thousands of particles. A useful distinction classifies clusters as small, medium-sized or large. Small clusters are those whose properties vary with size and shape so much that no simple, smooth dependence can be given for their dependence on number of component particles. If the cluster's properties are smoothly varying functions of the number of component particles, the cluster is medium-sized or large. If those properties vary smoothly but still reflect the small size of the cluster and the implications of that size, the cluster is medium-sized. If those properties approach those of the corresponding bulk material, the cluster is large.

Large clusters typically have dimensions on the order a few nanometers; they are approximated by spheres with radii between 1 and perhaps 50 nm, or microcrystals with sides of these dimensions.[1-3]

Aggregates in the small and middle range differ considerably from bulk matter in at least two important ways. First, a large fraction of their component particles are on the surface. For example in a cluster of 55 atoms of argon or sodium, at least 32 are in some sense on its surface. But small clusters also differ from bulk matter because the quantum states of bulk matter occur in bands of states so close together that we can disregard the energy gaps between the bands, such as that between those states. We can not, of course, neglect the gaps between the bands, such as that between filled and empty levels in an insulator or semiconductor, the very property that makes the substance an insulator or semiconductor. In a molecule or a small cluster, the spacing between the individual levels cannot be neglected. The spacings of the energy levels depend on the size of the object; the gaps between energy states of small clusters are quite like those of small and medium-sized molecules. Even in large clusters and nanoscale materials, the small dimensions of the particles give them some properties strongly characterized by quantum effects, properties whose counters seem quite classical in large systems.

Clusters differ from conventional molecules because of composition and structure. For the most part, molecules have definite, highly restricted numbers of atoms and specific compositions. Furthermore they almost always have unique structure. Clusters may be composed of any number N of component particles, and, for most kinds of clusters, as the number of particles of the cluster becomes larger, the number of locally stable structures available to the cluster grows rapidly.[1] This latter property has its

counterpart in the rapid increase, with number of component atoms, in the number of chemical isomers that exist for a distinct, isolable chemical species. Clusters of a given composition may exhibit a variety of structures, but we generally do not distinguish them as different chemical species. There are, however, a number of clusters of the same composition.

Clusters may be homogeneous, that is, composed of only one kind of atom or molecule, or heterogeneous, made of more than one kind of atom or molecule. Some clusters are held together by the strong force of attraction force of attraction between oppositely charged ions; clusters such as $(NaCl)_n$, C_{60} ions, are of this kind. Still others are held together by the kind of bonding that holds the atoms of bulk metal together; this is found in the large clusters of metal atoms, large clusters of sodium or copper or iron. Very small clusters of metal atoms may be held together by forces more like those of covalent bonds than like the force exerted by the nearly free-swimming electrons that glue atoms of metal together. Clusters of the rare gases, and of other closed shell atoms (like very small clusters of beryllium or mercury) belong to the class loosely called van der Waals clusters, held together by the weakest forces that still have their origins in electrical interactions. The last class of clusters we shall single out are those that are held together by hydrogen bonds. Clusters of water molecules are bound this way; the hydrogens of one water molecule are attracted to specific oxygen atoms of neighboring water molecules. Hydrogen-bonded clusters are held more tightly than van der Waals clusters, but less than typical covalent, metallic or ionic clusters.[1]

Clusters have drawn interest for several reasons. There are powerful ways to study clusters, both experimentally and theoretically, which simply did not exist twenty

years ago. Others are reason of purpose. Clusters may offer ways to make altogether new kinds of materials, to carry out chemical reactions in new ways, and to gain new kinds of understanding not only of this intermediate form of matter but of the behavior of bulk matter too, by learning how bulk properties emerge from properties of clusters, as the clusters grow larger and larger. Therefore, clusters are a potential source for new materials and new chemical reactions. Also the study of clusters gives us new insight into phase transitions, growth of crystals, chemical catalysis, a new method to grow thin films, organic superconductors, and above all, the slow transition from atomic/molecular/ chemical physics to the science of condensed matter.

Clusters can be made in the laboratory by making a vapor of the elementary component particles and letting them aggregate, or by knocking them directly out of a solid.[1-3] They can also, in principle, be made in solution; e.g. as small colloidal particles formed during precipitation or in submerged electric arcs. However most of the work during the explosion of interest in this field since the late 1960's has dealt with gaseous clusters. Beams of free clusters are typically one of these: i) the most popular and the best-understood source, is the "supersonic jet" with its many variants. A gas or vapor is expanded from a high pressure (typically 104 to 107 Pa) through a small nozzle (typically 0.03 to 1 mm in diameter) into a vacuum. The mean gas velocity increases during this adiabatic and isenthalpic expansion, but the random, thermal motion of the expanding gas is reduced dramatically. This leads to a reduction of the gas temperature and to effective cluster formation. Some of popular variants are: a) the source can be run continuously or pulsed, b) a pure gas, say Ar, He, or a mixture, say He with 1% I_2, can be used, c) the "mixture" to be expanded can be generated by a powerful pulsed laser or a strong electric

discharge, d) the cluster beam can run, after its formation, through a "cloud" of atoms, molecules, electrons, or ions, picking-up some of them, e) an electric discharge can be ignited on the high or low pressures side, f) Many different combinations have been tried and new sources are constantly developed. ii) Another effective means to generate clusters is the "gas aggregation source". Some material is evaporated or sputtered into a slow flow of argon or helium at a pressure of typically 50 to 500 Pa.[1] The atoms are slowed down by collisions with the rare gas, and start aggregating. This process is similar to cloud formation in the atmosphere. In this case water molecules are evaporated. They do not aggregate, if their density is low enough and their temperature is high enough. Only if these conditions are not fulfilled does aggregation (in common day language cloud formation) start. Other less common source are iii) sputtering, or iv) direct laser ablation, without cooling gas.

Once clusters have been made and are in the form of gaseous particles, it is frequently desirable to make them into some kind of controllable beam or stream that can be studied or captured. To observe clusters in a beam, one can probe them while they are free or trap them in a matrix, liquid, glassy or crystalline. Trapped clusters are most easily studied by infrared, visible and ultraviolet spectroscopy. These methods are also used to study free clusters in vacuum. Only for charged clusters has one effective and general means of mass selection and as a result, there are several areas in which more is known about charged clusters than about the neutrals.[1]

One may give clusters a positive charge by knocking out one or more electrons with a beam of electrons or energetic light quanta. One can also prepare clusters with a negative charges, this is, with an extra electron. These may be prepared by electron

transfer from an easily ionized donor such as gaseous rubidium atoms, by the capture of electrons from swarms of slow electrons (followed by collision with inert carrier gas atoms or molecules, to carry off the binding energy released by the electron capture and thereby to stabilize the negatively charged clusters), or in the primary process in which the cluster is generated, for example in ablation of material from a solid when it is struck by a high-intensity laser burst or high energy projectile. An effective way to produce intense beams of charged clusters is to generate a plasma in or after the condensation zone. This can be either by a laser or –less expensively –by an electric discharge.[1]

Electron(s) can be also ejected from neutral or charged clusters. The electrons emitted this way may be collected and studied; so may the newly produced ions. If one collects electrons, one wants normally to measure their energies. If one collects electrons. one may wish to measure their energies and their charge and mass, but Maxwell's laws allow one only to measure the ratio of their charge to their mass.

It is possible to excite clusters. neutral or charged, with light or electron impact and study the radiation they then emit or the particles they lose. The most frequently seen mode by which a cluster loses excess energy is ejection of atoms or large fragments. It seems that the dominant decay channel is always that having the lowest barrier. If the binding energy of the dimer or trimer becomes larger, the ejection of dimers can become the dominant decay channel.

Loss of energy by emission of atoms and of radiation occurs for those clusters, which have large band gaps in the bulk, like rare gases. As there are no potential curve crossings in the rare gases between the ground and electronically excited states, the electronic energy cannot be converted effectively into heavy particle motion. Thus

electronic excitation leads to photoemission. Fission into large fragments is observed only for multiply charged clusters. Loss of an electron can of course occur if the excitation energy is higher than the ionization energy.

Charged clusters have the special attraction that they can be sorted easily by electrostatic, magnetic or time-of-flight mass analysis to yield mass spectra and beams of a cluster of a single, known size. The numbers of particles in these beams are very small in terms of macroscopic samples, but are sufficient for many experiments. Among the first studied characteristics of charged clusters were their size distributions, which led to the understanding that some sizes and shapes of clusters are particularly stable, in a manner analogous to the stable shells seen in atoms and in nuclei. The numbers N of particles in these particularly stable clusters are sometimes called "magic numbers". One can also study the wavelengths of light that these clusters absorb; for elements-rare gases, alkalis, and mercury-the optical absorption spectrum from the atom and the cluster to bulk could thus be studied. Some of the other properties of charged clusters that have been studied include their modes of fragmentation, their chemistry, and the effects of their collisions with surfaces.

Clusters are of course tantalizing subjects for theoretical studies.[1-4] It is possible to apply to them the same theoretical tools that are applied to studying molecules; the quantum mechanical methods range from ab initio variational calculations of the entire electronic structure, through more approximate methods such as the local, non-local, gradient correction approximation, to density functionals which approximate the consequences of electron exchange interactions with effective potentials, to efficient but

highly oversimplified, effective potentials to describe the motions of the atoms, molecules or ions comprising the cluster.

One aspect of the theory of the structure of clusters has brought the subject into close contact with nuclear physics. This is the interpretation of structures of clusters in terms of shell models. This idea is that clusters of particular sizes have structures that correspond to closed shells of component particles and therefore are relatively more stable than clusters lacking one or a few particles that would fill out a closed shell, or than clusters with one or a few particles more than the number for a closed shell. The numbers corresponding to completely filled shells are often called magic numbers. Clusters may exhibit different structure under various external conditions of temperature and pressure. They can show many of the characteristics of solid-like and liquid-like behavior and of the equilibrium and passage between these forms. Some clusters can, under the right conditions, behave like soft solids or like slush, this is one of the areas in which new phenomena have appeared and new insights have arisen concerning the dynamics of small, medium, and large clusters, and into the nature of phase transitions.

Clusters offer several ways to make new kinds of materials; all of them still at the frontiers of research. One is based on differences between the structures of small clusters and the structures of bulk matter.

Chapter I References

1 H. Haberland, "*Clusters of Atoms and Molecules I and II*", Springer-Verlag, New York, 1995.

2 C.-Yiu Ng, T. Baer, and I. Powis, "*Cluster Ions*", John Wiley & Sons, New York, 1993.

3 M. Moskovits, "*Metal Clusters*", John Wiley & Sons, New York, 1986.

4 P.-Olov Lowdin, J. R. Sabin, M. C. Zerner, E. Brandas, A. Lami, and V. Barone, "*Advences in Quantum Chemistry*" Vol. 30, Academic Press, New York, 1999.

CHAPTER II

II.1 METAL CLUSTER ION PHOTOFRAGMENTATION

Since the introduction of the laser-vaporization techniques for the production of supersonic metal cluster beams,[1] the study of isolated gas phase metal clusters has proceeded with increasing vigor. For many researchers a prime motivating interest has been the possibility that these metal clusters will provide detailed molecular models with which to study such classic questions of surface science as the nature of the metal-metal bond, the electronic structure at a reactive surface site, or the molecular details of chemisorption. Indeed, such diverse probes as mass-selected resonant two-photon ionization[2] (R2PI), laser-induced fluorescence[3] (LIF), electric[4(a)] and magnetic[4(b),4(c)] field deflection, and gas phase reaction followed by photoionization and mass spectroscopic detection[5] have been applied to alkali metal, transition metal, and even semiconductor cluster species.

As promising as this seems, the current arsenal of probes for neutral metal cluster beams is not quite as powerful as one would like.[3] A key problem has been finding a sufficiently sensitive detection scheme that is also highly selective as to the identity of the cluster species contributing to the signal. All neutral cluster beams contain a broad range of species; the experimental procedure must clearly label each observed signal with the name-or at least the mass-of the species responsible. Most metal cluster species have fairly low ionization potentials, so sensitive detection is easily accomplished by counting the ions produced by photoionization. Mass spectral analysis of the cluster photoions provides mass selectivity but, too often, the photoionization process cannot be relied upon to

produce only the parent ion so it is frequently impossible to uniquely assign a particular signal to a particular cluster.

Particularly troublesome has been the difficulty of using either of the two most powerful laser spectral techniques LIF or R2PI, on metal cluster species. Both techniques require that the first laser-induced transition populate an excited electronic state which survives long enough to be detected by either its fluorescence (LIF), or its lower ionization threshold (RIPI). Although successful with a small number of metal dimers and trimers, these spectral techniques are not generally applicable to larger metal clusters. Simply stated, the problem is that these metal clusters behave too much like metals. Even very small transition metal clusters are expected to have hundreds of electronic states within the first few eV. In such a circumstance even quite weak interactions between the various electronic states are sufficient to produce an extensively scrambled, high-density manifold of vibronic states. Radiationless transitions in such nearly metallic systems are extremely rapid, and this degradation of electronic excitation generally renders such systems invisible to both LIF and R2PI.

On the other hand, sensitive and selective detection of cluster ions is free of such problems. Since they are charged standard particle counting techniques ensures that each cluster ion can be detected with near unit efficiency. Mass selection can be performed initially, so spectral probes can target only the desired parent ion. Absorption can be readily detected by fragmentation of the parent ion-a one-photon, process if the photon energy is above the dissociation threshold, or a multiphoton process otherwise. Using high peak intensity probe lasers, both one and multiphoton absorption spectra and dissociation processes can easily be studied at high yield. Laser photofragmentation of cold metal

cluster ions should therefore be a particularly rich field of study.[3]

Photodissociation of molecular ions has a firm foundation,[6,7] and already this type of investigation has been extended to a variety of cluster species. Experimenters have used the photofragmentation of molecular cluster ions[8-12] to learn about the "solvation" and "caging" of small organic species in the gas phase. Cluster cations of silicon atoms have been photodissociated[13] and the structure and stability of these species have been inferred from the fragment mass distribution. Cesium cluster cations, generated by field ionization of a continuous metal beam, have been photodissociated and the products subjected to kinetic energy analysis.[14]

Fragmentation of optically excited metal cluster molecules has been inferred from the observation of a decreased ground state population via the reduction in a single-photon ionization signal,[15] and from an abrupt shortening of excited state lifetimes above the apparent dissociation energy in a resonant two-photon ionization scheme.[16] Fragmentation during the photoionization process has been mentioned as an uncontrolled and unwanted experimental byproduct in many metal cluster experiments.[17]

In appropriate circumstances, however, this fragmentation process can be turned into a major advantage. There is a remarkable switch in the experimental implications of radiationless transitions when one turns from neutrals to ions. In the ion, efficient radiationless processes are actually preferred since they ensure eventual fragmentation if the ion is excited above its dissociation limit. Since the daughter ion resulting from this fragmentation can always be detected at high efficiency, one is assured of being able to monitor the spectrum of the cluster ion.

In cases like the transition metal clusters where there are hundreds of low-lying

excited electronic states and these states are intimately coupled to one another, the resulting eigenstates will tend to be fairly global mixtures of the vibrational and electronic motions available at a given total energy. Above the lowest dissociation threshold this means that every eigenstate will contain a small contribution from the dissociation continuum, and dissociation will occur fairly rapidly as soon as it is energetically allowed- regardless of the details of the initially excited state. Although this "vibronic soup" limit is a nightmare for spectroscopy, it is a height for thermochemistry. Simply by scanning the dissociation laser, the binding energy of a cluster may be determined as the lowest energy at which a one- or multi-photon dissociation becomes possible.

Photofragmentation studies are described for mass-selected transition metal cluster ions cooled in a supersonic expansion. The spectral utility of this is powerful technique to accurately determine the electronic structure of the dimer or small cluster ions by monitoring fragment yield as a function of dissociation laser wavelength. For larger, more complicated metal clusters the absorption spectrum is far too congested and perturbed for analysis, but photodissociation can reveal the thresholds and time scales of various fragmentation pathways. The order of the absorption events leading to dissociation is found from the extent of fragmentation as a function of laser fluence.

Smalley et al have measured the binding energy of small iron clusters[3] by using this method. The authors has been found one-photon dissociation threshold of Fe_2^- to lie between 2.43 and 2.92 eV, which determines the binding energy of this transition metal dimer cation; similarly, the threshold for dissociation of Fe_3^+ into Fe_2^+ + Fe was found to lie between 1.17 and 2.18 eV, placing the Fe_3 neutral binding energy between 1.27 and 2.3

8 eV.[3] Far more accurate measurements of these dissociations should be possible by studying cold cluster ion photodisscіation as a function of wavelength. Arguments are presented to the effect that these dissociation thresholds should generally provide valid measures of the true binding energies of transition metal clusters. In this work, the dissociation energies of $^{90}Zr_2^-$, Nb_2^- and Nb_3^--Nb were accurately determined to be 4.184 ± 0.005 eV, 5.907 ± 0.056 eV, and 5.994 ± 0.004 eV.

We also studied multiphotofragmentation of Nb_3^- into Nb_2^- and Nb_1^- products in the range 16,000-17900 cm^{-1} regions. The photofragmentation spectrum of the Nb_2^- exhibits a sharp rise in the background of the spectra at 16,190 ± 10 cm^{-1}. This sharp rise at this energy was not expected with respect to results of collision-induced experiments. We purposed three possible cases in order to explain this sharp rise and we will discuss them in Chapter VIII.

II.2 EXPERIMENT

An instrument which was originally designed by Joseph G. Eaton, Shelley B. Deosaran, John R. Lombardi and Derek M. Lindsay to study gas phase cluster photo-fragmentation using a laser vaporization source and time of flight techniques, was used in this thesis. The simplicity and versatility of this technique provide us with a useful advantage to do different types of experiments from first or higher atomic/molecular ionization energy to electronic structure of charged/neutral molecules. Because of the mass selectivity properties of the technique, all collected data came from the desired molecule. On the other hand, there is no possibility to record any information, which comes from any impurity because mass selection is performed initially, so spectral probes

target only the desired cluster ion, then fragmented and unfragmented particles are counted by this technique. Such flexibility would enable us to study different cluster types, van der Waals, metal and semi-metallic clusters. The primary intention was to maximize the production and extraction of ions formed in the expansion, rather than relying on an electron gun or laser to ionize the neutral clusters produced. Ionization tends to add the unwanted benefit of heating up the clusters. The decision to go via the pulsed route was based on a desire to minimize the pumping requirements of the system. Additionally a pulsed system was ideally suited for time of flight (TOF) mass spectrometry techniques. a second harmonic pulsed YAG (Yttrium Aluminum Garnet) laser was used as the vaporization laser because exceedingly high laser powers were not needed to vaporize even the refractory metals.[1-5] The cluster source needed to be as simple as possible to accommodate the dual role of being able to function as both a regular seeded source and a laser vaporization source. Therefore, a target rod was used due to the easy availability of metals either as sheets (easily cut into target disks) or in powdered form (sintered into disks).[1-6] Though the manipulation of a target rod to obtain a fresh surface was easier, we could obtain adequate rotation and translation with the use of a hypocycloidal planetary gear assembly.[7] The choice of an on-axis beam and the use of a simple ion repeller mass gate, rather than off-axis beam was again to simplify the construction and reduce the need for extraneous ion deflectors and lens. The option to fragment clusters axially, 'head on', as well as trans-axially, was also an important consideration. The instrument as constructed is shown in Fig. 2.1.

The instrument can be viewed as being comprised of three integral parts contained in a vacuum. The first region is laser vaporization source where the clusters are produced.

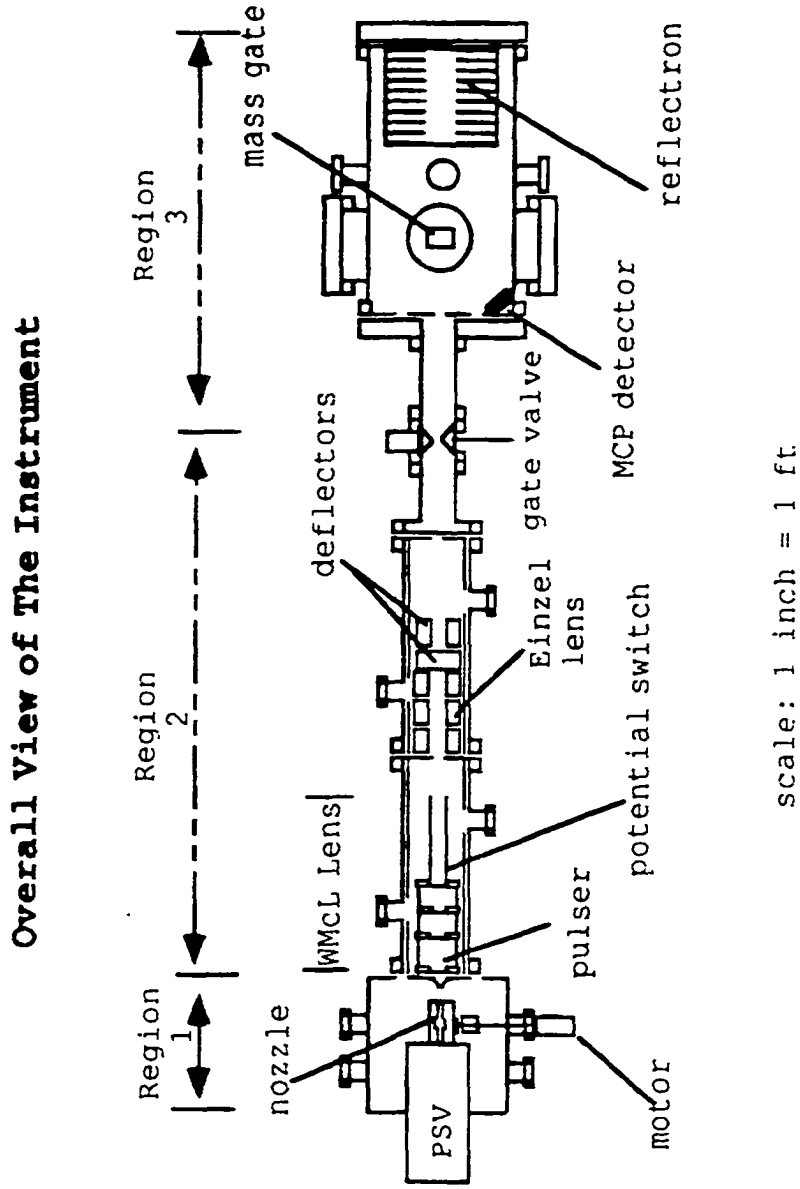

Figure 2.1: Diagram of Time-of-flight (TOF) mass spectrometer with laser vaporization source for production of gas phase metal cluster ions. Viewed from the top looking down.

second region (detection) is linear time-of-flight (TOF) where the produced cluster ions are separated and third region is photofragmentation, mass selection and reflectron(second time-of flight).

II. 2.1 LASER VAPORIZATION SOURCE.

Clusters were produced in the laser vaporization source, which was the most crucial part of this instrument. Laser vaporization sources which produce metal clusters were pioneered by R. E. Smalley.[1-5] The source used here was a modified version of one that was originally designed by Winston A. Saunders.[8] The source shown in Fig. 2.2, consisted of the laser, a pulsed supersonic valve, a Teflon nozzle, a target metal disk and a target rotation assembly with a motor. These were installed in an eight inch cube, which sat above a Balzers turbo pump. The YAG laser vaporized metal from the target disk, producing a "*superheated plasma*"[9] of metal ions.[10] The laser was triggered to fire when the helium pulse was over the target orifice, or in some cases just before it arrived over the target. The helium that was at supersonic flow enveloped the expanding plasma. Plasma collisions within the confines of the dense helium cloud enabled the metal to condense and initiate cluster growth and formation. Further clustering and cooling of the internal degrees of freedom occurred as the gas expanded supersonically while exiting the nozzle into surrounding vacuum.[11] The supersonic expansion coverts the random thermal motion of the gas and its associated energy into directed center-of-mass motion, reducing the translational temperature of the beam.[10] All the particles in the beam then travel at about the same velocity as the helium, given by the following equation:[4]

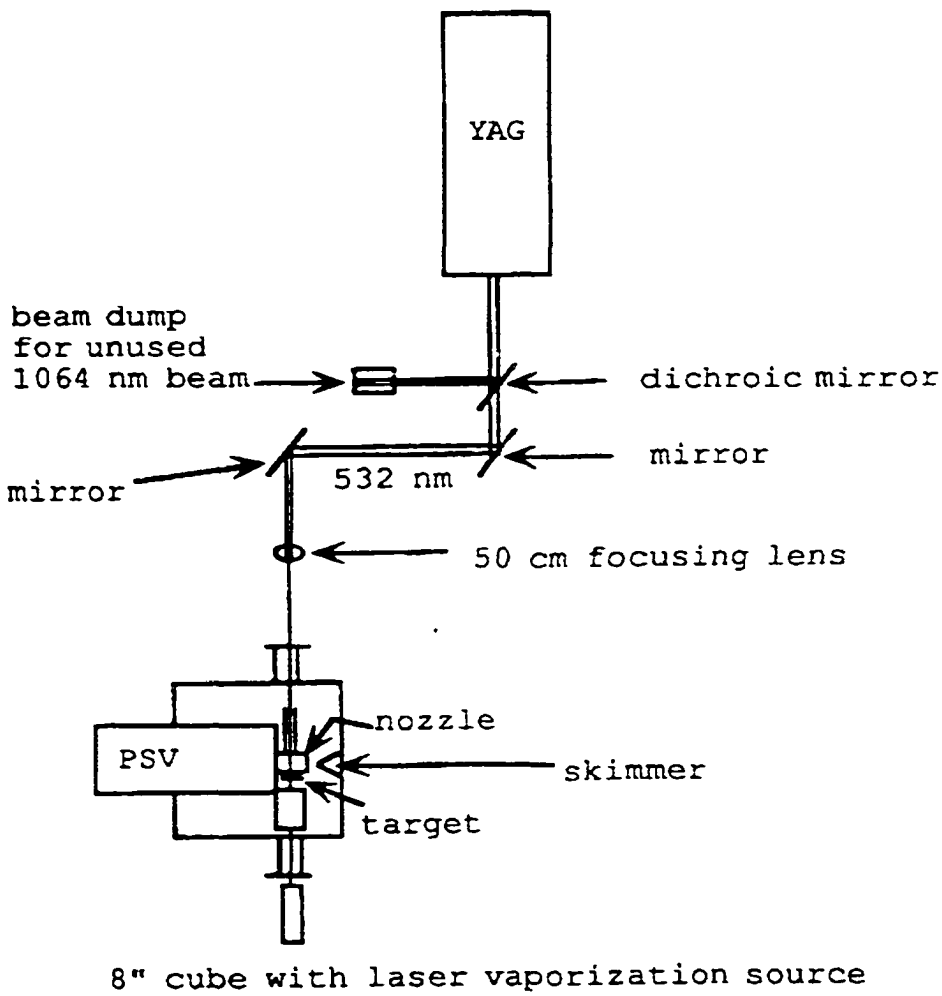

Figure 2.2 : Diagram illustrating how the vaporization laser is focused on the target disk.

$$V \approx (5kT_o/m_{He})^{1/2} \qquad 2.1$$

Where m_{He} is the mass of helium, V is the supersonic velocity, T_o is the temperature of helium before expansion and k is Boltzman's constant. This gives a velocity of about $2x10^5$ cm/s for particles in the beam. Cluster vaporization is achieved with the use of the 532 nm, (second harmonic) green line of a Spectra Physics GCR-11 YAG pulsed laser. The second harmonic of the YAG had a 7 ns pulse width, a pulse energy of 135 mJ at 10 Hz and could be operated at variable repetition rates of 1-10 Hz, when externally triggered. Figure 2.2 also indicates how the laser is directed in the cluster source. The fundamental 1064 nm light was separated and directed to a beam dump by a 45° dichroic beam splitter. The 532 nm laser beam was then guided through a window into the source with the use of two mirrors. The laser beam was brought to a sharp focus in the source. from a 6.4 mm beam diameter to 0.5 mm diameter spot on the target surface; this was achieved by using a 50 cm lens focusing.

II.2.2 PULSED SUPERSONIC VALVE

The pulsed supersonic valve (PSV) was R. M. Jordan valve which operated on the magnetic beam repulsion principle pioneered by Dimov.[12] Magnetic beam repulsion allows for the passage of a 5 kA current of 20 ms duration through a pair of parallel conductors in a 'hairpin configuration', with the current traveling in opposite directions. The opposing flow of current set up a magnetic force, which lifts the top beam from the O-ring seal over

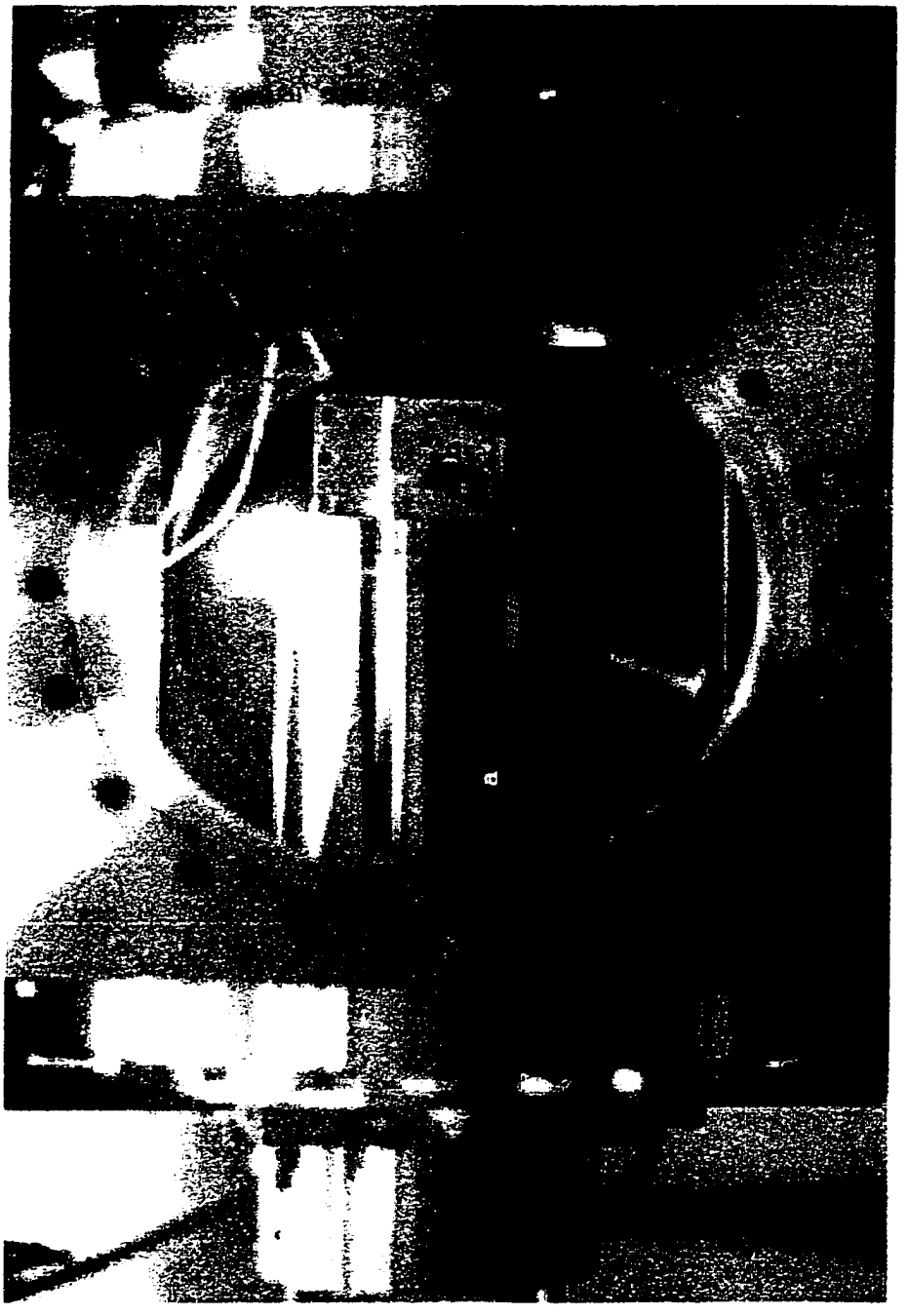

Figure 2.3: Close-up photograph of the source chamber showing the PSV (a) and the Teflon backed nozzle support (b). The dark spot in the center of the nozzle support is the laser orifice.

the nozzle and opens the valve. The valve admits carrier gas into the supersonic free expansion nozzle, which then injects gas pulses of varying widths. The magnitude of the current, the backing pressure of the gas and the elasticity of the 'hairpin' spring determine these gas pulse-widths. The PSV valve shown in Figure 2.3 had a 0.5 mm diameter nozzle, could withstand a backing pressure of 150 psi and was operated at a repetition rate up to 10 Hz. The instrument was normally run at rate of 4 Hz, since at higher repetition rates there was an increased gas load for the pump to handle, which created a very 'noisy' cluster beam signal.

II.2.3. CLUSTER SOURCE NOZZLE

The cluster source nozzle, as shown in figures 2.4 and 2.5, was constructed from two cylindrical sections of Teflon. Both nozzle sections were almost identical and were set up in a mirrored configuration. One part of the nozzle section consisted of two regions, a cylindrical channel (1 mm diameter and length 1 cm), opening out into another cylindrical region (5 mm diameter and length 5 mm). The other section, which formed the front part of the nozzle had an additional region which extended out into a 30 degree angle Laval cone, through which cluster beam supersonic expansion occurred. The size and geometry of nozzle were very important as they determined the cluster size distribution.[10,11]

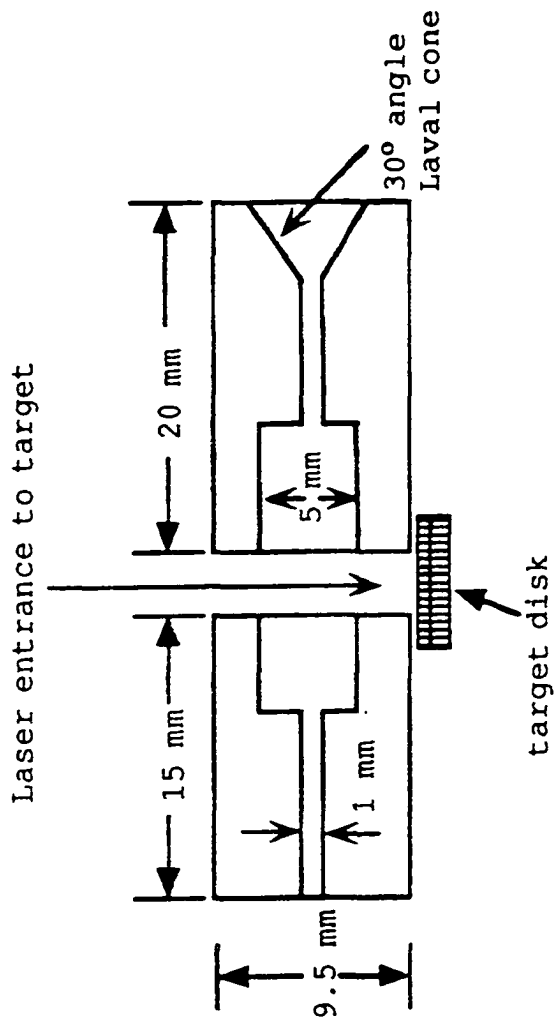

Figure 2.4: Diagram of both halves of the threaded Teflon nozzle insert.

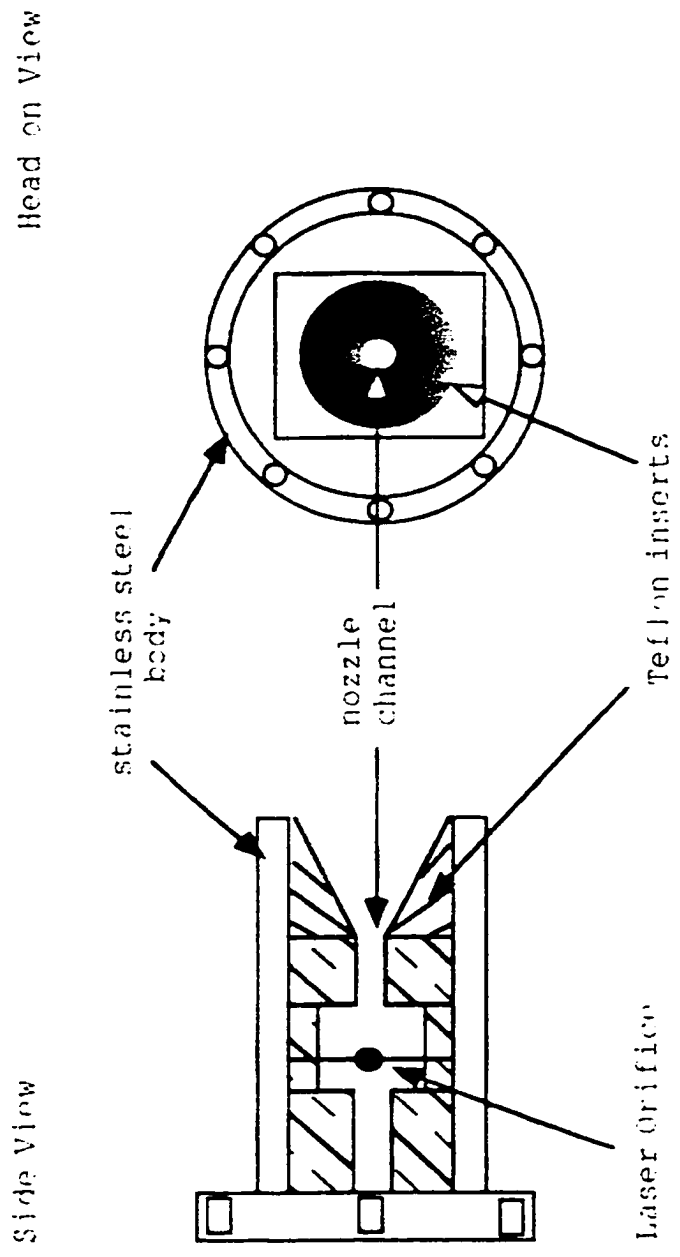

Figure 2.5 : Diagram of the nozzle support with the Teflon nozzle inserts. The nozzle support is bolted to the face of the PSV.

II.2.4. TARGET ASSEMBLY

The target assembly, as shown in Figure 2.6 (A,B,C), consisted of a linear rotation motor, a target holder shaft, a offset coupling, a internal and external gear. The assembly could accommodate targets varying in diameter from 0.8-1.0 inch and thickness up to 0.2 inch. Abrasion formed on the target by the laser removal of target material resulted in the emergence of a hypocycloidal pattern, as shown in Figure 2.7A, on the surface of the target disk. The simulation is a plot of the equation of the form as follows:

$X = R\sin(At)\cos(Bt)$

$Y = R\sin(At)\sin(Bt)$

When the gears were well aligned and the laser was properly focused on the target disk, the 'rosette' pattern of the hypocycoidal shown in Figure 2.7B, is well defined and symmetrical.

II.2.5. THE SKIMMER

Supersonic expansions are usually skimmed[13] to produce lower pressure in the detection region and to produce intense beams with a small range of velocities[14]. The skimmer was a nickel-plated electroformed cone (1 mm diameter entrance aperture and a 20° angle cone of length 5 cm), manufactured by Beam Dynamics. Cluster ions leaving the nozzle expanded outwards upon ejection. The cluster distribution produced in the cluster source therefore needed skimming to select only those clusters with the components of translation motion mainly in the forward direction. The skimmer collimated the ion packet into a narrow beam of ions. Ions that had their velocity components in other directions were not allowed to enter the mass spectrometer, and were instead deflected off the walls of the skimmer.

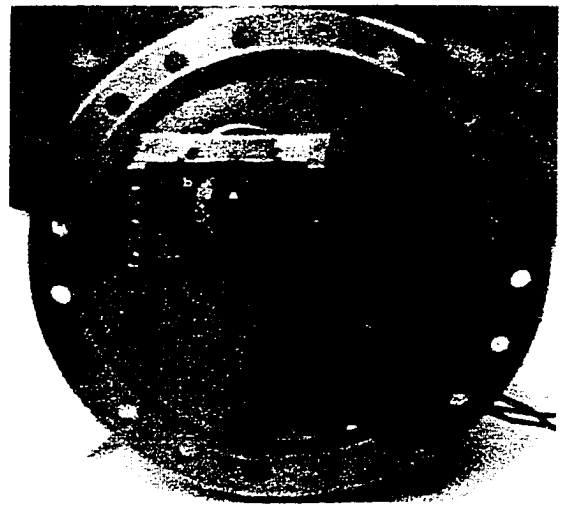

Figure 2.6A: Photograph of the target holder and gear assembly mounted on the 8″ flange. The target (a) is facing the viewer. Also visible is the gear assembly, which surrounds the target. The front piece denoted (b) is the internal gear.

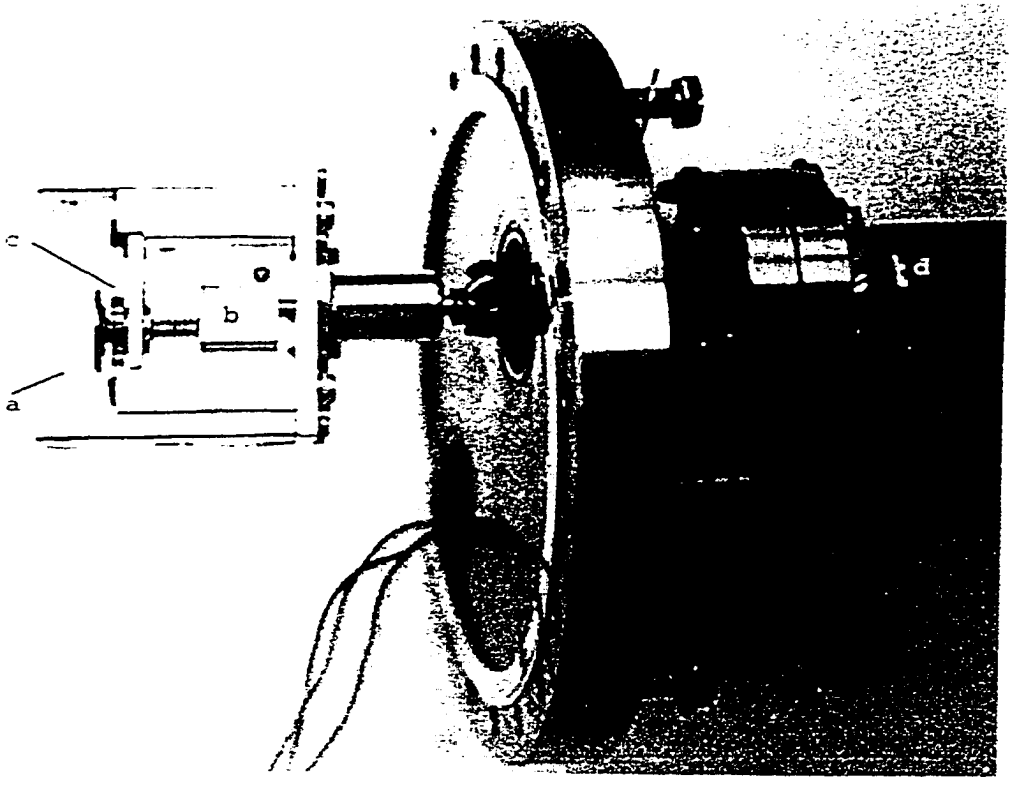

Figure 2.6B : Photograph of the side view of the target holder and gear assembly: (a) target, (b) offset coupling, (c) external gear, and (d) the motor which rotates the target.

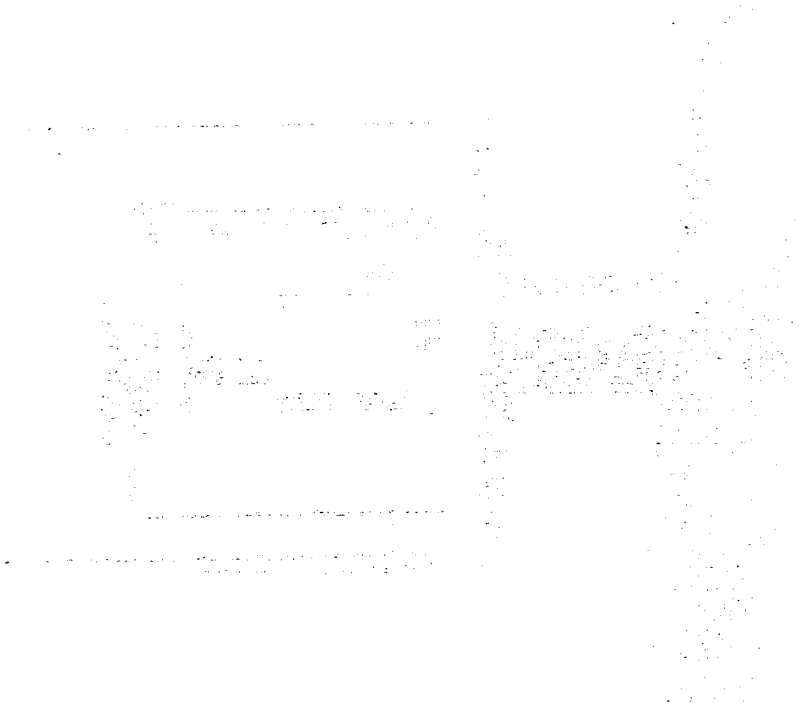

Figure 2.6C : Photograph with a close-up view of the target holder and gear assembly: (a) target, (b) offset coupling, (c) external gear, (d) the block containing the internal gear, and (e) the target shaft with a spring.

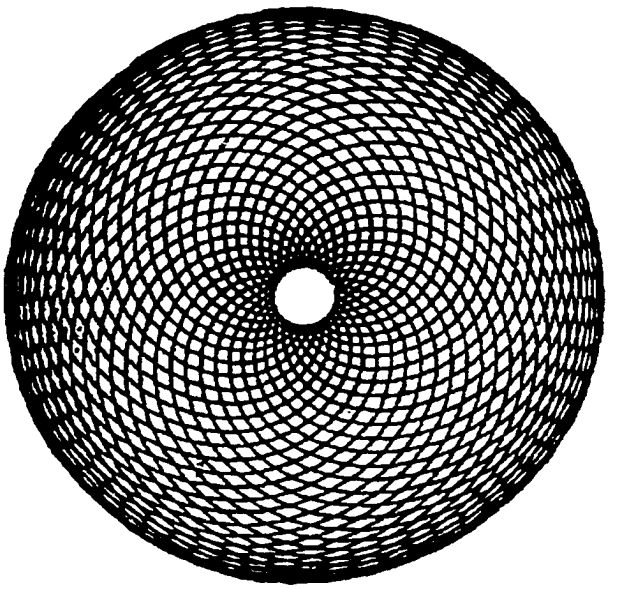

Figure 2.7A : Simulation of the laser burn pattern produced by laser vaporization.

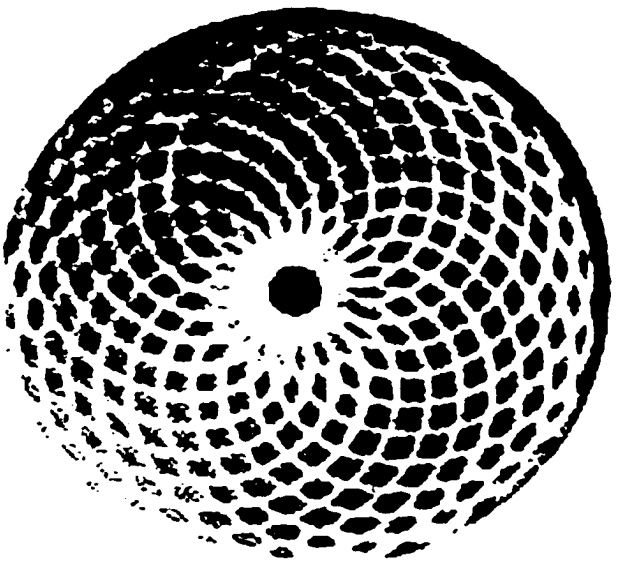

Figure 2.7B : Photo-graph of a niobium target after 100 hours of use.

II.3. THE PRIMARY MASS SPECTRA: LINEAR TIME-OF-FLIGHT (TOF)

The primary mass spectra utilized the technique of time-of-flight mass spectroscopy to characterize the cluster size distribution. At its simplest, this technique could be viewed as a separation of different masses of ions, which by simultaneously pulsing an electrical field, would energize the ions. Allowing them to drift some fixed distance and become separated due to the differing velocities they would have acquired due to the different masses. The technique of TOF mass spectroscopy has undergone a renaissance in the last few years.[5-20] Due to its inherently pulsed nature, its marriage to the pulsed laser, vaporization cluster source was inevitable. Our system was based on the dual field accelerating system devised by Wiley and McLaren.[15] Upon arrival from the source, ion packets with the same mass may contain both an energy and a spatial spread which create a spread in their arrival times at the detector. In order to compensate for this discrepancy a system consisting of three ion lenses and two different electric fields was devised. This lens arrangement is commonly referred to as the Wiley McLaren time-of-flight system. For positively charged ions, a negative field on the third lens attracts the ions forward, while a positive field on the first lens repels them forward. The second (middle) lens separates both fields which are alternately pulsed on and then off. The primary mass spectrometer enabled us to obtain a mass spectrum containing the cluster distribution and relative abundance. It consisted of a Wiley McLaren time-of-flight lens assembly, a set of Einzel lens and a pair of ion deflectors. The cluster ion packet, consisting of positive and negative cluster ions and neutral clusters, exit the nozzle and expand out supersonically with a velocity on the order of $2x10^5$ cm/s. A 100 μs pulse of helium carrier gas can produce a packet of ionic and neutral clusters of varying masses

spread out over a distance of about 10 cm.

II.3.1. WILEY MCLAREN LENS

The entire Wiley McLaren (WMcL) assembly begins just after the skimmer. It is an arrangement of three different sets of lenses, shown in Figs. 2.1 and 2.8. The first lens array consists of a series of 4 stainless steel guard rings. The first ring of this lens series had a 90% transmission grid and subsequent rings were separated from each other with sapphire ball insulators. Each guard ring was in electrical contact with its neighbor via a series of 5.6 kΩ resistors, which enabled the lens array to provide a uniformly decreasing field when pulsed with a voltage for a short time. This set of lenses was maintained at ground potential until pulsed with a positive voltage. Upon arrival within the lens array, the cylindrical volume of ions was subjected to the effects of a rapidly pulsed positive voltage, which repelled the cluster cations forward. The 10 cm length of this lens array restricted the ions centered between its ends to an initial length of 10 cm, (later compressed to 1 cm at the WMcL focus). A Kiethley Instrument 245 Power Supply, supplied approximately +1 kV to this lens, commonly referred to as the 'pulser'.

The Wiley McLaren second lens array consisted of an almost identical set of lens as the previous set, including a 90% transmission grid on the first element. Individual guard rings were likewise physically insulated from each other and similarly connected via a series of 470 kΩ resistors, to provide a uniform field. This lens series was kept at ground potential, and served as a transition for the field change from +1 kV at the first lens array to -2 kV at the third lens. The Wiley McLaren third array consisted of a guard ring similar to the others in addition to a 9.5 inches long stainless steel tube.

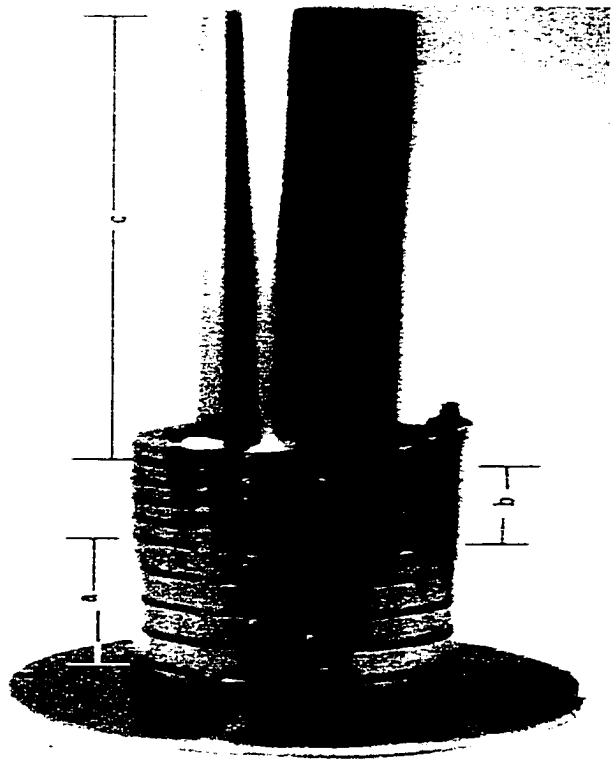

Figure 2.8: Photograph of the Wiley McLaren TOF lens assembly: (a) 1st array (pulser), (b) 2nd lens array, and (c) 3rd lens array (potential switch).

This third set of lens was referred to as the 'potential switch'. It was kept at a potential of -2 kV, which was supplied by a Bertan 205B-03F, high voltage power supply. This lens was rapidly pulsed to ground as the ions entered the potential switch. The field change accelerated the positive ions forward and repelled negative ions off the flight tube axis, neutral clusters were unaffected by either of the charged fields. The ions' ground potential at the end of Wiley McLaren lens system were defined as -2 kV, the potential switch was switched to ground to redefine it to earth ground, causing the ions to be re-referenced to earth ground. The total array, about 40 cm long, was supported on a triangular arrangement of rods.

Those ions that entered the first lens array early were repelled less strongly than the ones that arrived after. This compensated for the fact that the earlier ones had a higher velocity while the latter ones were slower. By the time they have reached the Wiley McLaren focus 1 meter downstream from the second lens, the slower ions have caught up to the faster ones and the original ion packet 10 cm long would be compressed to less than 1 cm in length. An ion's arrival time at the focus could be calculated (since we know the various lens voltages, distances and relative masses of the ions) using equations devised by Wiley and McLaren:

$$T_{total} = T_s + T_d + T_D \qquad 2.2$$

where the time is viewed as the sum of the time for the three different regions of the mass spectrometer as illustrated in Fig 2.9.

$$T_s = 1.02[m / (2qU_t)]^{1/2}[2k_o^{1/2} S_o] \qquad 2.3$$

m is the mass of the ion in amu, while U_t, the ion's energy in eV, is given by the following expression:

$$U_t = -V_d + V_s S_o/S \qquad 2.4$$

where $-V_d$ is the potential switch voltage, V_s is the pulser voltage, S is the distance between the start of the pulser and the second lens and so is the distance between the ion and the beginning of the pulser as shown in Fig. 2.9. k_o is an instrument constant defined as follows:

$$k_o = (S_o V_s + dV_d)/(S_o V_s), \qquad 2.5$$

d is the distance shown and T_d is the time it takes to travel through the distance d given by:

$$T_d = 1.02[m/(2qU_t)]^{1/2}(2k_o^{1/2})(k_o^{1/2}+1)^{-1}d \qquad 2.6$$

T_D is the time it takes to transverse the field free region, where D is the distance (1 m), from start of the potential switch to the Wiley McLaren focus.

$$T_D = 1.02[m/(2qU_t)]^{1/2}D \qquad 2.7$$

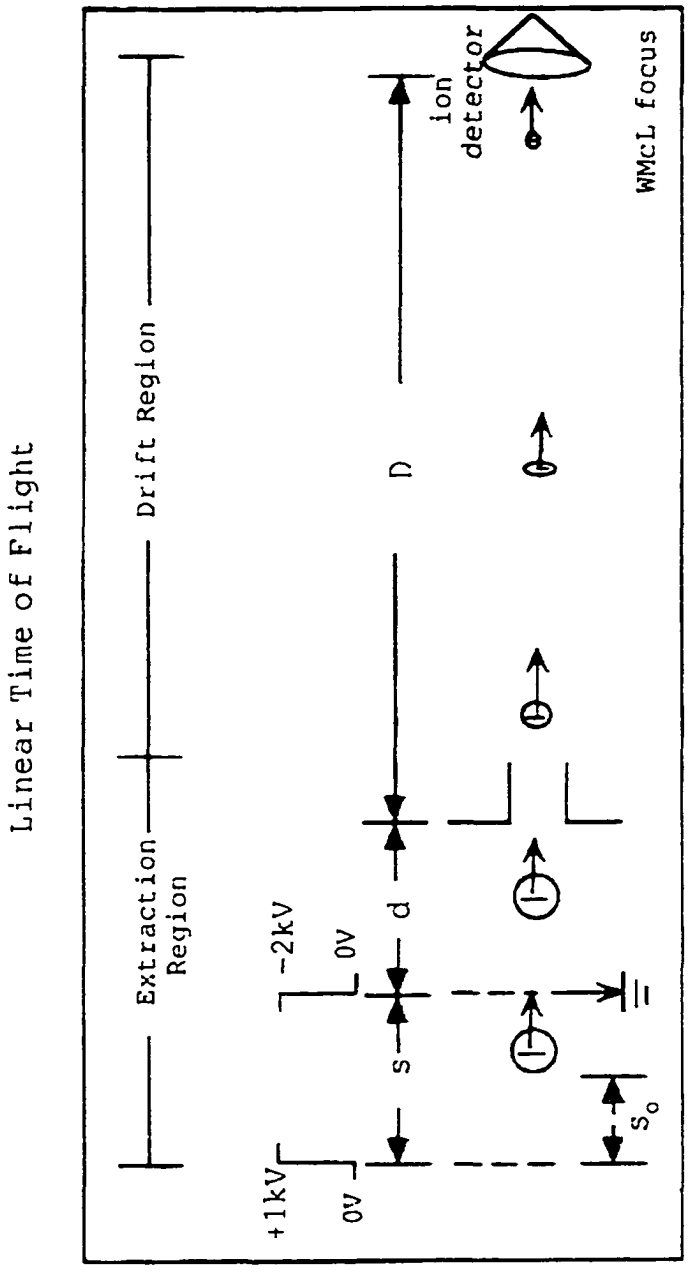

Figure 2.9: Schematic of Wiley-McLaren TOF lens setup indicating the various regions, voltage pulses and parameters. An ion packet is shown narrowing as it approaches the Wily-Mclaren focus where the detector is located. When mass selection is being performed, the mass gate is situated at the focus.

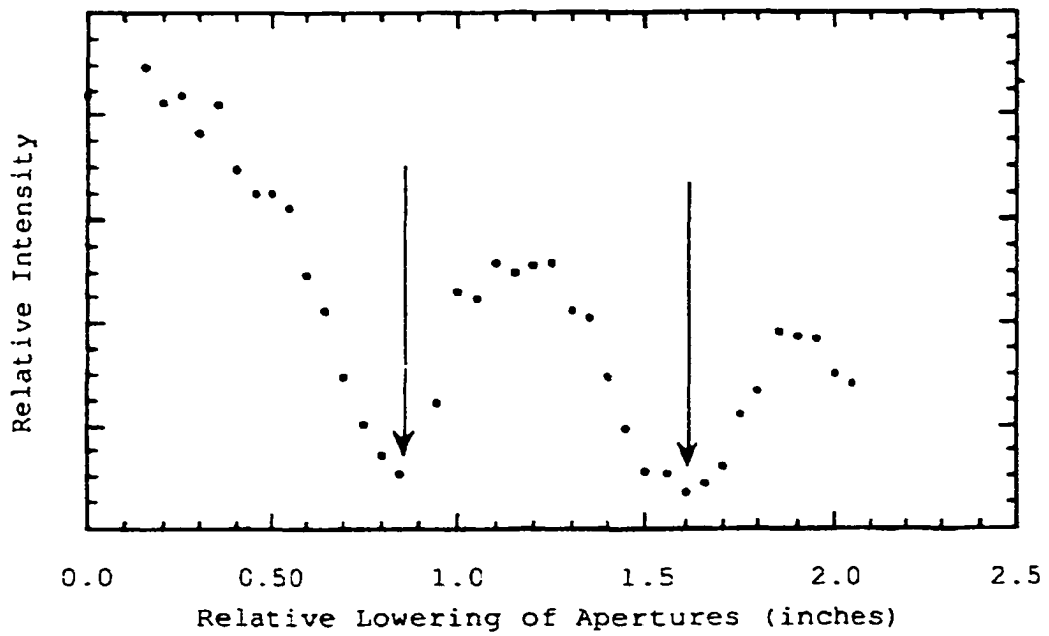

Figure 2.10: Plot of ion intensity vs relative lowering of three different sized apertures (1". 0.5", and 0.25"). The beam width was extracted out from the only region on the curve where three is an increase. a maximum and a decrease in ion intensity (shown by the arrows).

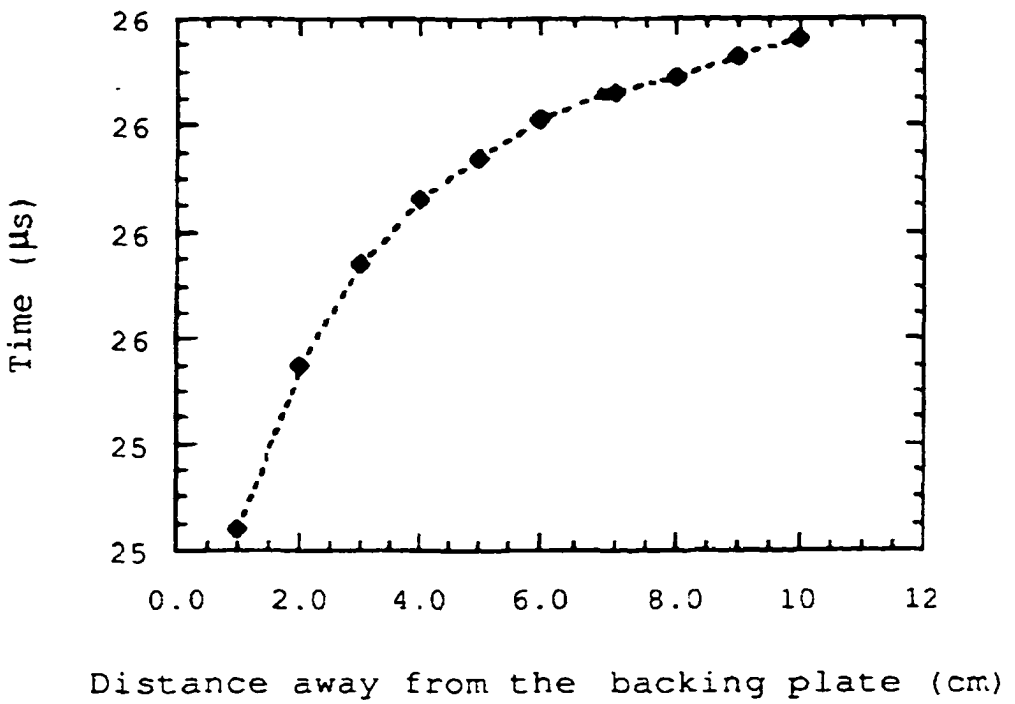

Figure 2.11: Plot of time spread of the arrival time of Nb_2^- at the WMcL focus dimer as a function of distance from the backing plate of the first element of the pulser lens.

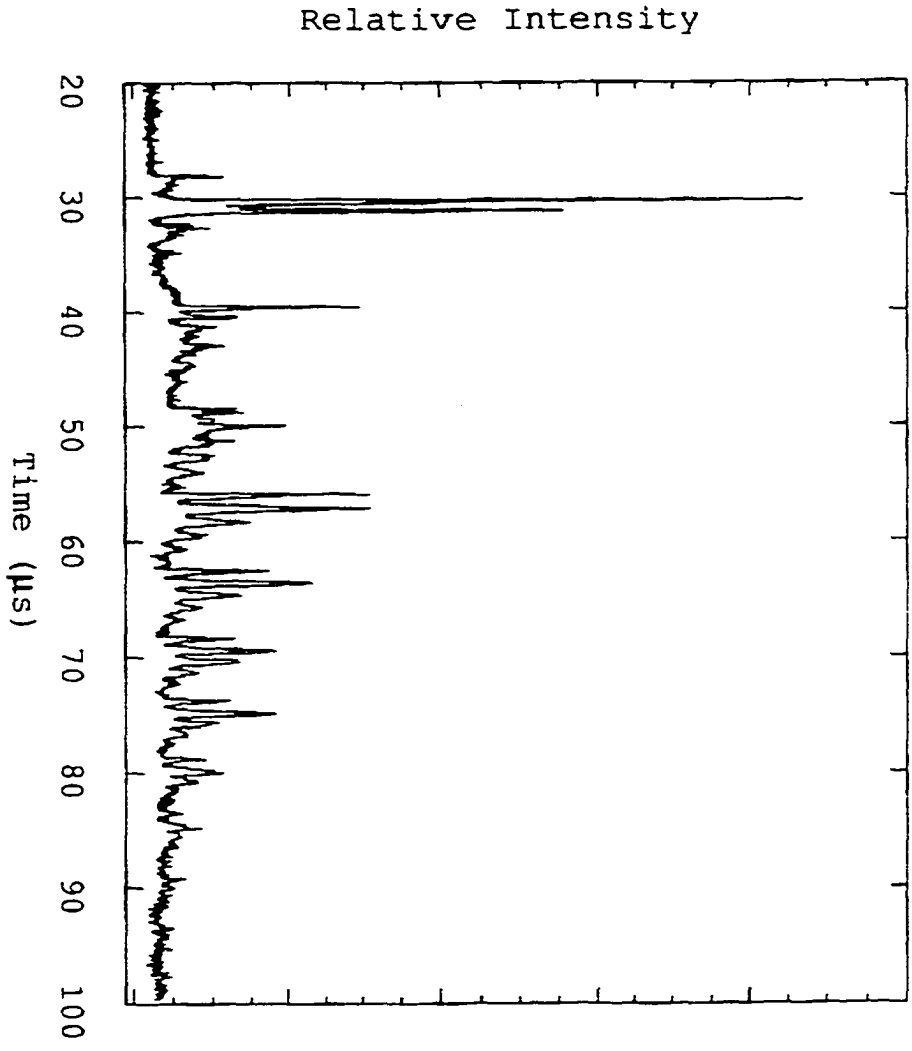

Figure 2.12A: Mass spectrum of Nb_n^- and $NbnO_m^-$ cluster cations, where n =1 to 10 and m ≤ 4.

Finally the combined expressions are given in Eq. 3.8

$$T_{total} = 1.02\{m/(2qU_t)\}^{1/2}\{ 2k_o^{1/2} S_o + 2k_o^{1/2} (k_o^{1/2}+1)^{-1} d + D\} \qquad 2.8$$

The Wiley McLaren TOF lens spatially focuses the ions with the same charge to mass ratio (q/m) at the mass gate, which is located 1 meter away from the start of the third Wiley McLaren lens. These ions of similar masses which were temporally and spatially compressed (10 cm down to 1 cm), still contained a significant energy spread. Slow ions had been speeded up to meet the fast ions at the transient Wiley McLaren focus. The originally slower ions would eventually pass the initially faster ions once they have passed the focus and the ion packet would eventually spread out again. It was essential that we did the primary mass selection and laser photo-fragmentation at or near the Wiley McLaren focus, where the ion packet was at it's shortest length; this is the rationale for the position of the mass gate. The width of the ion beam was measured at the mass gate by lowering a metal plate with three apertures, (diam. 0.25 inch. 0.50 inch and 1.00 inch, respectively) across the beam and measuring the ion beam intensity through each aperture. Fig. 2.10 shows a plot of ion beam intensity vs. the relative lowering of the apertures. The ion beam was shown to have a width of approximately 0.5 inch diameter. The focusing characteristics of the spectrometer are shown in Fig. 2.11, (plot of arrival times of the Nb_2^- versus it's position away from the grounded front plate). The ions that were further away from the plate achieved a sharper focus at those particular operating voltages. A spreadsheet was used to calculate estimated flight times as well as spread in ion arrival times at various voltage conditions and distances (spreadsheet calculations setup shown

Table 1. Spreadsheet set up to calculate Wiley-McLaren linear Time-Of-Flight (TOF) arrival times of the niobium dimer cation. Where S, S_o, d, D in cm, Vs, V_d, U_{tot} in volt, M in amu, and t in μs. T_{tot} = t(W-McL) + t(fft)

S	S_o	d	V_s	$-V_d$	K_o	D	M	U_{tot}	t(W-McL)	t(fft)	T_{tot}	ave. T/ st.dev. T
10	1	5	850	2,000	24.53	100.00	185.8	2085.00	3.92	21.53	25.45	
10	2	5	850	2,000	13.76	100.00	185.8	2085.00	4.66	21.10	25.76	
10	3	5	850	2,000	8.84	100.00	185.8	2085.00	5.24	20.70	25.94	26.08
10	4	5	850	2,000	6.88	100.00	185.8	2085.00	5.74	20.32	26.06	0.286
10	5	5	850	2,000	5.71	100.00	185.8	2085.00	6.18	19.96	26.14	
10	6	5	850	2,000	4.92	100.00	185.8	2085.00	6.58	19.62	26.20	
10	7	5	850	2,000	4.36	100.00	185.8	2085.00	6.95	19.30	26.25	
10	8	5	850	2,000	3.94	100.00	185.8	2085.00	7.29	18.99	26.28	
10	9	5	850	2,000	3.61	100.00	185.8	2085.00	7.62	18.70	26.32	
10	10	5	850	2,000	3.35	100.00	185.8	2085.00	7.93	18.42	26.35	

Table 2. Spreadsheet set up to calculate Reflectron TOF arrival times for Nb_2^+ and Nb^+.

E(p)	phi	M(p)	M(f)	U(f)	D	V_r	L_r	t(L)	t_{ref}	t_{tot}	Y(f)	av./Y(f)	ave. t	Ytot	ave.Ytot
Volt	degree	amu	amu		cm	V	cm	μs	μs	μs	cm	st. dev.	μs	μs	μs
2050	6	185.8	93.9	1036	11.7	3,000	39	8.42	3.42	11.84	1.67	2.037	11.434	5.77	6.137
2150	6	185.8	93.9	1087	11.7	3,000	39	8.22	3.05	11.72	1.75	0.246	0.241	5.85	0.230
2250	6	185.8	93.9	1137	11.7	3,000	39	8.04	3.58	11.62	1.83		11.434	5.93	
2350	6	185.8	93.9	1188	11.7	3,000	39	7.87	3.66	11.53	1.92		11.434	6.02	
2450	6	185.8	93.9	1238	11.7	3,000	39	7.70	3.74	11.44	2.00		11.434	6.10	
2550	6	185.8	93.9	1289	11.7	3,000	39	7.55	3.82	11.37	2.08		11.434	6.18	
2650	6	185.8	93.9	1339	11.7	3,000	39	7.41	3.89	11.30	2.16		11.434	6.26	
2750	6	185.8	93.9	1390	11.7	3,000	39	7.27	3.96	11.23	2.24		11.434	6.43	
2850	6	185.8	93.9	1440	11.7	3,000	39	7.14	4.03	11.17	2.32		11.434	6.42	
2950	6	185.8	93.9	1491	11.7	3,000	39	7.02	4.10	11.12	2.40		11.434	6.65	

in Table 1 and 2). A mass spectrum of niobium cluster cations is shown in Fig. 2.12A, and Fig. 2.12B shows a plot of ionic mass vs. arrival time (μs), where one observes that the arrival time of the various ions scale as the square root of the mass.

II.3.2 ION LENS & DEFLECTORS

The ion beam required a set of ion lens (Einzel lens) to guide it down the flight tube. These consisted of three stainless steel cylindrical lens located after the TOF lens (see Fig. 2.2). The lens were tuned to focus the ions transversely at the longitudinal focus of the Wiley-McLaren TOF mass spectrum. Using the SIMION (ion simulation software package),[22] we obtained an optimal Einzel lens focusing voltage of 1200 volts. The Einzel lens voltage was supplied by a Bertan high voltage power supply. The deflectors which were located just after the Einzel lens, are a set of two horizontal and two vertical stainless steel plates. These plates deflect ions horizontally and vertically along the beams axis, thereby minimizing the loss of ions. They both required very small voltages to keep the beam aligned. The use of SIMION simulation software in correctly estimating the Einzel lens voltage (minimized the deflector requirement).

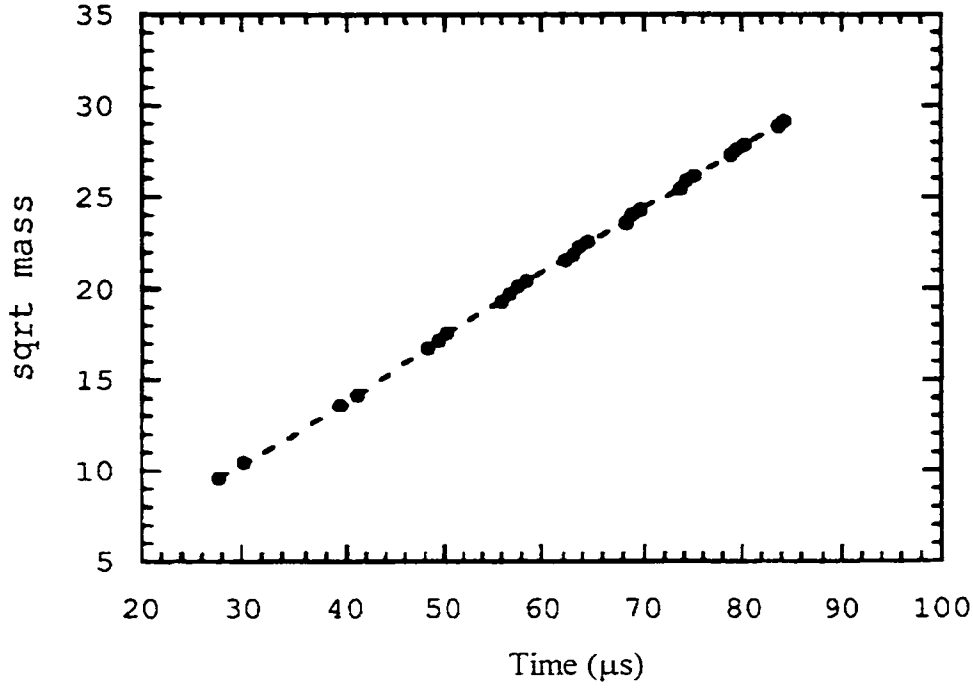

Figure 2.12B: Plot of the square root of the ion's mass vs. the arrival time of ion for niobium and niobium oxides. This plot indicates that linear relationship between $m^{1/2}$ and the arrival time of the cation is:

Nb^-	NbO^-		
Nb_2^-	Nb_2O^-		
Nb_3^-	Nb_3O^-	$Nb_3O_2^-$	
Nb_4^-	Nb_4O^-	$Nb_4O_2^-$	$Nb_4O_3^-$
Nb_5^-	Nb_5O^-	$Nb_5O_2^-$	$Nb_5O_3^-$
Nb_6^-	Nb_6O^-	$Nb_6O_2^-$	
Nb_7^-	Nb_7O^-	$Nb_7O_2^-$	
Nb_8^-	Nb_8O^-	$Nb_8O_2^-$	
Nb_9^-	Nb_9O^-		

II.4. MASS SELECTION, FRAGMENTATION & DETECTION

Our experiment involved selecting a particular size cluster and subjecting it to irradiation from a YAG pumped dye laser. The effects of the irradiation (e.g. increase, decrease and absence of fragmentation as well as changes in fragment energies and fragmentation times) were investigated with the use of a reflectron mass spectrometer and a dual plate microchannel detector. The reflectron mass spectrometer was also a secondary mass spectrometer, which compensated for the energy spread in the ion beam and thus improved the resolution of the instrument.

11.4 .1. MASS-GATE

The study of size-selected cluster ions required the isolation of selected ion packets (ions with the same mass). Mass selection was based on the following principle: at the transient focus the ion beam consists of packets of ions grouped according to their masses, lighter ions followed by heavier ones. From spreadsheet calculations, we could easily assign a mass and arrival time to each packet of ions. Knowing the mass and time of a chosen ion packet, we can 'close' the mass-gate thereby blocking entrance to all ions, and 'reopen' it just as 'the selected ions' arrived and then 'close' it again once these ions have passed through the mass-gate.

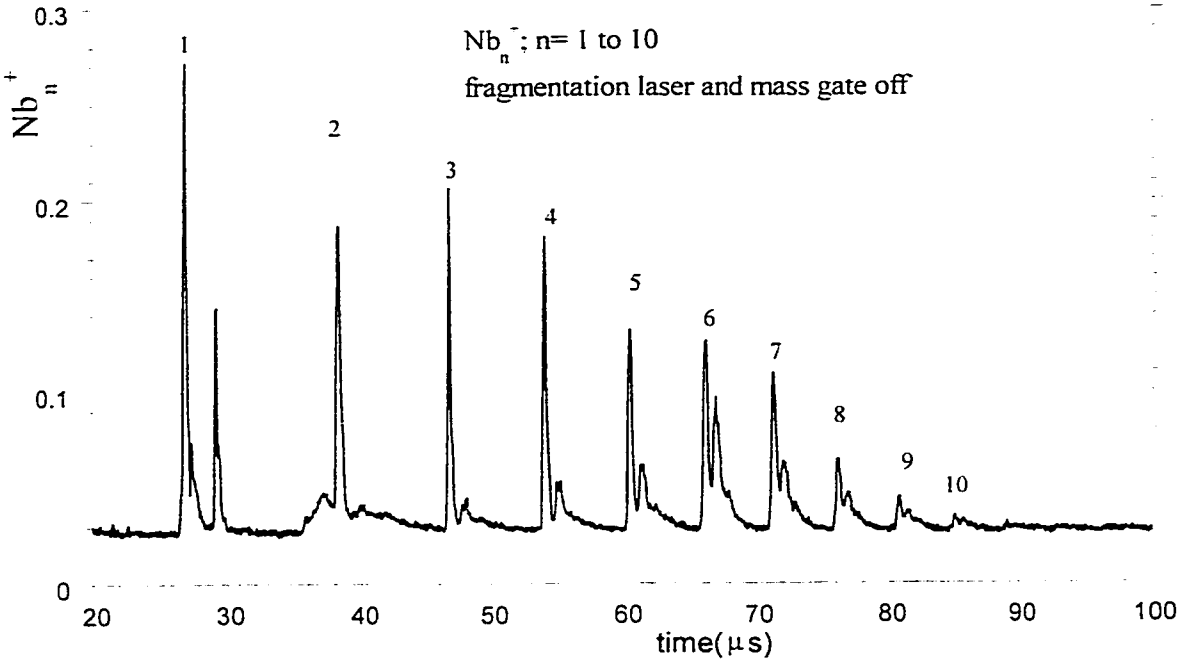

Figure 2.13A: Mass spectrum of niobium cluster cations Nb_n^+, n=1 to 10, in the absence of the mass gate.

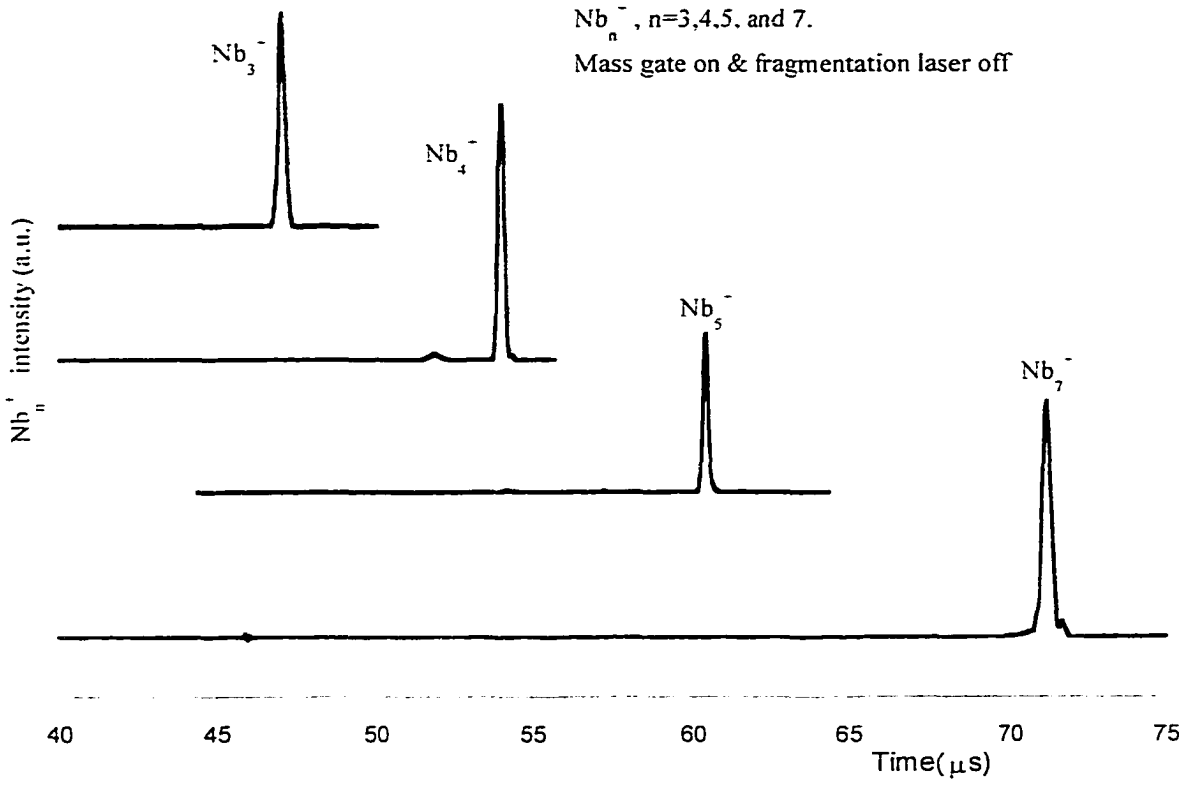

Figure 13B: Mass spectrum of mass selected Nb_n^-. n=3, 4, 5, and 6, when mass gate was on and the fragmentation laser was off.

Mass selection was achieved with the use of a pulsed ion repeller mass-gate, located at the transient focus of the Wiley-McLaren lens. The mass-gate was a simple affair consisting of two parallel metal plates, suspended parallel to the path of the cluster beam, one plate was above the ion beam and the other below it. Both plates were biased with a voltage of +300 volts, which formed a positive field between the plates and resulted in deflection of positive ions off the flight tube axis. At the precise moment that the ion of interest approached the mass-gate, the deflection voltage was pulsed to ground thereby enabling the passage of the selected ion species into the reflectron region. The pulse activating the mass gate needed to be both narrow (on the order of a few hundred ns) and to also have a very fast rise time (on the order of a few ns). Pulse switching was accomplished with a Behlke HTS 31 fast high voltage switch (supplied by Eurotek Inc., NJ. USA) with a turn-on rise time of less than 10 ns. It was pulsed to ground for approximately 200 ns (this corresponded to the resolution of the counter timer plug-in board which was limited to 200 ns) giving the ability to select ion packets approximately 400 ns apart. Once the mass selected ions were through the mass gate, the voltage was pulsed on again, preventing the passage of other ionic masses. When the mass gate was off, all ions were admitted to the reflectron mass spectrometer. Figure 2.13A shows a mass spectrum of niobium cluster ions (transmission of all ions) with the mass gate off and Fig. 2.13B shows a mass spectrum of one ion, (transmission of a selected cluster ion) when the mass gate was turned on.

II.4.2 SECONDARY MASS SEPARATION

Secondary mass separation was achieved with the use of a R. M. Jordan single stage reflectron mass spectrometer. The reflectron assembly that was 20 cm deep and 15 cm in diameter, consisted of a combination of plates with grids and mesh which when powered, combined to create a uniform electric field within the reflectron. It was inclined at an angle of 6° relative to the cluster beam, and situated just after the mass gate (see Figs. 2.1 and 2.2). Figure 2.14 is a photograph of the reflectron mounted on a 12 inch flange. The reflectron was housed in a large 'T-shaped' chamber (12 inch diam.). A large chamber was required so that the ion beam, when reflected by the reflectron's 'ion mirror', curved around and was focused on the detector located at the lower front of the chamber. The entrance to the reflectron was held at the beam potential of 3 kV and the rear were biased so that ions of interests were reflected at 50% - 90% of the total depth.

The reflectron was an ion reflector based on the system pioneered by Mamyrin et al.[21] It compensated for the energy spread present in the ion packet that was due to the distribution of initial ion positions along the length of the extraction cylinder. Ion packets of the same mass were spatially and temporally compressed at the WMcL linear TOF focus, however once past the focus they were decompressed because of their original spread in energy. The reflectron resolved problems due to the energy spread in the ions. High-energy ions of the same mass penetrated deeper through the reflecting fields than low energy ions of 'the same' mass. Ions that penetrated deeper, spent more time in the reflectron and so allowed low energy ions to catch up at a focal plane in the field free region as they exited the reflectron. Narrower mass peaks well spaced in time (better resolution) was the result. Ions of different masses entering the reflectron coincidentally

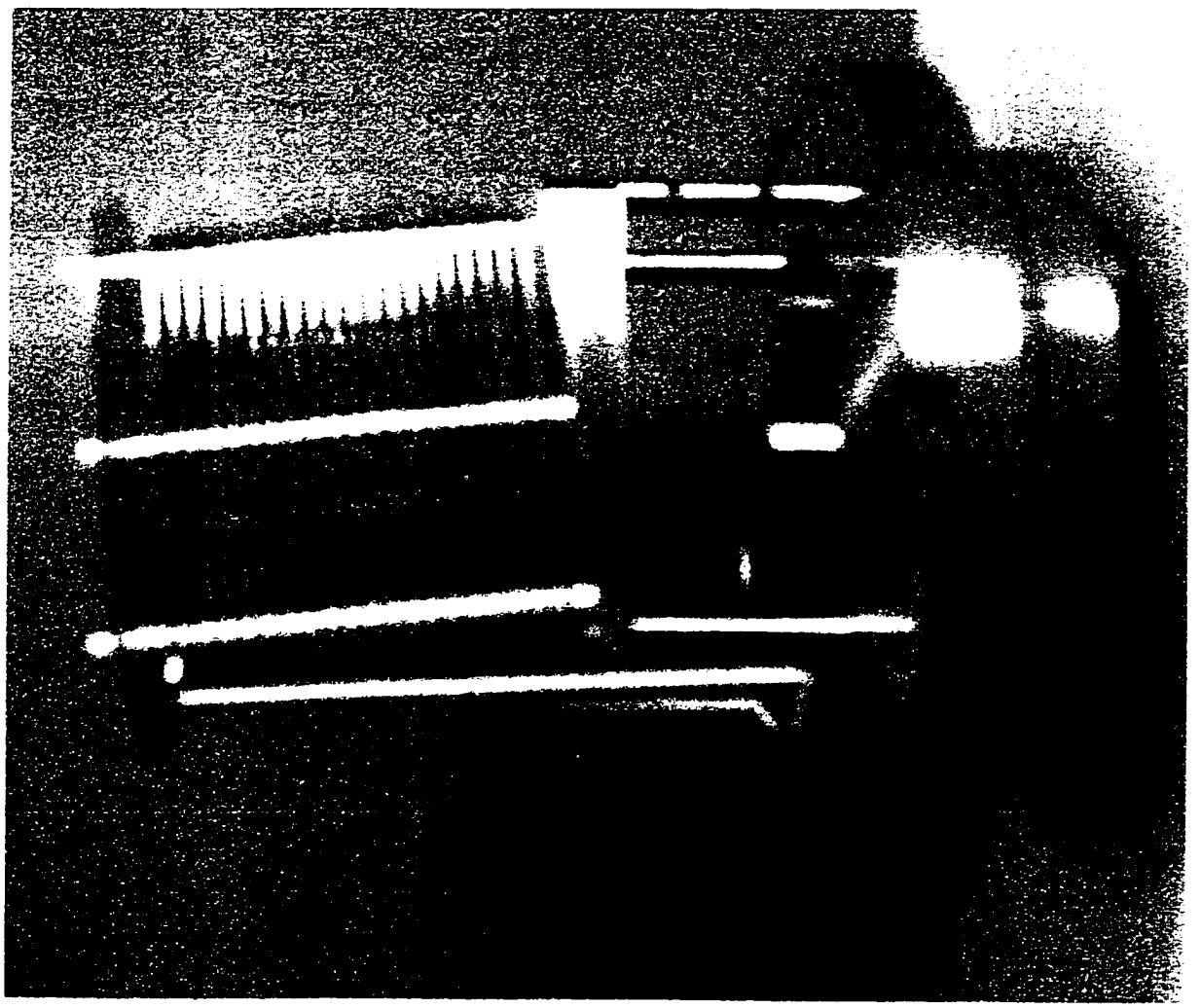

Figure 2.14: Photograph of the reflectron TOF assembly mounted on the 12″ flange. Clearly visible is the plate with grids.

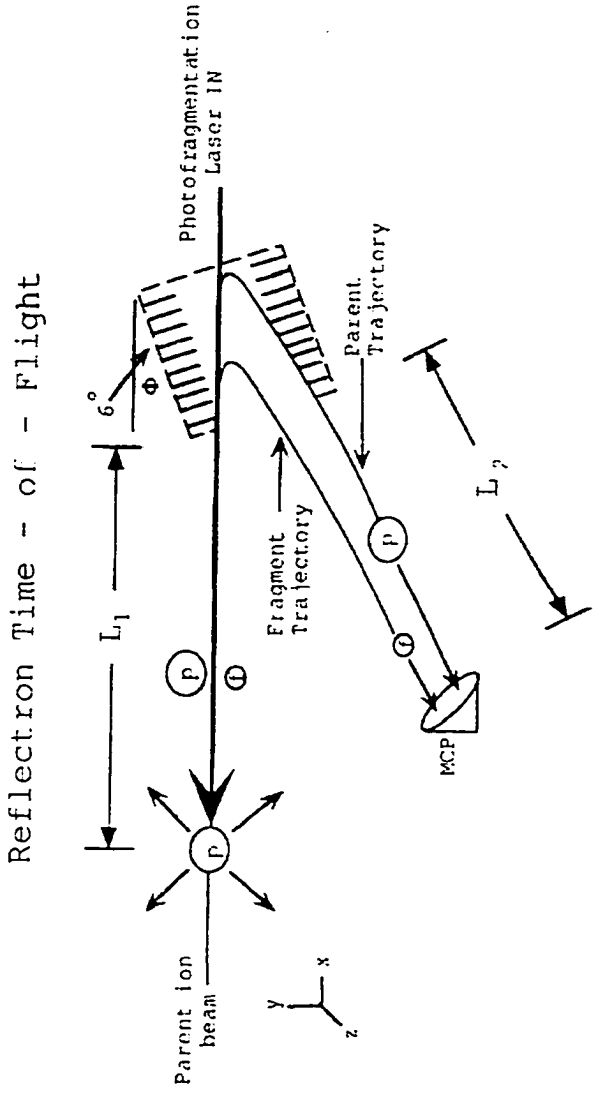

Figure 2.15 : Schematic of reflectron TOF showing an ion (p) breaking up to produce a fragment ion (f). The trajectories of both ions are shown entering and exiting the reflectron. Also shown are the free flight regions L_1, L_2, and the coordinate axes.

focus in a manner such that the heavier ions penetrated deeper into the reflectron and thus arrived at the focus where the detector is located, after the lighter ions had arrived. In this manner when ions were photofragmented, the daughter fragments could be resolved from the parent ions even though they would have had the same energy when they entered the reflectron. The equations used to calculate the time spent in the reflectron (t_{ref}) were developed as follows: The axes (x, y) were set up with origin at the entrance point of the reflectron. The positive x-axis was parallel to the incoming beam, and positive y-axis was defined so that the z-axis was perpendicular to the paper (a right hand coordinate system) with ions moving from left to right, (Fig. 2.15)

$$F_x = mdv_x/dt = -qE_x = -qE\cos(\phi) \qquad 2.9a$$

$$F_y = mdv_y/dt = -qE_y = -qE\sin(\phi) \qquad 2.9b$$

where the subscripts x and y refer to the x and y components, and F, V, m and q are force, velocity, mass of the parent ion and charge of the ion respectively, E is the electric, field strength and ϕ is the tilt angle of the reflectron (ions are deflected by 2ϕ).

$$v_x(t) = -qE\cos(\phi)t/m + v_x(0) \qquad 2.10a$$

$$v_y(t) = -qE\sin(\phi)t/m + v_y(0) \qquad 2.10b$$

where $v_x(0) = (2U/m)^{1/2}$, $v_y(0) = 0$ and U is the ion kinetic energy.

The energy of the ions is the same before entering and after exiting the reflectron.

$$2U/m = (v_x(t))^2 + (v_y(t))^2 = \{-qE\cos(\phi)t/m + (2U/m)^{1/2}\}^2 + \{-qE\sin(\phi)t/m\}^2 \qquad 2.11$$

solving for t by squaring, canceling and using $\sin^2\phi + \cos^2\phi = 1$ gives

$$t = (2m)\cos(\phi)\{qE(m/2U)^{1/2}\}^{-1} \qquad 3.12$$

The factor of 2 comes about because the ions make two passes through the reflectron (going in and coming out).

$$t_{ref} = (2D/V_{ref})\cos(\phi)m^*(2U/qm)^{1/2} \qquad 2.13$$

where t_{ref}, m^* can be either the mass of the parent or daughter ion (when calculating parent arrival or daughter arrival respectively) , D is the depth of the reflectron and V_{ref} is the reflectron voltage.

The time spent in the field free region t_L is given as follows:

$$t_L = L\cos(\phi)(m/2qU)^{1/2} \qquad 2.14$$

where $L = L_1 + L_2$ (L_1 is the length of the region from WMcL focus to the beginning of the reflectron and L_2 is the length of the region from the beginning of the reflectron to the detector) . Time spent in both the field free region and the reflectron. t_{total} is given by:

$$t_{total} = L\cos(\phi)\{m/2qU\}^{1/2} + 2D/V_{ref}\cos(\phi)\, m^*\{2U/qm\}^{1/2} \qquad 2.15$$

Arrival times of ions through the reflectron and total flight times (from pulser through reflectron and to the detector) were also calculated using a spreadsheet calculation.

II.4.3 FRAGMENTATION LASER

The fragmentation laser was a Spectra Physics YAG pumped PDL-3 Dye laser system. There were two configurations for cluster fragmentation, (1) coaxial fragmentation, (collinear and counter propagating to the ion beam) and (2) trans-axial, (perpendicular to the ion beam). In the perpendicular configuration, the laser entered through a side port and intersected the clusters as they emerged from the mass gate. This configuration involved a measure of difficulty especially in the space/time overlap between the cluster beam and the pulsed laser. The advantages of this arrangement are as follows: (1) absence of a noisy background due to photo-ions from the laser hitting the mesh or other metal hardware, (2) no significant laser reflections off the metal walls within the chamber would reach the detector, (3) it was easier to monitor the laser power by measuring it as it exited the chamber after interaction with the cluster ions. The axial configuration was chosen because it was simpler to align and gave earlier success. The laser entered the chamber through the rear of the reflectron TOF, and was positioned to interact with the clusters at the linear TOF focus (mass gate). This point was ideal for fragmenting the clusters because the ion packets had been spatially and temporally compressed to their smallest dimensions thereby providing the best overlap between the laser and cluster beam. Co-axial fragmentation however had some significant drawbacks, which were: (1) by going through the reflectron, the laser encountered some of the wire meshes which provided field uniformity, laser/mesh interactions gave rise to ejected photo-ions which reach the microchannel plate detector and created a noisy signal at times, (2) the laser could hit everything coming down the flight tube, including larger ions, before they arrived at the mass gate. Laser beam/ion beam overlap alignment presented problems

which were aggravated by the non-uniform laser beam power density profile and variations in laser pointing when dyes were changed. One also assumed that the cluster density was uniform across the collimated beam, however this was not necessarily so. Therefore, on-axis alignment could still result in detected ions not being exposed to the laser pulse and thereby creates a nondepletable background. The laser diverged slightly to produce a quasi-uniform beam. Power measurements were made by passing the laser through a glass slide set at a 45° angle and measuring the power of the 90° reflected light with a very sensitive power meter. The glass slide was calibrated at different powers and wavelengths to correlate the laser's reflected and transmitted powers. Laser fluence was determined by assuming that the pulse energy was uniformly distributed over a circle of radius 0.5 cm, to give an area of 0.785 cm^2.

II.4.4 ION DETECTION

Mass spectra were obtained by adjusting the extraction voltages and associated delays, together with the ion optics until the spatial focus of the mass spectra was at the ion detector. At first we used a large Faraday plate with the output to an oscilloscope to obtain crude mass spectra, however we finally opted for two dual microchannel plate detectors (Galileo MCP-18B), 40 mm and 25 mm diameter, respectively, supplied by R M Jordan & Co. Each detector was coupled to a 50 Ω anode assembly. One MCP was situated at the end of the flight tube in the absence of the reflectron, the other which was enclosed in conical structure, was positioned at the lower front of the reflectron chamber directly in the path of ions exiting the reflectron (see Fig.2.2). Microchannel plate detectors are costly, fragile and tend to degrade with use, however they were ideally

suited for handling fast ion pulses and provided high gain with a sub- nanosecond rise time. The signal from the MCP was acquired using a LeCroy 9450A digital oscilloscope to display a fresh cluster mass spectrum at the 4 Hz repetition rate of the experiment.

II.4.5. INSTRUMENT CONTROL AND DATA ACQUISITION

Combined software and hardware control enabled the instrument to function and thus acquire and store data effectively. Figure 2.16 gives an outline of the experiment. The operator was required to set the parameters that determined cluster distribution and intensity, while the computer coordinated the functions of the different components that made up the laser vaporization dual TOF mass spectra. Inherent delays between the various devices required microsecond adjustments to synchronize the individual event that each one controlled. The entire experiment was a combination of several synchronized events. Timing parameters were set by the operator and controlled by the computer. The pulsed supersonic valve initiated the cycle with a burst of helium, followed by a pulse from the vaporization laser, which fired at the peak of the helium pulse. This burst of laser power effectively vaporized material from the rotating metal target disk. Smalley *et al.*[1-5]

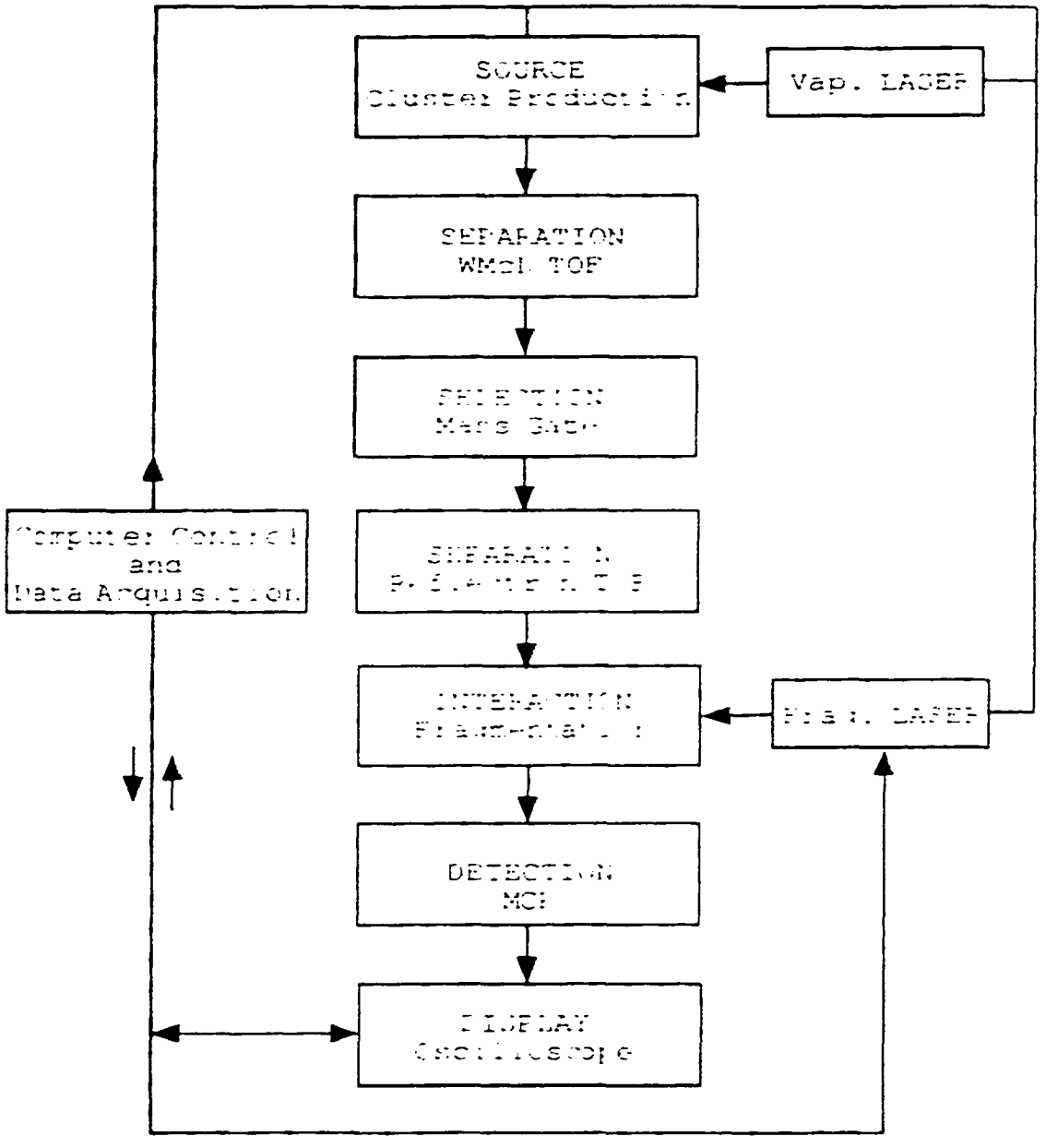

Figure 2.16 : Block diagram illustrating the data acquisition and control outline.

have determined that the vaporization laser should be fired at the peak of the helium pulse when it's density over the target is at the highest so that the vaporized metal could be effectively blanketed and thermalized. The potential switch which was maintained at a negative potential of -2 kV (it was necessary to supply it with -2.4 kV to obtain an effective output voltage of -2 kV) for the purpose of studying positively charged cluster ions was pulsed to ground potential next. A negatively charged field induced by the potential switch provides an attraction to the positively charged clusters increasing their velocity in the forward directions. Within a few microseconds of the pulsing of the potential switch, the first WMcL lens (pulser), is switched from ground potential to a positive potential of +850 V. This field provides a forward 'kick' to the positive ions. During the tuning of the source the mass gate was kept at ground potential to allow the passage of all ions to the detector. Tuning refers to the act of adjusting the control parameters e.g. voltages, timing delays, laser power and helium backing pressure. An optimized cluster ion distribution exhibited peak repetitiveness, maximized stable intensities and smooth peaks with narrow widths.

Mass selection occurred by the turning on/off of an electrical field which deflected ions off the flight tube axis effectively blocking their passage. This electrical field which is kept at +300 V was pulsed off (to ground potential) to coincide with the arrival of a chosen cluster mass. By pulsing the field off for extremely short time periods (200 ns) it was possible to isolate clusters of a particular size and thereby enable the study of individual cluster species.

Following cluster mass selection, the isolated cluster species were observed closely on the oscilloscope using an expanded timescale to determine whether metastable

fragmentation was occurring. Metastable fragmentation of vibrationally hot clusters is a normal occurrence in molecular beams whereby a small proportion of ions break apart enroute to the detector producing daughter ion fragments.[4] It cannot be totally eliminated, however it could be minimized by adjusting the source conditions to prevent over heating of the cluster ions produced. Minimization of metastables was a necessary step; because to observe effective frgmentation, there must be a maximum cluster intensity with a minimum metastable ion production. It would be difficult to distinguish between daughter ions from laser induced fragmentation and daughter ions from metastable decomposition if the production of metastable ions was left unchecked. Figure 2.17A shows the Nb_4^- cation together with Nb_3^-, Nb_2^- and Nb^- ions produced from metastable Nb_4^- ions in the absence of the fragmentation laser; Fig. 2.17B shows the daughter ions produced by laser induced fragmentation. Following the elimination or minimization of metastable decomposition, proper overlap between the fragmentation dye laser and the cluster beam was necessary to achieve maximum cluster fragmentation. The cycle of events, began with the pulsing of the supersonic valve and ended with the measurement of the dye laser power. Although it could be performed at a rate of 10 Hz, the existing conditions favored operating at 4 Hz. The signal acquired by the oscilloscope was averaged for 400 shots of the laser, approximately 100 seconds, after which the intensities of the parent and daughter peaks and the average background intensity were extracted and stored by the computer. The dye laser wavelength was incrementally scanned while a waveform plot of cluster intensity versus wavelength was updated on the computer monitor.

A Dell Dimension XPS 60 personal computer with an Intel Pentium microprocessor, two serial ports (RS 232), a 540 megabyte hard drive and 24 megabytes

of random access memory, running Microsoft Windows 3.2 operating system coordinated the operation of the various devices. The data acquisition and control system included three National Instruments interface boards (PC TIO-10 Data Acquisition board, Lab PC+ Data Acquisition board, and a IEEE 488.2 AT- GPIB). (For more information see Ref. Deorasan.)[23]

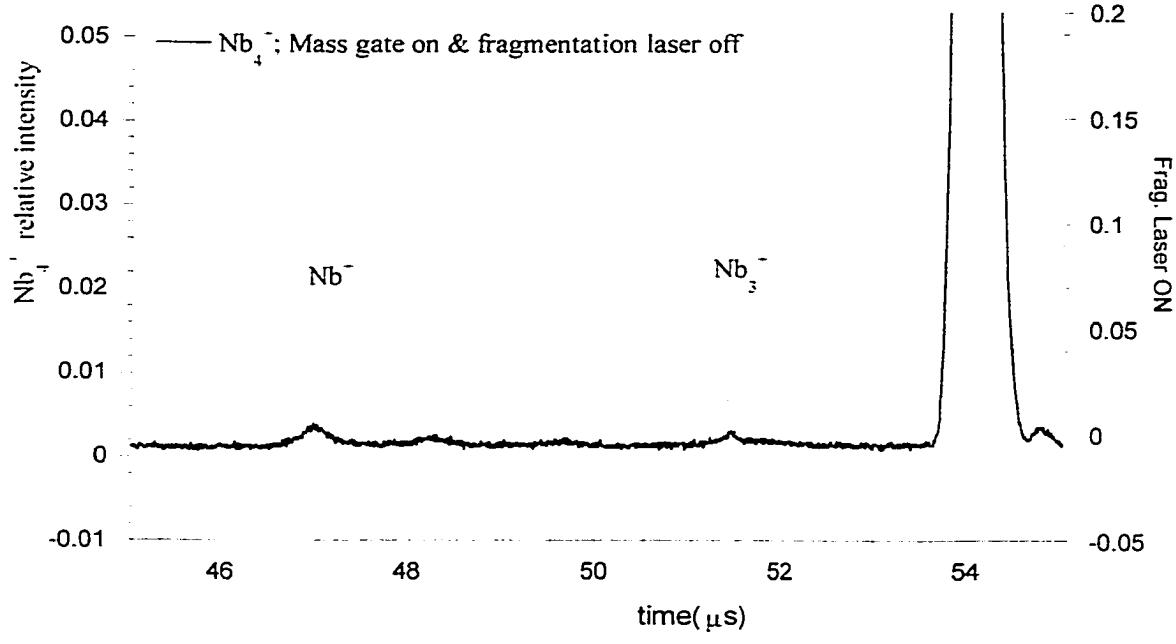

Figure 2.17A: Mass spectrum of Nb_4^- showing some metastable daughter ions (Nb^- and Nb_3^-). The Nb_4^- peak is off scale because this plot has been expanded to show the metastable fragment ions.

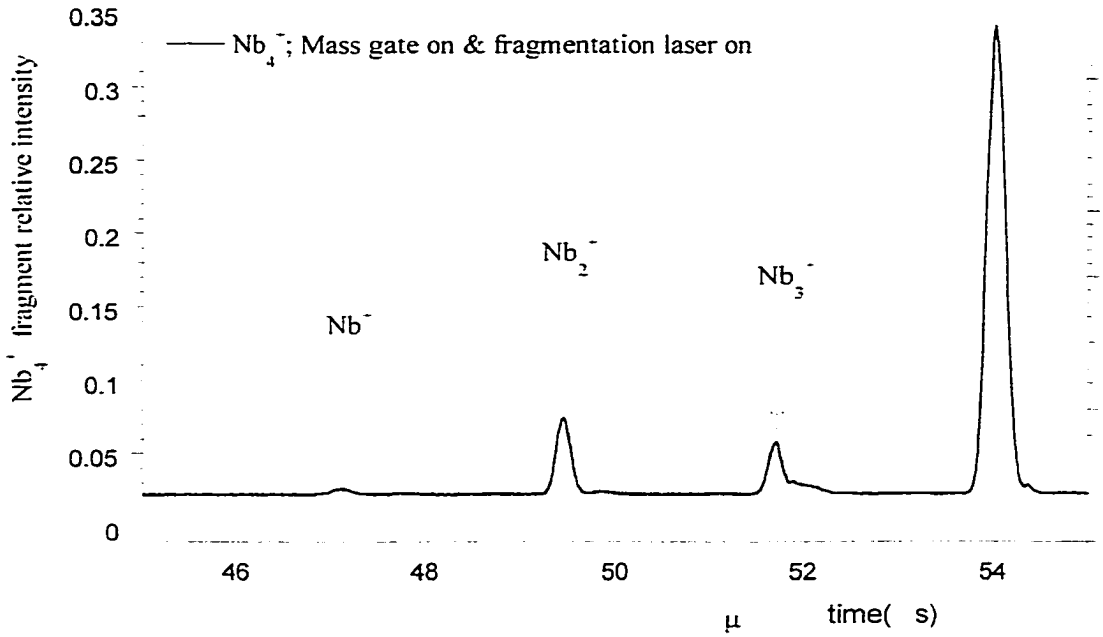

Figure 2.17B: Mass spectrum of Nb_4^- after fragmentation to produce daughter ions: Nb_3^-, Nb_2^-, and Nb^-.

Chapter II References

1) Y. Liu, Q. L. Zhang, F. K. Tittel, R. F. Curl and R. E. Smalley, J. Chem. Phys., 85, 7434 (1986).

2) D. E. Powers, S. G. Hansen, M. E. Geusic, D. L. Michalopoulos and R. E. Smalley, J. Chem. Phys., 78, 2286 (1983).

3) P. J. Brucat, L. S. Zheng, C. L. Pettiette, S. Yang and R. E. Smalley, J. Chem. Phys., 84, 3078 (1986).

4) D. E. Powers, S. G. Hansen, M. E. Geusic, A. C. Puiu, J. B. Hopkins, T. G. Dietz, M. A. Duncan, P. R. R. Langridge-Smith and R. E. Smalley, J. Chem. Phys., 86, 2556 (1982).

5) S. Maruyama, L. R. Anderson and Richard E. Smalley, Rev. Sci. Instrum., 61, 3686 (1990).

6) P. Milani and W. A. deheer, Rev. Sci. Instrum., 61, 1835 (1990).

7) P. Gangopadhyay and J. M. Lisy Rev. Sci. Instrum., 62, 502 (1991).

8) W. A. Saunders, Department of Physics, Swiss Federal Institute of Technology - Lausanne, Switzerland.

9) P. K. Carroll and E.T. Kennedy, Contemp. Phys., 22, 61, (1981).

10) P. C. Engelking, Chem. Rev., 91, 399 (1991).

11) O. F. Hagena, Rev. Sci. Instrum., 63, 2374 (1992)

12) G. I. Dimov Pribory I Technika Experimenta, Nuclear Physics Institute, Academy of Sciencea of the USSR, No.5, pp. 168-171, (1968).

13) J. M. Hayes, Chem. Riv., 87, 745 (1987).

14) J. M. Pendlebury and K. F. Smith, Contemp. Phys.,28, 3, (1987).

15) W. C. Wiley and 1. H. McLaren, Rev. Sci. Inst., 26, 1150, (1955).

16) J. A. Syage and J. Steadman, Rev. Sci. Instrum.,61, 1204 (1990).

17) a) H. Haberland, H. Kornmeier, C. Ludewight, A. Risch and M. Schmidt, Rev. Sci. Instrum., 62, 2368 (1991)

b) H. Haberland, H. Kornmeier, C. Ludewight, A. Risch and M. Schmidt, Rev. Sci. Instrum., 62, 2621 (1991)

18) D. S. Cornett, M. Peschke, K. LaiHing, P. Y. Cheng, K. F. Willey and M. A. Duncan, Rev. Sci. Instrum., 63, 2177 (1992)

19) R. T. Laaksonen, D. A. Goetsch, D. W. Owens, D. M. Poirier, F. Stepniak and J. H. Weaver, Rev. Sci. Instrum., 65, 2267 (1994) .

20) W. Begemann, S. Dreihofer, G. Gantefor, H. R. Siekmann, K. H. Meiwes-Broer and H. 0. Lutz, Springer Ser. Mater. Sci., 230 (1988).

21) B. A. Mamyrin, V. I. Karataev, D. V. Shmikk and V. A. Zagulin, Sov. Phys.-JETP., 37, 45 (1973).

22) SIMION PC Version 4.0, courtesy D. A. Dahl, Indaho Natl. Lab. Idaho Falls, ID 83415, USA.

CHAPTER III

PHOTOFRAGMENTATION SPECTROSCOPY OF THE NIOBIUM AND ZIRCONIUM CATION CLUSTERS

III.1. ION PHOTOFRAGMENTATION SPECTROSCOPY

Ion photofragmentation spectroscopy, otherwise known as ion photodissociation spectroscopy, refers to any study using ion dissociation, in which a photofragment is observed directly as the carrier of the information sought.[1] It can also be viewed as optical spectroscopy performed on gas phase ions. The difference, however is that instead of measuring the change of photon flux through the sample, the effect of the photons on the sample is observed.[2] Ion dissociation can occur when an ion absorbs one or more photons with a greater total energy than the bond energy of a particular state. This may occur because of several reasons[3-9]: (1) excitation directly into a repulsive state from which dissociation occurs directly, (2) absorption to a bound excited state, followed by internal conversion to a lower electronic state whose energy may be greater than the bond dissociation energy, resulting in dissociation, (3) dissociation via the absorption of more than one photon. The simplest example of case 3 is infrared multiphoton dissociation which does not involve excitation to a different electronic state, only rapid sequential absorption of photons to reach the dissociation limit at the top of the Morse potential well. Case 1 is termed direct dissociation, and may be characterized by a structure-less absorption spectrum for the parent ion and would tend to occur very fast, on a timescale of about 100 femtoseconds. Case 2, on the other hand, presents several interesting possibilities because of the predissociation phenomenon that makes it occur on a longer

timescale (t > 1 picosecond). This phenomenon may be characterized by a structured absorption spectrum, which indicates the presence of a potential well for the excited state, followed by dissociation (brought about by tunneling through a potential barrier or by change of electronic state near a curve crossing).[3] A structured absorption spectrum (narrow peaks that have a semblance of order) may contain details (vibronic and rovibronic states) of the predissociation mechanism for the ion. Figure 3.1 gives a conceptual illustration of dissociation and predissociation.

The detection of ionized fragments produced in ion dissociation provide information such as the dissociation channels, measurement of the photodissociation cross section and dissociation energies. Photodissociation cross sections are essentially equivalent to absorption spectra when predissociation occurs rapidly.[9] Detailed studies of the photofragments may also be carried out to determine the kinetic energy, angular distribution and internal energy of an ion. Laser induced fluorescence (LIF) and resonant two photon ionization (R2PI), two of the best spectral techniques used in the spectroscopy of ions, are difficult to apply to metal cluster studies. They both require that the laser induced transition to an excited electronic state have a long enough lifetime for its fluorescence (LIF) or lowered ionization potential (R2PI) to be detected. In transition metal clusters, there exist many close low lying electronic states with the possibility of a dense manifold of vibronic states. Radiationless transitions between these states will be very rapid, preventing the detection of LIF and R2PI and rendering both techniques ineffective;[4,5] photodissociation spectroscopy overcomes this problem. In the case of photodissociation spectroscopy, the only requirement to obtain a

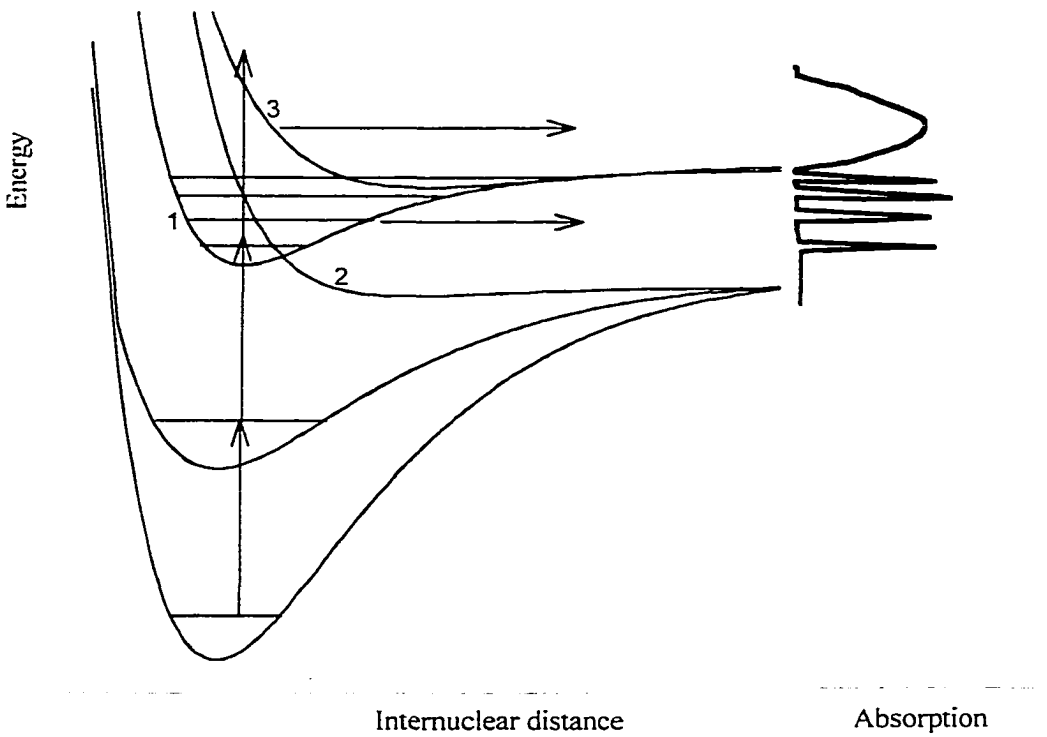

Figure 3.1 A conceptual diagram illustrating dissociation and photodissociation for cases 1, 2 and 3.

dissociation spectrum is that the cluster dissociates upon photon absorption. This can be carried out either as a single color dissociation or as a two color dissociation using two different color lasers. One of the lasers may be set at a frequency to excite the ion to a virtual state, while the other would be scanned to dissociate the ion as a function of the laser wavelength or vice versa.

A primary difficulty of photofragmentation experiments had been the production of ions in sufficient densities, a problem that is only now being overcome. Typically ions would be produced by using an ArF laser to ionize neutrals clusters produced in an expansions. This, however, has the unfortunate tendency of producing ions in various states of excitation, which when photofragmented result in congested spectra. The preferred method is to use a cluster ion source with a supersonic expansion to produces cooler ions. The cooling collisions experienced by these ions lead to drastic reduction of the temperatures for the translational (T_t), vibrational (T_v) and rotational (T_r) degrees of freedom, compared to the temperature of the environment. Possible temperatures obtained by this method are $T_t < 20K$, $T_v < 100$ K and $T_r < 50K$. The level of cooling achieved in the ion is heavily dependent on the prevailing source conditions at the time.[10,11] Cooling the ions does not necessarily imply that one will obtain uncongested spectra. If the ion contains a high density of states, as is expected for some transition metal ions, the possibility exists that unquenched low lying states might be observed under conditions that would normally be expected to cool them to their electronic ground state, resulting in a congested spectrum.[12,13]

III.2 PHOTOFRAGMENTATION OF Nb_2^+, Nb_3^+, Nb_4^+, and Zr_2^+

III.2.1 INTRODUCTION

Niobium (Group VB) and zirconium (Group IVB) transition metals belong to the 4d transition series, Niobium has a valence electronic configuration of $4d^4 5s^1$ and oxidation states of +2, +3, +4 and +5. Zirconium has a valence electronic configuration of $4d^2 5s^2$ and oxidation states of +2, +3, and +4. Niobium, which has no known isotopes and a propensity for clustering, has been the subject of many studies, including reactivities, binding energies, spectroscopy, dissociation energies and theoretical. There is, however, very little information concerning the nature of the bond in the niobium dimer cation[5,14-21], the niobium trimer cation,[28, 48] and the niobium tetramer cations.[28, 48, 47] Also as far as we can tell, there is no any information on the zirconium dimer cation.

III.2.2 EXPERIMENTAL

Niobium and zirconium clusters were generated by vaporizing niobium and zirconium metal (Goodfellow, 99.99%), then mass analyzed in the Wiley-McLaren TOF mass spectrometer. The cation clusters were initially mass selected and the desired cluster was fragmented with light of varying wavelength from a YAG-pumped PDL-3 dye laser. Typical scan conditions were given in Table.1.

The intensities of both the daughter and the parent ions were collected as a function of the dye laser wavelength. Four hundred laser shots were averaged at each wavelength increment and the result stored by the computer. Intensities of the parent and daughter ions and the background level were measured in volts, with the laser power and wavelength in mW and nm respectively. Parent ion intensity was on average about 2.0±

0.5 V for Nb_2^+, 150±50 mV for Nb_3^+, 200± 50 mV for Nb_4^+ and 150± 30mV for $^{90}Zr_2^+$. Relative intensities were calculated by normalizing the daughter ion intensity to the parent intensity by using the following equation:

$$\frac{\textbf{(Daughter – Background)}}{\textbf{(Parent + Daughter -Background)(Fluence)}} \qquad 3.1$$

Niobium dimer, trimer, and tetramer cation clusters were investigated between 15,000 – 21,000, 16,000-17,900, and 16,060-17,980 cm^{-1} regions, respectively. The dizirconium dimer cation ($^{90}Zr_2^+$) was investigated between 16100-18450 cm^{-1} region. Scans were performed using the following dyes: Rhodamine 590, Coumarin 500, Coumarin 540A, DCM, Sulfarhodamine 640, Kiton Red 610 and Fluorescein 548.Wavelength shifting of those dyes were also carried out to cover areas in between the dye range. Fluences for the yellow dyes were typically 60 mW/cm^2, while these of the blue dyes tended to be much lower, 10 mW/cm^2. Additional experimental details can be found in Chapter II.

In this present work, we used the one-color multiphotofragmentation techniques to investigate the molecular properties of the Zr_2^+, Nb_2^+, Nb_3^+, and Nb_4^+ in the 15,400-18,500 cm^{-1} region. In order to determine the number of photons which caused fragmentation of the zirconium and niobium dimer cations, we studied the dissociation fluence dependence on the dimer ions. The dissociation energy of the $^{90}Zr_2^+$ was determined to be 4.184 ± 0.005 eV; this was done from the observed onset of the threshold in the spectrum (16,870 ± 40 cm^{-1}) when the fragmentation changes from a three photon processes to a two photon process. In the 16,100-18,400 cm^{-1} region, only

Table 3.1. The Experimental conditions which were used in this study.

Laser energy	15-25 mJ/pulse
PSV to Laser delay	100-130 μs
PSV current	3.2-3.4 kA
Laser to Pulse delay	100-120 μs
Pulser voltage	850-900 V
Pulser to Pot Switch delay (depend on the cluster mass).	5-15 μs
Pot. Switch voltage	2000 kV
He backing pressure	120-140 psi
Mass gate voltage	300 V
Reflectron voltage	3000 V
Einzel lens voltage	1200 V
Deflector voltage	0-50 V
MCP voltage	2400 V
Frag. Laser to mass gate delay	1μs
Frag. Laser power	30-60 mW

three transitions are seen at 17,880 cm^{-1} (relatively week), 18,290 and 18,350 cm^{-1}. In the Nb_2^+ spectrum, we observed several intense peaks centered around 16,127, 17,065, and 17,891 cm^{-1} as well as many weak transitions. This suggests that these transitions are due to the quartet - quartet transitions. We also observed a threshold in the background of the niobium dimer cation spectra at 15,880 ± 50 cm^{-1}. The fluence studies and previous collision-induced dissociation (CID) measurement indicate that the observed threshold is due to a change of the multi-photon processes of the Nb_2^+ fragmentation from a four photon processes to a three-photon process. The dissociation energy of the Nb_2^+ was then found to be 5.907 ± 0.056 eV, in good agreement with the CID measurement 5.87 ± 0.19 eV. In the Nb_3^+ spectrum, we studied the multiphoton fragmentation of the Nb_3^+ into the two possible fragments, Nb_2^+ + Nb and Nb^+ + Nb_2, in the 16,060-17,100 cm^{-1} regions. In this region, only multiphoton fragmentation spectrum of the Nb^+_3 to Nb_2^+ + Nb exhibits a sharp rise in the background at 16,190 ± 10 cm^{-1}. We did not find any electronic bands in the both fragmentation pathways. This observed threshold was unexpected at this energy according to the previous CID measurement. In Chapter VIII, we propose two possible cases one of which should be responsible for this observed threshold. In the Nb_4^+ spectrum, only the fragmentation of the Nb_4^+ into the Nb_3^+ + Nb showed a sharp rise at the 16,115 ± 10 cm^{-1}. At this energy, the multiphotofragmentation is a three-photon processes. The measured dissociation energy 5.994 ± 0.001 eV is in good agreement with the CID measurements 6.00 ± 0.30 and 5.90 ± 0.20 eV, see Chapter IX.

Furthermore, we calculated spectroscopic properties of the Zr_2^+, $Nb_2^{0/+}$, $Nb_3^{0/+}$, and $Nb_4^{0/+}$ using *ab initio methods*. To test the methods, we attempt to calculate the

spectroscopic properties of the first and second transition metals as test calculations. In the chapter, we present the results of the calculations for the neutral and ionic clusters with the previous experimental and theoretical studies for the comparison. In the conclusion (Chap. XI), we present the calculated force constants for the first-, second-, and third-row transition metal neutral dimer molecules.

Chapter III References

1. John T. Moseley, Photodissociation and Photoionization, edited by K. P. Lawley (Wiley, 1985).
2. S. P. Goss, J. D. Morrison and D. L. Smith J. Chem. Phys.**75**, 757 and 1820 (1981).
3. R. N. Dixon, Chem. Soc. Rev., (1994).
4. C. R. C. Wang, S. Pollack, D. Cameron and M. Kappes, J. Chem. Phys., **93**, 3787 (1990).
5. P. J. Brucat, L. S. Zheng, C. L. Pettiette, S. Yang and R. E. Smalley, J. Chem. Phys., **84**, 3078 (1986).
6. A. W. Castleman Jr., and R. G. Keesee, Chem. Rev., **86**, 589 (1986) .
7. K. F. Willey, D. L. Robbins, C.-S. Yeh and M. A. Duncan. Faraday Discuss. **92**, 269 (1991).
8. M. F. Jarrold and K. M. Creegan, I.nt. J. Mass Spec. and Ion Processes, **102**, 161 (1990).
9. M. F. Jarrold and K. M. Creegan, Chem. Phys. Lett., **166**, 116 (1990).
10. P. C. Engelking, Chem. Rev., **91**, 399 (1991).
11. J. M. Hayes, Chem. Rev., **87**, 745 (1987).
12. J. B. Hopkins, P. R. R. Langridge-Smith, M. D. Morse and R. E. Smalley, J. Chem. Phys., **78**, 1627 (1983).
13. Jacqueline C. Pinegar, Jon D. Langenberg, Caleb A. Arrington, Eileen M. Spain and Michael D. Morse, J. Chem. Phys., **102**, 666 (1995).
14. R.J. Van Zee, S. Li and W. Weltner Jr., Chem. Phys. Lett. **217**, 381 (1994) .

15. A. M James, P. Kowalczk, E. Langlois, M. D. Campbell, A. Ogawa and B. Simard, J. Chem. Phys., **101**, 4485 (1994).

16. A. M. James, P. Kowalczk, R. Fournier and B. Simard J. Chem. Phys., **99**, 8504 (1993).

17. Z. Hu, B. Shen, Q. Zhou, S. Deosaran, J. R. Lombardi and D. M. Lindsay, SPIE Proceedings Vol. **1599**, (1992).

18. D. A. Hales, L. Lian, P.B. Armentrout, Int. J. Mass Spec. and Ion Processes. **102**, 269 (1990).

19. S. K. Loh, Li Lian and P.B. Armentrout, J. Chem. Phys., **91**, 6148 (1989.

20. Y. Hamrick, S. Taylor, G. W. Lemire, Z. W. Fu, J, C, Shui and M. D. Morse, J. Chem. Phys., **88**. 4095 (1988).

21. M. Moskovits and W. Limm, Ultramicroscopy **20**, 83 (1986).

22. J. R. Heath, Y. Liu. S. C. O'Brien, Q.-L. Zhang, R. F. Curl, F. K. Tittel, and R. E. Smalley, J. Chem. Phys., **63**, 5520 (1985).

23. R. L.- Asher, D. Bellert, T. Buthelezi and P. J. Brucat, Chem. Phys. Lett., **224**, 525 and 529 (1994).

24. Private communication with P. J. Brucat, University of Florida, Gainesville.

25. Private communication with M. A. Duncan, University of Georgia, Athens.

26. Benoit Simard, Andrew M. James, P. Kowalczyk, R. Fournier and P. A. Hackett, preprint (High Resolution spectroscopy of small transition metal molecules. Recent experimental and theoretical progress on group 5 diatomics.

27. J. C. Weisshaar, J. Chem. Phys., **90**, 1429 (1989).

28. C. W. Bauschlicher Jr., S. R. Langhoff, Chem. Rev., **91**, 701, (1991).

29. S. Taylor, G. W. Lemire, Y. M. Hamrick, Z. Fu and M. D. Morse, J. Chem. Phys., **89**, 5517 (1988).

CHAPTER. IV

IV.1 INTRODUCTION

This is a short description of the commonly used calculational procedures to solve Schrodinger's equation, known as the ab initio and semi-empirical approximation such as Hartree Fock (HF), Density Functional Theory (DFT) and etc. These calculations are fundamental to an understanding of molecules. Within the framework of the approximations used in the Hartree-Fock approach, the distribution of electric charge is determined. In addition, a molecular wavefunction is calculated and various molecular properties are found. The principle type of calculation is called Hartree-Fock using a set of approximations to reduce the complexity of the 4N dimensional problem. where N is the number of electrons and nuclei. The factor of 4 arises from spatial coordinates plus the spin. The basic approximation is due to Born-Oppenheimer; it decouples the electronic and nuclear degrees of freedom. This assumes the nuclear centers of mass are fixed for a given calculation, i.e., the wave function is parameterized with respect to the nuclear coordinates.

In the Hartree-Fock approximation, the many electron problem is approximated by a sequential calculation of the response of the i^{th} electron in the average potential of the rest of the electrons. This one-electron operator is called the Fock operator. Wave functions describing electrons obey Fermi Dirac statistics, that is, they must be anti-symmetric with respect to an interchange of coordinates. This is conveniently expressed in terms of a determinant called the Slater Determinant. The Hartree-Fock equations are a set of coupled integro-differential equations. Using basis vectors of Hilbert space, this can be transformed into a set of algebraic equations. This gives a generalized eigenvalue

problem to solve called Roothan Equations. Hartree-Fock Self Consistent Field (HF-SCF) is a name of the procedure to calculate the charge distribution. The problem is non-linear (the Fock matrix is dependent on the variational coefficients that are being calculated) thus an iterative approach is used (self consistency). Hartree-Fock calculations have a built in deficiency; electron-electron correlation is ignored. Thus, further work needs to be performed. Lumped as post Hartree-Fock calculations, most of these schemes involve the diagonalization of large matrices.

Density Functional Theory (DFT) is a general approach to the *ab initio* description of quantum many-particle systems, in which the original many-body problem is rigorously recast in the form of an auxiliary single-particle problem. For the simplest case (nondegenerate) of stationary problems, DFT is based on the fact that any ground state observable is uniquely determined by the corresponding ground state density n, i.e. can be understood as a functional of n. This statement applies in particular to the ground state energy, which allows us to indirectly represent the effects of the particle-particle interaction as a density-dependent single-particle potential. In addition to the Hartree (direct) contribution this potential contains an exchange-correlation (xc) part, which is obtained from the so-called xc-energy functional. The exact density functional representation of this crucial quantity of DFT is not known, the derivation of suitable approximations being the major task in DFT. Extensions of this scheme to spin-dependent, relativistic or time-dependent systems, utilizing the spin-densities, the four current or the time-dependent density as basic variables, are also available. Recently, a DFT approach to quantum hadrodynamics (as a model for the relativistic description of nuclei) has been developed. The main areas for applications of DFT are condensed matter

and cluster physics as well as quantum chemistry. In this chapter we shall take a look at perhaps the most fundamental difficulty in quantum physics, the many-particle problem or many electron system.

IV.2. THE MANY-PARTICLE SYSTEM

So what is a many-particle or -body situation, and why is it such a problem? Let us start with a classical example. Consider a hard ball (ball A) moving in some kind of force field which may be spatially and temporally varying, but which is uncoupled to the motion of the ball (i.e. unaltered by the presence of the ball). If we know the force on the ball at every point in space and time then we can easily calculate the trajectory of the ball by using Newton's laws. This situation is that of a single particle moving in an external field. It doesn't matter that the field is varying; as long as the variation does not depend upon the position or velocity of the ball the problem remains easy. Now add a second hard ball (ball B) to the problem, and furthermore let us attach it to the first by means of a spring. At a ball separation equal to the natural length of the spring there will be no force between the balls, but in general the spring will either be stretched or compressed and so ball A will exert a force on ball B and vice versa. The motion of the balls is still described perfectly well by Newton's classical laws of motion, but now the motion of ball A is intimately linked with the motion of ball B. That is, one cannot solve the trajectories of ball A and ball B separately: their equations of motion are coupled and must be solved simultaneously. Fortunately, with two balls this is not too much of a problem. However, if there are many balls then the problem rapidly becomes insoluble. It should be stressed that the balls are still subject to Newton's laws, but the difficulty of solving the equations which result from those laws increases rapidly because of the coupling. This is the

essence of the Many Body Problem. However, all is not doom and gloom. Imagine that the balls are not connected by springs, what happens then? The answer is that the balls move precisely as single particles until they collide with each other. Now the problem has become easier again, because we can use single particle theory to describe the trajectories of individual balls, until such times as they instantaneously scatter from each other. Thus we don't have to solve any equations simultaneously. Instead we have to know a bit about scattering theory. Now, it would not be correct to describe these balls simply as single particles because that would be to ignore the effect of the scattering, but we can call them single-particle-like particles or, to use the accepted term, quasiparticles.[1,2]

Somewhere between these last two cases there is a grey area in which the balls interact with each other only when they are within a certain range of each other. That is, when the balls are well-separated, they do not significantly interact, but when they come close together they exert a force on each other. Thus there are times when a given ball will behave as a single-particle and times when it will not. In the limit when the critical range is very small this situation reduces to the quasiparticle case, and in the opposite limit of a very large critical range the situation is that of a true many body problem. Thus the applicability of the quasiparticle approach to a given many body problem is largely dependent on the range of the inter-particle forces involved.

The electrons in a system interact strongly with the ion cores making up the molecular structure and with each other. The electron-ion interaction does not constitute a many particle problem, however, because the ions are essentially stationary on the time-scale of the motion of the electrons (i.e. the electronic and ionic degrees of freedom are not coupled). On the other hand, the electron equations of motion are most certainly

strongly coupled to each other by the electrostatic interaction. The long range nature of the electrostatic interaction does not bode well for a quasiparticle description. Nevertheless, the most successful current method for electronic structure calculations in large system is based on the even more radical approximation of single-particle behaviour. In order to understand the problem better let us look at some of the different apporaches taken by different workers over the years.[1-3]

IV.3. HARTREE AND HARTREE-FOCK THEORY

To completely describe the quantum mechanical behaviour of electrons in many particle systems or in solids it is strictly necessary to calculate the many-electron wavefunction for the system. In principle this may be obtained from the time-independent Schrodinger equation, but in practice the potential experienced by each electron is dictated by the behaviour of all the other electrons is the system. Of course, the influence of nearby electrons will be much stronger than that of far-away electrons since the interaction is electrostatic in nature, but the fact remains that the motion of any one electron is strongly coupled to the motion of the other electrons in the system. To solve the Schrodinger equation directly for all these electrons would thus require us to solve a system of around 10^{23} simultaneous differential equations. Such a calculation is beyond the capabilities of present-day computers, and is likely to remain so for the forseeable future.

One of the earliest attempts to solve the problem was made by Hartree. He simpified the problem by making an assumption about the form of the many-electron wavefunction, namely that it was just the product of a set of single-electron

wavefunctions. In a uniform system these wavefunctions would take the form of simple plane waves. Having made this assumption it was possible to proceed using the variational principle.

This principle is a very powerful concept in mathematics. In the form most commonly applied to theoretical physics it states that if a given system may be described by a set of unknown parameters then the set of parameter values which most correctly describes the ground state of the system (i.e. the state in which the system exists when not perturbed by outside influences) is just that set of values which minimises the total energy. A simple example of this principle is the case of a ball sitting in a valley in a gravitational field. The system may be described by a single parameter: the height of the ball above the bottom of the valley. The ground state of the system may be determined by finding the value of this parameter which minimises the total energy. Clearly this value of the parameter corresponds to the ball sitting at the very bottom of the valley.

By using the variational method Hartree found the Hamiltonian equation of the many-electron system. In fact, for an N-electron system there are N equations; one for each of the N single-electron wavefunctions which made up the many-electron product wavefunction. These equations turned out to look very much like the time-independent Schrodinger equation, except the potential (the Hartree potential) was no longer coupled to the individual motions of all the other electrons, but instead depended simply upon the time-averaged electron distribution of the system. This important fact meant that it was possible to treat each electron separately as a single-particle. Consequently the Hartree approximation allows us to calculate approximate single-particle wavefunctions for the electrons in the system, and hence calculate other related properties. Unfortunately, the

Hartree approximation does not provide us with particularly good results. For example, it predicts that in a neutral uniform system there will be no binding energy holding the electrons in the system. This, of course, is in direct contradiction to the experimental evidence that electrons must be given a finite amount of energy before they can be liberated from system.

The most obvious reason for the failure of the Hartree approach lies in the initial assumption of a product wavefunction. The famous Pauli exclusion principle states that it is not possible for two fermions (the class of particles to which electrons belong) to exist at the same point in space with the same set of quantum numbers. This principle is manifest as an effective repulsion between any pair of identical fermions possessing the same set of quantum numbers. Mathematically, the Pauli exclusion principle can be accounted for by ensuring that the wavefunction of a set of identical fermions is antisymmetric under exchange of any pair of particles. That is to say that the process of swapping any one of the fermions for any other of the fermions should leave the wavefunction unaltered except for a change of sign. Any wavefunction possessing that property will tend to zero (indicating zero probability) as any pair of fermions with the same quantum numbers approach each other. The Hartree product wavefunction is symmetric (i.e. stays precisely the same after interchange of two fermions) rather than antisymmetric, so the Hartree approach effectively ignores the Pauli exclusion principle! [1,5]

The Hartree-Fock approach is an improvement over the Hartree theory in that the many-electron wavefunction is specially constructed out of single-electron wavefunctions in such a way as to be antisymmetric. The wavefunction has to be much more

complicated than the Hartree product wavefunction, but it can be written in a compact way, such as a so-called Slater determinant.

$$\psi(\mathbf{r}_1s_1, \mathbf{r}_2s_2, \ldots, \mathbf{r}_Ns_N) = 1/\sqrt{N!} \begin{vmatrix} \psi_1(\mathbf{r}_1s_1) & \psi_1(\mathbf{r}_2s_2) & \ldots & \psi_1(\mathbf{r}_Ns_N) \\ \psi_2(\mathbf{r}_1s_1) & \psi_2(\mathbf{r}_2s_2) & \ldots & \psi_2(\mathbf{r}_Ns_N) \\ \cdot & & & \cdot \\ \cdot & & & \cdot \\ \cdot & & & \cdot \\ \psi_N(\mathbf{r}_1s_1) & \psi_N(\mathbf{r}_2s_2) & \ldots & \psi_N(\mathbf{r}_Ns_N) \end{vmatrix}$$

Starting from this assumption it is once again possible to derive the Hamiltonian equation for the system through the variational principle. Just as before, this results in a simple equation for each single-electron wavefunction. However, this time in addition to the Hartree potential (which described the direct Coulomb interaction between an electron and the average electron distribution) there is now a second type of potential influencing the electrons, namely the so-called exchange potential. The exchange potential arises as a direct consequence of including the Pauli exclusion principle through the use of an antisymmetrised wavefunction.

We can get a visual impression of the effect of exchange by considering the region surrounding a given electron with a particular quantum mechanical spin. In this context spin is a quantum mechanical property (in some ways analogous to mechanical spin) which is related to magentism. Electrons can be either in the spin-up state or the spin-down state. In a non-magnetic sample half of the electrons will be spin-up while the

other half will be spin-down. If we look at an electron with spin-up, then the Pauli exclusion principle means that other nearby spin-up electrons will be repelled. Spin-down electrons will not be affected since they have a different spin quantum number. Thus our spin-up electron is surrounded by a region which has been depleted of other spin-up electrons. Thus this region is positively charged (remember that the average electron distribution exactly balances the positive charge of the ion cores, and that this region is relatively depleted of electrons). Similarly, if we had considered a spin-down electron from the start, then we would have found a region depleted of other spin-down electrons. The edge of the electron depleted region is not clearly defined, but nevertheless we call this region the exchange hole.

Notably, the exchange potential contributes a binding energy for electrons in a neutral uniform system, so correcting one of the major failings of the Hartree theory. However, in calculating many other properties the Hartree-Fock approach is actually **worse** than the Hartree approach. How is it that improving the physics which went into the theory can actually give us worse answers?

The reason the Hartree-Fock theory gives worse answers than the Hartree theory is simply that there is another piece of physics which we are still ignoring. To some extent it cancels out with the exchange effect and so when we use the Hartree approach (i.e. we ignore both effects) we get reasonable results. On the other hand the Hartree-Fock approach includes the exchange effect but ignores the other effect, which balances it somewhat, completely. This new effect is the electrostatic correlation of electrons.

Ignoring the Pauli exclusion principle generated exchange hole for the moment, we can also visualise a second type of hole in the electron distribution caused by simple

electrostatic processes. If we consider the region immediately surrounding any electron (spin is now immaterial), then we should expect to see fewer electrons than the average simply because of their electrostatic repulsion. Consequently, each electron is surrounded by an electron-depleted region known either as the Coulomb hole (because of its origin in the electrostatic interaction) or the correlation hole (because of its origin in the correlated motion of the electrons). Just as in the case of the exchange hole, the electron depleted region is slightly positively charged. The effect of the correlation hole is twofold. The first is obviously that the negatively charged electron and its positively charged hole experience a binding force due to simple electrostatics. The second effect is more subtle and arises because any entities which interact with the electron over a distance larger than the size of the correlation hole will not interact with the bare electron, but rather with the electron+correlation hole (which of course has a smaller charge than the electron alone). Thus any other interaction effects, such as exchange, will tend to be reduced (i.e. screened) by the correlation hole.

Clearly, we can now see why the Hartree-Fock approach fails for large systems: firstly, the exchange interaction should be screened by the correlation hole rather than acting in full, and secondly the binding between the correlation hole and electron has been ignored. At this point we should mention that the Hartree-Fock approach gives quite creditable results for small molecules. This is because there are far fewer electrons invloved than in a large system, and so correlation effects are minimal compared to exchange effects. Although neither of the above methods succeeded in solving the many-body of problem of electrons in solids did at least elucidate the important physical processes which we must describe: namely exchange and correlation.

To derive the Hartree-Fock equations, we begin with the time independent Schrodinger wave equation. This equation can be written as follows:

$$H\psi = E\psi \qquad 1.1$$

where H is the Hamiltonian energy function describing the system and ψ is the wave function. For a single molecule, the total Hamiltonian can be written as follows:

$$H = -1/2\sum\{(m_e/M_A)\nabla^2_A + V(R_A)\} + \sum_{A<B} Z_A Z_B/R_{AB} - 1/2\sum_{A,i} Z_A/r_{A,i} - \sum_i \nabla^2_i + \sum_{i<j} 1/r_{ij} \qquad 1.2$$

where

M_A and m_e are the masses of the nuclei and electrons, respectively.

A and B denote nuclei,

j and i denote electrons,

R_{AB} is the distance between nuclei A and B,

Z_A is the charge of nucleus A and

r_{ij} is the distance between the electrons i and j.

∇^2_A is the gradient operator with respect to the nuclear coordinates and

∇^2_i is the gradient operator with respect to the electronic coordinates.

The first term in Eq.(1.2) is the kinetic energy of each nucleus, the second term is any external force acting on the nuclei (usually zero), and the third term is the electrostatic repulsion between the nuclei. The next term is the electrostatic attraction between electron i and nuclei A. The last two terms are the kinetic energy and electrostatic repulsion of the electrons, respectively. At this stage the problem is

intractable except for a small number of physically uninteresting cases (from a molecular point of view), so we need to reduce the complexity of Eq. (1.2). Note; physically uninteresting cases refers to solving H_2. The first step is the Born-Oppenheimer approximation.

IV3.1. THE BORN-OPPENHEIMER APPROXIMATION

First re-write the Hamiltonian in Eq. (1.2) using atomic units and then express the Hamiltonian as a sum of nuclear H_N and electronic H_e parts,

$$H_N = -1/2\sum_A \nabla^2_A + V(R_A) \qquad 1.3$$

$$H_e = \sum_{A<B} Z_A Z_B/R_{AB} - 1/2\sum_{A,i} Z_A/r_{A,i} - \sum_i \nabla^2_i + \sum_{i<j} 1/r_{ij} \qquad 1.4$$

and let the wave function from Eq. (1.1) be a product of a nuclear and electronic wave functions, $\psi = \psi_N\psi_e$. Note that $\psi = \psi_N(R_A)\psi_e(R_e r_i)$. H_i is a function of r_i only, the R_A are treated as constants due to the Born-Oppenheimer approximation. That is, rewriting the wave function separates the problem into electronic and nuclear regimes, and the electronic problem is solved given a specific nuclear configuration. Then the energy eigenvalues determined from H_e called $\varepsilon_e(R_A)$, depend on R_A. Let ε_e be the eigenvalues of the electronic Hamiltonian.

$$H_e\psi_N\psi_e = \varepsilon_e(R_A)\psi_N\psi_e \qquad 1.5$$

Using Eq. (5), we can rewrite the left side of Eq. (1) as,

$$H_e\psi_N\psi_e = [H_N + \varepsilon_e(R_A)]\psi_N\psi_e \qquad 1.6$$

If the external force on the nuclei is zero, then H_N is just the kinetic energy operator and.

$$H_N\psi_N\psi_e \approx \varepsilon \sum_A \psi_e\nabla^2{}_A\psi_N + 0(m_e/m_p) \qquad 1.7$$

where m_e/m_p the ratio of the electron mass to the mass to the proton. is on the order of 1/1836 and can be neglected. Thus.

$$H_N\psi_N \approx \varepsilon_N\psi_N \qquad 1.8$$

where, ε_N is the kinetic energy of the nuclei.

In the Born-Oppenheimer approximation, the motion of the nuclei is decoupled from the motion of the electrons, and for most cases the motion of the nuclei can be ignored. This approximation is valid because the ratio of the mass of the proton to the mass of the electron is 1/1836. Thus, the motion of the nuclei is negligible compared to the motion of the electrons.

IV3.2 THE MO-LCAO APPROXIMATION

Now, we solve for the total electronic wavefunction ψ_e of N particles, by writing ψ_i as a product of N single particle orbitals, $\phi_i(r_j)$ in 3N dimensional space. The total electronic wave function must be antisymmetric with respect to interchange of electron coordinates due to the Pauli exclusion principle. The antisymmetrized wavefunction can be written as,

$$\psi_e(r_1 \ldots r_N) = \sum_p(\pm)^P P_{op}[\phi_1(r_1), \phi_2(r_2), \ldots, \phi_N(r_N)] \qquad 1.9$$

where $\phi_i(r_i)$, denotes the single particle quantum state, a state vector in 3N dimensional space and is the particle label (position) and P_{op} is the permutation operator. The sum is over all permutations of the states $\phi_i(r_i)$, and $(\pm)^P$, and indicates a -1 for odd permutations and a +1 for even permutations. This can also be written as a determinant, known as the Slater Determinant or single determinant wave function. Note that each electron is in its own 3 dimensional space. The product space is 3N dimensional and derivatives are with respect to the 3N dimensional space. The total electronic energy E of the system, is written as

$$E = < \psi_e \mid H_e \mid \psi_e > = \int \psi^*_e(r_1 \ldots r_N) H_e \psi_e(r_1 \ldots r_N) dr_1 \ldots dr_N \qquad 1.10$$

Note, the symbols $\mid \psi_e >$ and ψ_e denote a state vector in Hilbert space, and $< \psi_e \mid$ and ψ^*_e are the complex conjugates of $\mid \psi_e >$.

IV.3.3 THE HARTREE-FOCK EQUATIONS

Now we apply the variational principle to $< \phi_i \mid \phi_j > = \delta_{ij}$, subject to the orthonormality of the total wavefunction, to determine $\phi_i(r_j)$. This constraint appears as Lagrange multipliers, written as ε_{ij}, in the minimization and are identified as the energy required to remove the i^{th} particle from the system. This is known as Koopman's theorem. The result of minimizing E gives a set of integro-differential equations known as the Hartree-Fock Equations (HF).

One can then expand the single particle orbitals in terms of a set of basis functions as follows ($\chi_\mu \equiv \phi_i$).

$$\phi_i = \sum_{i\mu} c_{i\mu}\chi_\mu(r_i) \qquad 1.11$$

where μ is a dummy index labelling the single particle orbitals. Now minimize the total energy with respect to the variational parameters subject to orthonormality of the total wave function $< \chi_\mu \mid \chi_\nu > = \delta_{\mu\nu}$. This constraint appears as Lagrange multipliers, written as $\varepsilon_{\mu\nu}$, in the minimization and are identified as the energy required to remove the particle from the system. This minimization plus the expansion in terms on Hilbert Space basis functions, gives the Hartree-Fock Roothaan (HFR) algebraic equations to solve for the variational parameters , written as,

$$\sum_\nu (F_{\mu\nu} - \varepsilon_i S_{\mu\nu})c_{\nu i}= 0 \qquad 1.12$$

where the Fock matrix is given by,

$$F_{\mu\nu} = H_{\mu\nu} + \sum_{\lambda\sigma} P_{\lambda\sigma} [<\mu\nu|\lambda\sigma> - 1/2<\mu\lambda|\nu\sigma>] \qquad 1.13$$

$P_{\lambda\sigma} = 2\sum_i c^*_{\lambda i}c_{\sigma i}$, is the density matrix and $S_{\mu\nu}$ is the overlap matrix which arises from the non-orthogonality of the basis functions.

In matrix form, the HFR equations are of the following form

$$FC = SCF \qquad 1.14$$

where C is the expansion coefficient matrix $c_{\nu i}$ and E is the energy. To solve Eq.(1.14), transform to a standard eigenvalue problem, solve, and then transform back. The types of

integrals needed are, one electron integrals giving the overlap between different states, χ_μ and χ_ν

$$S_{\mu\nu} = \int \chi_\mu(r_i)\chi_\nu(r_i)dr_i \qquad 1.15$$

one electron kinetic energy integrals,

$$T_{\mu\nu} = \int \chi_\mu(r_i)(-1/2\nabla^2_1)\chi_\nu(r_i)dr_1 \qquad 1.16$$

coulomb attraction between a single electron and the nuclei.

$$V_{\mu\nu} = \int \chi^*_\mu(r_i)(\sum_A Z/r_{1A})\chi_\nu(r_i)dr_i \qquad 1.17$$

and two electron integrals, one for the coulomb repulsion and one for the quantum mixing due to indistinguishability of particles.

$$V_{\mu\nu\lambda\sigma} \equiv \langle\mu\nu\,|\,\lambda\sigma\sigma\rangle = \int \chi^*_\mu(r_1)\,\chi^*_\mu(r_2)(1/|r_{1A}|)\,\chi_\lambda(r_1)\chi_\sigma(r_2))dr_1dr_2 \qquad 1.18$$

The system of HFR equations are solved iteratively and might be outlined as follows:

(a) make an initial guess for c_i

(b) calculate $F_{\mu\nu}$ and $S_{\mu\nu}$

(c) solve HFR equations for ε_i and $c_{\mu\nu}$.

(d) repeat steps (a)-(d) until ε_i and/or c_i converge.

One major concern of the HFR equations are, of course, the basis functions, which can be summarized as:

- Basis Set Superposition Error
- Physical validity of basis sets

- Spanning Hilbert space
- Number of degrees of freedom
- Polarization and diffusivity

The derivation above makes no distinction between closed shells or open shells. In fact, the distinction is in how one treats the basis sets. The easiest is the Restricted Hartree Fock (RHF) where only closed shells are considered. This removes the spin symmetry problem. Open shell calculations are called Unrestricted Hartree Fock (UHF) or any of its variants (e.g. Spin Unrestricted Hartree Fock, and many others.) For all of these calculations, the equations are nearly the same. Up to this point, no reference to the particular functions to be used as basis functions has been made for some terminology. A minimum basis set is a set of functions that assigns one function to each orbital. An extended basis set assigns a linear combination of functions to each orbital. Basis sets need only be any complete set that spans Hilbert Space. However, for computational ease, Cartesian Gaussians, Gaussian Type Functions or Gaussian Type Orbitals (GTF or GTO) are used. These are written as.

$$\chi_i(r_1) = (X - X_1)^n x_i (y - y_1)^n y_i (Z - Z_1)^n z_i \cdot \exp(-a_i \mid r - r_1 \mid^2) \qquad 1.19$$

A physically more accurate basis sets are the Slater Type Orbitals (STO), written as,

$$\chi_i(r_1) = r^{n-1}\exp(-\zeta r) Y_{lm}(\theta, \vartheta) \qquad 1.20$$

To regain the computational ease of the GTF with the accuracy of the STO's, a basis set may be constructed from a linear combination of n GTF's fitted (in the least

square sense or energy minimized) to STO's. This type of basis set is denoted as STO-nG. A common variant of these is the STO-3G basis set.

Various extensions and combinations of these basis sets have been used. The double zeta basis set is two STO's per orbital to increase accuracy near the nucleus. To increase accuracy at high energy where the valance electrons contribute more, different basis sets were developed to include the valence shells. These are denoted 6-31G, 4-31G, 4-31G*, etc. In practice, most of the common basis sets are incorporated in ab initio codes, or can be put in explicitly.

The variants of the Hartree-Fock SCF procedure are all single determinant solutions. Other approaches include the Multi Configuration SCF (MCSCF). This procedure consists of using many (more than one) Slater determinants. One implementation is the Complete Active Space SCF, CASSCF. Either a single or multi-determinant approach is an all electron procedure. To treat larger systems (more electrons) one can use an effective core potential to represent the core electrons with a single function and the valance electrons with individual orbital functions. All of the derivation thus far, is non-relativistic. For example, spin-orbit coupling is not included.

IV.4. SEMI-EMPRICAL HARTREE-FOCK

Hartree-Fock theory is a useful tool for many problems. Results can be systematically improved through an increasingly rigorous choice of the basis set (if the basis set becomes too large then it becomes difficult for the system to achieve self-consistency). It gives good structures and vibrational modes for small molecules, although tends to underpredict bond lengths with a corresponding overprediction of frequencies. The Hartree-Fock approach provides the basis for methods covering a wide

spectrum of accuracies. At the lower level there are semi-empirical methods such as CNDO[12,13], MINDO/3, MNDO[6-11], etc., which are described in more detail below. These attempt to compensate for the lack of correlation through their parameterization methods, additionally fitting to experimental ionization energies and/or heats of formation of molecules. At the other end of the scale, many computationally expensive improvements can be utilised to overcome the correlation problem, such as the configuration interaction (CI) method[5], where the wavefunction is constructed from a combination of determinants. These are only really viable for small molecular systems at present.

In addition, the calculation size scales as $O(N^4)$, *i.e.* doubling the system size leads to a 16-fold increase in calculation time. This poor scaling with system size, coupled with the heavy computational cost of Hartree-Fock theory, currently limits it to smaller systems. Nonetheless, Hartree-Fock based calculations (when incorporating the high level corrections such as CI) often provide the benchmarks that other theoretical methods aspire to.

The first step in such methods is to expand the one-electron wavefunctions as a set of atomic orbitals; this is known as the tight binding method. or sometimes LCAO (Linear Combination of Atomic Orbitals),

$$\psi_i = \sum_\mu c_{\mu i}\phi_\mu \qquad 1.21$$

This reduces the problem to the determination of the linear expansion coefficients, $c_{\mu i}$.

Different ranges of atomic orbitals can be used depending on the accuracy required; commonly these are either Minimal (all atomic orbitals up to and including the valence shell), Extended (Minimal with a few more), or Valence (only the orbitals in the valence

shell of the atom). Despite being the least accurate, the valence basis set is commonly employed for very large systems due to its speed and is used in CNDO.

Since ψ_is are orthogonal, it follows that

$$\sum_{\mu\nu} c_{\mu i}^{*} c_{\nu j} S_{\mu\nu} = \delta_{ij} \qquad 1.22$$

where δ_{ij} is the Kronecker delta and $S_{\mu\nu}$ is the overlap between atomic orbitals.

$$S_{\mu\nu} = \langle \mu \mid \nu \rangle \qquad 1.23$$

This means that the Hartree Fock equations can be rewritten as the Roothaan equations, a set of algebraic expressions

$$\sum_{\nu} (F_{\mu\nu} - \varepsilon_i S_{\mu\nu}) c_{\nu i} = 0 \qquad 1.24$$

is the one-electron energy. $F_{\mu\nu}$ is the Fock matrix and consists of two sets of matrix elements, the core Hamiltonian elements, $H_{\mu\nu}$, and those due to interactions between the different orbitals. These are expressed in terms of a density matrix, $P_{\lambda\sigma}$, which is a matrix of the orbital coefficients $c^{*}_{\mu i} c_{\nu j}$, coupled with various two-electron integrals over atomic orbitals, $\langle \mu\nu \mid \lambda\sigma \rangle$,

$$F_{\mu\nu} = H_{\mu\nu} + \sum_{\lambda\sigma} P_{\lambda\sigma} (\langle \mu\nu \mid \lambda\sigma \rangle - 1/2 \langle \mu\lambda \mid \nu\sigma \rangle) \qquad 1.25$$

$$H_{\mu\nu} = \langle \mu | H^{core} | \nu \rangle \qquad 1.26$$

$$P_{\lambda\sigma} = 2 \sum_i c^{*}_{\lambda i} c_{\lambda i} \qquad 1.27$$

$$\langle \mu\nu \mid \lambda\sigma \rangle = \iint \phi_\mu(r_1) \phi_\nu(r_1) |\mathbf{r}_1 - \mathbf{r}_2|^{-1} \phi_\lambda(r_2) \, \phi_\sigma(r_2) d\,\mathbf{r}_1 d\mathbf{r}_2 \qquad 1.28$$

Now it is possible to make several selective approximations. The first of these is the *zero* differential overlap approximation (ZDOA). This says that since the atomic orbitals on a given atom are roughly orthogonal, the overlap between these can be considered zero; in terms of the two-electron integrals, most of these are therefore set to zero,

$$<\mu\nu \mid \lambda\sigma> = <\mu\mu \mid \lambda\lambda>\delta_{\mu\nu}\delta_{\lambda\sigma} \qquad 1.29$$

The corresponding overlap integrals are also ignored for the same reason. This approximation removes all the three and four centre integrals, vastly simplifying the calculation. The chemical bonding is, however, reliant on the overlap character, and this is maintained through the core integrals. These are parameterised to experimental results, compensating for the ZDOA to some extent. For CNDO[13],

$$H_{\mu\nu} = \int\phi_\mu(1)\{-1/2\nabla^2 - \sum_B V_B\ \})\phi_\nu(1)d\mathbf{r}_1; \quad \mu\neq\nu \qquad 1.30$$

where $-V_B$ is the potential due to the nucleus and core electrons of atom B.

Applying the ZDOA simplifies the Roothaan equations to

$$\sum_\nu F_{\mu\nu}\, c_{\nu i} = \varepsilon_i c_{\mu i} \qquad 1.31$$

with

$$F_{\mu\mu} = H_{\mu\mu} - 1/2\ P_{\lambda\sigma}<\mu\mu \mid \mu\mu> + \sum_\lambda P_{\lambda\lambda}(<\mu \mid \lambda\lambda> \qquad 1.32$$

and

$$F_{\mu\nu} = H_{\mu\nu} - 1/2\ P_{\mu\nu}<\mu\mu \mid \nu\nu> \qquad 1.33$$

However in the form described here, the ZDOA leads to inconsistencies. The orbitals on a given atom can be transformed into a different orbital set which would breach the zero differential overlap approximation, *i.e.*

$$\phi_\mu\phi_\nu\ (\mu\neq\nu) = \sum_{\mu\nu} A_{\mu\nu}\phi'_\mu\phi'_\nu\ ;\quad A_{\mu\nu} \text{ is constant.} \qquad 1.34$$

This means that the results would be basis dependent, and to avoid this further constraints need to be applied. The simplest scheme to achieve this is CNDO.

Under CNDO, only the valence electrons are considered explicitly. Interactions between electrons on the same atom are handled simply. Since the atomic orbital basis is built from orthonormal atomic functions, then the interaction between different orbitals are vanish due to their symmetry. The core Hamiltonian elements are fitted to experiment. In CNDO/1 these were fitted to atomic ionisation energies, but in CNDO/2 that was modified by fitting to the average of the ionisation potential and electron affinity, making the system more applicable to both electron gain and loss. In order to overcome the basis dependency of the ZDOA, the remaining two-centre integrals only depend on their host atoms and not on the orbital type. This is achieved by using an average electrostatic repulsion on any atom A caused by atom B, (the electron repulsion integral), so that

$$\langle\mu\mu|\lambda\lambda\rangle = \gamma_{AB} \qquad 1.35$$

In CNDO/1, this is approximated by s-orbital integrals on the atoms,

$$\gamma_{AB} = \iint s^2_A(r_1)\,|\,\mathbf{r}_1 - \mathbf{r}_2\,|^{-1}\, s^2_B(r_2)d\mathbf{r}_1d\mathbf{r}_2 \qquad 1.36$$

Similarly if the core potential (consisting of the nucleus and core electrons) on an atom B is V_B then to maintain rotational invariance, the interaction between an electron on atom *A* and this core on atom *B* must be a constant, V_{AB} (the potential integrals).

Similarly to γ_{AB}, in CNDO/1 V_{AB} is calculated using an *s*-orbital on atom *A*:

$$V_{AB} = Z_B \int s^2_A(r) \, | \mathbf{r} - \mathbf{R}_B |^{-1} \, d\mathbf{r} \qquad 1.37$$

In CNDO/2, an improved parameterisation, this was replaced with a simple approximation,

$$V_{AB} = Z_B \gamma_{AB} \qquad 1.38$$

The lack of monatomic differential overlap removes all terms of the form

$$\langle \mu | V_B | \nu \rangle = 0 \; ; \; \mu \neq \nu \qquad 1.39$$

Next the interaction between an electron and the field of two atoms, A and B is simplified (the resonance integral, $\beta_{\mu\nu}$), by setting it proportional to the overlap integral, $S_{\mu\nu}$,

$$H_{\mu\nu} = \beta_{\mu\nu} = \beta^0_{AB} \qquad 1.40$$

where β^0_{AB} are known as the bonding parameters and are dependent on the atom types *A* and B. Under CNDO/1 these are approximated to $\beta^0_{AB} = \frac{1}{2}(\beta^0_A + \beta^0_B)$, and β^0_A is fitted to *ab initio* calculations for each species. The precise parameterization technique used to determine, $S_{\mu\nu}$, $U_{\mu\nu}$, γ_{AB}, V_{AB}, and β^0_{AB} varies.

IV.5 DENSITY FUNCTIONAL THEORY

The methods outlined in the previous section were both essentially based upon the variational principle. As already mentioned, this is an extremely powerful approach, but it depends for its success upon a good parametric description of the problem in the first instance. To go back to the "ball in the valley" example from the previous section, it is clear that choosing the height of the ball as our adjustable parameter is a good idea, but that choosing the ambient temperaure instead is not. We can vary the temperature all we like, but still get no nearer to finding a solution. Similarly, in quantum mechanics, the better the form of wavefunction we take (i.e. the more suited it is to describing the problem at hand) then the better results we will get from the variational approach. Thus the Hartree-Fock antisymmetric wavefunction allowed us to correctly describe the exchange interaction, whereas the Hartree product wavefunction did not. Accordingly we can view the ultimate failure of both of these models as being due to not having good enough approximate forms for the wavefunction to start with. This is hardly surprising, since we assumed that the many-electron wavefunction was expressible in terms of many single-electron wavefunctions, which is not necessarily possible at all.

Hohenberg and Kohn[14], in 1964, suggested that the problem really was that the many-electron wavefunction was too complicated an entity to deal with as the fundamental variable in a variational approach. Firstly, it cannot adequately be described without $\sim 10^{23}$ parameters, and secondly it has the complication of possessing a phase as well as a magnitude. They chose instead to use the electron density as their fundamental variable. That is, they considered the ground state of the system to be defined by that electron density distribution which minimises the total energy. Furthermore, they showed

that all other ground state properties of the system are functionals of the ground state electron density. That is, once the ground state electron density is known all other ground state properties follow (in principle, at least).

In 1965, Kohn and Sham showed that the Hamiltonian equation derived from this variational approach took a very simple form. The so-called Kohn-Sham[15] equation is similar in form to the time-independent Schrodinger equation, except that the potential experienced by the electrons is formally expressed as a function of the electron density. Again it is effectively a single-particle equation. In addition to the contribution from the electron-ion interaction, the electron-electron interaction potential is split for convenience into two parts: the Hartree potential, which we have met before, and an exchange-correlation potential, whose form is, in general, unknown. For many years now, density functional theory has been used with great succes to investigate the ground state properties of solids, both in the bulk form and at surfaces and interfaces. However, as a variational approach, it cannot reliably be used to provide information about excited states of the system (i.e. states other than the ground state). [16,17]

IV.5.1 KOHN-SHAM THEORY

The kinetic energy provides a large contribution to the total energy. Therefore even the 1% error in the kinetic energy of the Thomas-Fermi-Weizsacker model prevented DFT from being used as a quantitative predictive tool. Thus density functional theory (DFT) was largely ignored until 1965 when Kohn and Sham[15] introduced a method which treated the majority of the kinetic energy exactly. The theory begins by considering the noninteracting reference system: N noninteracting electrons, each in one of N orbitals, ψ_i. Such a system will be defined by the Hamiltonian

$$H_i = \sum_i^N(-1/2\nabla_i^2)+\sum_i^N v_i(\mathbf{r}_i) \qquad 2.1$$

which has an exact eigenfunction that is the single determinant constructed from the *N* lowest eigenstates of the one-electron equations

$$[-1/2\nabla_i^2 + v_i(\mathbf{r}_i)]\psi_i = \varepsilon_i\psi_I \qquad 2.2$$

The corresponding Euler-Lagrange equation is

$$\mu = \mathbf{v}_i(\mathbf{r}_i) + \delta\mathbf{T}_i[\rho]/\delta\rho(\mathbf{r}) \qquad 2.3$$

For this system the kinetic energy and electron density are given exactly by

$$\mathbf{T}_i[\rho] = \sum_i^N\langle\psi_i|-1/2\nabla_i^2|\psi_i\rangle \qquad 2.4$$

$$\rho(\mathbf{r}) = \sum_i^N|\psi_i|^2$$

and the total energy is given by

$$E[\rho] = \mathbf{T}_i[\rho] + \int\mathbf{v}_i(\mathbf{r}_i)\rho(\mathbf{r})d\mathbf{r} \qquad 2.5$$

The quantity $\mathbf{T}_i[\rho]$ is well-defined, but not the exact kinetic energy. $\mathbf{T}_i[\rho]$ is defined in Ref 14, $E[\rho] = \mathbf{T}[\rho]+\mathbf{V}_{ee}[\rho] + \int\mathbf{v}(\mathbf{r})\rho(\mathbf{r})d\mathbf{r}$. Kohn and Sham reformulated the interacting problem so that its kinetic component is defined to be $\mathbf{T}_i[\rho]$ and rearranging the $E[\rho]$ in Ref 14 to give

$$E[\rho] = \mathbf{T}_i[\rho] + \mathbf{J}[\rho] + \int\mathbf{v}_i(\mathbf{r}_i)\rho(\mathbf{r})d\mathbf{r} + \mathbf{E}_{xc}[\rho] \qquad 2.6$$

where $\mathbf{E}_{xc}[\rho]$ is the exchange-correlation energy, made up of the non-classical electron-electron repulsion and also the difference between the exact and noninteracting kinetic energy

$$\mathbf{E}_{xc}[\rho] = \mathbf{T}[\rho] - \mathbf{T}_i[\rho] + \mathbf{V}_{ee}[\rho] - \mathbf{J}[\rho] \qquad 2.7$$

The Euler-Lagrange equation in Ref. 14, $\mu = \mathbf{v}(\mathbf{r}) + \delta\mathbf{T}_i[\rho]/\delta\rho(\mathbf{r}) + \delta\mathbf{V}_{ee}[\rho]/\delta\rho(\mathbf{r})$, now becomes

$$\mu = \mathbf{v}_{eff}(\mathbf{r}) + \delta\mathbf{T}_i[\rho]/\delta\rho(\mathbf{r}) \qquad 2.8$$

where the Kohn-Sham (KS) effective potential, v_{eff} is defined as

$$\mathbf{v}_{eff}(\mathbf{r}) = \mathbf{v}(\mathbf{r}) + \int\rho(\mathbf{r}')d\mathbf{r}'/|\mathbf{r}-\mathbf{r}'| + v_{xc}(\mathbf{r}) \qquad 2.9$$

and the exchange-correlation potential, v_{xc} is

$$v_{xc}(\mathbf{r}) = \delta\mathbf{E}_{xc}[\rho]/\delta\rho(\mathbf{r}) \qquad 2.10$$

Kohn and Sham noticed that equation 2.8 is the same as that for a non-interacting system moving in the potential $v_{eff}(\mathbf{r})$. Thus, the exact density can be obtained by solving the N one-electron equations (the restricted KS equations)

$$[-1/2\nabla_i^2 + v_{eff}(\mathbf{r})]\psi_i = \varepsilon_i\psi_I$$

Notice that v_{eff} depends on $\rho(\mathbf{r})$, via Equation 2.10, hence the KS equations must be solved iteratively.

The KS equations are very similar to the Hartree-Fock equations. In fact, setting the exchange-correlation potential to the HF exchange potential,

$$\mathbf{v}_{xc}(\mathbf{r}) = - \int \sum_j \psi_j(\mathbf{r}') \psi_j(\mathbf{r}) \mathbf{P}_{rr'} d\mathbf{r}' / |\mathbf{r}-\mathbf{r}'| \qquad 2.13$$

yields the HF equations. Drawing too many similarities to HF is dangerous, however. Firstly, the KS orbitals are simply a way of representing the density; they are not (as in HF) an approximation of the wavefunction. In particular, Koopmans' theorem,[74] that the ionization potentials and electron affinities are approximated by the negative of the HF occupied and virtual orbital eigenvalues, respectively, is invalid for KS orbitals. However, the highest occupied KS eigenvalue has been shown to be the negative of the first ionization potential, though[75]. Also, HF theory is variational, providing an upper bound to the exact energy, yet DFT is only variational if the exact energy functional is used.

The above analysis is only appropriate for closed shell molecules. Because the KS equations so closely follow the restricted HF equations, both the restricted open shell and unrestricted methodologies are readily available. However, the KS equations are formally exact (given the exact $\mathbf{E}_{xc}[\rho]$), so it must be able to produce an excess of β (spin down) electron density at points in the molecule[76], and therefore only the unrestricted formalism is appropriate. The unrestricted KS equations are

$$[-1/2\nabla_i^2 + v^{\alpha}_{eff}(\mathbf{r})]\psi^{\alpha}_i = \varepsilon^{\alpha}_i \psi^{\alpha}_i \qquad 2.14$$

$$[-1/2\nabla_i^2 + v^{\beta}_{eff}(\mathbf{r})]\psi^{\beta}_i = \varepsilon^{\beta}_i \psi^{\beta}_i \qquad 2.15$$

where

$$\mathbf{v}^{\alpha}_{eff}(\mathbf{r}) = \mathbf{v}(\mathbf{r}) + \delta \mathbf{J}_i[\rho]/\delta\rho(\mathbf{r}) + \delta \mathbf{E}_{xc}[\rho_{\alpha};\rho_{\beta}]/\delta\rho_{\alpha}(\mathbf{r})$$

$$\mathbf{v}^{\beta}_{\mathrm{eff}}(\mathbf{r}) = \mathbf{v}(\mathbf{r}) + \delta\mathbf{J}_i[\rho]/\delta\rho(\mathbf{r}) + \delta\mathbf{E}_{xc}[\rho_\alpha;\rho_\beta]/\delta\rho_\beta(\mathbf{r}) \qquad 2.16$$

One problem with the above derivation of the KS equations is that the density must be non-interacting v-representable. That is, there must exist a potential v_s that will produce the same density as the exact wavefunction. If the density is not non-interacting v-representable, the determinant formed from the KS orbitals will be an excited state.[77] The criteria that make a density non-interacting v-representable are unknown.

Just as in HF theory, the KS equations are solved by expanding the orbitals over a basis set. The major advantage of DFT is that the basis set requirements are far more modest than the more conventional correlated methods.[78,79] In DFT the basis set only needs to represent the one electron density - the inter-electron cusp is accounted for by the effective potential, v_{eff}. In the more traditional methods the basis set describes the entire *N*-electron wavefunction, requiring an accurate description of the cusp which is sensitive to the basis set.

IV.5.2. THE LOCAL DENSITY APPROXIMATION

The local density approximation (LDA) states that, for regions of a material where the charge density is slowly varying, the exchange correlation energy (E_{xc}) at that point can be considered the same as that for a locally uniform electron gas of the same charge density. In this case we can write E_{xc} as

$$E_{xc} = n(\mathbf{r})\varepsilon_{xc}(n)d\mathbf{r}$$

The spin polarized variation (local spin density approximation, or LSDA) replaces the spin averaged energy density in the above equation with the energy density for a

polarized homogeneous electron gas. Although this approximation is extremely simple, it is surprisingly accurate, and forms the core of most modern DFT codes. It even works reasonably well in systems where the charge density is rapidly varying. However it tends to underpredict atomic ground state energies and ionization energies, while overpredicting binding energies. It is also known to overly favor high spin state structures. For these reasons there have been attempts to move beyond the LDA, notably through the addition of gradient corrections to incorporate longer range gradient effects.[20] However in practice, although these improvements seem to give better total energies, the resultant structure is often worse, and at a greatly increased computational cost. In general, the LDA is worse for small molecules and improves with increased system size.

The only remaining problem is to find an approximate solution for the homogeneous electron gas exchange-correlation term, $\varepsilon_{xc}(n)$. There are several parameterized prescriptions for this, the one used in AIMPRO is based on the work by Ceperley and Alder.[21]

IV.5.3. NONLOCAL DENSITY FUNCTIONALS FOR THE EXCHANGE-CORRELATION ENERGY

The standard approximation for the exchange-correlation (xc) energy functional, the crucial quantity in density functional theory, is the local density approximation (LDA). For a given density, the LDA replaces the true xc-energy density at each point in space by the xc-energy density of a homogeneous electron gas of the same density. In recent years it has become clear that, although the LDA has been very successful for a large variety of problems, the description of many interesting systems in atomic physics

(see e.g.[1]), quantum chemistry[23,24] and condensed matter physics[25,26] requires nonlocal corrections to the LDA. The gradient expansion (GE), in which in addition to the local density n(r) its gradients, are also used for the density functional representation of the xc-energy; it is the most simple and systematic nonlocal extension of the LDA. While the lowest order GE was found to be inadequate for the description of atoms and solids[27], gradient corrected functionals have received renewed attention since the introduction of generalized gradient approximations (GGAs).[33-35] GGAs can be interpreted as semiempirical partial resummations of the complete GE including only terms depending on *grad(n(r))* but no higher density gradients.

It has been demonstrated that GGAs give excellent atomic ground state energies[23,24,28] and significantly improve dissociation energies and bond lengths of small molecules.[23,24,28-30] Most notably, however, GGAs are able[27] to correct one of the most well known deficiencies of the LDA. Energy differences like ionization potentials and electron affinities, on the other hand, are not always improved by GGAs.[28,31] Moreover, for solids, GGAs do not give results which are consistently superior to those of the LDA.[6,16,18-22]

IV.5.4. CORRECT ASYMPTOTIC BEHAVIOR APPROXIMATION TO DENSITY FUNCTIONAL ENERGY, BECKE TYPE ONE PARAMETER EXCHANGE FUNCTIONAL (B).

Gradient-corrected density-functional approximations for the exchange energies of atomic and molecular systems fail to reduce the correct 1/**r** asymptotic behavior of the exchange-energy density. A. D. Becke[34] reported a gradient-corrected exchange-energy functional with the proper asymptotic limit. This functional, containing only one

parameter, fits the exact Hartree-Fock exchange-energies of a wide variety of atomic systems with remarkable accuracy.

It is well-known that the Hartree-Fock exchange energy of an inhomogeneous many-electron system can be reasonably approximated by the so-called local-density approximation (LDA) which, in atomic units, is given by

$$E_X^{LDA} = -C_X \sum_\sigma \int \rho_\sigma^{4/3} d^3\mathbf{r} \qquad 3.1a$$

$$C_X = (3/2)[3/4\pi]^{1/3} \qquad 3.1b$$

Where σ denotes either "up" or "down" electron spin, and where the integrand is essentially the volume exchange-energy density of a uniform spin-polarized electron gas of spin density ρ_σ. The LDA typically underestimates the exchange energies of atomic and molecular systems by roughly 10%, and corrections for the obvious nonuniformity of atomic and molecular densities. Corrections depending on local density gradients have been derived by Sham,[36] among others.[37] Nonlocal corrections of other types, such as the weighted density scheme of Gunnarsson and Jones,[46] have also been proposed, but gradient-type corrections have received most attention due to their great simplicity.[1]

The lowest-order gradient correction (LGC) to the local-density approximation is uniquely determined by dimensional analysis, and is given by

$$E_X^{LGC} = E_X^{LDA} - \beta \sum_\sigma \int (\nabla \rho_\sigma)^2 / \rho_\sigma^{4/3} d^3\mathbf{r} \qquad 3.2$$

Where β is a constant. This LGC functional (named "X$\alpha\beta$" by Herman et al.[45]) has, however, well-known and severe deficiencies. First of all, the corresponding exchange potential diverges asymptotically in atomic and molecular systems and thus requires ad

hoc adjustment in practical applications. Secondly, the value of the constant β is a matter of considerable confusion.[34]

Motivated by the first of these problems by following "modified" gradient-corrected exchange-energy functional on semiempirical grounds.[38]

$$E_X^{SE} = E_X^{LDA} - \beta\sum_\sigma \int \rho_\sigma^{4/3} X_\sigma^2 / (1 + \gamma X_\sigma^2) d^3\mathbf{r} \qquad 3.3$$

where SE denotes semiempirical, and where X_σ is the dimensionless ratio

$$X_\sigma^2 = |\nabla\rho_\sigma| / \rho_\sigma^{4/3} \qquad 3.4$$

and β and γ are parameters. This functional, named $X\alpha\beta\gamma$ in Ref.38, is determined by the reasonable criteria that (1) dimensionless is satisfied, (2) the LGC functional is obtained in the case of small density gradients, and (3) the exchange potential is well behaved in the large- gradient (i.e., large-X_σ) limit. Note that the X_σ limit corresponds to the asymptotic exponential tail of an atomic or molecular charge distribution. The functional of Eq.3 is certainly not the only conceivable such functional, but is probably the simplest. If parameters β and γ are chosen on the basis of a least-squares fit to selected atomic data, SE functional approximates a wide range of atomic Hartree-Fock exchange energies extremely well.[38]

Nevertheless, the somewhat arbitrary choice of large gradient behavior in Eq.3 leaves much to be desired. Perdew[44] and Becke[39] have presented improved theoretical models with large-X_σ limits close to that of Eq.3, and other researchers[40,41] have proposed still other gradient correction terms. Therefore, the optimum form of the large-

X_σ limit is, unfortunately, ambiguous at the present time. However, the exact asymptotic behavior of the exchange-energy density of any finite system is known, and is given by

$$\lim_{r\to\infty} U^\sigma_X = -1/r \qquad 3.5$$

where U^σ_X is the coulomb potential of the exchange energy or Fermi hole density $\rho^\sigma_X(\mathbf{r},\mathbf{r}')$ at reference point $\mathbf{r}$ (Ref. 42), and is related to the total exchange energy by

$$E_X = (1/2)\sum_\sigma \int \rho_\sigma U^\sigma_X d^3\mathbf{r} \qquad 3.6$$

This result reflects the fact that, for reference points very far from a finite system, the Fermi hole remains "attached" to the system. Given also that the Fermi hole contains exactly one electron, Eq. 3.5 is obvious. A discussion of this result has been provided by March.[43]

Furthermore, the asymptotic behavior of the spin density ρ_σ is also known,[48] and is given by

$$\lim_{r\to\infty} \rho_\sigma = \exp(-a_\sigma r) \qquad 3.7$$

where a_σ is a constant related to the ionization potential of the system. In view of this known asymptotic density dependence, Becke[34] has proposed a new gradient-corrected exchange-energy functional that reproduces the exact asymptotic behavior of Eqs. 3.5 and 3.6:

$$E_X = E_X^{LDA} - \beta\sum_\sigma \int \rho_\sigma^{4/3} X_\sigma^2 / (1 + 6\beta X_\sigma \sinh^{-1} X_\sigma) d^3\mathbf{r} \qquad 3.8$$

Where β is constant. It is easily verified that this functional generates the asymptotic potential of Eq.3.5 under substitution of the asymptotic spin density of Eq.3.7. Furthermore, this new exchange-energy functional reduces to the LGC expression in the limit of small density gradients and antisymmetry of the function $\sinh^{-1}X_\sigma$, is expressible as a Taylor series in even power of X_σ as a required of any analytically well-behaved function.[34]

Notice, also, that Becke's functional contains only one parameter β because the coefficient of $X_\sigma \sinh^{-1}X_\sigma$ is fixed by Eq. 3.5. Considering that the previous functionals of Ref.38 and Ref. 39-41,44 contain at least two parameters. The parameter β may be easily determined by a least-square fit to exact atomic Hartree-Fock data. Becke has determined value of β to be 0.0042 a.u. from best fits to exchange energies of six noble gas atoms helium through radon.

IV.5.4.1. DEVELOPMENT OF THE COLLE-SALVETTI CORRELATION-ENERGY FORMULA INTO A FUNCTIONAL OF THE ELECTRON DENSITY.

Interest in the calculation of the correlation energy continues unabated.[52,53] Robert G. Parr *et al.* reported a new development in which the Colle-Salvetti formula for the calculation of the correlation correction energy from the Hartree-Fock second order density matrix[54] is converted into a density-functional formula.

Let ρ(r) be the Hartree-Fock electron density and $\rho_2^{HF}(\mathbf{r}_1,\mathbf{r}_2)$ be the diagonal element of the second-order Hartree-Fock reduced density matrix,

$$\rho_2^{HF}(\mathbf{r}_1,\mathbf{r}_2) = (1/2)N(N-1)\int \dots \int |\psi^{HF}(\mathbf{r}_1\sigma_1\mathbf{r}_2\sigma_2 \dots)|^2 \, d\sigma_1 d\sigma_2 \dots d\sigma_N d\mathbf{r}_3 d\mathbf{r}_4 \dots d\mathbf{r}_N. \quad 3.9$$

ρ_2^{HF} can also be expressed in terms of interparticle coordinates, where

$$\mathbf{r} = (\mathbf{r}_1 + \mathbf{r}_2)/2; \; \mathbf{s} = \mathbf{r}_1 - \mathbf{r}_2. \qquad 3.10$$

The Colle-Salvetti formula for correlation energy is then

$$E_c = -4a\int[\rho_2^{HF}(\mathbf{r}_1,\mathbf{r}_2)/\rho(\mathbf{r})]\{1 + b\rho(\mathbf{r})^{-8/3}[\nabla_s^2\rho_2^{HF}(\mathbf{r},\mathbf{s})]_{s=0}\exp(-c\rho(\mathbf{r})^{-1/3})\}/(1 + d\rho(\mathbf{r})^{-1/3}) \qquad 3.11$$

Where a=0.04918, b = 0.1320, c = 0.2533, and d = 0.349. This formula was arrived at by Colle and Salvetti by a theoretical analysis accompanied by a series of approximations, beginning (essentially) from the reasonable proposition that the second-order density matrix including correlation may approximated by the Hartree-Fock second-order density matrix times a correlation factor. The constants a, b, c, and d in the final formula were obtained by a fitting procedure using only the Hartree-Fock orbital for helium atom. Colle and Salvetti demonstrated that Eq.3.11 gave good predicted correlation energies for atoms and molecules.[54]

IV.5.4.2. FORMULA INVOLVING LOCAL KINETICK-ENERGY DENSITY

First consider a closed-shell atom or molecule, having an even number of electrons. Then

$$\rho_2^{HF}(\mathbf{r}_1,\mathbf{r}_2) = 1/2\rho(\mathbf{r}_1)\rho(\mathbf{r}_2) - 1/4\rho_1^{HF}(\mathbf{r}_1,\mathbf{r}_2)\,\rho_1^{HF}(\mathbf{r}_2,\mathbf{r}_1), \qquad 3.12$$

where ρ_1^{HF} is the Hartree-Fock reduced density matrix,

$$\rho_2^{HF}(\mathbf{r}_1,\mathbf{r}_1') = N\int\ldots\int\psi^{HF*}(\mathbf{r}_1\sigma_1\,\mathbf{r}_2\sigma_2\ldots)\psi^{HF*}(\mathbf{r}_1'\sigma_1\,\mathbf{r}_2\sigma_2\ldots)\,d\sigma_1 d\sigma_2\ldots\,d\mathbf{r}_2 d\mathbf{r}_3\ldots \qquad 3.13$$

where $\rho_1^{HF}(\mathbf{r},\mathbf{r}) = \rho(\mathbf{r})$ and $\rho_2^{HF}(\mathbf{r},\mathbf{r}) = (1/4)\rho^2(\mathbf{r})$. In the interparticle coordinates of Eq.3.12 leads

$$\rho_2^{HF}(\mathbf{r},\mathbf{s}) = (1/2)\,\rho(\mathbf{r}+\mathbf{s}/2)\rho(\mathbf{r}-\mathbf{s}/2) - (1/4)[\,\rho(\mathbf{r}+\mathbf{s}/2,\mathbf{r}-\mathbf{s}/2)], \quad 3.14$$

and there follows

$$\{\nabla_s^2\rho(\mathbf{r},\mathbf{s})\}_{s=0} = \rho(\mathbf{r})[t_{HF}(\mathbf{r}) - 2t_w(\mathbf{r})]. \quad 3.15$$

where

$$t_w(\mathbf{r}) = (1/8)\,|\nabla\rho(\mathbf{r})|^2/\rho(\mathbf{r}) - (1/8)\,\nabla^2\rho \quad 3.16$$

is a local "Weizsacker" kinetic-energy density and

$$t_{HF}(\mathbf{r}) = 91/2)\{\nabla_{r1}\nabla_{r2}\rho(\mathbf{r}_1,\mathbf{r}_2)\}_{r1=r2=r} - (1/8)\nabla^2\rho = (1/8)\Sigma\,|\nabla\,\rho_i|^2/\rho_i(\mathbf{r}) - (1/8)\nabla^2\rho \quad 3.17$$

is the local Hartree-Fock kinetic-energy density. $t_{HF}(\mathbf{r})$ and $t_W(\mathbf{r})$,

$$E_c = -a\int\{\rho(\mathbf{r}) + b\rho(\mathbf{r})^{-2/3}\}\{\,t_{HF}(\mathbf{r}) - 2t_w(\mathbf{r})\}\exp(-c\rho(\mathbf{r})^{-1/3})d\mathbf{r}/\{1+d\rho(\mathbf{r})^{-1/3}\} \quad 3.18$$

For a system in which the α-electron density differs from β-electron density (in the open- shell restricted Hartree-Fock case, the α-spin orbitals are the same as the β-spin orbitals in closed-shell part, but an excess of α- or β-spin orbitals in the rest.), Eq.3.12 is replaced by

$$\rho_2^{HF}(\mathbf{r}_1,\mathbf{r}_2) = 1/2\rho(\mathbf{r}_1)\rho(\mathbf{r}_2) - 1/2\rho_{1,\alpha\alpha}^{HF}(\mathbf{r}_1,\mathbf{r}_2)\,\rho_{1,\alpha\alpha}^{HF}(\mathbf{r}_2,\mathbf{r}_1) - 1/2\rho_{1,\beta\beta}^{HF}(\mathbf{r}_1,\mathbf{r}_2)\,\rho_{1,\beta\beta}^{HF}(\mathbf{r}_2,\mathbf{r}_1) \quad 3.19$$

so that

$$\rho_2^{HF}(\mathbf{r}_1,\mathbf{r}_2) = 1/2\rho^2(\mathbf{r}) - (1/2)[\,\rho_\alpha^2(\mathbf{r}) + \rho_\beta^2(\mathbf{r})], \quad 3.20$$

where $\rho_\alpha(\mathbf{r})$ and $\rho_\beta(\mathbf{r})$ are the α-spin and β-spin electron densities. With $t^\alpha_{HF}(\mathbf{r})$ and $t^\beta_{HF}(\mathbf{r})$ the corresponding kinetic-energy densities in the sense of Eq. 3.17, and with

$$\gamma(\mathbf{r}) = 2\{1 - [\rho_\alpha^2(\mathbf{r}) + \rho_\beta^2(\mathbf{r})]/\rho^2(\mathbf{r}) \qquad 3.21$$

Eq.3.15 is replaced by

$$\{\nabla_s^2 \rho_2^{HF}(\mathbf{r},\mathbf{s})\}_{s=0} = 2\{[\rho_\alpha(\mathbf{r})\, t^\alpha_{HF}(\mathbf{r}) + \rho_\beta(\mathbf{r})\, t^\beta_{HF}(\mathbf{r})] - \rho(\mathbf{r}) t_w(\mathbf{r})\} \qquad 3.22$$

and Eq.3.18 by

$$E_c = -a\int \{\rho(\mathbf{r}) + 2b\rho(\mathbf{r})^{-5/3}\}\{\rho_\alpha(\mathbf{r}) t^\alpha_{HF}(\mathbf{r}) + \rho_\beta(\mathbf{r}) t^\beta_{HF}(\mathbf{r}) - \{\rho(\mathbf{r}) t_w(\mathbf{r})\}\exp(-c\rho(\mathbf{r})^{-1/3})\gamma(\mathbf{r})d\mathbf{r}/\{1 + d\rho(\mathbf{r})^{-1/3}\} \qquad 3.23$$

IV.5.4.3. GRADIENT EXPANSION FORMULAS

Equations 3.18 and 3.23 lack being pure density functional only because of the appearance in them of the Hartree-Fock local kinetic-energy densities $t_{HF}(\mathbf{r})$, $t^\alpha_{HF}(\mathbf{r})$,and $t^\beta_{HF}(\mathbf{r})$, which depend on individual orbital densities. If the view is adopted that the orbitals are the Kohn-Sham orbitals, then these orbitals then these too are functionals of the density, and Eq. 3.18 and 3.23 are pure density-functional expressions (as would be Eq. 3.11 with this interpretation). Eschewing that view for the present, one can turn Eqs. 3.18 and 3.23 into explitic density-functional formulas by using gradient expansions, whereby $t_{HF}(\mathbf{r})$ is expanded about the Thomas-Fermi local kinetic-energy density t_{TF}.

The Thomas-Fermi kinetic-energy density is given by

$$t_{TF}(\mathbf{r}) = C_F\rho(\mathbf{r})^{5/3}, \quad C_F = (3/10)(3\,\pi^2)^{2/3} \qquad 3.24$$

In terms of this, the conventional closed-shell gradient expansion of $t_{HF}(\mathbf{r})$ gives,[59] to zero order,[60]

$$t_{HF}(\mathbf{r}) = t_{TF}(\mathbf{r}) = C_F\rho(\mathbf{r})^{5/3} \qquad 3.25$$

to second order,

$$t_{HF}(\mathbf{r}) = t_{TF}(\mathbf{r}) + [(1/9)t_W(\mathbf{r}) + (1/8)\nabla^2\rho] \qquad 3.26$$

and so on. An alternative formula is provided by the mean-path approximation,[61] to zero order,

$$t_{HF}(\mathbf{r}) = t_{TF}(\mathbf{r}) + [(1/9)t_W(\mathbf{r}) + (1/36)\nabla^2\rho] \qquad 3.27$$

for open-shell case, the corresponding formulas are readily derived using[62]

$$t^{\alpha}_{HF}(\mathbf{r}) = (1/2)t_{TF}(2\rho_{\alpha}(\mathbf{r}),\mathbf{r})$$

and

$$t^{\beta}_{HF}(\mathbf{r}) = (1/2)t_{TF}(2\rho_{\beta}(\mathbf{r}),\mathbf{r}) \qquad 3.28$$

The second correction energy formulas of Eqs 3.18 and 3.23 then become

$$E_c = \int \{1/(1+d\rho^{-1/3})\}\{\rho + b\rho^{-2/3}[C_F\rho^{5/3} - 2t_W + ((1/9)t_W(\mathbf{r}) + (1/18)\nabla^2\rho)]\exp(-c\rho(\mathbf{r})^{-1/3})\}d\mathbf{r} \qquad 3.29$$

and

$$E_c = \int \{\gamma(\mathbf{r})/(1+d\rho^{-1/3})\}\{\rho + 2b\rho^{-5/3}[2^{2/3}C_F{\rho_{\alpha}}^{8/3} + 2^{2/3}C_F{\rho_{\beta}}^{8/3} - \rho t_W + (1/9)(\rho_{\alpha}{t^{\alpha}}_W + \rho_{\beta}{t^{\beta}}_W) + (1/18)(\rho_{\alpha}\nabla^2\rho_{\alpha} + \rho_{\beta}\nabla^2\rho_{\beta})]\exp(-c\rho(\mathbf{r})^{-1/3})\}\}d\mathbf{r} \qquad 3.30$$

These are conventional second-order gradient expansion formulas, for closed and open shells, respectively. Zero order formulas are obtained by striking out the terms within the parentheses in each case. This zero-order mean-path formula is obtained by replacing 1/18 with 1/36 in these terms.

IV.5.4.4. CORRELATION POTANTIAL

The correlation potential is the functional derivative of E_c with respect to $\rho(\mathbf{r})$. Equation 3.30 yields, for open-shell case,

$$\partial E_c/\partial\rho = -a(F_2'\rho + F_2) - 2^{5/3}abC_F[G_2'(\rho_K^{8/3} + \rho_2^{8/3}) + (8/3)G_2\rho_K^{5/3}] - (ab/4)[\rho\nabla^2G_2 + 4\nabla G_2.\nabla\rho + 4G_2\nabla^2\rho + G_2'(\rho\nabla^2\rho - |\nabla\rho|^2)] - (ab/36)[3\rho_K\nabla^2G_2 + 4\nabla\rho_K.\nabla G_2 + 4G_2\nabla^2\rho_K + 3G_2'(\rho_K\nabla^2\rho_K + \rho_2\nabla^2\rho_2) + G_2'(|\nabla\rho_K|^2 + |\nabla\rho_2|^2)] \quad 3.31$$

where

$$F_2(\rho) = \gamma(\mathbf{r})/(1 + d\rho^{-1/3})$$

$$G_2(\rho) = F_2(\rho)\rho^{-5/3}\exp(-c\rho(\mathbf{r})^{-1/3}) \quad 3.32$$

$F_2'(\rho)$ (or $G_2'(\rho)$) is the first derivative of F_2 (or G_2) with respect to $\rho_K(\mathbf{r})$.

IV.5.5.1. THE EXCHANGE TERM IN VWN APPROXIMATION

The local density approximation requires that the exchange-correlation potential be given as a function of the electron density at a given point in space. The form of the exchange-correlation potential is given by Vosko, Wilk, and Nusair (VWN).[65] The form is a fit to the Ceperley-Alder electron gas study.[66] The VWN functional reproduces the random phase approximation (RPA) results for a uniform electron gas in the high density limit; it reproduces the spin-stiffness constant calculated in the RPA in the paramagnetic limit of a uniform electron gas, and it is uniformly differentiable as a function of the electron gas parameter. It is also in standard use, or available as an option, in many electronic structure codes, and thereby provides a convenient reference potential for

checking the accuracy of numerical calculations. We now summarize the form of the VWN functional.

The exchange-correlation energy per electron is separated into two parts, an exchange term and a correlation term. The exchange term is given by

$$\varepsilon_x(\mathbf{r}, \zeta) = \varepsilon^P_x(\mathbf{r}_s) + [\varepsilon^F_x(\mathbf{r}_s) - \varepsilon^P_x(\mathbf{r}_s)]f(\zeta) \quad 4.1$$

The electron gas parameter, $\mathbf{r}_s$, the spin polarization, ζ, and the ferromagnetic and paramagnetic exchange energies, $\varepsilon^F_x(\mathbf{r}_s)$, $\varepsilon^P_x(\mathbf{r}_s)$ are defined as

$$\mathbf{r}_s = [1/(3\pi n)]^{1/3} \quad 4.2$$

$$\zeta = (n_\uparrow - n_\downarrow)/n \quad 4.3$$

$$\varepsilon^P_x(\mathbf{r}_s) = 2^{-1/3}\varepsilon^F_x(\mathbf{r}_s) = -3[9/(32\pi^2)]^{1/3}\ \mathbf{r}_s^{-1} \quad 4.4$$

and $f(\zeta)$ is given by

$$f(\zeta) = [(1+\zeta)^{4/3} + (1-\zeta)^{4/3} - 2]/[2(2^{1/3}-1)] \quad 4.5$$

where n is the electron number density (implicitly a function of the spatial coordinates), and and its corresponding spin-up and spin-down components ($n = n_\uparrow + n_\downarrow$).

IV.5.5.2. THE CORRELATION TERM

The correlation term is related to the function,

$$F(\mathbf{r}_s; A,x_0,b,c) = A\{\ln(x^2/X(x)) + (2b/Q)\tan^{-1}d - bx_0/X(x_0)[\ln((x-x_0)^2/X(x)) + 2(b+2x_0)/Q\tan^{-1}d]\} \quad 4.6$$

where we have, $x = 1/r_s^{1/2}$, $X(x) = x^2 + bx + c$, $Q=[4c-b2]^{1/2}$, and $d = Q/(2x+b)$. The parameters, b, and c, given in the table below, are used to create three instances of F, using the table below.

	A	x_0	b	c
Paramagnetic $\varepsilon^P_c(r_s)$	0.0310907	-0.10498	3.72744	12.9352
Ferromagnetic $\varepsilon^F_x(r_s)$	0.01554535	-0.32500	7.06042	18.0578
Spin stiffness α_c	$-1/(6\pi^2)$	-0.00475840	1.13107	13.0045

The correlation energy is given by

$$\varepsilon_C(r_s) = \varepsilon^P_C(r_s) + \Delta\varepsilon_C(r_s, \zeta) \qquad 4.7$$

The paramagnetic correlation energy is given by $\varepsilon^P_C(r_s) = F(r_s; A, x_0, b, c)$ with the four parameters taken from the ``Paramagnetic" line in the table. (Similar definitions hold for $\varepsilon^F_x(r_s)$ and α_c.) The polarization contribution is given by $r_s = [1/(3\pi n)]^{1/3}$

$$\Delta\varepsilon_C(r_s, \zeta) = \alpha_c(r_s)[f(\zeta)/f''(0)][1+ \beta(r_s)\zeta^4] \qquad 4.8$$

with the function f as defined above, and where we have

$$\beta(r_s) = f''(0)\, \Delta\varepsilon_C(r_s, 1)/ \alpha_c(r_s) - 1 \qquad 4.9$$

where r_s represents the Wigner-radius and is defined by $r_s = r_s = [1/(3\pi n)]^{1/3}$ and

$$\Delta\varepsilon_C(r_s, 1) = \varepsilon_C(r_s, 1) - \varepsilon_C(r_s, 0) = \varepsilon^F_C(r_s) - \varepsilon^P_C(r_s) \qquad 4.10$$

is the difference of the ferromagnetic and paramagnetic correlation energies.

The exchange-correlation potential is given by

$$V_{xc}(n) = d[n(\varepsilon_X - \varepsilon_C)]/dn \qquad 4.11$$

IV.5.6. THE CORRELATION TERM IN THE PW91 APPROXIMATION

Due to the experiences with the LDA and as a consequence of some of its shortcomings, recent developments have resulted in a number of gradient corrections to local functionals like the aforementioned VWN, or a completely new class of gradient corrected functionals. Notable examples are, for instance, the Perdew group's PW91,[67-69] which, combined with a local functional like VWN or the PW92 functional, results in the following expression for E_C:

$$E_C^{PW91} = E^{LDA}{}_C(\rho) + \rho\beta/(2\alpha)\ln\{1 + 2\alpha(t^2 + At^4)/[\beta(1 + At^2 + A^2t^4)]\} + C_{C0}[C_C(\rho) - C_{C1}]t2\exp(-100s^2) \qquad 5.1$$

where :

$$A = 2\alpha/\beta\{\exp[-2\alpha\varepsilon^{LDA}{}_C(\rho)/(\rho\beta^2) - 1]\}^{-1}$$

$$t = (\pi/3)^{1/6}|\nabla\rho|/(4\rho^{7/6}) \qquad 5.2$$

and ,

α=0.09, β=0.0667263212, C_{C0} = 15.7559, C_{C1} = 0.0035521 and

$C_C(\rho) = C_1 + (c_2 + c_3 r_s + C_4 r^2{}_s)/(1 + C_5 r_s + C_6 r^2{}_s + C_6 r^3{}_s)$ with C_1 = 0.001667, C_2 = 0.002568, C_3 = 0.023266, C_4 = 7.389 10^{-6}, C_5 = 8.723, C_6 = 0.472 and C_7 = 0.07389.

IV.5.7. THE CORRELATION TERM IN THE BP86 APPROXIMATION

The density-functional approximation for the correlation energy of the inhomogeneous electron gas[70] is

$$E_C[n_\uparrow,n_\downarrow] = \int \varepsilon_C(n_\uparrow,n_\downarrow)d^3r + \int (r/d)\exp(-\Phi)[C(n)/n^{4/3}]|\nabla|d^3r \quad 6.1$$

where $C(n) = 0.001667 + (0.002\ 568 + \alpha r_s + \beta r^2_s)/(1 + \gamma r_s + \delta r^2_s + 104\beta r^3_s)$

with $\alpha = 0.023\ 266$, $\beta = 7.389 \times 10^{-6}$, $\gamma = 8.723$ (Ref.70)

$\Phi = 1.745f[C(\infty)/C(n)]|\nabla|/n^{7/6}$ with $C(\infty) \cong C^{RPA}(n)$ $(\approx = \int_0^\infty dkA(n)\exp[-B(n)k])$ 6.2

$$d = 2^{1/3}\{[(1 + \zeta)/2]^{5/3} + [(1 - \zeta)/2]^{5/3}\}^{1/2} \quad 6.3$$

$$r_s = [3/(4\pi n)]^{1/3}$$

Total correlation energy per particle of the uniform electron gas, $\varepsilon_C(n_\uparrow,n_\downarrow)$, is taken from a parametrization[71] of the Ceperley-Alder[72] results, and cutoff parameter f =0.11 is chosen to fit the exact correlation energy of the neon atom.[73] equation of $E_C[n_\uparrow,n_\downarrow]$ recovers the beyond-RPA gradient expansion in the unpolarized slowly varying limit.

IV 6. VIBRATIONAL FREQUENCY

IV 6.1. MASS WEIGHTED THE HESSIAN AND DIAGONALIZE:

The vibrational frequency of any diatomic or polatomic systems derived from the second derivatives of the potential **V** with respect to displacement of the atoms in Cartesian coordinates (CART):

$f_{CART} = (\partial^2 V/\partial\xi_i\partial\xi_j)_0$

This is a 3Nx3N matrix(N is the number of atoms), where $\xi_1, \xi_2, \xi_3 \ldots \xi_{3N}$ are used for the displacements in cartesian coordinates, Δx_1, Δy_1, Δz_1, ..., Δz_N refers to the fact that the derivatives are taken at the equilibrium positions of the atoms, and that the first derivatives are zero. We can rewrite the cartesian coordinates in mass weighted Cartesian coordinates (MWC) and force constants as follow:

$F_{MWCij} = f_{CART}/(m_i\, m_j)^{1/2} = ((\partial^2 V/\partial q_i\partial q_j)_0$

Where $q_1=(m_1)^{1/2}\xi_1=(m_1)^{1/2}\Delta x_1$, $q_2=(m_1)^{1/2}\xi_2 =(m_1)^{1/2}\Delta y_1$ etc.; these are the mass weighted Cartesian coordinates. The eigenvectors, which are the normal modes, are discarded; they will be calculated again after rotational and translational modes are separated out. The roots of eigenvalues are the fundamental frequencies of the molecule. Using the matrix form, we can find the vectors corresponding to the rotations and translations. Once these vectors are known, we know that the rest of the normal modes are vibrationals, so we can distinguish low frequency vibrational modes from rotational and tranlational modes. The center of mass (R_{CM}) is found in the usual way:

$\mathbf{R}_{CM}=\sum_i m_i\mathbf{r}_i/\sum_i m_i$, where the sums are over the atoms, i. The origin is shifted to the center of mass $\mathbf{r}_{COM} = \mathbf{r}_i - \mathbf{R}_{CM}$. The moments of inertia of the moment of inertia tensor (**I**) can be given as following:

$$\mathbf{I} = \begin{vmatrix} I_{xx} & I_{xy} & I_{xz} \\ I_{yx} & I_{yy} & I_{yz} \\ I_{zx} & I_{zy} & I_{zz} \end{vmatrix}$$

$$= \begin{vmatrix} \sum_i m_i(y_i^2+z_i^2) & \sum_i m_i(x_i y_i) & \sum_i m_i(x_i z_i) \\ \sum_i m_i(y_i x_i) & \sum_i m_i(x_i^2+z_i^2) & \sum_i m_i(y_i z_i) \\ \sum_i m_i(z_i x_i) & \sum_i m_i(z_i y_i) & \sum_i m_i(x_i^2+y_i^2) \end{vmatrix}$$

This symmetric matrix is diagonalized, yielding the principal moments (the eigenvalues **I**) and 3x3 matrix (**X**), which is made up of the normalized eigenvectors of **I**. The eigenvectors of the moment of inertia tensor are used to generate the vectors corresponding to translation and infinitesimal rotation of the molecule in the next step.

IV 6.2. GENERATE COORDINATES IN THE ROTATING AND TRANSLATING FRAME

The main goal in this section is to generate the transformation **D** from mass weighted Cartesian coordinates to a set of 3N coordinates, where rotation and translation of the molecule are separated out, leaving 3N-6 or 3N-5 modes for vibrational analysis. The three vectors ($\mathbf{D}_1$, $\mathbf{D}_2$, $\mathbf{D}_3$) of length 3N corresponding to translation are trivial to generate in cartesian coordinates. They are just $(m_i)^{1/2}$ times the corresponding coordinate axis. For example, for a homonuclear diatomic molecule, the translational vectors are:

$\mathbf{D}_1 = [m_1)^{1/2}, 0, 0, (m_2)^{1/2}, 0, 0, 1, 0, 0]^t$

$\mathbf{D}_2 = [0, (m_1)^{1/2}, 0, 0, (m_2)^{1/2}, 0, 0, 1, 0]^t$

$\mathbf{D}_3 = [0, 0, (m_1)^{1/2}, 0, 0, (m_2)^{1/2}, 0, 0, 1]^t$

Generating vectors corresponding to rotational motion of the atoms in Cartesian coordinates is a bit complicated. The vectors for these are defined this way:

$D_{4j,i} = [(Ry)_i X_{j,3} - (Rz)_i X_{j,2}] / (m_i)^{1/2}$

$D_{5j,i} = [(Rz)_i X_{j,1} - (Rx)_i X_{j,3}] / (m_i)^{1/2}$

$D_{6j,i} = [(Rx)_i X_{j,2} - (Ry)_i X_{j,1}] / (m_i)^{1/2}$

Where j = x, y, z; i is over all atoms and R is the dot product of **R** (the coordinates of the atoms with respect to the center of mass) and the corresponding row of **X**, the matrix used to diagonalize the moment of inertia tensor **I**. By using Schimidt orthogonalization, N_{vib}=3N-6 or 3N-5 remaining vectors can be generated, which are orthogonal to the five or six rotational and translational vectors. The result is a transformation matrix **D** which transforms from mass weighted Cartesian coordinates r to internal coordinates **S=Dq**, where rotation and translation have been separated out. The force constant can be transformed from mass weighted Cartesian coordinates, f_{MWC}, to new internal coordinates, f_{INT}.

$f_{INT} = \mathbf{D}^{\dagger} \mathbf{f}_{MWC} \mathbf{D}$

The N_{vib}xN_{vib} submatrix of f_{INT}, which represents that force constants internal coordinates, is diagonalized yielding N_{vib} eigenvalues $\lambda = (2c\pi\omega)^2$ (where $\nu = c\omega$ and c

is the speed of the light and ω is vibrational frequency in cm^{-1}.), and N_{vib} eigenvectors. If we call the transformation matrix composed of the eigenvectors **L**, then we have

$$\mathbf{L}^{\dagger}\mathbf{f}_{INT}\,\mathbf{L} = \Lambda,$$

where Λ is the diagonal matrix with eigenvalues:

$$\lambda_i,\ \lambda_i = (2c\pi\omega_i)^2 = k_i/\mu_i$$

or

$$\omega_i = (1/2c\pi)(\ k_i/\mu_i)^{1/2}$$

where k_i is force constant and μ_i is reduced mass.

Chapter III References

1. John T. Moseley, Photodissociation and Photoionization, edited by K. P. Lawley (Wiley, 1985).

2. S. P. Goss, J. D. Morrison and D. L. Smith J. Chem. Phys.**75**, 757 and 1820 (1981).

3. R. N. Dixon, Chem. Soc. Rev., (1994).

4. C. R. C. Wang, S. Pollack, D. Cameron and M. Kappes, J. Chem. Phys., **93**, 3787 (1990).

5. P. J. Brucat, L. S. Zheng, C. L. Pettiette, S. Yang and R. E. Smalley, J. Chem. Phys., **84**, 3078 (1986).

6. A. W. Castleman Jr., and R. G. Keesee, Chem. Rev., **86**, 589 (1986) .

7. K. F. Willey, D. L. Robbins, C.-S. Yeh and M. A. Duncan, Faraday Discuss. **92**, 269 (1991).

8. M. F. Jarrold and K. M. Creegan, Int. J. Mass Spec. and Ion Processes, **102**, 161 (1990).

9. M. F. Jarrold and K. M. Creegan, Chem. Phys. Lett., **166**, 116 (1990).

10. P. C. Engelking, Chem. Rev., **91**, 399 (1991).

11. J. M. Hayes, Chem. Rev., **87**, 745 (1987).

12. J. B. Hopkins, P. R. R. Langridge-Smith, M. D. Morse and R. E. Smalley, J. Chem. Phys., **78**, 1627 (1983).

13. Jacqueline C. Pinegar, Jon D. Langenberg, Caleb A. Arrington, Eileen M. Spain and Michael D. Morse, J. Chem. Phys., **102**, 666 (1995).

14. R.J. Van Zee, S. Li and W. Weltner Jr., Chem. Phys. Lett. **217**, 381 (1994) .

15. A. M James, P. Kowalczk, E. Langlois, M. D. Campbell, A. Ogawa and B. Simard, J. Chem. Phys., **101**, 4485 (1994).

16. A. M. James, P. Kowalczk, R. Fournier and B. Simard J. Chem. Phys., **99**, 8504 (1993).

17. Z. Hu, B. Shen, Q. Zhou, S. Deosaran, J. R. Lombardi and D. M. Lindsay, SPIE Proceedings Vol. **1599**, (1992).

18. D. A. Hales, L. Lian, P.B. Armentrout, Int. J. Mass Spec. and Ion Processes, **102**, 269 (1990).

19. S. K. Loh, Li Lian and P.B. Armentrout, J. Chem. Phys., **91**, 6148 (1989.

20. Y. Hamrick, S. Taylor, G. W. Lemire, Z. W. Fu, J, C, Shui and M. D. Morse, J. Chem. Phys., **88**, 4095 (1988).

21. M. Moskovits and W. Limm, Ultramicroscopy **20**, 83 (1986).

22. J. R. Heath, Y. Liu, S. C. O'Brien, Q.-L. Zhang, R. F. Curl, F. K. Tittel, and R. E. Smalley, J. Chem. Phys., **63**, 5520 (1985).

23. R. L.- Asher, D. Bellert, T. Buthelezi and P. J. Brucat, Chem. Phys. Lett., **224**, 525 and 529 (1994).

24. Private communication with P. J. Brucat, University of Florida, Gainesville.

25. Private communication with M. A. Duncan, University of Georgia, Athens.

26. Benoit Simard, Andrew M. James, P. Kowalczyk, R. Fournier and P. A. Hackett, preprint (High Resolution spectroscopy of small transition metal molecules. Recent experimental and theoretical progress on group 5 diatomics.

27. J. C. Weisshaar, J. Chem. Phys., **90**, 1429 (1989).

28. C. W. Bauschlicher Jr., S. R. Langhoff, Chem. Rev., **91**, 701, (1991).

29. S. Taylor, G. W. Lemire, Y. M. Hamrick, Z. Fu and M. D. Morse, J. Chem. Phys., **89**, 5517 (1988).

CHAPTER V

V.1 INTRODUCTION

Up to now, we have talked about the Hamiltonian in the ab initio and density functional theory that does not involve electron spin. In reality, the existence of spin adds an additional term, usually small, to the Hamiltonian. This term, called the spin-orbit interaction, causes the fine structure of atomic or molecular spectra. Spin-orbit interaction derive from a relativistic treatment of the electron. We will give a rough "derivation."

If we imagine ourselves riding on an electron in an atom, from our viewpoint the nucleus is moving around the electron (as the sun appears to move about the earth). This apparent motion of the nucleus gives rise to a magnetic field that interacts with the intrinsic (spin) magnetic moment of the electron, giving the spin-orbit interaction term in the Hamiltonian.

V.2. INTERACTIONS OF THE ELECTRON SPIN

The spins of the individual electrons form a resultant spin vector **S**, whose magnitude is defined by the spin quantum number S. (The magnitude of **S** is $[(S(S+1)]^{1/2}$). S is either a half-integer or an integer, dependent on if the total number of electrons in the molecule is odd or even. The motion of the electrons and nuclei in the molecule, the resultant spin and even the spins of the individual electrons are not wholly independent of one another; certain interactions exist among them. This becomes fairly obvious if one stops to think that the motions of the electrons and of the nuclei are in effect electric currents producing magnetic fields, further, that an intrinsic basic property

of the spin is its magnetic momentum. There is an interaction between the magnetic fields of the moving electrons and nuclei on the one hand, and the resultant spin (and also the spins of the individual electrons) on the other hand. In case a, when the molecule is best examined in the molecule-fixed system, the interaction between the spin and the parallel component of the resultant orbital angular momentum of the electrons makes the resultant spin vector **S** precess around the inter-nuclear axis in such a manner that its parallel component is Σ (Fig. 5.1), where Σ is the quantum number (in the present case, Σ does not refer to the electron state Λ=0 !). Σ can assume any one of the 2S+1 values: S, S - 1, .., -S + 1, - S.

To an electronic state of a given Λ there belong, then, 2S + 1 substates-according to the possible orientations of the **S** spin-whose energy levels are evenly spaced to a good approximation (the energy difference between any two neighboring substates is the same). This is why the number 2S + 1 is called the multiplicity of the electron state in question; it is used as a left-hand superfix of the term symbol. For example, the symbols $^1\Sigma$, $^2\Pi$, $^3\Delta$ etc. denote, in this order, the singled Σ, doublet Π, triplet Δ etc. terms. Each substate could be characterized by the appropriate value of the quantum number Σ; instead, the sum $\Omega = \Lambda+\Sigma$ is normally used, however. It is given as a right-hand suffix. Thus, for example, a $^2\Pi$ term (Λ = 1) has two substates or components; one of these (with Σ = -1/2) is denoted $^2\Pi_{1/2}$; the other is denoted $^2\Pi_{3/2}$. In the case of a $^3\Pi$ term, the components are $^3\Pi_0$, $^3\Pi_1$, $^3\Pi_2$.

The magnitude of multiplet splitting, i.e. the energy differences between the individual term components, can be rather different for the electron terms Π, Δ, . . ., of the molecules; however, for any Σ term, the multiplet splitting is zero in a first

approximation, i.e. the term components nearly coincide, since in the case of the Σ terms the parallel component of the resultant orbital angular momentum of the electrons $\Lambda = 0$, with the result that there is no interaction between the motion of the electrons and the spin. The spin can still be oriented in $2S + 1$ ways, but there is no reason for any energy difference to exist between these orientations.

Experience shows, however, a slight splitting here also. The explanation is that, in addition to the interaction mentioned above, there is a weaker spin-spin interaction among the spins of the individual electrons which produces energy differences between levels of different $|\Sigma|$. This interaction obviously occurs also when $\Lambda \neq 0$, but then it is overshadowed by the much stronger spin-orbit interaction. For the Σ term, however, the spin-orbit interaction is zero and it is the spin-spin interaction that produces a slight but observable splitting. There is also an even weaker interaction, due to rotation.

The rotation of the molecule affects the interactions. Hund[1] was the first to examine this phenomenon, and he did so even before the advent of the wave-mechanical conception. The essence of Hund's idea was to distinguish one by one the typical interactions among the numerous that occur in the molecule and to define in this way various limiting-case models which he called cases a, b, c, d, and e. In the present discussion we shall restrict our attention to Hund's cases a, b, and c.

In Hund's case a, rotation is assumed to have little influence upon the conditions existing in the fixed molecule. In other words, the spin is so strongly coupled to the inter-nuclear axis that its parallel component remains quantized even in the rotating molecule, so that Σ remains a well defined quantum number (and hence $\Omega = \Lambda+\Sigma$ also remains well defined). The molecule therefore behaves as a symmetric top whose angular momentum

with respect to the inter-nuclear axis is defined by Ω, while its total angular momentum is given by the quantum number J; J can assume the values $|\Omega|, |\Omega|+1, \ldots$ (Fig. 5.1).

In *Hund's case b* the spin is not coupled (or is very weakly coupled) to the inter-nuclear axis. By our previous statement, all Σ terms are of such nature. The molecule rotates, in fact, as if there existed no spin: the resultant **N** is composed of Λ and the (unquantized) angular momentum **R** of the rotation of the nuclei (Fig. 5.2). The magnitude of **N** is defined by the quantum number N; $N=|\Lambda|, |\Lambda|+1, \ldots$; therefore **N** plays the same role here as is a weaker **J** does in the singled states. This model is corresponds to the case described by the separated wave equation. The rotation of the molecule gives rise to a magnetic field (due to movement of the charges), having the same orientation as **N**. In the case of a strong rotation this magnetic field will become so strong that, compared with this interaction, the **S** spin will be only weakly coupled to the inter-nuclear axis and may be regarded as practically free. It will consequently combine with N to give the total angular momentum of the rotating molecule. The symbol for total angular momentum is, as usual, **J**. The quantum number J, determining the magnitude of **J**, can assume values as $N + S, N + S-1, \ldots, |N - S|$. In this case, too, for a given **N**, **S** can be oriented in $2S + 1$ ways (provided, as is usual, that $N \geq S$). Hence, each N level is split into 2S+1 sublevels, but the energy difference between these is zero in the ideal case b. In fact there is in most cases some slight splitting owing to the modified form, valid in case b, of the spin-orbit and spin-spin interactions. These splittings are taken into account in a rigorous discussion. As this section is about spin interactions, and as in Hund's case d the dominant interaction between rotation and orbital angular momentum, for the more detailed discussion of this case, see ref. 2 and 3. Let us here note only that this latter type

of interaction also appears in both cases a and b and leads to the splitting of the twofold degenerate levels deriving from the positive and negative orientation of Λ (which would coincide otherwise). This type of splitting was formerly called Λ-type doubling. Accordingly, Λ-type splitting is the beginning of the transition toward Hund's case d. Quantum-mechanically it can be treated by taking into account the terms neglected on the separation of the wave equation in both cases a and b. Let us do this separately for cases a and b.

V.2.1. Case a

The Breit wave equation for atoms containing two electrons has in the Pauli approximation and in the absence of external fields, six well-separable groups of terms.[4] The electron spin occurs only in two groups. One of these describes the spin-orbit interaction, i.e. the interaction between the magnetic momentum assigned to the orbital angular momentum of the electrons and the spin magnetic moments; the other corresponds to the interaction between the magnetic dipole moments of the two electron spins, i.e. to the spin-spin interaction.

$$\mathbf{H}^{s}_{a}(\sigma_i) = \mathbf{H}^{so}_{a} + \mathbf{H}^{ss}_{a} + \mathbf{H}^{sr}_{a} \qquad 1$$

where the first term on the right-hand side is the spin-orbit interaction, and second and third terms describe the spin-spin and spin-rotation interactions, respectively. Here we only discuss the spin-orbit interaction. For spin-spin and spin-rotation interactions, see Ref. 2. Following Heisenberg,[5] the term describing the interaction between the spin of an electron and its own orbit, on the one hand, and the spin of n electron and the orbit of another electron on the other, can be written as

$$\mathbf{H}^{so}_a = [he^2/(4\pi mc^2)]\sum_k\{[Z_a\mathbf{r}^{-3}_{ka}(\mathbf{r}_{ka} \otimes \mathbf{v}_k) + Z_b\mathbf{r}^{-3}_{kb}(\mathbf{r}_{kb} \otimes \mathbf{v}_k) - \sum_{k'>k} \mathbf{r}^{-3}_{kk'}(\mathbf{r}_{kk'} \otimes (\mathbf{v}_k - 2\mathbf{v}_{k'}))].\mathbf{s}_k\} \quad 2$$

where r_{ka} (r_{kb}) are the operators of the distance between the kth electron and the nucleus a (b); $r_{kk'}$ is the distance between the kth and the k'th electrons, Z_a and Z_b are the respective nuclear charges, $\mathbf{v}_k$ and $\mathbf{v}_{k'}$ are the operators of the velocities of the electrons in the molecule-fixed system, and s_k is the spin momentum operator of the kth electron.

Introducing into Eq. 2 the momenta by $\mathbf{v}_k = \mathbf{p}_k/m$ we can obtain

$$\mathbf{H}^{so}_a = [he^2/(4\pi m^2c^2)]\sum_k\{[Z_a\mathbf{r}^{-3}_{ka}(\mathbf{r}_{ka} \otimes \mathbf{p}_k) + Z_b\mathbf{r}^{-3}_{kb}(\mathbf{r}_{kb} \otimes \mathbf{p}_k) - \sum_{k'>k} \mathbf{r}^{-3}_{kk'}(\mathbf{r}_{kk'} \otimes (\mathbf{p}_k - 2\mathbf{p}_{k'}))].\mathbf{s}_k\} \quad 3$$

Introducing the vectors $\mathbf{r}_k$ (the radius vector of the kth electron as measured from mass center 0), and $\mathbf{r}_k$ (the vector of the internuclear distance, pointing from nucleus a to nucleus b; . Fig. 5.3) we may write

$$\mathbf{r}_{ka} = \mathbf{r}_k + (\mu/M_a)\mathbf{r},\ \mathbf{r}_{kb} = \mathbf{r}_k - (\mu/M_b)\mathbf{r} \quad 4$$

where μ is reduced mass of the molecule, and M_a (M_b) is mass of the molecules a (b). Substitution of these into Eq. 3 yields formula

$$\mathbf{H}^{so}_a = [he^2/(4\pi m^2c^2)]\sum_k(\{[Z_a(|\mathbf{r}_k + (\mu/M_a)\mathbf{r}|)^{-3} + Z_b(|\mathbf{r}_k - (\mu/M_b)\mathbf{r}|)^{-3} - \sum_{k'} r^{-3}_{kk'}](\mathbf{r}_{ka} \otimes \mathbf{p}_k) + [Z_a(\mu/M_a)(|\mathbf{r}_k + (\mu/M_a)\mathbf{r}|)^{-3} - Z_b(\mu/M_b)(|\mathbf{r}_k - (\mu/M_b)\mathbf{r}|)^{-3}](\mathbf{r} \otimes \mathbf{p}_k) + \sum_{k'} r^{-3}_{kk'}[(\mathbf{r}_{k'} \otimes (\mathbf{p}_k - 2\mathbf{p}_{k'})) + 2(\mathbf{r} \otimes \mathbf{p}_k)]\}.\mathbf{s}_k) \quad 5$$

Introducing the orbital angular momenta of the individual electrons by the relationship $l_k = r_k \otimes p_k$, Eq.5 becomes

$$\mathbf{H}^{so}_a = \sum_{kk'} a_{kk'}(\mathbf{l}_k \cdot \mathbf{s}_{k'}) = \sum_k a_k(\mathbf{l}_k \cdot \mathbf{s}_k) + \sum_{k \neq k'} a_{kk'}(\mathbf{l}_k \cdot \mathbf{s}_{k'}) \qquad 6$$

where by (Eq. 5) $a_{kk'}$ is a function of the electron distances as measured from the origin of the coordinate system (r_k) of the inter-nuclear distance (r) and of the distances between the electrons ($r_{kk'}$). Fontana[6] has shown that, in the case of two outer -valence electrons, if there is no change in the spin quantum number (i.e. if $\Delta S = 0$), then Eq. 6 becomes

$$\mathbf{H}^{so}_a = a'_1(\mathbf{l}_1 \cdot \mathbf{S}) + a'_2(\mathbf{l}_2 \cdot \mathbf{S}) \qquad 7a$$

and for $\Delta S = \pm 1$

$$\mathbf{H}^{so}_a = a''_1(\mathbf{l}_1 \cdot \mathbf{s}_1) + a''_2(\mathbf{l}_2 \cdot \mathbf{s}_2) \qquad 7b$$

where (in atomic units)

$$a'_1 = (K^2/4)[\, Z_a \mathbf{r}^{-3}_{1a} + Z_b \mathbf{r}^{-3}_{1b} - 3/\mathbf{r}^{-3}_{12}] \qquad 8a$$

$$a'_2 = (K^2/4)[\, Z_a \mathbf{r}^{-3}_{2a} + Z_b \mathbf{r}^{-3}_{2b} - 3/\mathbf{r}^{-3}_{12}]$$

$$a''_1 = (K^2/2)[\, Z_a \mathbf{r}^{-3}_{1a} + Z_b \mathbf{r}^{-3}_{1b} + 1/\mathbf{r}^{-3}_{12}] \qquad 8b$$

$$a''_2 = (K^2/2)[\, Z_a \mathbf{r}^{-3}_{2a} + Z_b \mathbf{r}^{-3}_{2b} + 1/\mathbf{r}^{-3}_{12}]$$

and α is the fine structure constant. Using the appropriate eigenfunctions, it can be shown that the matrix elements of Eq. 6 are different from zero only if, simultaneously, $\Delta S = 0$, ± 1 and $\Delta\Omega = 0$, in such a way that either $\Delta\Lambda = \Delta\Sigma = 0$ or $\Delta\Lambda = -\Delta\Sigma = \pm 1$ (van Vleck).[7]

It is general practice to assume that (7a) holds for $\Delta S = 0$ and (7b) for $\Delta S = \pm 1$, also for more than two valence electrons, in the following form (van Vleck):[8]

$$\mathbf{H}^{so}_a = A\,(\mathbf{L}.\mathbf{S})\,; \qquad \Delta S = 0 \tag{9a}$$

$$\mathbf{H}^{so}_a = \sum_k a_k(\mathbf{l}_k.\mathbf{s}_k)\,; \qquad \Delta S = \pm 1 \tag{9b}$$

Writing Eq. 9a in detail, we would obtain

$$H^{so}_a = A\{\mathbf{L}_\zeta \mathbf{S}_\zeta + 1/2[(\mathbf{L}_\xi + i\,\mathbf{L}_\eta)(\mathbf{S}_\xi - i\,\mathbf{S}_\eta) + (\mathbf{L}_\xi - i\,\mathbf{L}_\eta)(\mathbf{S}_\xi + i\,\mathbf{S}_\eta)]\} \tag{10}$$

Since the eigenvalues of the operators $\mathbf{L}_\zeta$, and $\mathbf{S}_\zeta$ are Λ and Σ, respectively, since $\mathbf{L}_\xi = \pm i\mathbf{L}_\eta$, the matrix elements of Eq. 9a are given by:

$$\mathbf{H}^{so}_a(n, v, \Lambda, \Sigma; n, v, \Lambda, \Sigma) = A\Sigma\Lambda \tag{11a}$$

$$\mathbf{H}^{so}_a(n, v, \Lambda, \Sigma; n', v', \Lambda\pm1, \Sigma\pm(-1)) = (AL_\xi)(n, v, \Lambda; n', v', \Lambda\pm1)\{S(S+1) - \Sigma(\Sigma\pm1)\}^{1/2} \tag{11b}$$

where

$$(AL_\xi)(n, v, \Lambda; n', v', \Lambda\pm1) = \sum_\Lambda \int \Phi^*_{n,\Lambda} R^*_{n,v} A(r) L_\xi \Phi^*_{n',\Lambda\pm1} R^*_{n',v'} r^2 dr d\tau \tag{12}$$

In order to calculate the values of the matrix elements for the ease $\Delta S = \pm 1$ one has to know the exact electron configuration and the forms of the corresponding eigenfunctions.

V.2.2. Case b

In case b, the operator $\mathbf{H}^s_b$ of the electronic part also contains the interaction operators for the spin, but since in this case the interaction between the rotation of the molecule and the

electron spin is weak (unable to follow the fast rotation, the spin vectors are lagging behind), it is appropriate to express these operators in the space-fixed coordinate system:

$$\mathbf{H}^{s}_{b}(\sigma_i) = \mathbf{H}^{so}_{b} + \mathbf{H}^{ss}_{b} + \mathbf{H}^{sr}_{b} \qquad 13$$

We now only examine the spin-orbit interaction here. According to van Vleck,[9] the form of spin-orbit interaction in the space-fixed coordinate system differs from Eq. 2 in that, apart from the velocities of the electrons, referred to the space-fixed system, the velocities of the nuclei are also to be taken into account. Then,

$$\mathbf{H}^{so}_{a} = [he^2/(4\pi mc^2)]\sum_k\{\sum_i Z_i \mathbf{r}^{-3}_{ki}[\mathbf{r}_{ki} \otimes (\mathbf{v}_k - 2\,\mathbf{v}_i)] - \sum_{k'>k} \mathbf{r}^{-3}_{kk'}(\mathbf{r}_{kk'} \otimes (\mathbf{v}_k - 2\mathbf{v}_{k'}))].\mathbf{s}_k\} \qquad 14$$

where the possible values of i are 1, 2; $\mathbf{v}_i$ is the velocity of the nuclei in the space-fixed system. The remainder of the notation is as that in Eq. 2, with the difference that the velocities of the electrons are also taken in the space-fixed system.

If, for the time being, the terms containing the velocities of the nuclei are disregarded, formula (14) can be treated in much the same way as Eq. 2; the matrix elements of the relationships

$$\mathbf{H}^{so}_{b} = \sum_{k'} a_{kk'}(\mathbf{l}_k.\mathbf{s}_{k'}) = \sum_k a_k(\mathbf{l}_k.\mathbf{s}_k) + \sum_{k\neq k'} a_{kk'}(\mathbf{l}_k.\mathbf{s}_{k'}) \qquad 15$$

can be calculated as if there are one, two or three valence electrons outside the closed shell. In order to obtain general expressions for $\Delta S = 0$ and $\Delta\Lambda = 0$, it is usual to replace Eq. 15 by an interaction of the following form:

$$\mathbf{H}^{so}_{b} = A\{\mathbf{L}_\zeta \mathbf{S}_\zeta + 1/2[(\mathbf{L}_\xi + i\,\mathbf{L}_\eta)(\mathbf{S}_\xi - i\,\mathbf{S}_\eta) + (\mathbf{L}_\xi - i\,\mathbf{L}_\eta)(\mathbf{S}_\xi + i\,\mathbf{S}_\eta)]\} \qquad 16$$

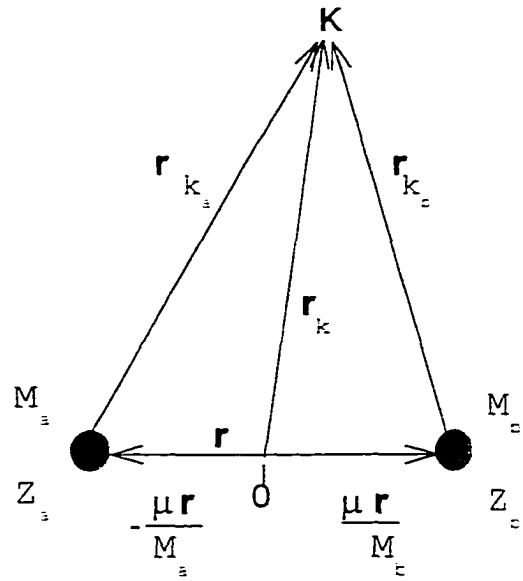

Fig. 5.3. Vector diagram of the kth electron orbiting around the nuclei.

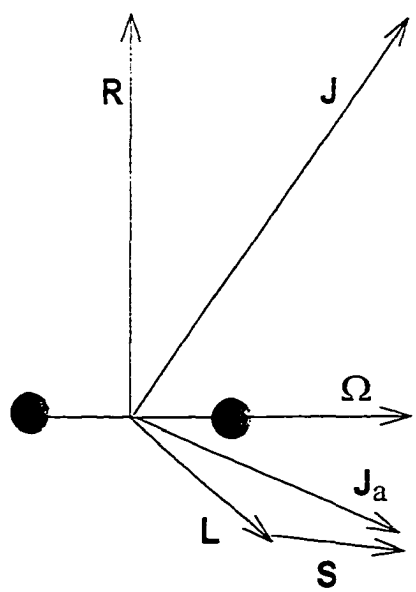

Fig. 5.4. Vector model of Hund's case c.

The first term of Eq. 16 can be written according to Hill and van Vleck[10] as

$$AL_\xi S_\xi = A(\Lambda S) = A[(\Lambda_{33} S) + (\Lambda_\perp S)] \qquad 17$$

Where Λ, the component in the direction of the inter-nuclear axis of the resultant orbital angular momentum of the electrons, is split into two components; one is parallel, the other is perpendicular to the vector **N**. Of these two terms, it is the former that provides those elements for which, in addition to $\Delta S=0$ and $\Delta\Lambda=0$, also $\Delta N = 0$; for the second term $\Delta N = \pm 1$. For these, Hill and van Vleck[10] have found

$$\mathbf{H}^{so}{}_b(n, J, S, \Lambda, N; n, J, S, \Lambda, N) = A\Lambda^2\,[J(J+1)-N(N+1)-S(S+1)]/[2N(N+1)] \qquad 18a$$

$$\mathbf{H}^{so}{}_b(n, J, S, \Lambda, N; n, J, S, \Lambda, N+1) = A\Lambda^2\{[(N+1)^2 - \Lambda^2][(J+N+1)(J+N+2)-S(S+1)]\}^{1/2}$$
$$x[S(S+1)-(J-N)(J-N-1)]^{1/2}/\{2(N+1)([(2N+1)(2N+3)]^{1/2}\} \qquad 18b$$

Suitable substitutions of Λ and S in the formulas (18a) and (18b) give the case b interaction energy and its perturbation-matrix elements for terms of any type and multiplicity.

Fontana[6] has found that for the case of two outer (valence) electrons the rigorous form of (15) for $\Delta N = 0$ yields an expression similar to Eq.18a.

$$\mathbf{H}^{so}{}_b(n, J, 1, \Lambda, N; n, J, 1, \Lambda, N) = \sum^2_{k=1} (a'_k \mathbf{l}_{k\xi})(n, \Lambda; n, \Lambda) = \Lambda[J(J+1) - N(N+1)$$
$$-2]/[2N(N+1)] \qquad 19a$$

According to Lue-Yung Chow Chiu,[11] the result is similar to that for $\Delta N = \pm 1$:

$$\mathbf{H}^{so}{}_b(n, J, 1, \Lambda, N; n, J, 1, \Lambda, N+1) = \sum^2{}_{k=1} (a'_k \mathbf{l}_{k\zeta})(n, \Lambda; n, \Lambda) = \{[(N+1)^2 - \Lambda^2][(J+N+1)$$

$$(J+N+2)-2]\}^{1/2}[2-(J-N)(J-N-1)]^{1/2}/\{2(N+1)([(2N+1)(2N+3)]^{1/2}\} \qquad 19b$$

In both cases the $\sum(a'_k \mathbf{l}_{k\zeta})$ replacing $\Delta\Lambda$ can be determined from the appropriate eigenfunctions by

$$\sum(a'_k \mathbf{l}_{k\zeta})(n, \Lambda; n, \Lambda) = \sum_\Lambda \int \Phi^*_{n,\Lambda}(a'_1 \mathbf{l}_{1\zeta} + a'_2 \mathbf{l}_{2\zeta}) \Phi_{n,\Lambda} d\tau \qquad 20$$

Likewise, according to Lue-Yung Chow Chiu,[11] the second term of Eq.16 yields for S = 1, $\Delta\Lambda = \pm 1$ and $\Delta N = 0, \pm 1$

$$\mathbf{H}^{so}{}_b(n, J, 1, \Lambda, N; n, J, 1, \Lambda+1, N) = \sum^2{}_{k=1} (a'_k \mathbf{\Gamma}_k)(n, \Lambda; n', \Lambda+1)[N(N+1) - J(J+1)+2]$$

$$x[(N-\Lambda)(N+\Lambda+1)(J+N+1)]^{1/2}/[4N(N+1)] \qquad 21a$$

$$H^{so}{}_b(n, J, 1, \Lambda, N; n', J, 1, \Lambda+1, N+1) = \sum^2{}_{k=1} (a'_k \mathbf{\Gamma}_k)(n, \Lambda; n', \Lambda+1)\{(J+N+3)(J+N)$$

$$x(N-J+2)(J-N+1)(N+\Lambda+1)(N+\Lambda+2)/[16(N+1)^2(2N+1)(2N+3)]\}^{1/2} \qquad 21b$$

$$H^{so}{}_b(n, J, 1, \Lambda, N; n', J, 1, \Lambda+1, N-1) = \sum^2{}_{k=1} (a'_k \mathbf{\Gamma}_k)(n, \Lambda; n', \Lambda+1)\{(J+N+2)(N-J+1)$$

$$x(J+N-1)(N-N+2)(N-\Lambda-1)(N-\Lambda)/[16N^2(2N-1)(2N+1)]\}^{1/2} \qquad 21c$$

Using

$$\mathbf{\Gamma}_k = \mathbf{l}_{k\zeta} - i\mathbf{l}_{k\eta} \qquad 22$$

and applying appropriate eigenfunctions, one finds that

$$\sum^2{}_{k=1} (a'_k \mathbf{\Gamma}_k)(n, \Lambda; n', \Lambda+1) = \sum_\Lambda \int \Phi^*_{n,\Lambda}(a'_1 \mathbf{\Gamma}_{1\zeta} + a'_2 \mathbf{\Gamma}_{2\zeta}) \Phi_{n,\Lambda+1} d\tau \qquad 23$$

The matrix elements of Eq. 21 were first given for actual cases by Kovacs[12] who derived them from case a.

In addition to the foregoing interactions between terms of the same multiplicity (i.e. for $\Delta S = 0$), Lue-Yung Chow Chiu[13] gave for two outer electrons also the matrix

elements for interactions between terms of multiplicity (i.e. for $\Delta S = \pm 1$). In this case Eq. 15 assumes the form Eq. 9b with coefficients given by Eq. 8b appropriate matrix elements are

$$\mathbf{H}^{so}{}_b(n, J, 0, \Lambda, N; n', J, 1, \Lambda, N) = \sum''_{k=1} (a''_k \Gamma_k)(n, \Lambda; n', \Lambda+1)[(J+N+2)(N-J+1) \times (J-N+1)(J+N)]^{1/2} \Lambda/[4N(N+1)] \qquad 24a$$

$$\mathbf{H}^{so}{}_b(n, J, 0, \Lambda, N; n', J, 1, \Lambda, N+1) = \sum''_{k=1} (a''_k \Gamma_k)(n, \Lambda; n', \Lambda+1)\{(J+N+3)(J+N+2) \times (N-J+2)(N-J+1)[(N+1)^2-\Lambda^2] /[16(N+1)^2(2N+1)(2N+3)]\}^{1/2} \qquad 24b$$

$$\mathbf{H}^{so}{}_b(n, J, 0, \Lambda, N; n', J, 1, \Lambda+1, N) = \sum''_{k=1} (a''_k \Gamma_k)(n, \Lambda; n', \Lambda+1)\{(J+N+2)(N-J+2) \times (J-N+1)(J+N)(N+\Lambda+1)(N-\Lambda)]^{1/2} /[8N(N+1)] \qquad 24c$$

$$\mathbf{H}^{so}{}_b(n, J, 0, \Lambda, N; n', J, 1, \Lambda+1, N+1) = \sum''_{k=1} (a''_k \Gamma_k)(n, \Lambda; n', \Lambda+1)\{(J+N+3)(N+J+2) \times (N-J+2)(N-J+1)(N+\Lambda+1)(N+\Lambda+2)]^{1/2} /[64(N+1)^2(2N+1)(2N+3)] \qquad 24d$$

$$\mathbf{H}^{so}{}_b(n, J, 0, \Lambda, N; n', J, 1, \Lambda+1, N-1) = \sum''_{k=1} (a''_k \Gamma_k)(n, \Lambda; n', \Lambda+1)x \times \{(J+N)(N+J-1)(J-N+2)(J-N+1)(N-\Lambda-1)]^{1/2} /[64(N-1)(2N+1)] \qquad 24e$$

$$\sum''_{k=1} (a''_k \mathbf{l}_{k\zeta})(n, \Lambda; n', \Lambda) = \sum_\Lambda \int \Phi^*_{n,\Lambda} (a''_1 \mathbf{l}_{1\zeta} - a''_2 \mathbf{l}_{2\zeta}) \Phi_{n',\Lambda} d\tau \qquad 25$$

$$\sum''_{k=1} (a''_k \Gamma_k)(n, \Lambda; n', \Lambda+1) = \sum_\Lambda \int \Phi^*_{n,\Lambda} (a''_1 \Gamma_1 - a''_2 \Gamma_2) \Phi_{n',\Lambda+1} d\tau$$

As is apparent in Eq. 25, the bar over the summation symbol means that the two terms should be subtracted from each other instead of being added. Formulas (24) were also derived by Kovacs[12] and likewise from *case a*.

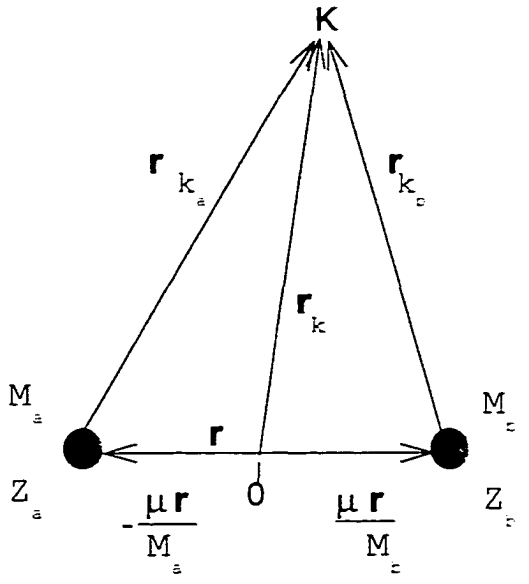

Fig. 5.3. Vector diagram of the kth electron orbiting around the nuclei.

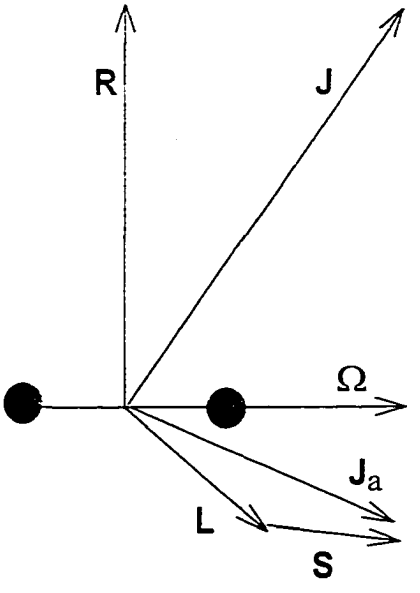

Fig. 5.4. Vector model of Hund's case c.

V.2.3. Case c

The interaction between **L** and **S**, in certain cases, particularly for heavy molecules, may be stronger than the interaction with the internuclear axis. In this case Λ and Σ are not defined; rather, **L** and **S** first form a resultant $\mathbf{J_a}$ which is then coupled to inter nuclear axis with a component Ω (Fig. 5.4). This coupling is entirely similar to that of an atom in a weak electric field when no Paschen-Back effect occurs. The electronic angular momentum Ω and the angular momentum **R** of nuclear rotation then form the resultant angular momentum J just as in case a. This type of coupling is *Hund's case c.*

Chapter V References

1 F. Hund, Z. Phys. **36**, 657(1926) and **42**, 93(1927).

2 Istvan Kovacs, "*Rotational Structure in the Spectra of Diatomic Molecules*", American Elsevier Publishing Company Inc., New York, 1969.

3 Gerhard Herzberg, "*Molecular Spectra and Molecular Structure. Vol. I-Spectra of Diatomic Molecules*", Krieger Publishing Company, Florida, Reprint Edition 1989

4 H. A. Bethe, E. E. saltpeter, "*Quantum Machanics of One- and Two-Electron Atoms*", Academic Press, Inc., New York, 1957.

5 W. Heisenberg, Z. Phys. **39**, 514(1926).

6 P. R. Fontana, Phys. Rev. **125**, 220(1962).

7 J. H. van Vleck, Phys. Rev. **33**, 467 (1929).

8 J. H. van Vleck, Phys. Rev. **40**, 544(1932).

9 J. H. van Vleck, Rev. Mod. Phys. **23**, 225 (1951).

10 E. L. Hill, J. H. van Vleck, Phys. Rev. **32**, 250 (1928).

11 A. Budo and I. Kovacs, Z. Phys. **109**, 393 (1938).

12 I. Kovacs, Can. J. Phys. **36**, 309 (1958).

13 L. Y. C. Chiu, J. Chem. Phys. **40**, 2276 (1964).

CHAPTER VI

DETERMINATION OF THE BOND STRENGTH OF THE METAL CLUSTER (IONS)

Since the introduction of laser-vaporization techniques for the production of supersonic metal cluster beams[1], the study of isolated gas phase metal clusters has proceeded with increasing vigor. For many researchers a prime motivating interest has been the possibility that these metal clusters will provide detailed molecular models with which to study such classical questions of surface science as the nature of the metal-metal bond, the electronic structure of a reaction surface site, or the molecular details of chemisorption. The fundamental goal in the study of metal clusters is to understand the electronic structures of these intermediate systems and their progression towards bulk band structure as the cluster size increases[2]. Of all the metal clusters, transition metal clusters are of particular interest due to their diverse physical and chemical behavior. Unusual physical and chemical properties are expected for these clusters.[3-6] Their chemical reactivity is also found to be strongly size-dependent, primarily due to the presence of partially filled d orbitals, however, the transition metal clusters have presented considerable challenges theoretically. Even dimer systems are found to display very complicated electronic structures and the nature of their bonding properties has not been completely understood[13-17]. Currently, very little is known about the detailed structures of transition metal clusters and their electronic properties and dissociation energy-limits. Usually the dissociation energy-limits of dimer molecules have been estimated:

1) From a Morse potential energy curve where assuming that the potential is well-defined by a single Morse potential all the way to dissociation energy limit and the relationship is given by the well-known formula:[18-19]

$$D_e = \omega_e^2 / 4\omega_e\chi_e \qquad 1$$

where ω_e is vibrational frequency and $\omega_e\chi_e$ is anharmonicity parameter. From this equation it is obvious that the accuracy of the dissociation energy-limit is very sensitive to accuracy of anharmonicty parameter. Minute errors on the $\omega_e\chi_e$ would produce a relatively large error in D_e.

2) From Knudsen effusion mass-spectrometric measurements using the second and third laws of thermodynamics. The dissociation energy of a diatomic species is again sensitive to the absolute entropy and the ratio of the dimeric and monomeric species in equilibrium. From the third-law relationship, the dissociation energy at 0 °K for the reaction $X_2(g) = 2X(g)$ is given by the following equation.[57]

$$D^\circ_o(X_2)/RT = -\ln P(X) + \ln[P(X_2)/P(X)] + \Delta fef/R \qquad 2$$

Where the P is pressure of designed species, T the absolute temperature, R the gas constant, and Δfef the difference of the free-energy functions for the above reaction. The pressure ratio P (X_2)/P (X) is estimated in terms of the observed ion intensities of dimer and monomer with the corresponding ratios of the ionization cross-sections and multiplier detection coefficients. When the total mass of any impurity species in the system corresponds to mass of dimer or monomer, this causes

overestimating or underestimating the true dissociation energy. Langenberg and Morse have discussed this problem for Rh_2.[56]

3) Collision-Induced Dissociation (CID) Experiment. Here the mass-selected cluster ion beam is collided with an inert target (typically xenon) and the energy threshold is measured for each observed fragment ion. The probability of the dissociated cluster ions is plotted as function of collision energy and then the dissociation energy of the cluster ion is determined by fitting the zero pressure data with an empirical cross-section of the form

$$\sigma = \sigma_o(E-E_o)^N/E \qquad 3$$

where σ is the cross-section, E is the ion translational energy (in center-of-mass frame of reference), E_o is the threshold energy, N is an adjustable parameter, and σ_o is a scaling factor. There are several effects that influence equation 3. a) The kinetic energy has two sources of the broadening in the CID experiments. One is the spread of energies in the ion beam and a second source is Doppler broadening due to the thermal motion of the inert gas. b) The lifetime of the collisionally energized clusters.
The relative uncertainty in reaction cross-section magnitudes was stated to be 5%[61,62] and the uncertainty in the dissociation energy is usually in ±0.05-0.5 eV range.

4) Significant studies of the electronic spectra of many neutral transition metal dimers have been performed by using resonant two-photon ionization (R2PI) spectroscopy.[43-47] From such studies molecular term symbols, vibrational and rotational constants, and bond lengths have been determined. Bond strengths have been measured by the observation of the sudden onset of the predissociation in electronic spectra.[47-49] With the advent of resonance-enhanced photodissociation

(REPD) spectroscopy,[50-53] similar studies of transition metal cluster ions have been performed. The bond strengths of charged species have been measured by the observation of predissociation thresholds.[50,51,53,54] As Smalley discussed in his paper in 1986, mass spectral analysis of the cluster photoions provides mass selectivity, but the photoionization process cannot be relied upon to produce only the parent ion, so it is frequently impossible to uniquely assign a particular signal to a particular cluster. Particularly troublesome has been the difficulty of using either of two powerful laser techniques, LIF or R2PI, on the metal clusters species. Both techniques require that the first laser-induced transition populate an excited electronic state which survives long enough to be detected by either its fluorescence (LIF), or its lowered ionization threshold (R2PI).[22]

5) The initially mass selected photofragmentation techniques is free of the problems mentioned above. Since clusters are charged, standard particle counting techniques ensure that each cluster (parent and daughter) ions can be detected. Mass selection is performed initially, so spectral probes target only the desired parent ions. Fragmented cluster (daughter) ions can be detected as long as the total energy of one- or multi-photon observed by parent ion is above the lowest dissociation energy limit.

This techniques is a very powerful tool to accurately determine the dissociation energy-limit from the threshold in the electronic spectra when the total excitation energy changes from an n-photon process to an (n-1)-photon process as well as other spectroscopic properties of cluster species.[20] This technique was used in this work, see experimental section.

The electronic structure and spectroscopic properties of second and third row transition metal dimers and main group metal dimers have been the topics of many experimental and theoretical investigations in recent years. Theoretical calculations of transition metal dimers and trimers in general are very difficult to achieve due to the problem of electron correlation and the large number of open-shell electronic states arising from the incomplete d shells of the metal atoms. In recent times the development of high speed computing has permitted the accurate calculation of spectroscopic properties and the structure of many challenging transition metal dimer systems. However, there remain voids in our knowledge of transition metal bonding, particularly with regard to experimental studies on dimers of the transition metals. Investigations of the these molecules are of particular importance, since their d orbitals are readily available for bonding, and it is these orbitals which are implicated in many aspects of catalysis. The transition metal diatomics provide a useful benchmark to assess the reliability with which ab initio calculations can treat the subtle interplay of overlap, exchange, and correlation effects contributing to the bonding in these molecular systems. Also, experimental studies in the gas and solid phase provide useful information about host-guest interactions for ab initio calculation models.

VI. 1 PHOTOFRAGMENTATION SPECTROSCOPY OF THE ZIRCONIUM DIMER CATION AND THE AB INITIO STUDIES ON Zr_2, Zr_2^+

ABSTRACT

The dissociation energy of the zirconium dimer cation molecule is reported for first time. The dimer cation was produced by laser vaporization of a zirconium target rod and cooled in a helium supersonic expansion. The molecular beam containing zirconium dimer cation was interrogated in the range 16,000-18,440 cm^{-1} using a pulsed dye laser to dissociate the molecule. The dissociation threshold was observed at the 16,870 cm^{-1}. The fluence study at 16,767 and 16,870 cm^{-1} and an ab initio calculation indicated that the multiphoton dissociation should be a two photon process, 16,870 cm^{-1} + E_{dissoc}, $E_{dissoc} \geq$ 16,870 cm^{-1}. The dissociation energy was accurately determined to be 4.184 ± 0.005 eV. In this region, only three transitions were observed: 17,880 (relatively weak), 18,290 and 18,350 cm^{-1}. Several different density functional calculations predicted the dissociation energy of Zr_2, Zr_2^- in remarkable agreement with experiment. Several spectroscopic properties of these molecules were calculated.

VI. 2. INTRODUCTION

The first reported experimental investigation of dizirconium molecule was an ultraviolet-visible spectral survey of matrix-isolated Zr_2. [23] Four bands were observed, at 390, 422, 585, and 615 nm, respectively. From concentration studies it was demonstrated that these bands belong to a single cluster species, which has been assigned as Zr_2 [23]. On the basis of extended Huckel calculation studies. Koltzbucher

and Ozin assigned the four bands listed above to $1\pi_u \rightarrow 3\sigma_g$, $1\sigma_g \rightarrow 2\pi_u$, and $1\sigma_g \rightarrow 2\sigma_u$ orbital transitions, respectively, with the latter assigned to both the 585 and 615 nm bands.[23] Miedema and Gingerich have predicted a value $D_o(Zr_2) = 3.20 \pm 0.24$ eV by using an empirical correlation between the heat of vaporization of zirconium metal, ΔH°_{vap}, the surface energy of pure solid zirconium, γ°_s , and the dimer dissociation energy [24]. The method is a generalization of previous work by Miedema on the heats of mixing and heat of formation of liquid and solid alloys of transition metals.[25-28] Years later Lindsay *et al.* published absorption ("scattering depletion ") spectra and Raman measurements for Zr_2 in an argon matrix.[10] They observed an intense absorption at 388 nm (with shoulder at 401 and 425 nm), a weaker absorption near 520 nm, and a vibrationaly resolved absorption at about 630 nm. However, they did not observe strong peaks at 422 and 585 nm. The T_o, ω_e'' and $\chi_e''\omega_e''$ were measured to be 15,230 cm^{-1} (1.888 eV), 305.7(35) cm^{-1} and 0.5(7) cm^{-1}, respectively[10]. Lindsay et al suggested that the ground state of Zr_2 could be $^3\Delta_g$ state rather than $^1\Sigma_g$ state.

The dissociation energy was roughly estimated from the well-known equation, $D_e = \omega_e^2 / 4\omega_e\chi_e$, to be 3.62 eV for ω_e =305.7 cm^{-1} and $\omega_e\chi_e$ = 0.8 cm^{-1}. In 1994, Morse *et al.* reported the dissociation energy of the dizirconium to be 3.052±0.001 eV from a resonant two-photon ionization (R2PI) experiment.[55] This is the most accurate determination of the dissociation energy. Balasubramian and Ravimohon studied State-Averaged-Complete Active Space Multiconfiguration Self-Consistent Field (SA-CASSCF) followed by Multireference Single + Doubles Configuration Interactions (MRSDCI) on thirty-four bound electronic states of Zr_2 lying below 23,000 cm^{-1} region.[11] At the SA-CASSCF level, which included 4f functions in the basis set the

Table 6.1.Calculated spectroscopic constants of the Zr_2.[a]

D_e(eV)	r_e(A)	ω_e(cm^{-1})	T_e(cm^{-1})	state
1.5 (2.45)	2.34 (2.31)	373 (351)	0	$^1\Sigma_g^-$
1.5 (1.85)	2.42 (2.386)	294 (253)	64 (312)	$^3\Sigma_u^-$
1.62 (2.63)	2.78 (2.66)	197 (225)	2,572(3,581)	$^7\Sigma_u^-$
1.43 (-)	2.35 (2.34)	286 (284)	589 (1,484)	$^3\Delta_g$
Exp:				
3.62[b]		305.7[35]		
3.20±0.24[29]				
3.052±001[36]				

[a] The calculated properties of Zr_2 were taken from ref. 37. The spectroscopic constants were calculated by state-averaged-complete active space multiconfiguration selfconsistent field (SA-CASSCF) and the values in parenthesis were calculated by multireference single plus doubles configuration (MRSDCI) methods.

[b] D_e was estimated by using the well-known formula, $D_e = \omega_e^2 / 4\omega_e\chi_e$, for ω_e =305.7 cm^{-1} and $\omega_e\chi_e$ = 0.8 cm^{-1}, ref. 35.

ground state symmetry was predicted to be $^1\Sigma_g^+(1\sigma_g^2 2\sigma_g^2 1\pi_u^4)$. The $^3\Sigma^-_u(1\sigma_g^2 2\sigma_g^1 1\sigma_u^1 1\pi_u^4)$ state is only 64 cm^{-1} above the ground state.[11] However, the $^3\Sigma^-_u$ state was predicted to be the ground state from the CASSCF potential energy curves for seven low-lying electronic states where the basis set did not include 4f functions. MRSDCI calculations following SA-CASSCF predicted the ground state of Zr_2 to be the $^1\Sigma^-_g$ state. They also calculated the spectroscopic constants of Zr_2 at SA-CASSCF/MRSDCI levels (both which include 4f functions in the basis set). They calculated the dissociation energy for $^1\Sigma_g^-$ and $^3\Sigma_u^+$ states relative to $^3F + {}^3F$ atomic limit and for $^7\Sigma_u^-$ state relative to $^3F + {}^5F$ atomic limit. Some selected spectroscopic constants of Zr_2 from ref. 11 are given in Table 6.1.

Balasubramian and Ravimohon[11] suggested that since the most probable candidate for the ground state of Zr_2 was the $^1\Sigma_g^-$ state, all four bands in ref. 23 are due to the transitions from the $X^1\Sigma_g^-$ ground state. They assigned these transitions as $A^1\Sigma_u^- — X^1\Sigma_g^-$ 15,083 cm^{-1}, $B^1\Pi_u — X^1\Sigma^-_g$ 17,120 cm^{-1}, $C^3\Pi_u — X^1\Sigma^-_g$ 18,615 cm^{-1}, $D^1\Sigma^-_u — X^1\Sigma^-_g$ 22,916 cm^{-1}.

VI 2.1. EXPERIMENTAL STUDY ON THE ZIRCONIUM DIMER CATION

VI 2.1.1. FLUENCE STUDY.

The fluence dependence of intensity on fragmented zirconium cation is shown in Fig. 6.1 and Fig. 6.2A and 2B. The pulsed photo-fragmentation dye laser beam is fixed at 595.4 nm, 590 and 559 nm, then the intensity of the fragmented zirconium cation was detected as a function of the fluence. The order of the absorption event leading to dissociation was found from the extent of fragmentation of laser fluence to

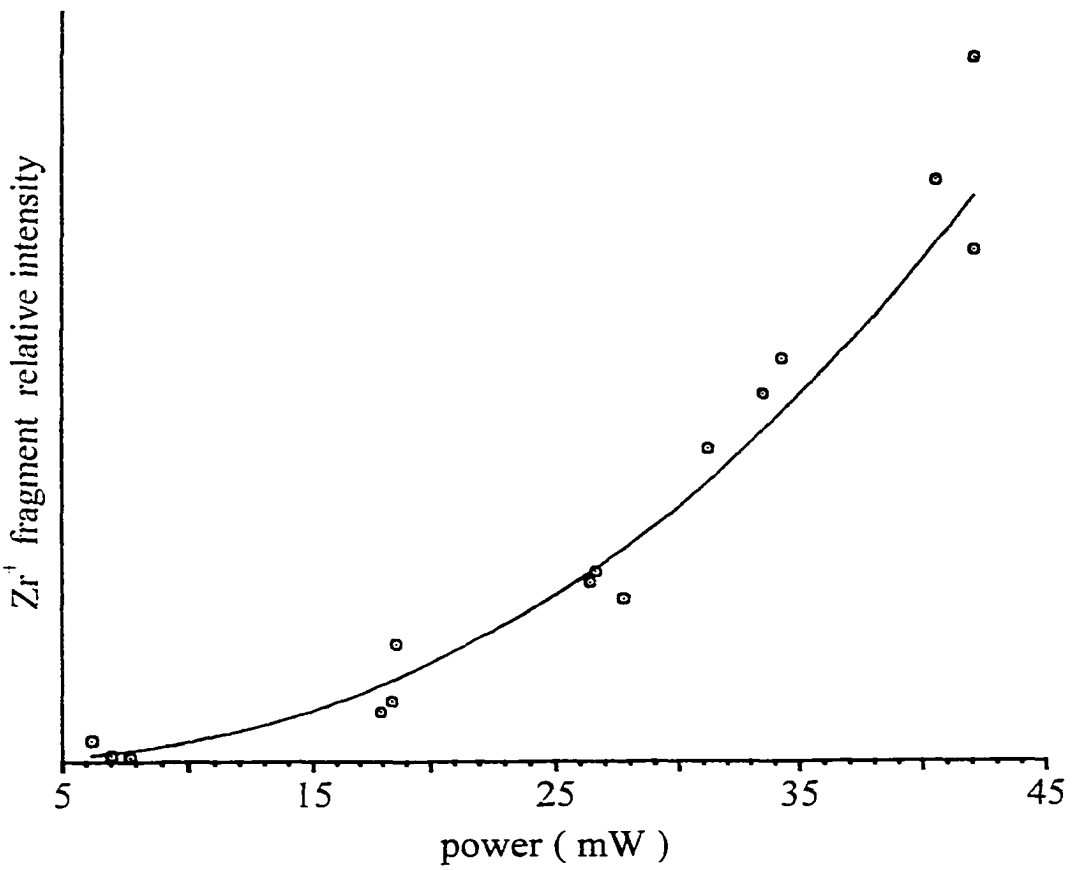

Figure 6.1. Plot of $^{90}Zr^+$ fragment relative intensity, (daughter - background)/parent, for fluence dependence studies of $^{90}Zr_2^+$ at 16,795 cm^{-1} (595.4 nm).

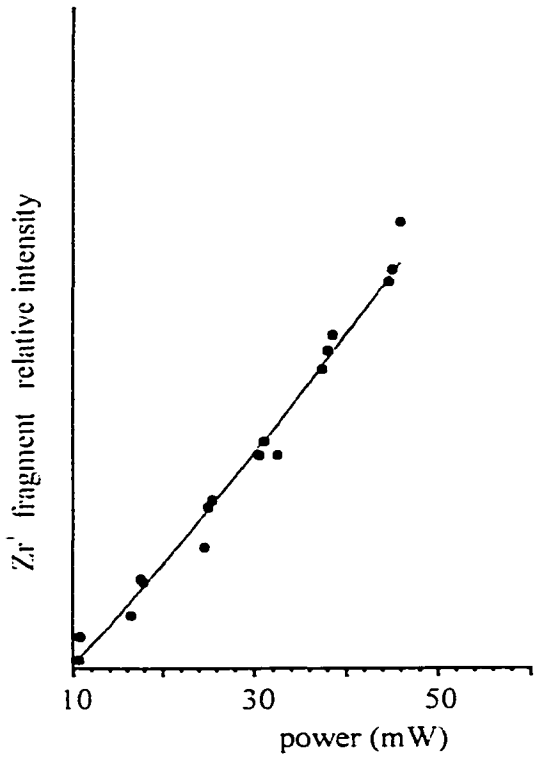

Figure 6.2A. Plot of $^{90}Zr^-$ fragment relative intensity,

(daughter - background)/parent,

for fluence dependence studies of $^{90}Zr_2^-$ at 16950 cm^{-1} (590 nm).

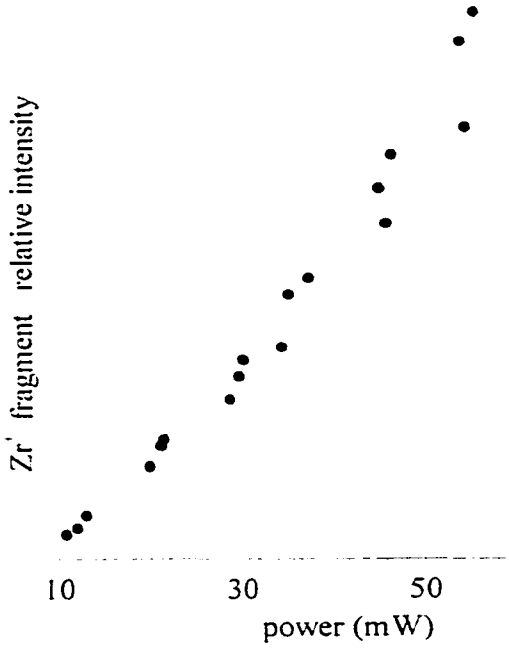

Figure. 6.2B. Plot of $^{90}Zr^-$ fragment relative intensity,

(daughter - background)/ parent,

for fluence dependence studies of $^{90}Zr_2^-$ at 17857 cm^{-1} (560 nm).

be 2.3 at 595.4 nm and 1.2 at 590.0 and 559 nm. The relative intensity of fragmented particle was expected to be inversely proportional to the third order of the fluence at 595.4 nm and to be second order of the fluence at 590 and 559 nm or elsewhere below the 590 nm, region. The order of the $^{90}Zr_2^+$ fluence dependent fragment intensity curve at 595.4 nm was greater than two and that at 590 and at 559 nm was greater than one. These results imply that photofragmentation at 595.4 nm was a three-photon process and at 590 and 559 nm, the fragmentation was two-photon process. The fluence dependence of the intensity of the fragmented particle could not give the true order of the fluence dependent fragmentation curves are due to: 1) Ideally, either in the determination of one-photon absorption cross section or in the discrimination between one- and multiphoton processes, one would irradiate an ensemble of absorbers with a homogeneous light field of known absolute flux (photons/cm^{2}s) and determine the per-molecule absorption rate as a function of this intensity. This scenario is practically unrealizable, particularly when intrinsically pulsed experiments are performed. In the pulsed case, the incident light field intensity varies in time from zero to some maximum value and back again, not necessarily monotonically (because of, for example, longitudinal cavity mode beating in a laser). The ideal experiment is then reduced to the measurement of the absorption of the molecular ensemble as a function of the pulse-integrated flux or fluence (photons/cm^2 pulse).[22] 2) the averaging over the temporal profile of the light pulse, most experimental situations have imperfect overlap of the light field and the molecular ensemble producing subensembles that receive different fluences, all contributing to the observed signal. This is typical for experiments with pulsed laser which exhibit high spatially structured output beams.

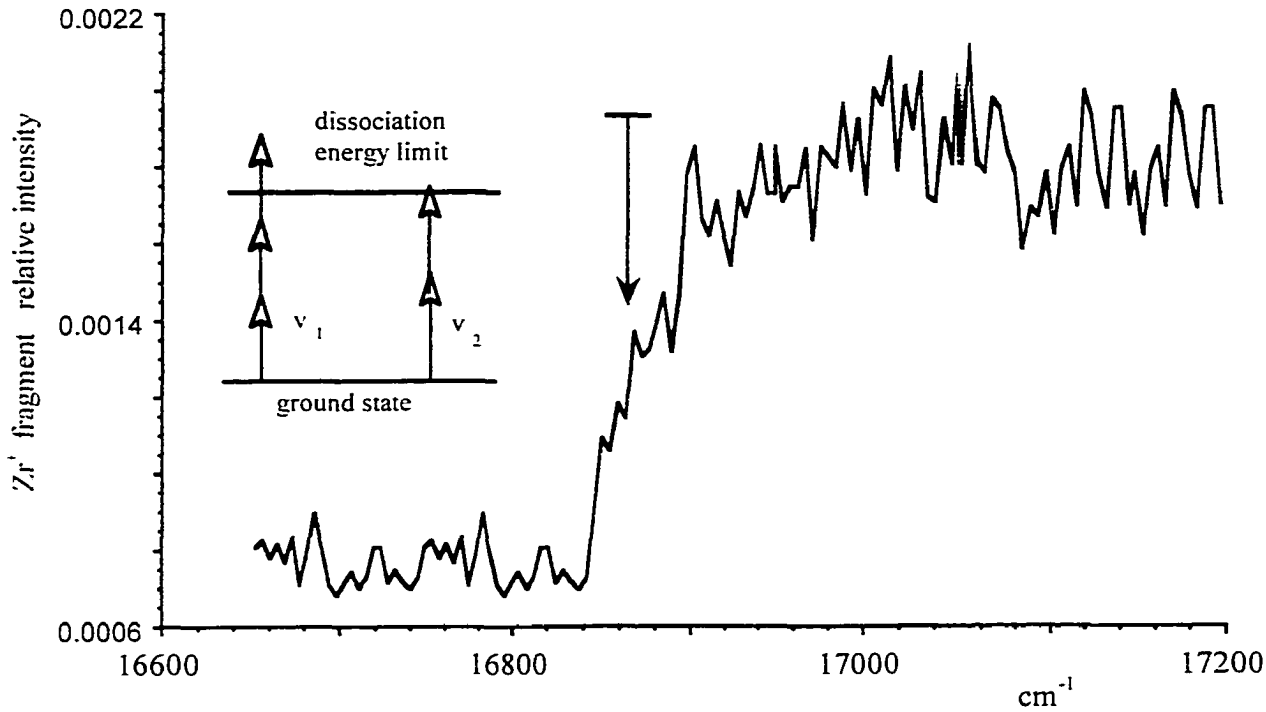

Figure 6.3. The photodissociation threshold of Zr_2^- was detected in a multiphoton photofragmentation action spectrum. The spectrum rises abruptly out of noise at 16,870 cm^{-1}.

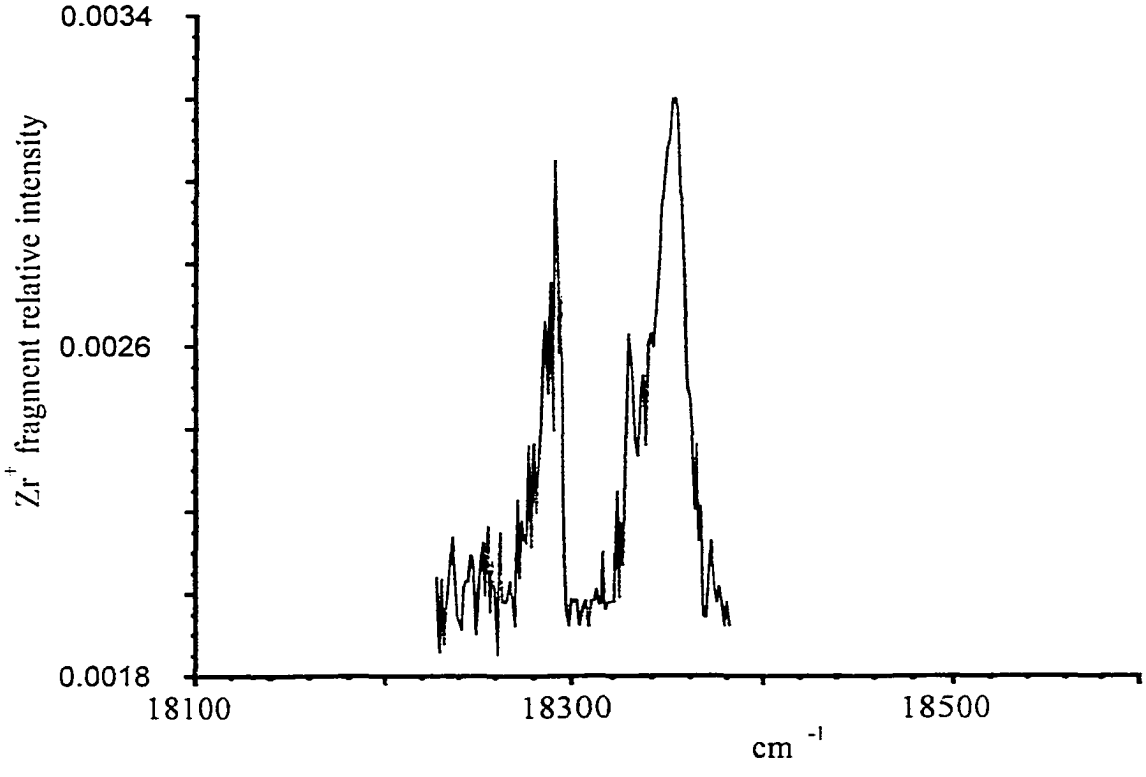

Figure 6.4. Two peaks were observed at 18,290 and 18,350 cm^{-1} in the low resolution spectra of $^{90}Zr_2^-$ by scanning dye laser. In addition, a weak peak was observed at 17,880 cm^{-1}, not shown in this figure.

Therefore, two-photon events look almost one-photon, three-photon events look almost two-photon, etc.[22]

VI 2.1.2. MULTIPHOTON FRAGMENTATION SPECTRUM OF Zr_2^+

Since cluster ions are charged, standard particle counting techniques ensure that each cluster ion can be detected with near efficiency and absorption spectra of the selected cluster ion can be readily detected by photofragmentation of the parent ion – a one or multiphoton process if the photon (or total absorbing photons) energy is above the lowest dissociation energy limit. Using the high peak intensity probe lasers, both one and multiphoton absorption spectra and dissociation energy limit can be studied at high yield.[22]

Because of this fact, for a multiphoton process, the molecule would be dissociated as soon as the total energy of the absorbing photons by the molecule is above the lowest dissociation threshold and the probability or intensity of fragmented cluster ions is inversely proportional to the number of absorbing photons by the parent ion. When the photofragmentation process changes from an n-photon process to an (n-1)-photon process, the background of the absorption spectra would exhibit a fairly sharp rise at the threshold, as shown in Fig. 6.3 for Zr_2^+ at 16,870 ± 40 cm^{-1}. The second supporting evidence for the lowest threshold energy of Zr_2^+ is the study of the fluence dependence of Zr_2^+ at 16,795, 16,950, and 17,890 cm^{-1}. As discussed above, the fluence study indicated that the multiphoton process is a three-photon process before the threshold and is a two-photon process after threshold energy (16,870 ± 40 cm^{-1}). This experimental evidence for the lowest dissociation energy limit of Zr_2^+ is in

agreement with calculated dissociation energy of Zr_2^- by various density function methods in section III-B. The purpose of these experiments was to accurately determine the lowest dissociation energy limit of Zr_2^-. Fig. 6.3 shows the dissociation energy limit or dissociation threshold energy of Zr_2^- obtained by a one-color multiphoton fragmentation scheme depicted in the figure. The threshold appears at total laser energy (16,870 ± 40 cm^{-1} + $E_{dissoc.}$) of 33,740 cm^{-1}. The fragmentation spectrum exhibits a fairly sharp rise at the threshold. The lowest dissociation threshold energy of Zr_2^- is therefore 33,730 ± 40 cm^{-1} (4.184 ± 0.005 eV).

We observed three transitions in the electronic spectra. One of them was relatively weak at 17,880 cm^{-1} (not shown in Fig. 6.4) and the other two were at 18,290 and 18,350 cm^{-1} as shown in Fig. 6.4. Without high resolution spectra, it is hard to say what type of the electronic transitions occurred in this region. We will discuss this in Sec. III-B based on density functional calculations.

VI 2.2. METHODS OF CALCULATIONS

VI 2.2.1. COMPUTING DETAIL

Several density functional calculations were performed on Zr_2, and Zr_2^-, such as BLYP, BVWN5, BPW91, BP86, and BPL. These are computer codes in Gaussian-94 and –98 packages. The calculation uses Beck's 88 functional (hereafter referred to as B), which includes the Slater exchange along with correction involving the gradient of the density [29], in combination with different type correlation functional which are: LYP, VWN, VWN5, PW91, BP86, and BPL. Where LYP is the correlation functional of Lee, Yang, and Parr, which includes both local and non-local terms [30, 31], VWN is

Vosko, Wilk, and Nusair 1980 correlation functional fitting the random phase approximation (RPA) to the uniform electron gas, often referred to as local spin density (LSD) correction [32], VWN5 is functional V from the VWN 80 paper which fits the Ceperley-Alder solution to the uniform electron gas [32], PW91 is Perdew and Wang's 1991 gradient-corrected correlation functional,[33-37] P86 is the gradient correction of Perdew, along with his 1981 local correction functional [38], PL is the local (non-gradient corrected) functional of Perdew (1981) [39]. Los Alamos effective core potential (ECP) plus DZ, LANL2DZ computer code, wavefunction[40-42] was used in of all the density functional calculations. The lanl2dz wave function consists of linear combination of the three s, three p, and two d (1s, 2s, 3s, 4p, 5p, 6p, 7d, and 8d are computer code in Gaussian94 and 98) atomic orbitals. 1s, 2s2p, 3s3p3d shells of zirconium atoms were assigned to the core and treated by frozen core approximation. All calculations were performed on Decalpha and Intel Pentium II 450 MMX computers.

VI 2.2.2. RESULT OF CALCULATIONS

VI 2.2.2.1. Zr_2 :

We calculated spectroscopic properties of Zr_2 ($^3\Delta_g$) as shown in Table 6.2 and 5. All six density functional calculations predicted the ground state symmetry to be $^3\Delta_g$, arising from the $1\sigma^2_g1\pi^4_u2\sigma_g\delta_g$ configuration. The dissociation energy of Zr_2 ($^3\Delta_g$) was predicted to be in the 2.792- 3.495eV range relative to $^3F + {}^3F$ atomic limit by the BLYP, BPW91, BP86, and BPL methods, but BVWN density functional was predicted to be 4.272 eV. We calculated atomic ground state energy for Zr(^{3}F) relative

to the calculated atomic ground state energy of the Zr^- ($5s^14d^2$; ^5F) and its known atomic ionization energy, IP(Zr) = 6.852 eV, because of the convergence difficulty, none of the DFs predicted the atomic ground state energy of Zr ($5s^24d^2$; ^3F). The calculated harmonic frequency (306- 313 cm^{-1}) of Zr_2 ($^3\Delta_g$) is in remarkable agreement with experiment ω_e = 305.7 cm^{-1}, ref. 10). The calculated equilibrium internuclear distance of Zr_2 ($^3\Delta_g$) is , 2.316-2.360 Å, in agreement with at SA-CASSCF and MRSDCI calculation[11]. As far as we can tell, there is no experimental information on the equilibrium nuclear distance of the Zr_2 to compare with the calculated value. The gross population in the components of 4d atomic orbitals on each Zr atom is given in Table 6.2. The $4d_{\pm2}$ and $4d_0$ atomic orbitals were partially occupied, 50% and 47%, respectively. This result implies that the repulsion energy between the two electrons in the occupied σ_d^2 molecular bond is strong enough to push one electron into a higher energy level, δ_d, due to the small gaps between the electronic bands of the transition metal atoms.

Density Functional calculations predicted that the lowest singlet low-lying state of the Zr_2 was $^1\Gamma_g$, arising from the $1\sigma^2_g1\pi^4_u\delta^2_g$ electronic configuration rather than the $1\sigma^2_g1\pi^4_u2\sigma^2_g$ configuration, as predicted by K. Balasubramian and Ch. Ravimohon using SA-CASSCF and MRSDCI calculations. The $^1\Gamma_g$ ($1\sigma^2_g1\pi^2_u\delta^2_g$) was calculated to be 8,226-9,823 cm^{-1} above the ground state, $X^3\Delta_g$ and dissociation energy and equilibrium bond distance and harmonic frequency were calculated to be 2.455-2.872 eV (relative to ^3F + ^3F atomic limit), r_e =2.385-2.413 A, and ω_e=261-269 cm^{-1}, respectively.

The calculated spectroscopic constants for the $^7\Sigma_u^-$ state, arising from the $1\sigma^2_g1\pi^2_u2\sigma_g\delta^2_g1\sigma_u$ electronic configuration, are given in tables 6.3 and 6.6: D_e = 3.371-4.211 eV relative to $^3F + {}^5F$ atomic limit, r_e =2.675-2.708 Å, and ω_e =226-238 cm^{-1}. The predicted bond distance and vibrational frequency of $Zr_2(^7\Sigma_u^-)$ are in agreement with SA-CASSCF and MRSDCI calculations where the $^7\Sigma_u^-$ state was 2,572/3,581 cm^{-1} above the ground state, $X^1\Sigma_g^-$, and 1,983/2,097 cm^{-1} above the $^3\Delta_g$ state, respectively.[11] We calculated the $^7\Sigma_u^-$ state was 3,823 - 5,988 cm^{-1} above the ground state, $X^3\Delta_g$, as shown in Table 6.3. The calculated orbital transitions of the $^7\Sigma_u^-$ state are given Table 6.7. Our calculated dissociation energy and harmonic-frequency, using density functional theory for the dizirconium molecule, were in better agreement with experimental values than SA-CASSCF and MRSDCI calculations are, as shown in Table.6.1 and 6.2.

We calculated the potential energy curves of Zr_2 for $X^3\Delta_g$, $^7\Sigma_u^-$, and $^1\Gamma_g$ as shown in Fig. 6.5. The potential energy curves of the $X^3\Delta_g$ and $^1\Gamma_g$ electronic states were extrapolated to the $^3F + {}^3F$ atomic limit and the $^7\Sigma_u^-$ state was extrapolated to $^3F + {}^5F$ atomic limit. The symmetry of the $X^3\Delta_g$ state was mixed with other triplet low-lying or excited states after nuclear distance 3.3± 0.2 Å and approximately 1.9± 0.2 eV above the ground state in the density functional calculations.

Klotzbucher and Ozin[23] have observed four bands of matrix-isolated dizirconium in the UV-visible region. These bands occur at 16,262, 17,096, 23,700, and 25,644 cm^{-1}. Lindsay *et al.* observed three absorption bands: 25,773 cm^{-1} (with shoulders at 24,938 and 23,529), a weaker absorption near 19,231 cm^{-1} and a

Table 6.2. Calculated spectroscopic constants of the Zr_2. ($^3\Delta_g$; $1\sigma_g^2 1\pi_u^4 2\sigma_g \delta_g$)

DFT	D_e(eV)	r_e(A)	ω_e(cm^{-1})	IE(Zr_2)	5s	4d(total).
BLYP	2.930	2.336	311	5.703	1.014	2.889
BVWN5	3.277	2.342	306	6.102	1.010	2.931
BPW91	2.792	2.316	308	6.062	1.001	2.930
BP86	3.495	2.360		6.445	1.003	2.931
BPL	3.428	2.344		6.100	1.010	2.930
Expt.	3.052±0.001[a]		305.7[c]	5.709[d]		2.401[e]
	3.20±0.24[b]					
	3.62[e]					

The D_e of Zr_2 (triplet) relative to the Zr ($5S^2$ $4d^2$, ^3F)+Zr ($5S^2$ $4d^2$, ^3F) atomic limit. [a] From ref. 36, [b] from ref. 30, [c] from ref. 35, [d] calculated thermochemical cycle, IE(Zr2) - IP(Zr)-D_o (Zr_2)+$D_o(Zr^-_2)$ = 0, [e] D_e was estimated by using the well-known formula, $D_e = \omega_e^2 / 4\omega_e\chi_e$, for ω_e =305.7 cm^{-1} and $\omega_e\chi_e$ = 0.8 cm^{-1}, ref. 35. [e] the number of electrons in d orbitals on each Zr atom from ref. 37.

Table 6.3. Calculated spectroscopic constants of the Zr_2 ($^7\Sigma_u^-$; $1\sigma_g^2 1\pi_u^2 2\sigma_g \delta_g^2 1\sigma_u$)

DFT	D_e(eV)	r_e(A)	ω_e(cm^{-1})	T_e(cm^{-1})	5s	4d(total).
BLYP	3.404	2.700	226	5,988	1.256	
2.628						
BVWN	3.491	2.701	228	5,980	1.209	
2.674						
BVWN5	3.411	2.706	226	4,973	1.224	
2.658						
BPW91	4.211	2.675	238	3,823	1.174	
2.693						
BP86	4.096	2.675	238	4.581	1.217	
2.705						
BPL	3.371	2.708	226	5,933	1.222	
2.659						
						1.799[#]

[#] The number of electrons in d orbitals on each Zr atom from ref. 37.

Table 6.4.Calculated spectroscopic constants of the $Zr_2(^1\Gamma_g; 1\sigma_g^2 1\pi_u^4 \delta_g^2)$

DFT	D_e(eV)	r_e(Å)	ω_e(cm^{-1})	T_e(cm^{-1})	5s	4d(total)
BLYP	2.455	2.397	261	8,768	0.992	3.007
BVWN	2.597	2.407	266	8,323	0.973	3.016
BVWN5	2.376	2.411	265	8,468	0.976	3.015
BPW91	2.872	2.411	269	9,755	0.967	3.018
BP86	2.842	2.385	264	9,823	0.977	3.012
BPL	2.484	2.413		8,226	0.998	3.000
						2.246[#]

[#] The number of electron in d orbital on each Zr atom from ref. 37.

Table 6.5. Calculated vertical orbital transition energies [a] (in cm^{-1}) for transitions from $X^3\Delta_g$ ground sate of Zr_2. The experimental values are also shown for comparison. [b]

Excitation	State	BLYP	BVWN	BVWN5	BPL	BPW91	BP86	Ref.35	Ref.29	Ref.37
Ground state* $^3\Delta_g$										
$1\sigma_g \rightarrow 1\sigma_u$	$^3\Delta_u$	13,065	13,388	11,775	13,227	13,952	13,710			
$2\sigma_g \rightarrow 2\pi_u$	$^3\Pi_u$,$^3\Phi u$	14,275	15,404	14,840	14,840	15,565	15,162	15,230	16,260	15,083
$2\sigma_g \rightarrow \delta_u$	$^3\Sigma_u$,$^3\Gamma_u$	15,162	15,001	17,582	14,920	16,049	15,888		17,096	17,120
$1\sigma_g \rightarrow 2\pi_u$	$^3\Pi_u$,$^3\Phi_u$	22,098	22,663	21,740	22,340	22,582	22,501			
$1\pi_u \rightarrow 1\pi_g$	$^3\Sigma_u$-,$^3\Delta_u$, $^3\Gamma_u$	22,098	23,147	22,663	22,582	23,872	23,388	23,529	23,700	18,615
$2\sigma_g \rightarrow 2\sigma_u$	$^3\Delta_u$	22,743	23,550	23,066	22,985	24,276	24,114	25,773	25,644	22,916
$1\pi_u \rightarrow 3\sigma_g$	$^3\Pi_u$,$^3\Phi_u$	28,711	30,889	29,841	29,760	30,970	30,808			

[a] The calculated orbital transitions are an average of orbital energies for alpha and beta spin manifolds. [b] The assignments of the transitions are tentative, but are consistent with theoretical calculations. Experimental values are from ref. 35 and 29. The calculated transitions in ref. 37 are from $X^1\Sigma_g^+$ ground state of Zr_2 and are assigned as shown in the table.

Table 6.6. Calculated orbital transitions and nuclear equilibrium distances of $Zr_2(^7\Sigma_u^+; 1\sigma_g^2 1\pi_u^2 2\sigma_g \delta_g^2 1\sigma_u)$ from potential energy curves.[-]

		T_e (cm^{-1})	r_e
Low-lying state[*]	$^7\Sigma_u$	0	2.34
$\delta_g \rightarrow \delta_u$	$^7\Sigma_g$, $^7\Gamma_g$	6,239	2.750
$\delta_g \rightarrow 2\pi_u$	$^7\Pi_g$, $^7\Phi_g$	12,327	2.675
$1\sigma_u \rightarrow 3\sigma_g$	$^7\Sigma_g$	17,102	2.800
$1\pi_u \rightarrow 1\pi_g$	$^7\Sigma_g$, $^7\Delta_g$	17,164	2.825
$2\sigma_g \rightarrow 2\sigma_u$	$^7\Sigma_g$	17,208	2.850
$2\sigma_g \rightarrow 2\pi_u$	$^7\Pi_g$	18,151	2.675
$1\pi_u \rightarrow 3\sigma_g$	$^7\Pi_g$	24,562	2.800
$1\sigma_g \rightarrow 2\pi_u$	$^7\Pi_g$	26,932	2.675
$1\sigma_u \rightarrow 2\pi_g$	$^7\Pi_g$	27,325	2.825
$1\sigma_g \rightarrow 2\sigma_u$	$^7\Sigma_g$	27,537	2.625

* Calculated to lie at –3.404 eV relative to $^3F + {}^5F$ atomic limit. [-] BLYP density functional was used here.

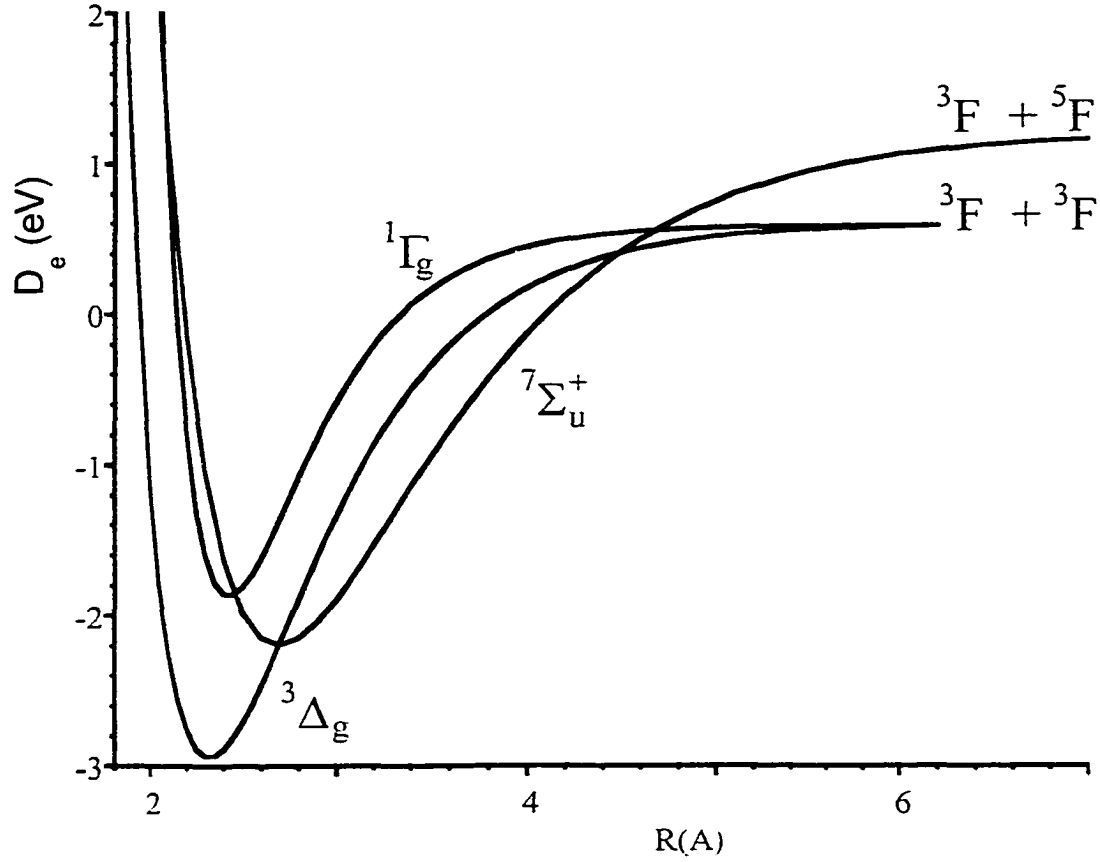

Fig. 6.5. Potential energy curves for $^3\Delta_g$, $^1\Gamma_g$ relative to $^3F + ^3F$ and $^7\Sigma_u$ relative to $^3F + ^5F$ atomic limit. BLYP density functional was used here.

vibrationally resolved absorption at about 15,873 cm^{-1} in absorption ("scattering depletion") spectra and Raman measurements for Zr_2 in an argon matrix experiment. However, Lindsay and co-workers[10] did not observe a strong peak at 23,700 and 17,096 cm^{-1} even though Klotzbucher and Ozin[23] had. Since the most probable candidate for the ground state of Zr_2 is the $^3\Delta_g$ state, we believe that all four bands in ref. 23 and two strong and one weaker band in Ref. 10 are due to the transitions from the $X^3\Delta_g$ ground state. To further confirm this, we calculated some of the vertical transitions of the triplet states of dizirconium as shown in Tables 6.5. This table shows the experimental transition energy, and most consistent assignments for these bands.

The assignments of the observed bands in the table are by no means definitive. However, the theoretical transition energies are consistent with the observed spectra. Furthermore, the transitions listed in Table 6.5 are dipole allowed and hence are probable candidates for the assignment. As seen from Tables 6.5, for the T_e's from ref. 10 and 11, more favorable candidates are $B^3\Pi_u$ -$X^3\Delta_g$, $C^3\Pi_u$ -$X^3\Delta_g$, $E^3\Delta_u$ -$X^3\Delta_g$, and $F^3\Delta_u$ -$X^3\Delta_g$ transitions on the based of the DF calculations. Although such an agreement should be considered fortuitous, there are not too many alternate possibilities for assigning the spectra consistent with the predicted energy separations.

The first ionization energy of the $Zr_2(^3\Delta_g)$ was estimated from the well-known thermodynamic cycle: $IE(Zr_2) = IE(Zr) + D_o(Zr_2) - D_o(Zr_2^-)$, to be 5.821 eV. Where the experimental values are: IE(Zr)=6.953 eV,[12] $D_o(Zr_2)$= 3.052 ± 0.001 eV,[55] and $D_o(Zr_2^-)$ = 4.184 ± 0.005 eV (present work). The calculated values of $IE(Zr_2)$ are:

5.709 eV(BLYP), 6.062 eV (BPW91), 6.102 eV (BVWN5), 6.100 eV (BPL), 6.445 eV (BP86), and 6.955 eV (BVWN).

VI 2.2.2.2. Zr_2^- :

As far as we can tell, there are no previous experimental or theoretical studies on Zr_2^-. The ground state of the Zr_2^- was predicted to be $^2\Sigma_g^-$ by three density functional calculations (BLYP, BVWN5, and BPL), arising from the $1\sigma^2\pi^4 2\sigma^1$ configuration and the $^2\Delta_g$ state, arising from the $1\sigma^2\pi^4\delta^1$, was calculated to be approximately 2,700 cm^{-1} above the $^2\Sigma_g^-$ state, as shown in Fig. 6.6. The potential energy curve and equilibrium nuclear distance for the $^2\Delta_g$ state was tentatively predicted by using the universal potential function fitting to calculated energies of the $^2\Delta_g$ state in the 2.0-2.1 and 3.1-3.6 region. We calculated the dissociation energy of the Zr_2^- with respect to the atomic limit $Zr(5s^2\ 4d^2;\ ^3F) + Zr^-(5s^1\ 4d^2;\ ^4F)$, to be 4.080 eV (BLYP), 3.580 eV (BVWN), 4.170 eV (BVWN5), 3.929 eV (BPW91), 4.179eV (BP86), and 4.017eV (BPL). This is in agreement with the experimental value of 4.184 ± 0.005 eV, see Table 6.7. The doublet state of Zr^- was calculated to be approximately 0.5 eV above the quartet state. The calculated vertical transition energies of the doublet states of Zr_2^- are given in Table 6.8; as shown, there are many electronic transitions in the visible region.

We observed (Fig. 6.4 in Sec. VI 2.1.2) a relatively weak peak at 17,880 and two relatively strong peaks at 18,290 and 18,350 cm^{-1}. Since the most probable candidate for the ground state of Zr_2^- is the $^2\Sigma_g^+$ state, we feel that the two relatively strong peaks are due to transitions from the X $^2\Sigma_g^-$ ground state. The calculated values

Table 6.7. Calculated spectroscopic constants of the Zr_2^+

D_e(eV)		r_e(A)	ω_e(cm^{-1})	T_e(cm^{-1})	d(total)	State	DFT
4.080[a]	(4.256)[b]	2.377	259	0	2.457	$^2\Sigma^-_g$	BLYP
		2.45		2,018		$^2\Delta_g{}^2\Delta_g$	
4.170	(4.164)	2.386	242	0	2.452	$^2\Sigma^-_g$	BVWN5
		2.45		2.800		$^2\Delta_g$	
4.017	(4.385)	2.390	243	0	2.450	$^2\Sigma^-_g$	BPL
		2.45		2.500		$^2\Delta_g$	
3.580	(4.039)	2.176	420		2.953	$^2\Delta_g$	BVWN
3.929	(4.448)	2.379	252		2.822	$^2\Delta_g$	BPW91
4.179	(4.645)	2.164	390		2.952	$^2\Delta_g$	BP86

4.184 ± 0.005 (Exp., this work)

[a] The D_e of Zr^-_2(doublet) relative to the Zr (triplet) + Zr^- (quartet) atomic limit.

[b] From potential energy curve.

Table 6.8. Calculated dipole allowed orbital-orbital transitions, T_e in cm^{-1}, of the doublet states of Zr_2^+ ($^2\Sigma_g^+$ and $^2\Delta_g$).

Excitation	State	BLYP	BVWN5	BPL	Exp (this work)
Predicted ground state is $^2\Sigma_g$					
$2\sigma_g \rightarrow 1\sigma_u$	$^2\Sigma_u^+$	12,742	13,226	13,145	
$1\sigma_g \rightarrow 1\sigma_u$	$^2\Sigma_u^-$	16,936	17,662	17,501	17,880(w), 18,290(s). and 8,350(s)
$2\sigma_g \rightarrow 2\pi_u$	$^2\Pi_u$	25,243	25,646	25,646	

Continued to Table 6.8: Predicted ground state is $^2\Delta_g$

Excitation	State	BVWN	BPW91	B86	Exp
$\delta_g \rightarrow \delta_u$	$^2\Delta_u$	14,356	14,523	14,920	
$1\sigma_g \rightarrow 1\sigma_u$	$^2\Delta_u$	19,921	19,840	21,050	17,880(w),18,290(s), and 18,350(s)
$\delta_g \rightarrow 2\pi_u$	$^2\Pi_u$	21,937	21,534	21,614	

Average of orbital energies for alpha and beta spin manifolds.

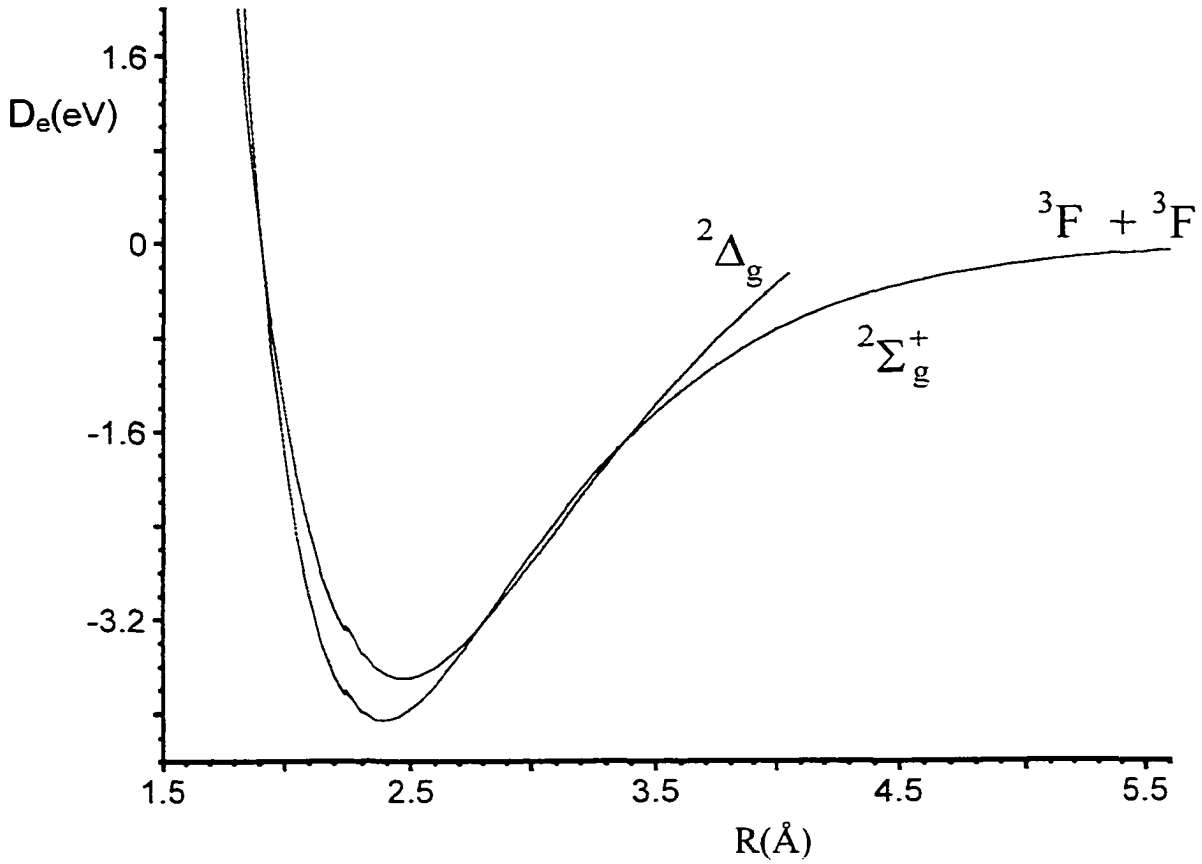

Figure 6.6. Potential energy curves for $^2\Sigma_g$ and $^2\Delta_g$ relative to $^3F + ^3F$ atomic limit. BLYP density functional result is given here.

of some of the vertical transitions of the doublet manifold of dizirconium cation are given in Table 6.8. Nevertheless, the theoretical transition energies are consistent with the observed spectra. The $1\sigma_g^2 \rightarrow 1\sigma_u^*$ transition (Table 6.8) is dipole allowed is probable candidate for the assignment, as seen in Table 6.8, $B^2\Sigma_u^+ - X^2\Sigma_g^-$. Although such an agreement should be considered fortuitous, there are not too many possibilities for assigning the spectra consistent with the predicted energy separations. Table 6.8 shows the experimental transitions and the most consistent assignments for these bands; the assignments of the observed bands are by no means definitive.

VI 3. DISCUSSION

The ground state symmetry of dizirconium is predicted to be $^3\Delta_g$, arising from the $1\sigma^2_g1\pi^4_u2\sigma_g\delta_g$ configuration, by all density functional methods with effective core potential (ECP) plus double zeta (DZ) basis set. In order to test the accuracy of the density functional calculations, we calculated the well-known ground state configurations of the Ti_2, V_2, and Nb_2. Several density functional methods predicted the lowest ground states of V_2 and Nb_2 to be $^3\Sigma_g^-$, arising from the $\ldots2\sigma_g^2\delta_g^2$ electronic configuration, in agreement with experiments and other theoretical calculations.[7-9,58-59]

As known there are several distinct factors which combine to determine the strength and character of the chemical bond between transition metal atoms such as in Ti_2. One such factor is the loss of exchange energy which occurs upon formation of d-electron bonds, thereby reducing the strength of the chemical bonding. While bonding considerations for Ti_2 favor the $4s\sigma_g^23d\pi_u^43d\sigma_g^2$, $^1\Sigma_g^-$ state, is as the lowest ground

state, the several density functional predicted to be $^3\Delta_g$, arising from the $...1\sigma_g^2 1\pi_u^4 2\sigma_g^1 \delta_g^1$, due to the exchange effects dominate in Ti_2, in agreement with experiment.[60] Therefore, as in V_2/Nb_2, the ground state of Zr_2 might be the same as in Ti_2 to be $^3\Delta_g$. The calculated vertical orbital transitions of the triplet states of zirconium dimer molecule: $2\sigma_g \rightarrow 2\pi_u(T_e(^3\Pi_u, {}^3\Phi_u)$= 14,275-15,565 cm^{-1}); $2\sigma_g \rightarrow 2\sigma_u(T_e(^3\Delta_u)$= 22,743-24,276 cm^{-1}); $1\sigma_g \rightarrow 2\pi_u(T_e(^3\Pi_u, {}^3\Phi_u)$= 22,098-22,663 cm^{-1}); using various density functional calculations. The $1\sigma_g$ and $2\sigma_g$ molecular orbitals are 5s-5s and 4d-4d atomic bonding orbitals, respectively. These are in agreement with the experimentally observed electronic transitions,[23,10] which are 25,641, 23,697, 17,094 and 16,260 cm^{-1}, ref. 23 and 15,230, 25,773, 25,773 (has shoulder at 24,938 and 23,529) cm^{-1}, ref. 10.

In summary, we have experimentally determined the dissociation energy of the zirconium dimmer cation to a very high degree of accuracy, by observing a sharp threshold between the two- and three-photon photodissociation continua. The value obtained, 4.184±0.005 eV, is in remarkable agreement with several density functional calculations. Further we extended these calculations to the neutral Zr_2, obtaining good agreement with previous experimental data from this and other laboratories, including vibrational frequencies. Several bands in the resonance photofragmentation spectra of Zr_2^- could also be fit to theory, although in these cases, the assignments are somewhat less certain.

Chapter VI References

1. T. G. Dietz, M. A. Duncan, D. E. Powers, and R. E. Smalley, J. Chem. Phys. **74**, 6511(1981)
2. See, for example, Physics and Chemistry of Finite Systems: From clusters to crystals, edit by P. Jena, S. N. Khanna, and B. K. Rao Kluwer Academic, Boston, (1992), Vols. I and II.
3. I. M. L. Billas, A. Chatelain, and N. A. de Heer, Science **265**, 1682(1994).
4. D. M. Cox, D. J. Trevor, R. L. Whetten, E. A. Rohlfing, and A. Kaldor, Phys. Rev. **B32**, 7290(1985).
5. W. A. de Heer, P. Milani, and A. Chatelain, Phys. Rev. Lett. **65**, 488(1990).
6. J. P. Bucher, D. C. Douglass, and L. A. Bloomfield, Phys. Rev. Lett. **66**, 3052(1991)
7. P. R. R. Langridge-Smith, M. D. Morse, G. P. Hansen. R. E. Smalley, and A. J. Merer, J. Chem. Phys. **80**, 593 (1984).
8. E. M. Spain, J. M. Behm, and M. D. Morse, J. Chem. Phys. **96**, 2512 (1992)
9. E. M. Spain and M. D. Morse, J. Phys. Chem. **96**, 2479 (1992).
10. Z. Hu, Q. Zhou, J. R. Lombardi and D. M. Lindsay, Physics and chemistry of Finite Systems: From Clusters to Crystals, edited by P. Jena et al. (Kluwer, The Netherlands, 1994), Vol. II, p. 969.
11. K. Balasubramanian and Ch. Ravimohan, J. Chem. Phys. **92**, 3659(1990).
12. S. R. Radel and M. H. Navidi, Chemistry, West Publishing Company, New York, (1994).
13. J. Harries and R. O. Jones, J. Chem. Phys. **70**, 830(1979).

14. I. Shim and K. A. Gingerich, J. Chem. Phys. **77**, 2490(1982).

15. D. G. Leopold, J. Almlof, W. C. Lineberger, and P. R. Taylor, J. Chem. Phys. **88**, 3780(1988).

16. T. Noro. C. Ballard. M. H. Palmer, and H. Tatewaki, J. Chem. Phys. **100**, 452(1994).

17. D. R. Salahub, in Ab Initio Methods in Quantum Chemistry-II, edit by K. P. Lawless Wiley, New York, (1987).

18. G. Herzberg, Spectra of Diatomic Molecules. Van Nostrand, New York, (1950).

19. Zhendong Hu, Jian-Guo Dong, John. R. Lombardi, and D. M. Lindsay, J. Chem. Phys. **101**, 95(1994).

20. B. Simard, P. I. Presunka, H. P. Loock, and A. Berces, J. Chem. Phys. **107**, 307(1997).

21. L. -S. Zeng, P. J. Brucat. C. L. Pettiette, S. Yang, and R. E. Smalley, J. Chem. Phys. 83, 4273(1985).

22. P. J. Brucat, L. -S. Zheng, C. L. Pettiette, S. Yang, and R. E. Smalley, J. Chem.Phys. **84**, 3078 (1986)

23. W. E. Klotzbucher, G. A. Ozin, Inorg. Chem. **19,** 3767(1980).

24. A. R. Miedema, K. A. Gingerich, J. Phys. B **12**, 2081 (1979).

25. A. R. Miedema, R. Boom, F. R. de Boer, J. Less-Common Met. **41**, 283 (1975).

26. A. R. Miedema, J. Less-Common Met. **46**, 67 (1976).

27. R. Boom, F. R. de Boor, A. R. Miedema, J. Less-Common Met. **45**,

237(1976).

28. R. Boom, F. R de Boer, A. R Miedema, J. Less-Common. Met. **46**, 271 (1976).

29. A. D. Becke, Phys. Rev. A **38**, 3098 (1988).

30. C. Lee, W. Yang and R. G. Parr, Physical Review B **37**, 785 (1988).

31. B. Miehlich, A. Savin, H. Stoll and H. Preuss, Chem. Phys. Lett. **157**, 200 (1989).

32. S. H. Vosko, L. Wilk and M. Nusair, Canadian J. Phys. **58**, 1200 (1980).

33. K. Burke, J. P. Perdew and Y. Wang, in Electronic Density Functional Theory: Recent Progress and New Directions. Ed. J. F. Dobson, G. Vignale and M. P. Das (Plenum, 1998).

34. J. P. Perdew, in Electronic Structure of Solids '91, Ed. P. Ziesche and H. Eschrig, Akademie Verlag, Berlin, (1991) 11.

35. J. P. Perdew, J. A. Chevary, S. H. Vosko, K. A. Jackson, M. R. Pederson, D. J. Singh and C. Fiolhais, Phys. Rev. B **46** (1992).

36. J. P. Perdew, J. A. Chevary, S. H. Vosko, K. A. Jackson, M. R. Pederson, D. J. Singh and C. Fiolhais, Phys. Rev. B **48** (1993).

37. J. P. Perdew, K. Burke and Y. Wang, Phys. Rev. B **54**, 16533 (1996).

38. J. P. Perdew, Phys. Rev. B **33**, 8822 (1986).

39. J. P. Perdew and A. Zunger, Phys. Rev. B **23**, 5048 (1981).

40. P. J. Hay and W. R. Wadt, J. Chem. Phys. **82**, 270 (1985).

41. W. R. Wadt and P. J. Hay, J. Chem. Phys. **82**, 284 (1985).

42. P. J. Hay and W. R. Wadt, J. Chem. Phys. **82**, 299 (1985).

43. M. Doverstal, B. Lingren, U. Sassenberg, C. A. Arrington, and M. D. Morse, J. Chem. Phys. **97**, 7087 (1992).

44. S. Taylor, E. M. Spain, and M. D. Morse, J. Chem. Phys. **92**, 2698 (1990).

45. S. Taylor, G. Lemire, Y. M. Hamrick, Z. Fu, and M. D. Morse, J. Chem. Phys. **89**, 5517 (1988).

46. S. Taylor, E. M. Spain, and M. D. Morse, J. Chem. Phys. **92**, 2710 (1990).

47. E. M. Spain, J. M. Behm, and M. D. Morse, J. Chem. Phys. **96**, 2511 (1992).

48. E. M. Spain and M. D. Morse, J. Phys. Chem. **96**, 2479 (1992).

49. M. D. Morse, G. P. Hansen, P. R. R. Langridge-Smith. L.-S. Zheng, M. E. Geusic, D. L. Michalopoulos, and R. E. Smalley, J. Chem. Phys. **80**, 5400 (1984).

50. D. E. Lessen, R. L. Asher, and P. J. Brucat, Chem. Phys. Lett. **182**, 412 (1991).

51. L. M. Russon, S. A. Heidecke, M. K. Birke, J. Conceicao, P. B. Armentrout, and M. D. Morse, Chem. Phys. Lett. **204**, 235 11993).

52. K. F. Willey, C. S. Yeh, D. L. Robbins, and M. A. Duncan, Chem. Phys. Lett. **192**, 179 (1992); C. S. Yeh, K. F. Willey, D. L. Robbins, and M. A. Duncan, ibid. **196**, 233 (1992).

53. L. M. Russon, S. A. Heidecke, M. K. Birke, J. Conceicao, M. D. Morse, and P. B. Armentrout, J. Chem. Phys. **100**, 4747 (1994)

54. R. L. Hettich and B. S. Freiser, J. Am. Chem. Soc. **109**, 3537 (1987).

55. C. A. Arrington, T. Blume, and M. D. Morse, M. Doverstal and U. Sassenberg, J. Phys. Chem. **98**, 1398 (1994)

56. J. D. Langenberg and M. D. Morse, J. Chem. Phys. **108**, 2331 (1998).

57. A. Kant and Sin-Shong Lin, J. Chem. Phys. **51**, 1644 (1969)

58. D. R. Salahub and N. A. Baykara, Surf. Sci. **156**, 605 (1985).

59. A. M. James, P. Kowalczyk, R. Fournier, and B. Simard, J. Chem. Phys. **99**, 8504 (1993).

60. M. Doverstal, B. Lindgren, U. Sassenberg, C. A. Arrington, M. D. Morse. J. Chem. Phys. **97**, 7087 (1992).

61. K.M. Ervin and P. B. Armentrout, J. Chem. Phys., **83**, 166 (1985).

62. D. A. Hales, L. Lian, and P. B. Armentrout, Int. J. Mass Spectrometry and Ion Process, **102**, 269 (1990).

CHAPTER VII

PHOTOFRAGMENTATION SPECTROSCOPY OF THE NIOBIUM DIMER CATION AND THE AB INITIO STUDIES ON Nb_2, Nb^+_2

Abstract

The dissociation energy of the niobium dimer cation molecule is measured by multiphoton fragmentation. The molecule is produced by laser vaporization of a niobium target rod and cooled in a helium supersonic expansion. The molecular beam containing niobium dimer cation is interrogated in the range 15,500-20,000 cm^{-1}, using a pulsed dye laser to dissociate the molecule. The dissociation threshold was observed at 15,880 cm^{-1}. Fluence studies and density functional calculations indicate that the multiphoton process should be a three-photon process, 15,880 cm^{-1} + $E_{dissoc.}$ E_{dissoc} ≥ 31,760 cm^{-1}. With this knowledge the dissociation energy was accurately determined to be 5.907 ± 0.056 eV. Several different density functional calculations predict the dissociation energy of Nb_2 and Nb_2^- in remarkable agreement with experiment.

VII.1. INTRODUCTION

The dissociation energy of niobium dimer was measured by Gupta and Gingerich[7] from third-law determination and gave $D^\circ(Nb_2)$ = 5.22 ± 0.02 eV. A collision-induced dissociation measurement of the Nb_2 bond energy gave D° =5.22±0.31 eV.[18] Simard *et al.*[10] have determined the lowest ground state to be the $^3\Sigma_g$, arising from the $1\sigma^2\pi^4 2\sigma^2\delta^2$ electronic configuration; the vibrational frequency and the bond distance were found to be 424.8917(12) cm^{-1} and 2.077 81(18) Å, respectively, from rotationally resolved electronic spectra of Nb_2. Simard and co-workers[10] have calculated the dissociation

energy D_e, equilibrium distance and vibrational frequency to be 4.05 eV, 2.08 Å, and 450 cm^{-1}. Walch and Bauschlicher[14] have calculated the dissociation energy, equilibrium distance and vibrational frequency for diniobium to be 2.24 eV, 2.1 Å and 448 cm^{-1}, respectively, by CASSCF calculation. Three density functional calculations give 5.1 eV,[12] 5.0 eV,[13] and 5.24 eV.[14] Shellers[15] in an effective core potential treatment, and Shim[16] both predict that Nb_2 has a $^1\Sigma^+_g$ ground state, arising from the same configuration.

The electron spin resonance (ESR) study on Nb_2^+ by Zee, Li, and Weltner[17] suggested that Nb_2^+ has $^2\Sigma^+_g$ ground state, arising from the electronic configuration $5s\sigma^2 4d\sigma^1 4d\pi^4 4d\delta^2$. A collision-induced dissociation measurement of the Nb_2^+ bond energy gave $D^o(Nb_2^+) = 5.87 \pm 0.21$ eV.[18]

VII.1. EXPERIMENTAL STUDY ON THE NIOBIUM DIMER CATION

VII 2.1. FLUENCE STUDY

Fluence dependent studies at 560 and 560.24 nm were performed in an attempt to determine whether the absorption process was a one-photon or multi-photon process. Figures 7.1 and 7.2 show the results of these fluence dependent studies at different wavelengths. The order of the absorption event leading to dissociation was estimated from the extent of fragmentation of laser fluence to be 2.7 at 560nm and 2.3 at 560.24 nm. These nonlinearities in the curves at the different wavelengths negate the possibility that the absorption was a one photon process,[5,22] however the determination of whether the dissociation was two or three photon process is still unclear. But as

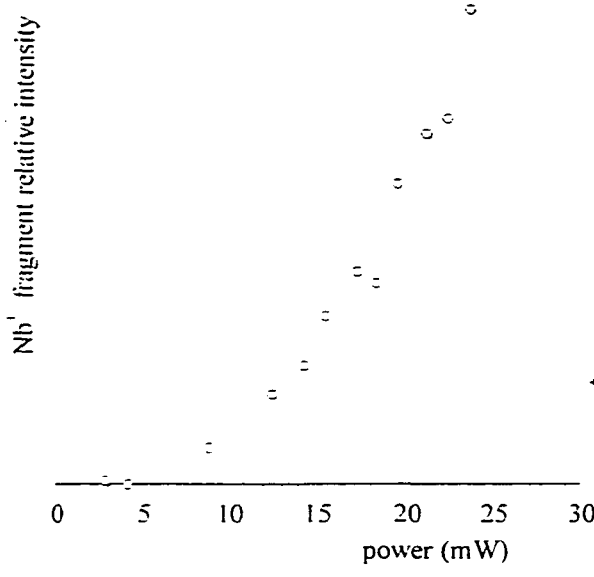

Figure 7.1. Plot of Nb^+ fragment relative intensity,

(daughter –Background)/Parent

vs laser power for fluence dependence studies at 560.24 nm (or 17,849 cm^{-1}).

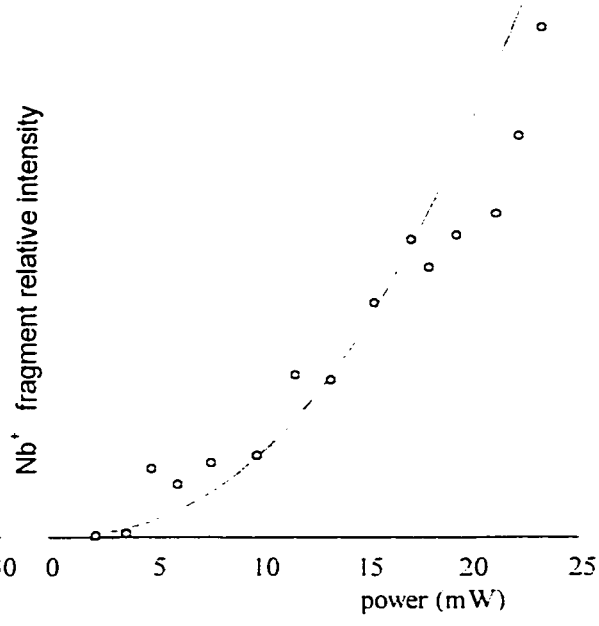

Figure 7.2. Plot of Nb^+ fragment relative intensity.

(daughter –Background)/Parent,

vs laser power for fluence dependence studies at 560 nm (or 17,857 cm^{-1}).

discussed in section VI. 2, because of the fluctuations in the laser and cluster beams, and mismatch in the laser and cluster ion beam overlap, two photon process look like one photon, three photon processes look like two-photon processes. Additional information supporting this view comes from knowing that the bond dissociation energy[18] of Nb_2^+ is 5.87 ± 0.19 eV. The calculated dissociation energy of the Nb_2^+ by several DF methods indicated that the multiphoton fragmentation of the Nb_2^+ in this experimental region must be three photon process, see Chapter VII.2.2. These coupled to the fact that the power studies at 560 and 560.24 nm ~ 2.2 eV, a three-photon process was a minimum possibility to dissociate the niobium dimer cation.

VII .1.1. DETERMINATION OF THE LOWEST DISSOCIATION ENERGY LIMIT AND THE THRESHOLD ENERGY SPECTRUM OF THE Nb^+_2:

Figure 7.3 shows the multiphoton photofragmentation spectrum of Nb_2^+ in 15,400-16,100 cm^{-1} region. The background of the spectrum exhibits a fairly sharp rise at the threshold, 15,880±150 cm^{-1}, when the multiphoton fragmentation changes from a four-photon process to a three-photon process. The threshold appears at total laser energy (15,880 ± 150 cm^{-1} + $E_{dissoc.}$) of 47,640 cm^{-1}. The lowest dissociation threshold energy of Nb_2^+ is therefore 47,640 ± 450 cm^{-1} (5.907 ± 0.056 eV). Experimental determination of the lowest dissociation energy limit of Nb^+_2 is in agreement with the collision-induced dissociation experiment (CID)[18] and the calculated dissociation energy by various DF methods in section VII 3.

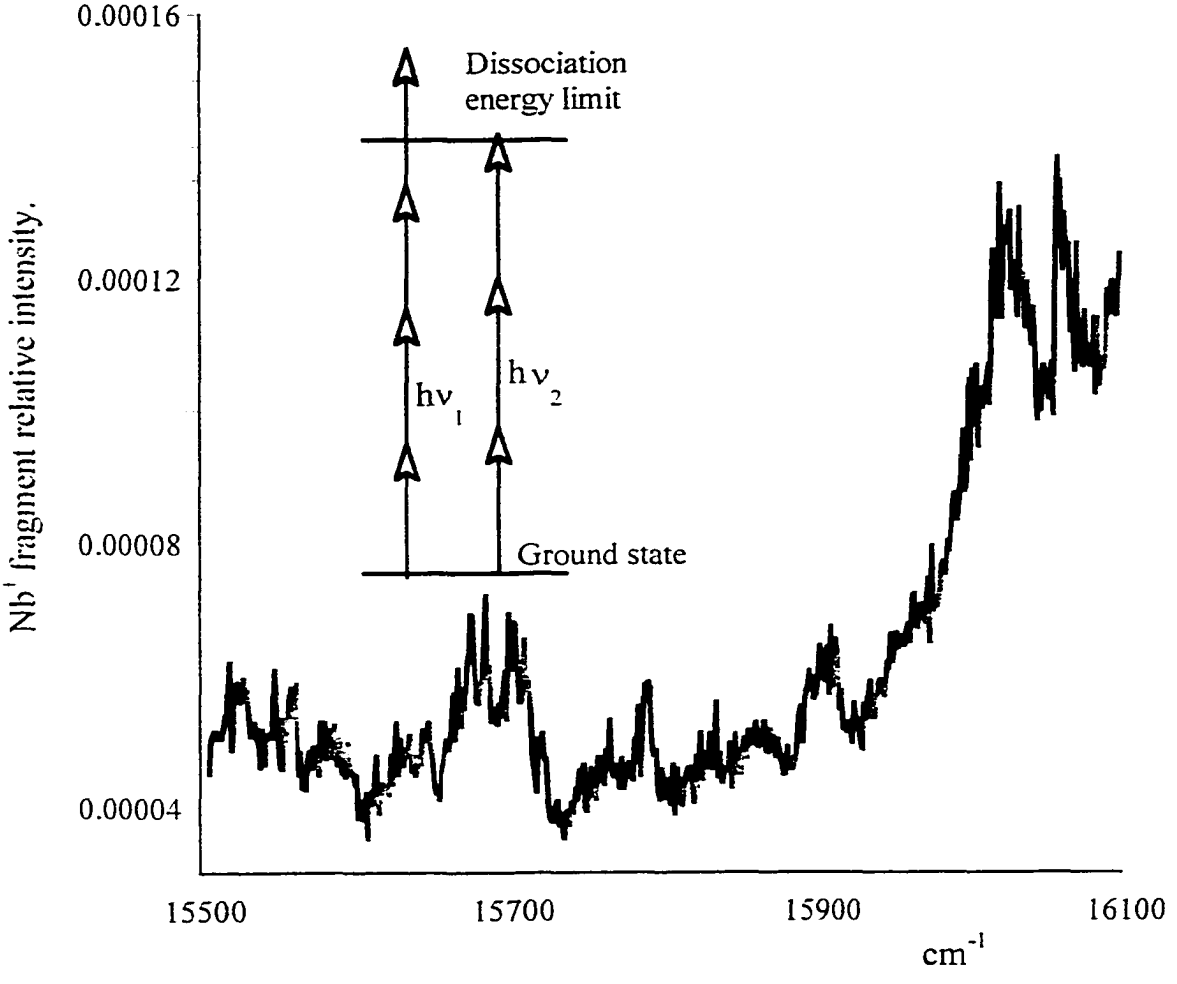

Figure 7.3. The photodissociation threshold of Nb_2^+ was observed in an one color multiphoton fragmentation action spectrum. The spectrum rises abruptly out of background at 15,880 ± 150 cm^{-1}.

VII 2.2. RESULT OF CALCULATIONS

VII 2.2.1. Nb_2 :

Several density functional calculations predict the ground state of niobium dimer to be $^3\Sigma^-_g$, arising from $5s\sigma^2 4d\sigma^2 4d\pi^4 4d\delta^2$ electronic configuration, in agreement with rotationally resolved electronic spectra[10] and other theoretical predictions.[10,11-14] The calculated equilibrium bond distance and vibrational frequency in the ground state, $^3\Sigma^-_g$, are in agreement with experiment[10] within 4% and 5% errors, respectively. The dissociation energy of $Nb_2(^3\Sigma_g^-)$ was calculated from the lowest energy of $Nb_2(^3\Sigma_g^-)$ relative to the $Nb(5s^14d^4)$ + $Nb(5s^14d^4)$ atomic limit and potential energy curves, see Fig. 7.4., of $Nb_2(^3\Sigma^-_g)$. The best results were predicted by BLYP and BP86 density functional methods, as shown in Table 7.1. The lowest singlet ($^1\Gamma_g$; $...2\sigma_g^2\,\delta_g^2$) and quintet ($^5\Delta_u$; $...2\sigma_g^1\,\delta_g^2\,\delta_u^1$) states of Nb_2 were predicted to be 0.295 eV and 0.476 eV above $X^3\Sigma^-_g$ state. The experimentally observed $\Omega = 0 \leftarrow \Omega = 0$ transitions: 14,648 (A system), 14,705 (B system), 14,829 (C system), 14,834 (D system) , 14,845 (E system) and observed $\Omega = 1 \leftarrow \Omega = 1$ transitions: 14,441 (A′ system), 15,245 (B′ system), 15,634 (C′ system)[10] could be fit to theory, BLYP/BP86: $\delta_g \rightarrow \delta_u$ = 12,722/13,150 $2\sigma_g \rightarrow 1\sigma_u$ =12,642/13,500, $1\sigma_g \rightarrow 1\sigma_u$ = 16,601/17,400, and $\delta_g \rightarrow 2\pi_u$ = 18,384/19,100.

The assignment of the observed bands in Table 7.2 is by no means definitive. Nevertheless, the theoretical transition energies are consistent with the observed spectra. Furthermore, the transitions listed in Table 7.2 are dipole allowed and hence are probable candidates for the assignment, as seen from Table 7.2, $(A,B,C)^3\Sigma^-_u/A^3\Pi_u - X^3\Sigma^-_g$. Although such an agreement may be considered fortuitous, there are not too many

Table 7.1. Calculated spectroscopic properties of $Nb_2(^3\Sigma^-_g)$.

D_e (eV)	ω_e (cm^{-1})	r_e (Å)	$^3X\Sigma_g - {}^1\Gamma_g$ (eV)	$5s^c$	$4d^c$	DFT
4.915[a] (4.809)[b]	444	2.157	0.296	1.024	3.903	BLYP
4.769	454	2.154	0.363			BP86
5.22±0.02[7]	424.8[10]	2.078[10]				Expt.
5.22±0.31[18]						.

[a]$E(Nb_2; \ldots 2\sigma_g^2\delta_g^2) - 2E(Nb; \ldots 5s^1 4d^4)$, [b]from potential energy curve, see Fig. 7.4. and [c]gross population on each niobium atom.

Table 7.2. Some of selected calculated orbital-orbital transitions. T_e in cm^{-1}, of triplet states of $Nb_2(X^3\Sigma_g(1\pi_u^4 1\sigma_g^2 2\sigma_g^2 \delta_g^2))$.

		BLYP	BP86	Exp.[10]
$\delta_g \rightarrow \delta_u$	$^3\Sigma^-_u$, $^3\Gamma_u$	12,722	13,150	14,648/14,705 A/B system
$2\sigma_g \rightarrow 1\sigma_u$	$^3\Sigma^-_u$	12,642	13,500	14,829/14,834 C/D system
$2\sigma_g \rightarrow \delta_u$	$^3\Delta_u$	15,965	16,400	
$1\sigma_g \rightarrow 1\sigma_u$	$^3\Sigma^-_u$	16,601	17,400	14,845 E system
$\delta_g \rightarrow 2\pi_u$	$^3\Pi_u$, $^3\Phi_u$	18,387	19,100	15,242/15,634 B′/C′ system

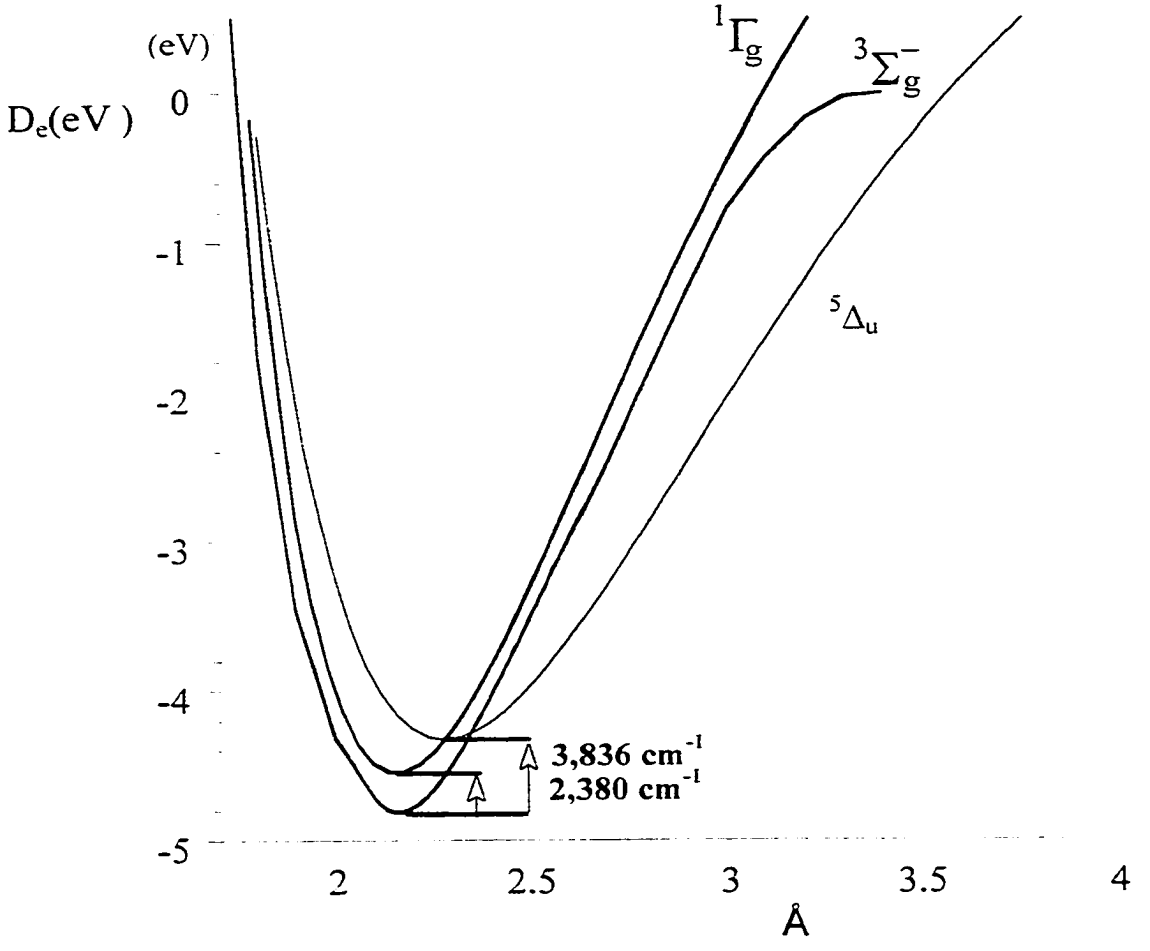

Figure 7.4. Potential energy curves of Nb_2 ($X\ ^3\Sigma^-_g$, $^1\Gamma_g$, and $^5\Delta_u$), $D_e(Nb_2;X\ ^3\Sigma^-_g)$ = 4.809 eV. BLYP density functional used here.

alternative possibilities for assigning the spectra consistent with the predicted energy separations.

VII 2.2.2. Nb_2^+:

Several density functional and complete active space self-consistent-field (CASSCF) were performed on the niobium dimer cation. All methods predicted the lowest ground state of Nb_2^+ to be $^4\Sigma^-_g$, arising from the $1\sigma_g^2\pi_u^4 2\sigma_g^1\delta_g^2$ electronic configuration. Even though the electron spin resonance (ESR) study on Nb_2^+ by Zee, Li, and Weltner[17] suggested that the lowest ground state of Nb^+_2 is $^2\Sigma^+_g$ state, arising from the electronic configuration $1\sigma_g^2\pi_u^4 2\sigma_g^1\delta_g^2$; the lowest doublet state of the Nb_2^+ using Hund's rules is predicted to be a $^2\Gamma_g$, arising from the electronic configuration $1\sigma_g^2\pi_u^4 2\sigma_g^1\delta_g^2$. The $^2\Gamma_g$ was calculated to be 0.20-0.35 eV above the $X^4\Sigma^-_g$ ground state, see Fig. 7.5. The calculated spectroscopic properties of $Nb_2^+(^4\Sigma^-_g)$ are given in Table 7.3. All the density functional methods underestimated the dissociation energy with respect to the $Nb(5s^14d^4)$ + $Nb^-(4d^4)$ atomic limit, but the potential energy curve of $Nb_2^+(^4\Sigma^-_g)$ overestimated the dissociation energy limit by 0.28 eV. The assignment of the observed bands in Table 7.4 is by no means definitive. Nevertheless, the theoretical transition energies are consistent with the observed spectra. Furthermore, the transitions listed in Table 7.4 are dipole allowed and hence are probable candidates for the assignment, as seen from Table 7.4, $(A,B)^4\Sigma^-_u$ and $(A,B)^4\Pi_u \rightarrow X^4\Sigma^-_g$.

Table 7.3. Calculated spectroscopic properties of $Nb_2^+(^4\Sigma^-_g)$.

$D_e(Nb_2^+;X^4\Sigma_g)$	ω_e (cm^{-1})	r_e (Å)	IP(Nb) (eV)	IP(Nb_2) (eV)	$X^4\Sigma^-_g$- $^2\Gamma_g$ (eV)	$5s^g$	$4d^g$	DFT
5.283 [a] (6.189)[e]	436	2.120	6.853	6.485	0.201	0.547	3.866	BLYP
5.168	467	2.092				0.549	3.858	B3LYP
4.764	474	2.087				0.555	3.852	B1LYP
5.907 ± 0.056[b]			6.894[c]	6.207 ± 0.3 [d]				**Exp.**
5.87 ± 0.12 [f]				6.368±0.001[h]				

[a]$E(Nb_2^+; {}^4\Sigma^-_g, 1\pi_u^4 1\sigma_g^2 2\sigma_g^1 \delta_g^2) - E(Nb; 5s^1 4d^4) - E(Nb^+; 5s^1 4d^3)$. [b]present work. [c]from ref. 8, [d]calculated from thermocycle; $IP(Nb_2; X^3\Sigma^-_g) = IP(Nb; {}^6D_J) + D_e(Nb_2; X^3\Sigma^-_g) - D_e(Nb_2^+; X^3\Sigma^-_g)$, and [e]from potential energy curve, see Fig. 7.5. [f]From ref. 18 [g]Gross population on each niobium atom and [h]R2PI experiment, see Chap. IX.

Table 7.4. Some the calculated orbital-orbital transitions of quartet states of niobium dimer cation.

Symmetry	configuration	$T_e(cm^{-1})$
$X^4\Sigma^-_g$	$1\pi_u^4 1\sigma_g^2 2\sigma_g^1 \delta_g^2$	0
$^4\Sigma^-_g$	$1\pi_u^4 1\sigma_g^1 2\sigma_g^2 \delta_g^2$	6,739
$^4\Delta_g$	$1\pi_u^4 1\sigma_g^1 2\sigma_g^1 \delta_g^3$	6.863
$^4\Pi_u$	$1\pi_u^3 1\sigma_g^2 2\sigma_g^2 \delta_g^2$	11,369
$^4\Pi_u(II)$, $^4\Phi_u$	$1\pi_u^3 1\sigma_g^2 2\sigma_g^1 \delta_g^3$	11.496
$^4\Sigma^+_u$, $^4\Gamma_u$	$1\pi_u^4 1\sigma_g^2 2\sigma_g^1 \delta_g^1 1\delta_u^1$	13.365
$^4\Delta_u$	$1\pi_u^4 1\sigma_g^2 \delta_g^2 \delta_u^1$	13.492
$^4\Delta_u$	$1\pi_u^4 1\sigma_g^2 2\sigma_g^1 \delta_g^1 1\sigma_u^1$	16,886
$^4\Sigma^-_u$	$1\pi_u^4 1\sigma_g^2 2\sigma_g^1 \delta_g^2 1\sigma_u^1$	17.013
$^4\Pi_u(III)$, $^4\Phi_u$	$(1\pi_u^3 1\sigma_g^1 2\sigma_g^2 \delta_g^3)$	18,232
$^4\Pi_u(IV)$	$(1\pi_u^3 1\sigma_g^1 2\sigma_g^1 \delta_g^4)$	18,359
$^4\Sigma^+_u$, $^4\Gamma_u$	$(1\pi_u^4 1\sigma_g^1 2\sigma_g^2 \delta_g^1 \delta_u^1)$	20.101
$^4\Delta_u$	$1\pi_u^4 1\sigma_g^1 2\sigma_g^1 \delta_g^2 \delta_u^1$	20.228
$^4\Sigma^-_u$	$1\pi_u^4 1\sigma_g^1 2\sigma_g^1 \delta_g^2 1\sigma_u$	23.749
$^4\Pi_g$, $^4\Phi_g$	$1\pi_u^3 1\sigma_g^2 2\sigma_g^2 \delta_g^2 \delta_u^1$	24.861
$^4\Pi_g$, $^4\Phi_g$	$(1\pi_u^3 1\sigma_g^2 \delta_g^3 \delta_u^1)$	24,988
$^4\Pi_g$	$(1\pi_u^3 1\sigma_g^2 2\sigma_g^1 \delta_g^2 1\sigma_u^1)$	28.382
$^4\Pi_u$	$(1\pi_u^4 1\sigma_g^2 2\sigma_g^1 \delta_g^1 2\pi_u^1)$	28.504
$^4\Pi_u$	$(1\pi_u^4 1\sigma_g^2 2\sigma_g^1 \delta_g^2 2\pi_u^1)$	28,631
$^4\Sigma^-_u$, $^4\Delta_u$	$(1\pi_u^4 1\sigma_g^2 2\sigma_g^1 \delta_g^1 2\sigma_u^1)$	31.165
$^4\Sigma^-_u$	$(1\pi_u^4 1\sigma_g^2 2\sigma_g^1 \delta_g^2 2\sigma_u^1)$	31.292

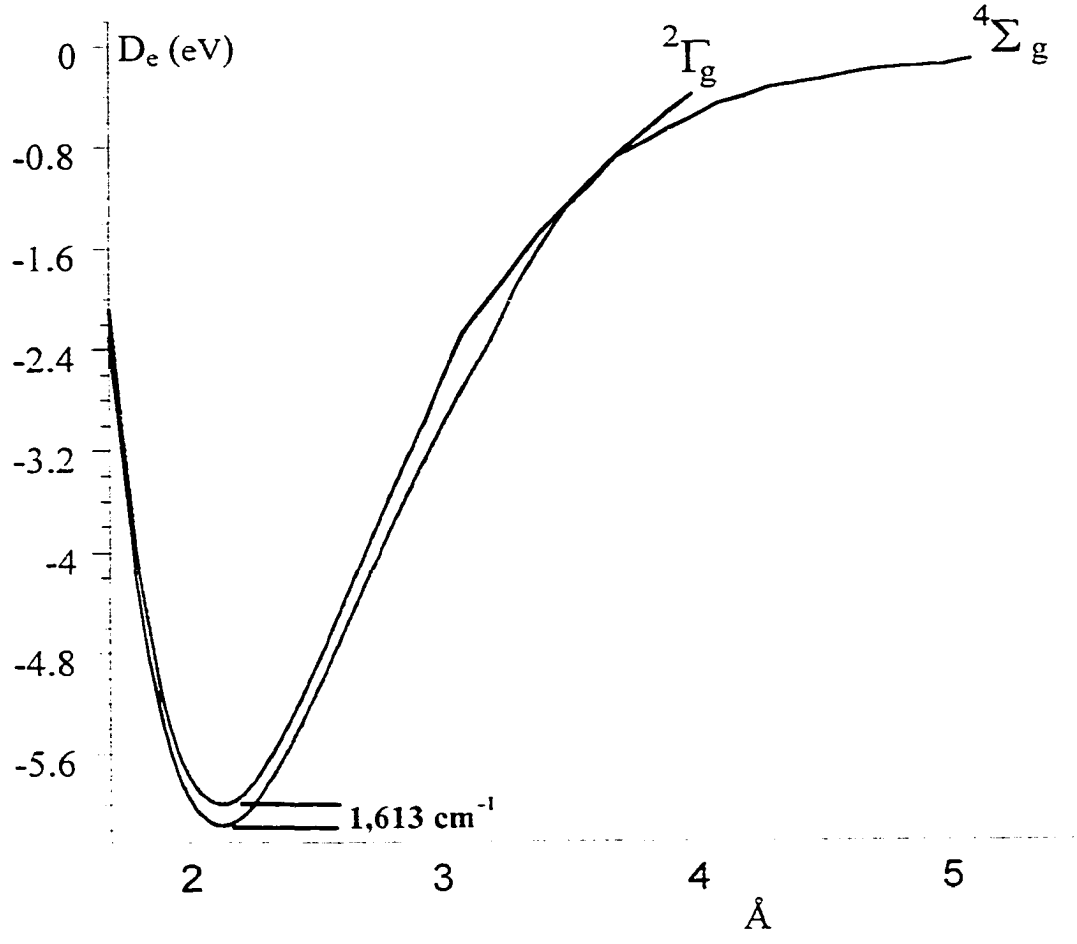

Figure 7.5. Potential energy curves of Nb_2^+($X\ ^4\Sigma^-_g$ and $^2\Gamma_g$), $D_e(Nb_2^+;X\ ^4\Sigma^-_g)$ = 6.186 eV. BLYP density functional used here.

VII 2.3. DISCUSSION

The ground state symmetry of diniobium was predicted to be $^3\Sigma^-_g$, which arises from the $1\sigma_g^2 1\pi_u^4 2\sigma_g^2 \delta_g^2$ configuration, in agreement with experiment[10] and other theoretical treatments.[10-14] The spectroscopic constants and dipole allowed transitions of triplet states of diniobium are in remarkable agreement with experiments[7,9,10,18] and several other calculations.[10-14] Even though an electron spin resonance (ESR) study on Nb^+_2 by Zee, Li, and Weltner[17] suggested that Nb^+_2 has a $^2\Sigma^+_g$ ground state, arising from the electronic configuration $5s\sigma^2 4d\sigma^1 4d\pi^4 4d\delta^2$, several density functional calculations and CASSCF methods predicted the ground state of Nb_2^+ to be $^4\Sigma^-_g$ state, arising from the electronic configuration $5s\sigma^2 4d\sigma^1 4d\pi^4 4d\delta^2$; James *et al.*[31] predicted the lowest ground state of niobium dimer cation to be $^4\Sigma^-_g$ state using the density functional and CASSCF methods. The lowest doublet state of Nb_2^+, $^2\Gamma_g$, was predicted to be over 0.2 eV above $X^4\Sigma^-_g$ state.

In summary, we have experimentally determined the dissociation energy of the niobium dimer cation by observing a sharp threshold between the four- and three-photon photodissociation continua. The value obtained, 5.907 ± 0.056 eV, is in agreement with several density functional calculations within 5-15% errors. We further extended these calculations to the neutral Nb_2, obtaining good agreement with previous experimental data from other laboratories, including vibrational frequencies. Several bands in the multiphotofragmentation spectrum of Nb_2^+ could also be fit to theory.

Chapter VII References

1 T. G. Dietz, M. A. Duncan. D. E. Powers, and R. E. Smalley, J. Chem. Phys. **74**, 6511(1981).

2 See. for example, "Physics and Chemistry of Finite Systems: From Clusters to Crystals", edited by P. Jena, S. N. Khanna, and B. K. Rao, Kluwer Academic, Boston, (1992), Vols. I and II.

3 B. Simard, Marie-Angle Lebeault-Dorget, A. Marijnissen, and J. J. ter Meulen. J. Chem. Phys. **108**, 9668 (1998).

4 M. Harada and H. Dexpert. J. Phys. Chem. **100**, 565 (1996).

5 W. Kohn and L. J. Sham. J. Phys. Rev. A **140**, 1133, (1965).

6 M. Aydin, D. M. Lindsay, and John R. Lombardi, " Photofragmentation spectroscopy of zirconium dimer cation and ab initio study on Zr_2 and Zr_2^+". Submitted to Phys. Rev.

7 S. K. Gupta and K. A. Gingerich. J. Chem. Phys. **70**, 5350 (1979).

8 S. R. Radel and M. H. Navidi, Chemistry, West Publishing Company, New York, (1994).

9 M. D. Morse. Chem. Rev. **86**, 1049 (1986).

10 A. M. James, P. Kowalczyk, R. Fournier, and B. Simard, J. Chem. Phys. **99**, 8505(1993).

11 S. P. Walch and C. W. Bauschlicher, Jr., in "Comparison of Ab Initio Quantum Chemistry with Experiment for Small Molecules", edited by R. J. Bartlett (Reidel, Dondrecht, 1985).

12 K. S. Sohn, S. Lee, D. M. Bylaander, and L. Kleinman, Phys. Rev. B **39**, 9983 (1989).

13 D. R. Salahub, Adv. Chem. Phys. **69**, 447 (1987).

14 L. Goodwin and D.R. Salahub, Phys. Rev. A **47**, R774 (1993).

15 H. Sellers, J. Phys. Chem. **94**, 1338 (1990).

16 I. Shim, Matematisk-fysiske Meddelelser **41** (1985).

17 R. J. Van Zee, S. Li and W. Weltner Jr. Chem. Phys. Letters Vol. **217**, 381 (1994).

18 D. A. Hales, L. Lian, and P. B. Armentrout. Int. J. Mass Spectr. And Ion Proc. **102**, 269 (1990).

19 L. -S. Zeng, P. J. Brucat, C. L. Pettiette, S. Yang, and R. E. Smalley, J. Chem. Phys. **83**, 4273(1985).

20 P. J. Brucat, L. -S. Zheng, C. L. Pettiette, S. Yang, and R. E. Smalley, J. Chem.Phys. **84**, 3078 (1986)

21 A. D. Becke, Phys. Rev. A **38**, 3098 (1988)

22 C. Lee, W. Yang and R. G. Parr, Physical Review B **37**, 785 (1988).

23 B. Miehlich, A. Savin, H. Stoll and H. Preuss, Chem. Phys. Lett. **157**, 200 (1989).

24 J. P. Perdew, Phys. Rev. B **33**, 8822 (1986).

25 A. D. Becke, J. Chem. Phys. **98**, 5648 (1993).

26 A. D. Becke, J. Chem. Phys. **104**, 1040 (1996).

27 C. Adamo and V. Barone, Chem. Phys. Lett. **274**, 242 (1997).

28 P. J. Hay and W. R. Wadt, J. Chem. Phys. **82**, 270 (1985).

29 W. R. Wadt and P. J. Hay, J. Chem. Phys. **82**, 284 (1985).

30 P. J. Hay and W. R. Wadt, J. Chem. Phys. **82**, 299 (1985).

31 A. M. James, P. Kowalczyk, E. Langlois, and M. D. Campbell, A. Ogawa, and B. Simard, J. Chem. Phys. 101, 4485 (1994).

CHAPTER VIII

Photofragmentation Spectroscopy and Ab Initio Study of the Niobium Trimer Cation

Abstract

The photofragmentation of the initially mass-selected Nb_3^+ to Nb_2^+ + Nb unexpectedly exhibits a sharp rise in the background of the spectrum of Nb_2^+ fragment at 16,190±10 cm^{-1} according to the collision-induced dissociation (CID) measurement. Based on the CID result, the atomic energy levels of Nb, and several theoretical predictions, we propose two possible cases of which one of these must be responsible for this threshold: (1) the $Nb_3^+(^3A'_1)$ may dissociate by a three photon process to a higher energy limit of $Nb_2^+(^4\Sigma^-_g)$+$Nb(^2G_J)$ where the total energy of the three photons (6.022 ± 0.004 eV) is 1.012 ± 0.19 eV above the CID measurement. If it dissociates to $Nb_2^+(^4\Sigma^-_g)$ + $Nb(^4F)$ separated fragment limit in the CID experiment, then the distance between two threshold energy in the CID and the photofragmentation experiment, 1.012 ± 0.19 eV, is in excellent agreement with the distance between the ^2G_J and ^4F_J levels (1.095 eV) of Nb. Making a correction for this higher energy limit for the separated fragment then brings the photofragmentation measurement into agreement with CID measurements and allows the bond energy to be determined as $D(Nb_2^+\text{-}Nb)$ = 4.992 ± 0.004 eV. (2) The Nb_3^+ may be internally excited by collisions in the source region, which must be metastable with respect to collision and 0.99±0.19 eV above the ground state, or strongly populated into a low-lying state and dissociated into the lowest energy limit by two-photon absorption. There is currently no experimental evidence to support this model.

VIII.1. INTRODUCTION

Since the application of laser-vaporization techniques coupled with time-of-flight mass-spectroscopy for production of the jet-cooled cationic transition metal cluster beams, the study of metal clusters in gas phase has received special interest due to its high sensitivity[1-13] and mass-selectivity. This has allowed collision-induced dissociation, resonant two-photon ionization, and mass selected photofragmentation experiments. These have included examinations of their reactivity,[14-23] reaction rate,[25-34] equilibria,[35-40] dissociation energies,[41-49] ionization potential,[50-54] and band structures.[55-58] Due to partially occupied open d-subshell orbitals of transition metal clusters, even for a dimer, hundreds of electronic states are expected in the 1 eV range. This makes the spectra of the transition metals become more complicated and sometimes it is impossible to make a useful assignment due to strong interaction between the high density of vibronic states and strong first order or second order spin-orbit interaction.[59-63] Therefore, the transition metal clusters are still a challenge to both experimental and theoretical investigations despite a considerable improvement in the both fields in resent years.

We shall review some of the previous relevant studies. There are several previous experimental and theoretical investigations on the behavior of the neutral and cationic niobium clusters.[14-23] A few topics that have aroused special interest are structural isomerism,[28,64,65] size dependent reactivity and electron binding,[66-68] reactivity with CO.[69,70] Hales et al.[43] determined the dissociation energies of Nb_2^+-Nb and Nb^+-Nb_2 by collision-induced (CID) experiments to be 5.01 ± 0.19 and 5.69 ± 0.25 eV, respectively. We found three theoretical studies on the neutral and cationic niobium clusters. Sellers[71] in 1990 reported a relativistic effect core potential-configuration interaction single and

double (RECP-CISD) predictions for $Nb_n^{0/+}$, n =1 to 4. He reported sextet and quintet ground states for neutral and cation niobium trimer and a peak atom to base midpoint of 2.90 Å in neutral and 2.94 Å in the cation. Goodwin and Salahub[72] using DF with local potential, found an isosceles triangle with ground state multiplicity of 2 for the neutral and a D_{3h} triplet ground state for cation a with bond length 2.37 Å. In 1999, Fowler *et al.*[22] used Becke's three parameter hybrid method with the Lee, Yang, and Parr[77,78] correlation functional gradient-corrected density functional methods, B3LYP. They reported the dissociation energy for the $Nb_3^+(^3A_1')$ relative to various spin states of Nb_2^+ + Nb fragment limit: $D(^4Nb_2^+\text{-}^4Nb)$ = 4.50 eV, $D(^2Nb_2^+\text{-}^4Nb)$ = 4.87 eV, $D(^4Nb_2^+\text{-}^2Nb)$ = 5.82 eV, and $D(^2Nb_2^+\text{-}^2Nb)$ = 6.19 eV. Section II presents a brief description of the experimental methods used in this study, and our results are given in Sec. III. In Sec. IV we will present the results of calculations, and concluding remarks are then given in Sec. V.

VIII. 2. Calculations

BLYP (a computer code in Gaussian-94 and –98 packages) type density functional calculations were performed on $Nb^{0/+}$, $Nb_2^{0/+}$, and Nb_3^+. The calculation uses Beck's 88 functional, which includes the Slater exchange along with correction involving the gradient of the density[76] in combination with LYP type correlation functional where LYP is the correlation functional of Lee, Yang, and Parr, which includes both local and non-local terms.[77,78] Los Alamos effective core potential (ECP) plus DZ, LANL2DZ computer code, basis set[79-81] was used in the calculations. The LANL2DZ basis set consists of linear combination of the three s, three p, and two d (1s, 2s, 3s, 4p, 5p, 6p, 7d, and 8d are computer code in Gaussian94 and 98 packages) atomic orbitals. 1s, 2s2p,

3s3p3d shells of niobium atoms were assigned to the core and treated by frozen core approximation. All calculations were performed on Decalpha and Intel Pentium II 450 MMX computers.

The BLYP method with the LANL2DZ basis set predicted the ground state of Nb_3^+ to be a $^3A_1'$ state, arising from the electronic configuration $...2(e')^4 3(a_1')^2 1(e'')^2$ and $^4\Sigma_g^-$ $(...1\sigma^2\pi^4 2\sigma^1\delta^2)$ for Nb_2^+. $^2G(4d^3 5s^2)$ atomic energy levels of Nb, except the $^6S(4d^5)$ level, due to the partially occupied d-orbitals. By using the differences between $^6D(4d^4 5s^1)$, $^2G(4d^4 5s^1)$ atomic energy levels of Nb,[73,74] we calculated the dissociation energy of Nb_3^+ relative to the possible separated fragments (Table 8.1): $Nb_2^+(^4\Sigma_g^-)$ + $Nb(^6D)$ (4.826 eV), $Nb_2^+(^4\Sigma_g^-)$ + $Nb(^2G)$ (5.920 eV), $Nb_2^+(^4\Sigma_g^-)$ + $Nb(^6S)$ (6.233 eV), and $Nb_2(^3\Sigma_g^-)$ + $Nb^+(^5D)$ (5.429 eV). These results indicated that Nb_3^+ most likely dissociates to $Nb_2^+(^4\Sigma_g^-)$ + $Nb(^6D)$ in the CID experiment and $Nb_2^+(^4\Sigma_g^-)$ + $Nb(^2G)$ in the photofragmentation experiment. The dissociation energy of Nb_3^+ relative to the $Nb_2(^3\Sigma_g^-)$ + $Nb^+(^5D)$ fragment limit (5.429 eV) is in good agreement with that estimated from thermochemical cycle, 5.439±0.001 eV. The calculated bond length (2.449 Å) is 0.08 Å and 0.028 Å longer than local potential treatment[23] and the B3LYP[11] predictions, respectively. We also calculated vibrational frequency of the Nb_3^+ to be 238 cm^{-1} (E' symmetry) and 361 cm^{-1} (A_1' symmetry).

Table 8.1. Calculated spectroscopic properties of $Nb_3^+(^3A_1'$ in D_{3h} symmetry). The experimental values are given for comparison.

	BLYP	**Experiment.**	
Ground state	$^3A_1'$ in D_{3h}		
$R_{12,\,13,\,23}$ (A)	2.449		
$\omega_{1,2}(E')$, cm^{-1}	238		
$\omega_3(A_1')$, cm^{-1}	361		
$D_e(Nb_3^+; {}^3A_1')$, eV			
$Nb_2^+(^4\Sigma_g^-) + Nb(^6D)$	4.826	**4.992±0.004**	This work
		5.01±0.19	Ref. 43
$Nb_2^+(^4\Sigma_g^-) + Nb(^2G)$,	5.997	**6.022 ±0.004**	This work
$Nb_2(^3\Sigma_g^-) + Nb^+(^5D)$,	5.429	**5.504±0.004**	This work [a]
		5.69±0.25	Ref. 43

[a] Estimated from thermochemical cycle. The global energy of the ^2G and ^6D states of the Nb were estimated relative to the calculated global energy of $Nb(^6S, 4d^5)$ by using the experimentally known atomic energy levels of Nb.

Table 8.2. Calculated orbital transition energies[a] (in eV) of triplet states of Nb_3^- are averaged alpha and beta manifolds. The ground state electronic configuration of Nb_3^- is $1(a_1')^2 1(a_2'')^2 2(a_1')^2 1(e')^4 3(a_1')^2 1(e'')^2$, $^3A_1'$. BLYP

Ground state ($^3A_1'$)	**$(1e'')^2$**	**$(2e')^0$**	**$(3e')^0$**	**$(2e'')^0$**	**$(1a_1'')^0$**
$(1e'')^2$ →		1.477	1.965	2.373	2.647
$(2a_1')^2$ →	0.199	1.676	2.164	2.572	2.846
$(1e')^4$ →	0.616	2.093	2.581	2.989	
$(1a_1')^2$ →	0.786	2.263	2.751		
$(1a_2'')^2$ →	1.377	3.053			

[a] Except $(1a_2'')^2 \rightarrow (1a_1'')^0$ transition. all orbital transitions are dipole allowed.

VIII. 3. MULTIPHOTON FRAGMENTATION OF THE Nb_3^+

We studied multiphoton fragmentation caused by pulsed laser photolysis of initially mass selected Nb_3^+ into Nb_2^+ and Nb^+ products in 16,060-16,330, 16,800-17,100, and 17,700-18,000 cm^{-1} ranges. We did not observe any peaks in these regions. However, the spectrum of the Nb_2^+ product unexpectedly exhibits a sharp rise in the background at 16,190±10 cm^{-1} (Fig. 8.1). As mentioned earlier, Hales *et al.*[43] determined the dissociation energy of Nb_3^+ to Nb_2^+ + Nb fragment by the CID experiment to be 5.01±0.19 eV. They did not mention the state of the fragments. The CID measurement indicates that the multiphotofragmentation of Nb_3^+ to Nb_2^+ + Nb separated fragment limit is three photon process in this range, 16,060-16,330 cm^{-1}, but the total energy of the three photons (6.022 ± 0.004 eV) at the observed threshold is 1.01 ± 0.19 eV above the CID result. We propose two possible mechanisms, one of which may explain this discrepancy. (depicted in Fig. 8.2):

1) The observed threshold in the photofragmentation experiment may be due to the fragmentation of Nb_3^+ to a higher energy limit of the Nb_2^+ + Nb fragment 1.01 ± 0.19 eV above the CID measurement. Hales and co-workers did not mention the states of the fragments in the CID experiment. Humphreys and Meggers[73,74] have tabulated the atomic energy levels of Nb. The BLYP density functional methods with LANL2DZ basis set predicted the ground state of Nb_3^+ and Nb_2^+ to be $^3A_1'$ in D_{3h} symmetry and $^4\Sigma_g^-$, respectively, Sec. IV. If the calculation predicted the true ground state of $Nb_3^+(^3A_1')$, then the dipole allowed excited states of Nb_3^+, having also S = 1, can dissociate when a particular excited fragment limit is reached. The discrepancy between the two observed threshold energies, 1.01 ± 0.19 eV, suggests that $Nb(^6D_J, 4d^45s^1)$ is excited to the $4d^35s^2$:

^2G_J state of the Nb in the photofragmentation experiment. The known energy difference between the ^2G_J and ^6D_J atomic energy levels of the Nb is 1.095 eV (or 8,832 cm^{-1}), in good agreement with the difference between the two observed threshold energies. It should be noted that triplet state, of the Nb_3^+ can be generated by the combination of a ground state of $Nb_2^+(^4\Sigma^-_{1/2})$ with the excited state, ^2G_J, of the Nb, S = 1 and 2 and transition from the ^2G_J excited states of Nb to the ^6D_J ground state is forbidden. Making a correction for the energy of the Nb, $4d^35s^2$, $^2G_{7/2}$ state then provides $D_o(Nb_2^+\text{-}Nb) = 4.927 \pm 0.001$ eV in excellent agreement with the CID measurement of 5.01 ± 0.19 eV.[43]

The dissociation energies of Nb_3^+ relative to $Nb^+ + Nb_2$ separated fragment limit can be readily calculated using the bond energies of Nb_2^+-Nb, $D_o(Nb_2^+\text{-}Nb) = 4.927 \pm 0.001$(this work) and ionization energies of Nb (IE = 6.88 ± 0.0001 eV)[75] and

$$D(Nb_2\text{-}Nb^+) = IE(Nb)\text{-}IP(Nb_2) + D(Nb_2^+\text{-}Nb)$$

Nb_2 (IE = 6.368 ± 0.001 eV)[12] using the thermochemical cycle to give $D(Nb_2\text{-}Nb^+) = 5.439 \pm 0.001$ eV.

2) A low lying state of the Nb_3^+ cation (0.99 ± 0.19 eV above the lowest ground state) could be appreciably populated when the Nb_3^+ form in the quenching plasma, and is metastable with respect to collisional depopulation (the life-time of this state must be greater than 30 μs according to our experimental conditions), or there may be a alternatively low lying state which is strongly populated in our experiment (case-2 in Fig 8.2). Then, Nb_3^+ can dissociate by two photons (at $16,190 \pm 10cm^{-1}$) to the $Nb_2^+ + Nb$

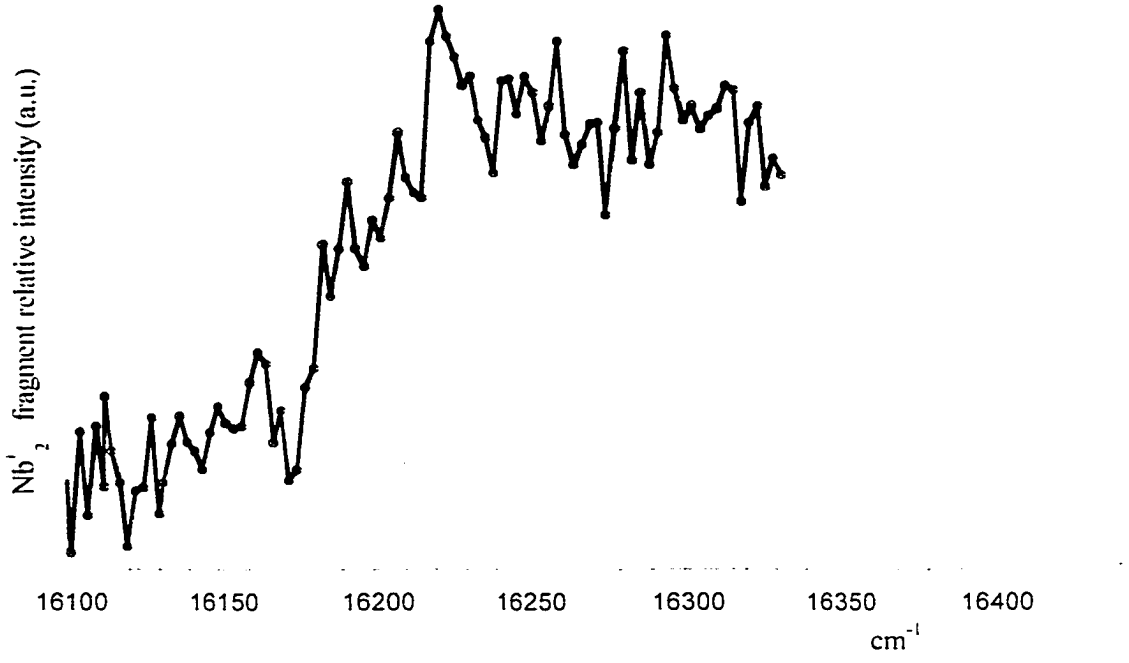

Figure 8.1. The spectrum of Nb_2^+-Nb exhibits a sharp rise at 16,190 ± 10 cm^{-1}. The threshold energy is determined to be 6.022 ± 0.004 eV.

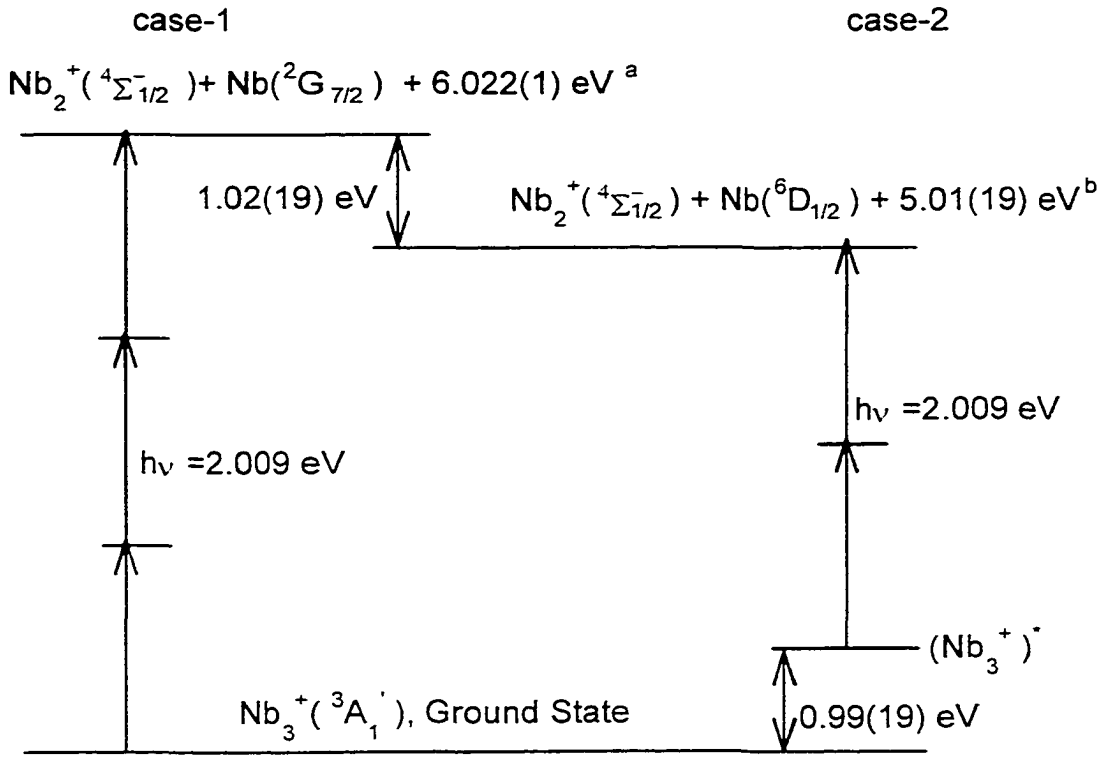

Figure 8.2. The case –1 and –2 illustrate the dissociation of $Nb_3^+(^3A_1')$ to two different dissociation energy limits: $^aNb_2^+(^4\Sigma^-_{1/2})$ + $Nb(^2G_J)$ by three photon (6.022 ± 0.004 eV, this work) and $^bNb_2^+(^4\Sigma^-_{1/2})$ + $Nb(^6D_J)$ (5.01 ± 0.19 eV ,CID experiment, Ref. 43). The lowest ground state of Nb_3^+ and Nb_2^+ were predicted by several density functional to be $^3A_1'$ and $^4\Sigma^-_g$, respectively.

fragment limit with respect to the CID measurement and this may cause a sharp rise at the threshold. The calculated dipole allowed orbital transitions from $Nb_3^+(^3A_1')$ to various excited electronic states are given in Table 8.2. Based in part on theoretical predictions, if the observed threshold in the photon fragmentation experiment originates from the excited Nb_3^+, then there are only two candidates: $^3A_2''$, 0.765 eV and $^3E'$, 1.450 eV above the ground state, $^3A_1'$. There is currently no experimental evidence to support this proposal. Simard et al.[10] observed several weak electronic transitions which originate from the low-lying states, $^1\Gamma_u \leftarrow {}^1\Gamma_g$ and $^3\Delta_u \leftarrow {}^3\Delta_g$, and the lowest ground state of neutral niobium dimer was determined to be $^3\Sigma_g^-$. We feel that case-1 is most likely responsible for the observed threshold in the multiphoton fragmentation spectrum of Nb_2^+-Nb.

VIII. 4. CONCLUSION

A sharp threshold has been observed in the multiphotofragmentation spectrum of Nb_3^+. This observed threshold is significantly larger (1.01±0.19 eV) than the bond energy of Nb_3^+ measured by collision-induced dissociation methods. The differences between atomic energy levels of Nb and theoretical prediction suggest that the $Nb_3^+(^3A_1')$ dissociated to the $Nb_2^+(^4\Sigma_{1/2}^-)$ + $Nb(^6D_{1/2})$ in the CID experiment and $Nb_2^+(^4\Sigma_{1/2}^-)$ + $Nb(^2G_{7/2})$ in our experiment. Making a correction for the energy of Nb, $4d^35s^2$, $^2G_{7/2}$ state then provides $D(Nb_2^+\text{-Nb}) = 4.927 \pm 0.001$ eV in good agreement with the CID measurement. This $D(Nb_2^+\text{-Nb})$ may be combined with literature values of other properties to give $D(Nb_2\text{-}Nb^+) = 5.439 \pm 0.001$ eV. The atomization energy (AE) of Nb_3^+ is calculated to be $AE(Nb_3^+) = 10.899 \pm 0.056$ eV using the thermochemical cycle.

$AE(Nb_3^+) = D(Nb_2^+\text{-}Nb) + D(Nb_2^+)$ with $D(Nb_2^+\text{-}Nb) = 4.927 \pm 0.001$ eV and $D(Nb_2^+) = 5.907 \pm 0.056$ eV.[48]

Several density functional methods were performed on Nb_3^+. All of them predicted ground state of Nb_3^+ to be $^3A_1'$ in D_{3h} symmetry (results of BLYP methods with ECP plus DZ basis set are only presented here). The predicted bond energies of $Nb_3^+(^3A_1')$ relative to various separated fragment limit in remarkable agreement with their experimental values.

Chapter VIII References

1 L. –S. Zheng, P. J. Brucat, C. L. Pettiette, S. Yang, and R. E. Smalley, J. Chem. Phys. **83**, 4273 (1985).

2 L.N. Ding, M. A. Young, P. D. Kleiber, and W. D. Stwalley, J. Phys. Chem. **97**, 2181 (1993).

3 J. B. Hopkins, P. R. R. Langridge-Smith, M. D. Morse, and R. E. Smalley, J. Chem. Phys. **78**, 1627 (1983).

4 P. R. R. Langridge-Smith, M. D. Morse, G. P. Hansen, R. E. Smalley, and A. J. Merer, J Chem. Phys. **80**, 593 (1984).

5 Taylor, G. W. Lemire, Y. M. Hamrick, Z. Fu, and M. D. Morse, J. Chem. Phys. **89**, 5517 (1988).

6 Taylor, E. M. Spain, and M. D. Morse, J. Chem. Phys. **92**, 2710 (1990).

7 Taylor, E. M. Spain, and M. D. Morse, J. Chem. Phys. **92**, 2698 (1990).

8 E. M. Spain, J. M. Behrn, and M. D. Morse, J. Chem. Phys. **96**, 2511 (1992).

9 M. Doverstal, B. Lindgren, U. Sassenberg, C. A. Arrington, and M. D. Morse, J. Chem. Phys. **97**, 7087 (1992).

10 A. M. James, P. Kowalczyk, R. Fournier, and B. Simard, J. Chem. Phys. **99**, 8504 (1993).

11 A. M. James, P. Kowalczyk, and B. Simard, Chem. Phys. Lett **216**, 512 (1993).

12 A. M. James, P. Kowaiczyic, E. Langlois, M. D. Campbell, A. Ogawa, and B. Simard, J, Chem. Phys. **101**, 4485 (1994).

13 A. M. James, P. Kowalczyk, and B. Simard, J. Mol. Spectrosc. **164,** 260 (1994).

14 L. Song, A. Eychmuller and M. A. El-Sayed, J. Phys. Chem. **92,** 1005 (1988).

15 J. L. Elkind, F. D. Weiss. J. M. Alford, R. T. Laaksonen and R. E. Smalley. J. Chem. Phys. **88,** 5215 (1988).

16 M. R. Sakin, R. O. Brickman, D. M. Cox, and A. Kaldor. J. Chem. Phys. **88,** 3555 (1988).

17 M. R. Sakin, D. M. Cox and A. Kaldor. J. Chem. Phys. **91,** 5224 (1987).

18 S. Li, A. Eychmuller, R. J. St. Pierre, and M. A. El-Sayed J. Phys. Chem. **93,** 2485 (1989).

19 D. J. Trevor and A. Kaldor, J. Chem. Phys. **88,** 111 (1988).

20 S. Li and M. A. El-Sayed, Chem. Phys. Lett. **152,** 281 (1988).

21 S. Li and M. A. El-Sayed, J. Phys. Chem. Phys. **94,** 7907 (1990).

22 J. E. Fowler, A. Garcia, and J. M. Ugalde, J. Phys. Rev. A. **60,** 3058 (1999).

23 K. D. Ball, R. S. Berry, R. E. Kunz, F. Y. Li, and D. J. Wales, Science **271,** 963 (1996).

24 M. D. Morse, M. E. Geusic, J. R. Heath, and R. E. Smalley, J. Chem. Phys. **83,** 2293 (1985)

25 D. J. Trevor, R. L. Whetten, D. M. Cox, and A. Kaldor, 1. Phys. Chem. **107,** 518 (1985).

26 R. J. St. Pierre and M. A. El-Sayed, J. Phys. Chem. **91,** 763 (1987).

27 D. M. Cox, D. J. Trevor, R. L. Whetteri, and A. Kaidor, J. Phys. Chem. **92,** 421 (1988).

28 Y. Hamrick, S. Taylor, G. W. Lemire, Z.-W. Fu, J.-C. Shui, and M. D. Morse, J. Chem. Phys. **88,** 4095 (1988).

29 Y. M. Hamrick and M. D. Morse, J. Phys. Chem. **93**, 6494 (1989).

30 S. Nonose, Y. Sone, K. Onodera, S. Sudo, and K. Kaya, 1. Phys. Chem. **94**, 2744 (1990).

31 X. Ren, P. Hintz, and K. M. Ervin, J. Chem. Phys. **99**, 3575 (1993).

32 S. A. Mitchell, L. Lian, and P. A. Hackett, J. Chem. Phys. **103**, 5539 (1995).

33 S. A. Mitchell, D. Ni. Rayner, and P. A. Hackett, J. Chem. Phys. **104**, 4012 (1996).

34 A. Brces, P. A. Hackett, L. Lian, S. A. Nttchell, and D. M. Rayner, J. Chem. Phys. **108,** 5476 (1998).

35 E. K. Parks, K. P. Kerns, and S. J. Riley, J. Chem. Phys. **112**, 3384 (2000).

36 J. Conceigao, S. K. Loh, L. Lian, and P. B. Armentrout, J. Chem. Phys. **104**, 3976 (1996).

37 J. B. Griffin and P. B. Armentrout, J. Chem. Phys. **106**, 4448 (1997).

38 J. B. Griffin and P. B. Armentrout, 1. Chem. Phys. **107**, 5345 (1997).

39 J. B. Griffin and P. B. Armentrout, J. Chem. Phys. **108**, 8062 (1998).

40 J. B. Griffin and P. B. Armentrout, J. Chem. Phys. **108**, 8075 (1998).

41 S. K. Loh, L. Lian, and P. B. Arrnentrout,1. Am. Chem. Soc. **111**, 3167 (1989).

42 S. K. Loh, D. A. Hales, L. Lian, and P. B. Arinentrout, J. Chem. Phys. **90**, 5466 (1989).

43 D. A. Hales, L. Lian, and P. B. Armentrout, Int. J. Mass Spectrom. Ion Proc. **102**, 269 (1990).

44 L. Lian, C.-X. Su, and P. B. Armentrout, J. Chem. Phys. **97**, 4084 (1992).

45 C.-X. Su and P. B. Armentrout, J. Chem. Phys. **99**, 6506 (1993).

46 C.-X. Su, D. A. Hales, and P. B. Armentrout, J. Chem. Phys. **99**, 6613 (1993).

47 D. A. Hales, C.-X. Su, L. Lian, and P. B. Armentrout, J. Chem. Phys. **100**, 1049 (1994).

48 M. Aydin and John R. Lombardi, "*Photofragmentation spectroscopy of niobium dimer cation molecule and ab initio study on* Nb_2, Nb^-_2", submitted.

49 M. Aydin, D. M. Lindsay and John R. Lombardi, submitted.

50 M. B. Knickelbein and S. Yang, J. Chem. Phys. **93**, 5760 (1990).

51 M. B. Knickelbein, S. Yang, and S. J. Riley, J. Chem. Phys. **93**, 94 (1990).

52 S. Yang and M. B. Knickelbein, Z. Phys. D **31**, 199 (1994).

53 M. Knickelbein, J. Chem. Phys. **102**, 1 (1995).

54 G. M. Koretsky and M. B. Knickelbein, J. Chem. Phys. **106**, 9810 (1997).

55 J. Ho, K. M. Ervin, and W. C. Lineberger, J. Chem. Phys. **93**, 6987 (1990).

56 H. Wu, S. R. Desai, and L. -S. Wang, Phys. Rev. Lett. **76**, 212 (1996).

57 L.-S. Zheng, C. M. Karner, P. J. Brucat, S. H. Yang, C. L. Pettiette, M. J. Craycraft, and R. E. Smalley, J. Chem. Phys. **85**, 1681 (1986).

58 K. J. Taylor, C. L. Pettiette-Hall, 0. Cheshnovsky, and R. E. Smalley, J. Chem. Phys. **96**, 3319 (1992).

59 E. M. Spain and M. D. Morse, J. Phys. Chem. **96**, 2479 (1992).

60 L. M. Russon, S. A. Heidecke, M. K. Birke, J. Conceicao, P. B. Armentrout, and M. D, Morse, Chem. Phys. Lett. **204**, 235 (1993).

61 C. A. Arrington, T. Blume, M. D. Morse, M. Doverstil, and U. Sassenberg, J. Phys. Chem, **98**, 1398 (1994).

62 L. M. Russon, S. A. Heidecke, M. K. Birke, J. Conceicao, M. D. Morse, and P. B Armentrout. J. Chem. Phys. **100**, 4747 (1994).

63 J. D. Langenberg and M. D. Morse, J. Chem. Phys. **108**, 2331 (1998).

64 S. K. Nayak, B. K. Rao, S. N. Khanna, and P. Jena, Chem. Phys. Lett. **259**, 588 (1996).

65 M. B. Knickelbein and S. Yang, J. Chem. Phys. **93**, 1476 (1990).

66 R. L. Whetten, M. R. Zakin, D. M. Cox. D. J. Trevor and A. Kaldor. J. Chem. Phys. **85**, 1697 (1986).

67 M. R. Sakin, R. O. Brickman, D. M. Cox and A. Kaldor. J. Chem. Phys. **88** (1988).

68 J. Zhao, X. Chen, and G. Wang, Phys. Lett. A **214**, 211 (1966).

69 M. Andersson, H. Gronbeck, L. Holmgren, and A. Rosen, Laser Techniques for State-Selected and State-to-State Chemistry III, edited by J. W. Hepburn (SPIE International Society for Optical Engineering, Bellingham, WA, 1995), Vol. **2548**, p 157.]

70 L. Holmgren, M. Andersson, and A. Rosen, Surf. Sci. 331-333 (1995) 231.

71 H. Sellers, J. Phys. Chem. **94,** 1338 (1990).

72 L. Goodwin and D. R. Salahub, Phys. Rev. A. **47**, R774 (1993).

73 C. J. Humphreys and W. F. Meggers, J. Research Nat. Bur. Std. **34**, 515. RP1656 (1945).

74 J. Mack, Rev. Mod. Phys. **22**, 64 (1950).

75 J. M. Chase, C. A. Davies, J.J. R. Downey, D. J. Frurip, R. A. McDonald, and A. N. Syvrud, J. Phys. Chem. Ref. Data Suppl. **14**, 1 (1985).

76 A. D. Becke, Phys. Rev. A **38,** 3098 (1988).

77 C. Lee, W. Yang and R. G. Parr, Phys. Rev. B **37**, 785 (1988).

78 B. Miehlich, A. Savin, H. Stoll and H. Preuss, Chem. Phys. Lett. **157**, 200 (1989).

79 P. J. Hay and W. R. Wadt, J. Chem. Phys. **82**, 270 (1985).

80 W. R. Wadt and P. J. Hay, J. Chem. Phys. **82**, 284 (1985).

81 P. J. Hay and W. R. Wadt, J. Chem. Phys. **82**, 299 (1985).

CHAPTER IX

PHOTOFRAGMENTATION SPECTROSCOPY OF THE NIOBIUM TETRAMER CATION AND THE AB INITIO STUDY ON Nb_4, Nb_4^+

Abstract

The dissociation energy of the niobium tetramer cation molecule was measured by one color multiphoton fragmentation. The molecule was produced by laser vaporization of a niobium target rod and cooled in a helium supersonic expansion. The molecular beam containing niobium tetramer cation was interrogated in the range 16,060-16,380 cm^{-1}, using a pulsed dye laser to dissociate the molecule. The dissociation threshold for Nb_3^+-Nb product was observed at 16,115 ± 10 cm^{-1}. The previous collision-induced dissociation (CID) experiments and density functional (DF) calculations indicate that the multiphoton process should be a three-photon process at 16,115 cm^{-1}. Therefore, the dissociation energy is accurately determined to be 5.994 ± 0.001 eV. Calculated dissociation energies of Nb_4 and Nb_4^+ are in agreement with experiment.

IX.1. INTRODUCTION

Laser vaporization and molecular beam techniques have given tremendous scope to researchers investigating the chemistry and physics of transition metal clusters.[1-14] The partial occupation of d orbitals distinguishes transition metals from main group elements, and confers on them many of their special properties. Transition metal clusters present a particularly difficult challenge to our understanding of molecular structure due to strong electron correlation, and existence of many electronic states overlapping with one

another. The heavier transition metal clusters have the additional problem of large relativistic effects, which severely alter chemical bonding.

The niobium clusters have received special attention. The dissociation and ionization energies of Nb_2 have been reported to be 5.22 ± 0.28 eV [15] and 6.368 ± 0.001 eV,[12] respectively. Smalley and co-workers have studied photofragmentation with time-of-flight techniques and observed a small portion of the electronic spectrum of Nb_2^+.[1b] Hales *et al.*[15] have used collision-induced dissociation techniques to measure the bond energy of Nb_n^+, n = 2-11, where $D_o(Nb_2^+) = 5.87 \pm 0.19$ eV, $D_o(Nb_2^+\text{-}Nb) = 5.01 \pm 0.19$ eV, $D_o(Nb_3^+\text{-}Nb) = 6.00 \pm 0.30$ eV (5.90 ± 0.20 eV [16]). We have used photofragmentation with time-of-flight techniques to measure the dissociation energies of Nb_2^+,[14] Nb_3^+,[23] and Zr_2^+ [30] using a similar technique to Smalley et al.[1b]

We found a few theoretical works related with niobium clusters. In an investigation of the reaction of CO with small transition metal clusters, Anderson *et al.*[17] performed DFT calculations using a local spin density approximation to explore the characteristics of Nb_4. They found a near-tetrahedral structure of C_{3v} symmetry, a rhombic, and a square planer isomer. They reported that the C_{3v} structure had the lowest energy of the three, 15.7 kcal/mole below the rhombus, and 73.8 kcal/mol below the square. Goodwin and Salahub studied Nb_n, n = 2-7, using both local and nonlocal potentials.[18] With the local potentials, they found a singlet ideal tetrahedron to be the most stable isomer of Nb_4 and a doublet expanded ideal tetrahedron to be the most stable isomer of Nb_4^+. They also encountered a neutral triplet ideal parallelpiped, which was less stable than the singlet tetrahedron by 27.7 kcal/mole. Sellers, in 1990, used RECP-CISD methods and found planar C_{2v} minimum energy configurations for both Nb_4 and

Nb_4^+.[19] No mention was made of any nonplanar isomers and discussion was centered on the dimer/dimer character of this C_s structure. Fowler *et al.*[20] studied neutral and cationic niobium trimer and tetramer clusters by using several methods (PUHF, PMP2, PMP3, PMP4, CCSD, CCSD(T), and B3LYP). They reported that B3LYP with the SBJK basis set gave the best results for the dissociation energies of Nb_4 and Nb_4^+: $Nb_2(^3\Sigma_g^-)$-$Nb_2(^3\Sigma_g^-)$ = 4.35 eV, $Nb_3(^4A_1)$-$Nb(^4F)$ = 5.38 eV, $Nb_2^+(^4\Sigma_g^-)$-$Nb_2(^3\Sigma_g^-)$ = 5.27 eV, $Nb_3^+(^3A_1')$-$Nb(^4F)$=5.18 eV, and $Nb_3^+(^5A_1)$-$Nb(^4F)$ = 5.91 eV.[20] Section II presents a brief description of the experimental methods used in this study, and our results are given in Sec. III. In Sec. IV we will present the results of calculations, and concluding remarks are then given in Sec. V.

IX 2. MULTIPHOTON FRAGMENTATION SPECTRUM AND THE DETERMINATION OF DISSOCIATION ENERGY LIMIT OF $Nb_4^+ \rightarrow Nb_3^+ + Nb$.

We studied photofragmentation of the Nb_4^+ into three possible fragmentation pathways in the ranges 16,060-16,380, 16,800-17,100, and 17,700-18,000 cm^{-1}. We did not

$$Nb_4^+ \rightarrow Nb_3^+ + Nb \qquad 1$$

$$Nb_4^+ \rightarrow Nb_2^+ + Nb_2 \qquad 2$$

$$Nb_4^+ \rightarrow Nb^+ + Nb_3 \qquad 3$$

find any peaks in these regions. However, the multiphotofragmentation spectrum of the Nb_3^+ fragment ion exhibited a sharp rise in the background at 16,115 ± 10 cm^{-1} (Fig 9.1) As was mentioned earlier, the dissociation energy of the Nb_3^+-Nb has been found to be 6.00 ± 0.30 eV[15] and 5.90±0.20 eV [16] by Armentrout and co-workers. These results

suggest that the multiphoton process at the observed threshold (16,115 cm^{-1}) in the photofragmentation experiment should be a three-photon process. The threshold energy of the Nb_3^+-Nb fragment ion was then determined to be 5.994 ± 0.001 eV, in excellent agreement with both of the previous experimental results.[15,16] As will be discussed in Sec. V, the BLYP type density functional with an effective core potential basis set, predicted the dissociation energy of the Nb_4^+($^2B_1$) relative to the various spin states of the Nb and Nb_3^+($^3A_1'$) separated fragments limits (Table 9.2). The Nb_3^+($^3A_1$) + Nb($^4P;4d^35s^2$) fragment limit (5.917 eV) is more consistent with the experimental value instead of Nb_3^+($^3A_1$) + Nb($^4F;4d^35s^2$) fragment limit (5.439 eV). The calculation may underestimate the global energy of the both atomic energy levels, the ^4F and ^4P, of Nb.

This value may be combined with the known bond energies of Nb_2 (5.395 ± 0.056 eV, see Sec. IX. 4) and Nb_2^+-Nb(4.927 ± 0.001 eV)[23] and using the thermochemical cycle

$$\mathbf{D^o(Nb_2^+\text{-}Nb_2) = D^o(Nb_3^+\text{-}Nb) + D^o(Nb_2^+\text{-}Nb) - D^o(Nb_2)} \qquad 4$$

to give the bond energy of Nb_2^+-Nb_2 as $D^o(Nb_2^+\text{-}Nb_2)$ = 5.526 ± 0.056 eV in good agreement with theoretical prediction. Likewise, the bond energy of the Nb_4^+ relative to the Nb^+ + Nb_3 separated fragment limit can be readily calculated using a thermochemical cycle with the known ionization energy

$$\mathbf{D^o(Nb^+\text{-}Nb_3) = IE(Nb) - IE(Nb_3) + D^o(Nb_3^+\text{-}Nb)} \qquad 5$$

of the Nb(IE = 6.88 ± 0.0001 eV)[24] and the Nb_3 (IE = 5.81 ± 0.05 eV)[15] and using thermochemical cycle gives a value of 7.06 ± 0.05 eV for the bond energy of the Nb^+-Nb_3. The atomization energy (AE) of the Nb_4^+ may be calculated using the bond

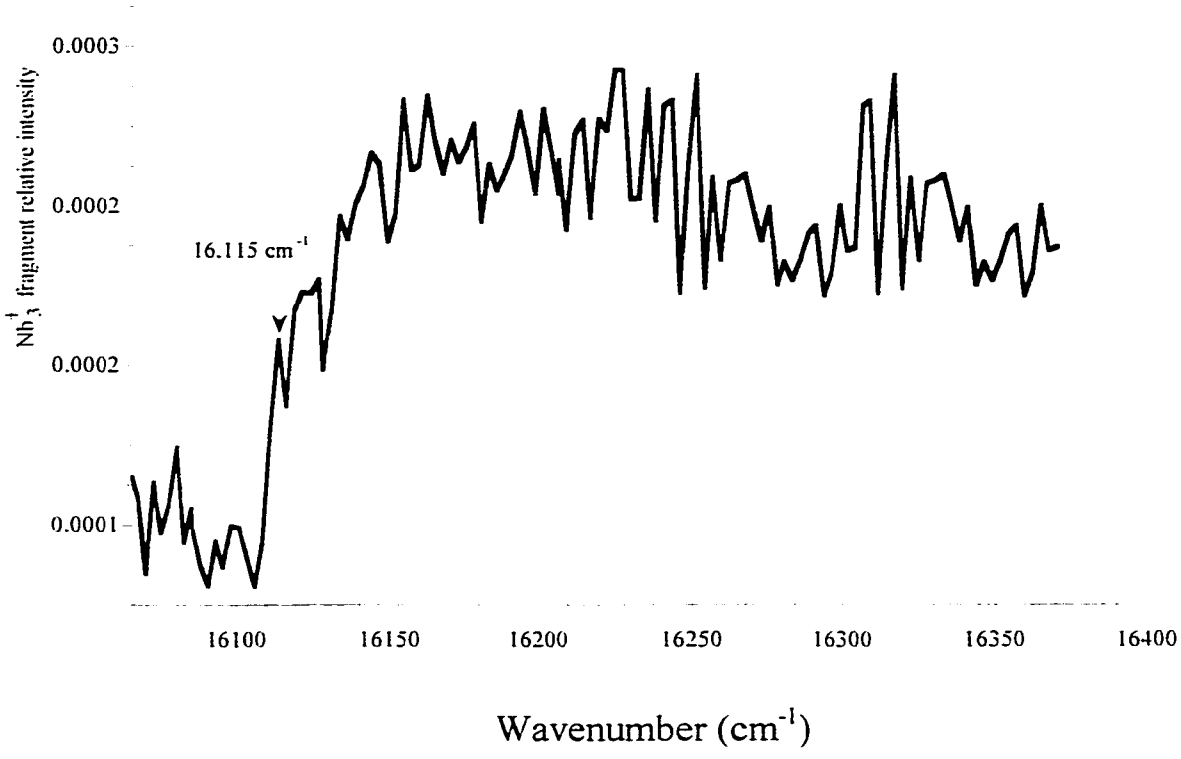

Figure 9.1. The multiphoton fragmentation spectrum of Nb_3^--Nb exhibits a sharp rise at 16.115 ± 10 cm^{-1}.

$$\mathbf{AE(Nb_4^+) = D^o(Nb_3^+\text{-}Nb) + D^o(Nb_2^+\text{-}Nb) + D^o(Nb_2^+)} \quad 6$$

energies of the Nb_3^+-Nb, Nb_2^+-Nb, and Nb_2^+ and the thermochemical cycle to give $AE(Nb_4^+) = 16.83 \pm 0.06$ eV.

The dissociation energies of Nb_4 and Nb_3 in possible fragment pathways can be readily calculated using bond energies of the Nb_2^+-Nb, Nb_2^+-Nb_2, and the literature values of the ionization energies of Nb_4(IE = 5.81 ± 0.05 eV) and Nb_3(IE =

$$D_o(Nb_2\text{-}Nb) = IE(Nb_3) - IE(Nb_2) + D_o(Nb_2^+\text{-}Nb) \quad 7$$

$$D_o(Nb_2\text{-}Nb_2) = IE(Nb_4) - IE(Nb_2) + D_o(Nb_2^+\text{-}Nb_2) \quad 8$$

$$D_o(Nb_3\text{-}Nb) = D_o(Nb_2\text{-}Nb_2) + D_o(Nb_2) - D_o(Nb_2\text{-}Nb) \quad 9$$

5.58 ± 0.056 eV) with the thermochemical cycle, Eq.7, 8, and 9, as $D_o(Nb_2\text{-}Nb) = 4.369 \pm 0.05$ eV, $D_o(Nb_2\text{-}Nb_2) = 4.798 \pm 0.056$ eV, and $D_o(Nb_3\text{-}Nb) = 5.824 \pm 0.056$ eV

IX 3. METHODS OF CALCULATIONS

IX 3.1. COMPUTING DETAIL

The BLYP type density functional method with the effective core potential basis set was performed on Nb, $Nb_2^{0/+}$, Nb_3^+, and $Nb_4^{0/+}$. The B3LYP is a computer code in Gaussian-94 and –98 programs. The calculations use Beck's 88 exchange functional,[25] in combination with LYP correlation functional, where LYP is the correlation functional of Lee, Yang, and Parr, which includes both local and non-local terms.[26] Los Alamos effective core potential (ECP) plus DZ, LANL2DZ computer code, basis set[27-29] was used in of all the density functional calculations. The wave function consists of linear

combination of the three s, three p, and two d (1s, 2s, 3s, 4p, 5p, 6p, 7d, and 8d are computer code in Gaussian94 and 98) atomic orbitals. 1s, 2s2p, 3s3p3d shells of niobium atoms were assigned to the core and treated by frozen core approximation. All calculations were performed on Decalpha and Intel Pentium II 450 MMX computers.

IX 3.2. RESULT OF CALCULATIONS

IX 3.2.1. Nb_4:

The lowest ground state of the neutral niobium tetramer cluster is predicted to be an $^1A_1$ state of tetrahedral (T_d) slightly distorted to C_{2v} symmetry. The calculated side bond lengths are given in Table 9.1. In the C_{2v} structure, there are three slightly different bond lengths. R_{12} bond is 0.001 Å longer and R_{34} bond is 0.001 Å shorter than its four equivalent bond lengths, $R_{13,14,23,24}$. Three fundamental vibrational frequencies of the $^1A_1$ state of niobium tetramer were predicted to be 167, 245, and 359cm^{-1} and the ratios of the fundamental frequencies are 1: 1.47: 2.15, which are close to the ratio of 1: $\sqrt{2}$: 2 expected for the regular tetrahedral structure. The DFs with ECP plus DZ (LANL2DZ) basis set predicted the dissociation energy of $Nb_4(^1A_1)$ with respect to the $Nb_2(^3\Sigma_g^-)$ + $Nb_2(^3\Sigma_g^-)$ separated fragment limit to be 4.367 eV in excellent agreement with value that estimated using thermochemical cycle, 4.369 eV (see Sec. IX. 2), and with the B3LYP prediction, 4.35 eV.[20] The calculated bond lengths, R_{13}, R_{34}, and $R_{13,14,23,24}$ are 0.0136 Å, 0.0128 Å, and 0.0135 Å longer than the B3LYP prediction (The B3LYP predicted the lowest ground state of Nb_4 to be $^1A_1$ state of T_d symmetry). The lowest triplet state of Nb_4 was predicted to be the $^3A_2$ state of C_{2v} symmetry (0.984 eV above the singlet ground state, $^1A_1$) with bond lengths: R_{13}= 2.6821 Å, R_{34} = 2.4832 Å, $R_{13,14,23,24}$ = 2.5656 Å, and dihedral angle: α(4-2-1-3) = 69.174°.

IX.3.2.2. Nb_4^+:

The ground state of the niobium tetramer cation cluster was predicted to be a $^2B_1$ state of C_{2v} symmetry with three slightly different bond lengths. R_{12} and R_{34} bond lengths are 0.0242 and 0.0773 Å shorter than its four equivalent bonds, $R_{13,14,23,24}$, respectively. We calculated the dissociation energy of $Nb_4^+(^2B_1)$ relative to the $Nb_2^+(^4\Sigma_g^-)$ + $Nb_2(^3\Sigma_g^-)$ and $Nb_3^+(^3A_1)$ + $Nb(^4F,\ 4d^35s^2;\ ^4P,\ 4d^35s^2)$ fragment limits. The calculations could not predict the global atomic energies of the ^4F and ^4P levels of Nb atom because of partially occupied d_0, $d_{\pm1}$, and $d_{\pm2}$ orbitals, but predicted true global energy for the ^6S ($4d^5$) atomic level. Therefore, we calculated the global energy of these states, $^4F(4d^35s^2)$ and $^4P(4d^35s^2)$, relative to the predicted global energy of the ^6S ($4d^5$) atomic level using the known energy difference between the ^6S-^4F (1.265 eV) and ^6S-^4P (0.787 eV)[30,31] atomic energy levels of Nb. The dissociation energy of $Nb_4^+(^2B_1)$, relative to the $Nb_2^+(^4\Sigma_g^-)$ + $Nb_2(^3\Sigma_g^-)$ fragment limit, is predicted to be 5.676 eV, in agreement with the CID measurement (5.50±0.21 eV)[15] and 5.526 ± 0.056 eV(from Eq. 4 in Sec. III). The calculated dissociation energy of $Nb_4^+(^2B_1)$ relative to the $Nb_3^+(^3A_1)$ + $Nb(^4F)$ separated fragment limit, 5.439 eV, is approximately 0.56 eV lower than the CID measurements, 5.90 ± 0.20 and 6.00 ± 0.30 eV,[15,16] and the photofragmentation measurement, 5.994 ± 0.001 eV. The $Nb_3^+(^3A_1)$ + $Nb(^4P)$ fragment limit (5.917 eV) is in good agreement with the experimental results (Table 9.2). Fowler and co-workers calculated the dissociation energy of Nb_4^+ leading to triplet Nb_3^+ with quartet Nb to be 5.18 eV and 5.91 eV for the quintet Nb_3^+ with quartet Nb.[20] They reported that the B3LYP prediction would agree with experiment if the threshold energy of Nb_3^+-Nb fragment was observed at a higher energy in the CID experiment.

Table 9.1. Calculated spectroscopic properties of Nb_4.

DFTs	**BLYP**	**Experiment**
Ground State	$^1A_1$	
R_{12}, Å	2.564	
$R_{13,14,23,24}$, Å	2.563	
R_{34}, Å	2.565	
$\alpha(4\text{-}2\text{-}1\text{-}3)^\circ$	70.886	
$D^\circ(Nb_4 : {}^1A_1)$, eV		
$Nb_2(^3\Sigma_g^-) + Nb_2(^3\Sigma_g^-)$	**4.809**	**4.798 ± 0.056** [a]
$Nb_3 + Nb$		**5.824 ± 0.056** [a]
		5.9±0.8 [24]
		6.26±72 [15]

[a] Estimated from the thermochemical cycle, see Sec. IX 2.

Table 9.2. Calculated spectroscopic properties of the doublet state of Nb_4^-.

DFTs	**BLYP**	**Expt.**
Ground State	$^2B_1$	
R_{12}, Å	2.576	
$R_{13,14,23,24}$, Å	2.600	
R_{34}, Å	2.523	
α(4-1-2-3)°	67.902	
$D^o(Nb_4^+, {}^2B_1)$, eV		
$Nb_2^+(^4\Sigma_g^-) + Nb_2(^3\Sigma_g^-)$	5.676	5.50 ± 0.21 [15]
		5.526 ± 0.056[a]
$Nb_3^-(^3A_1') + Nb(^4F)$	5.439	6.00 ± 0.30 [15]
$Nb_3^-(^3A_1') + Nb(^4P)$	5.917	5.90 ± 0.20 [16]
		5.994 ± 0.001 (present work)
$Nb^- + Nb_3$		7.06 ± 0.05 [a]
$AE(Nb_4^+)$, eV		16.83 ± 0.06
$IE(Nb_4)$, eV	5.618	5.64 ± 0.05 [33]
		5.80 ± 0.31 [15]
		$5.58_{-0.1}^{+0.0}$ [32]

[a] Calculated from the thermochemical cycle, Sec. IX 2.

The BLYP (this work) and B3LYP by Fowler and *et al.*[20] predicted two different ground states for the Nb_4, $^2B_1$ and $^2A_1$ in C_{2v} symmetry, and $^1A_1$ in T_d, slightly distorted to C_{2v}, and $^1A_1$ in T_d symmetry for the Nb_4^+, respectively. Our calculation (BLYP with LANL2DZ basis set) predicted the ionization energy of $Nb_4(^1A_1)$ to $Nb_4^+(^2B_1)$, 5.618 eV is in a remarkable agreement with experimental value, $IE(Nb_4) = 5.64 \pm 0.05$ eV,[33] within 0.4% error, while the B3LYP with the SBKJ basis set[20] predicted the ionization energy of $Nb_4(^1A_1)$ to $Nb_4^+(^2A_1)$, 5.37 eV, is in agreement with the experimental value within 4.8% error. Based in part on the ionization energy of Nb_4, the predicted ground state of the $Nb_4^{0/+}$ by the BLYP is more favored than the B3LYP predictions by Fowler *et al.*[20]

IX.3.2.3. CONCLUSIONS

The pervious experimental results suggest that the multiphoton fragmentation process should be a three-photon process at the dissociation threshold. The total energy of three photons gives a value of 5.994 ± 0.001 eV for the fragmentation of initially mass-selected Nb_4^+ ion to the Nb_3^+ + Nb separated fragment limit. This, $D(Nb_2^+\text{-Nb})$, may be combined with values of other properties, $IE(Nb) = 6.88 \pm 0.0001$ eV, [24] $IE(Nb_2) = 6.368 \pm 0.001$ eV,[12] $IE(Nb_3) = 5.81 \pm 0.05$ eV,[15] $D^o(Nb_2) = 5.395 \pm 0.056$ eV, $D^o(Nb_2^+\text{-Nb}) = 4.989 \pm 0.001$ eV,[23] to give $D^o(Nb_2^+\text{-}Nb_2) = 5.526 \pm 0.056$ eV, $D^o(Nb^+\text{-}Nb_3) = 7.06 \pm 0.05$ eV, and $AE(Nb_4^+) = 16.83 \pm 0.06$ eV.

The lowest ground state of Nb_4 was predicted to be an $^1A_1$ state of tetrahedral (T_d) symmetry, slightly distorted to C_{2v} symmetry. The calculated dissociation energy of $Nb_4(^1A_1)$ relative to the $Nb_2(^3\Sigma_g^-)$ + $Nb_2(^3\Sigma_g^-)$ fragment limit, was underestimated

approximately 1 ± 0.8 eV, but better than the B3LYP predicted value.[20] The calculated bond lengths are in agreement with other theoretical predictions.

The lowest ground state of Nb_4^+ is predicted to be $^2B_1$ state of C_{2v} symmetry is in disagreement with the B3LYP prediction, $^2A_1$ state of C_{2v} symmetry. The calculated dissociation energy of Nb4+ relative to the $Nb_3^+(^3A_1)$+Nb(^{4}P) fragment limit is good agreement with experimental result, but to the $Nb_3^+(^3A_1)$+Nb(^{4}F) fragment limit is approximately 0.5 eV lower than the experimental value.

The calculated dissociation energy of $Nb_4^+(^2B_1)$ to the $Nb_2^+(^3\Sigma_g^-)$ + $Nb_2(^3\Sigma_g^-)$ and ionization energy (5.618 eV) of $Nb_4(^1A_1)$ to $Nb_4^+(^2B_1)$ are in agreement with experimental value within 1.5%, 3%, and 0.9% errors, respectively (Table 9.2). The predicted dissociation energy of $Nb_4(^1A_1)$ with respect to $Nb_2(^3\Sigma_g^-)$ + $Nb_2(^3\Sigma_g^-)$ fragment limit is in excellent agreement with the value predicted from the thermochemical cycle and other theoretical predictions. So far we have not found any experimental information about the lowest ground state and geometric properties of $Nb_4^{0/+}$ and the states of the fragments for comparison with theoretical predictions.

IX. 4. BOND ENERGY OF THE Nb_2

The dissociation energy of neutral niobium dimer was determined to be 5.22 ± 0.28 eV[16] and 5.22 ± 0.31[15] eV by Hales and co-workers using thermochemical cycle. Gupta and Gingerich[21] measured $D^o(Nb_2)$ with a high-temperature mass spectrometric method, finding 5.57±0.41 eV using the second-law method and 5.22 ± 0.02 eV by a concurrent third-law determination, but when using calculated values for the molecular constants and an electronic degeneracy consistent with V_2, the third-law value was revised to $D^o(Nb_2)$ = 4.86 ± 0.02 eV.[22] This value may be combined with the known

ionization energy of Nb (6.88 ± 0.0001 eV)[24] and bond energy of the Nb_2^+(5.907 ± 0.056 eV[14] or 5.87 ± 0.12 eV[15]) and using thermochemical cycle to give a value of

$$\mathbf{IE(Nb_2) = IE(Nb) + D^o(Nb_2) - D^o(Nb_2^+)} \qquad 10$$

5.833 ± 0.056 eV for the $D^o(Nb_2^+)$ = 5.907 ± 0.056 eV or 5.87 ± 0.12 eV for the $D^o(Nb_2^+)$ = 5.87 ± 0.12 eV is 0.5 eV lower than the resonant two-photon ionization (R2PI) measurement, 6.368 ± 0.001 eV.[12]

We calculated the bond energy of Nb_2 to be 5.395 ± 0.056 eV using

$$\mathbf{D^o(Nb_2)=IE(Nb_2)+D^o(Nb_2^+)-IE(Nb)} \qquad 11$$

thermochemical cycle (with the value of IE(Nb) = 6.88 ± 0.0001 eV,[24] $IE(Nb_2)$ = 6.368 ± 0.001 eV,[12] and $D^o(Nb_2^+)$ = 5.907 ± 0.056 eV[14]) in agreement with the CID results.[15,16]

Chapter IX References

1 (a) L. –S. Zheng, P. J. Brucat, C. L. Pettiette, S. Yang, and R. E. Smalley, J. Chem. Phys. **83** (1985) 4273; (b) P. J. Brucat, L. –S. Zheng, C. L. Pettiette, S. Yang, and R. E. Smalley, J. Chem. Phys. **83** (1985) 4273;

2 L.N. Ding, M. A. Young, P. D. Kleiber, and W. D. Stwalley, J. Phys. Chem. **97** (1993) 2181.

3 J. B. Hopkins, P. R. R. Langridge-Smith, M. D. Morse, and R. E. Smalley, J. Chem. Phys. **78** (1983) 1627.

4 P. R. R. Langridge-Smith, M. D. Morse, G. P. Hansen, R. E. Smalley, and A. J. Merer, J Chem. Phys. **80** (1984) 593.

5 Taylor, G. W. Lemire, Y. M. Hamrick, Z. Fu, and M. D. Morse, J. Chem. Phys. **89** (1988) 5517.

6 Taylor, E. M. Spain, and M. D. Morse, J. Chem. Phys. **92** (1990) 2710.

7 Taylor, E. M. Spain, and M. D. Morse, J. Chem. Phys. **92** (1990) 2698.

8 E. M. Spain, J. M. Behrn, and M. D. Morse, J. Chem. Phys. **96** (1992) 2511.

9 M. Doverstal, B. Lindgren, U. Sassenberg, C. A. Arrington, and M. D. Morse, J. Chem. Phys. **97** (1992) 7087.

10 A. M. James, P. Kowalczyk, R. Fournier, and B. Simard, J. Chem. Phys. **99** (1993) 8504.

11 A. M. James, P. Kowalczyk, and B. Simard, Chem. Phys. Lett. **216** (1993) 512.

12 A. M. James, P. Kowaiczyic, E. Langlois, M. D. Campbell, A. Ogawa, and B. Simard, J, Chem. Phys. **101** (1994) 4485.

13 A. M. James, P. Kowalczyk, and B. Simard, J. Mol. Spectrosc. **164** (1994) 260.

14 M. Aydin. D. M. Lindsay and John R. Lombardi. "Photofragmentation spectroscopy of niobium dimer cation molecule and ab inito study on Nb_2, Nb_2^+", submitted to J. Phys. Chem.

15 D. A. Hales, L. Lian, and P. B. Armentrout, Int. J. Mass Spectrom. Ion Proc. **102** (1990) 269.

16 S. K. Loh, L. Lian, and P. B. Arrnentrout,1. Am. Chem. Soc. **111** (1989) 3167.

17 M. Andersson. H. Gronbeck. L. Holmgren. and A. Rosen. Laser Techniques for State-Selected and State-to-State Chemistry III, edited by J. W. Hepburn (SPIE International Society for Optical Engineering. Bellingham. WA. 1995). Vol. 2548, p 157.

18 L. Goodwin and D. R. Salahub. Phys. Rev. A. **47** (1993) R774.

19 H. Sellers J. Phys. Chem. **94** (1990) 1338.

20 J. E. Fowler. A. Garcia. and J. M. Ugalde. J. Phys. Rev. A. **60** (1999) 3058.

21 S. K. Gupta and K. A. Gingerich, J. Chem. Phys. **70** (1979) 5350.

22 M. D. Morse. Chem. Rev. **86** (1986) 1049.

23 M. Aydin and John R. Lombardi, submitted.

24 J. M. W. Chase, C. A. Davies, J. J. R. Downey, D. J. Frurip, R. A. McDonald, and A. N. Syvrud. J. Phys. Chem. Ref. Data Suppl., **14** (1985)1.

25 A. D. Becke, Phys. Rev. A. **38** (1988) 3098.

26 (a) C. Lee, W. Yang and R. G. Parr, Phys. Rev. B **37** (1988) 785.

(b) B. Miehlich, A. Savin, H. Stoll and H. Preuss, Chem. Phys. Lett. **157** (1989) 200.

27 P. J. Hay and W. R. Wadt, J. Chem. Phys. **82** (1985) 270.

28 W. R. Wadt and P. J. Hay, J. Chem. Phys. **82** (1985) 284.

29 P. J. Hay and W. R. Wadt, J. Chem. Phys. **82** (1985) 299.

30 C. J. Humphreys and W. F. Meggers, J. Research Nat. Bur. Std. **34**, 515, RP1656 (1945).

31 J. Mack, Rev. Mod. Phys. **22** (1950) 64.

32 R. L. Whetten, M. R. Zakin, D. M. Cox, D. J. Trevor, and A. Kaldor, J. Chem. Phys. **85** (1986) 1697.

33 M. B. Knickelbein and S. Yang, J. Chem. Phys. **93**(1990) 5750.

CHAPTER X

ELECTRONIC STRUCTURE OF NIOBIUM DIMER CATION

ABSTRACT

Resonant multiphoton fragmentation spectra of niobium dimer cation (Nb_2^+) have been obtained by utilizing laser vaporization of a Nb metal target. Ions are mass-selected with a time-of-flight mass spectrometer followed by a mass gate, then fragmented with a pulsed dye laser, and resulting fragment ions are detected with a second time-of-flight reflectron mass spectrometer and multichannel plate. Photon resonances are detected by monitoring ion current as a function of fragmentation laser wavelength. A rich, but complex spectrum of the cation is obtained. The bands display a characteristic triplet structure which may be interpreted as involving transitions between a ground $^4\Sigma^-_{\pm1/2}$ and several excited $^4\Pi$ states. These are the A $^4\Pi_\Omega(\pi_u^3 1\sigma_g^2 2\sigma_g^1 \delta_g^3)$, B $^4\Pi_\Omega(\pi_u^3 1\sigma_g^2 2\sigma_g^2 \delta_g^2)$, C $^4\Pi_\Omega(\pi_u^3 1\sigma_g^2 2\sigma_g^1 \delta_g^3)$, and the D $^4\Pi_\Omega(\pi_u^3 1\sigma_g^2 2\sigma_g^1 \delta_g^3)$. In addition various vibrational progressions are identified. Spin orbit parameters, vibrational frequencies and anharmonic corrections are obtained.

X. 1. INTRODUCTION

The spectra of the diatomic molecules of transition metals are of particular interest both theoretically and experimentally due to their complex band structures. This is caused by the existence of partially occupied d-orbitals. The ionic and neutral transition metal clusters have received special interest since advent of techniques such as laser vaporization of a solid target, chemical reactions in laser-produced plasmas, supersonic

cooling, mass-selected resonant two-photon ionization, laser-induced fluorescence, and collision-induced dissociation.[1-29]

The clusters of $Nb^{0/+}$ and related compounds have been examined under numerous experimental conditions and several diatomic species including niobium have shown multiplet structures. The first detailed account of the NbO spectrum by V. R. Rao[30] was a classification of its visible emission bands into three systems which are denoted A(420-510 nm), B(510-610 nm), and C(610-640 nm). In 1952, V. R. Rao presented a rotational analysis of the A system and suggested that the lower state is a quartet. In 1953, V. R. Rao investigated various bands in the 600-770 nm regions and obtained vibrational assignments. The structure of the bands indicated the A and C bands share a common lower state. The ESR work of Brom *et al.*[33] confirmed that the ground state was $X^4\Sigma^-$ In 1987, however, the A and C bands were assigned to be due to $^4\Sigma^- - {}^4\Sigma^-$ transitions by Femenias *et al.*[22] from a rotationally resolved experiment. Still other rotationally resolved analyses of the B bands by Femenias *et al.*[22] and Adam *et al.*[21] indicate that the B band is due to a $^4\Pi - X^4\Sigma^-$ transition, and that the ground state and excited state arise from the electronic configuration $\ldots 2\sigma\ ^1\delta^2$ and $\ldots \delta\ ^2\pi$, respectively.

In a rotationally resolved electronic spectrum of NbC Simard *et al.*,[27] using laser-induced florescence (LIF) and resonant two-photon ionization (R2PI) spectroscopy, identify several bands in the 13,500-18,00 cm^{-1} regions. Evidence is presented that the transitions are to the $B^2\Pi_{1/2}(10\sigma 5\pi^4 11\sigma^2 2\delta 6\pi)$, C $^2\Pi_{1/2}(10\sigma 5\pi^4 11\sigma^2 2\delta 6\pi)$, and D $^2\Pi_{1/2}(10\sigma^2 5\pi^4 11\sigma^2 6\pi)$ states which originate from the same lower ground state $X^2\Delta_{3/2}(10\sigma 5\pi^4 11\sigma^2 2\delta 6\pi)$. They report that the A and B bands extrapolate to the second and third lowest atomic energy limits of Nb and C separated fragments. B and C bands

are observed to be about 906 and 1052 cm^{-1} above the A band. Simard *et al.*[27] also observed three other systems which terminate to the same B/C/D $^2\Pi_{1/2}$, but originate from the $A^2\Sigma^+$ low-lying state (830 cm^{-1} above the ground state) as well as many unassigned weak transitions. Their density functional calculations predicted ground state and low-lying state in agreement with the their experimental observations, but the DF predicted the $^2\Pi$ - $^2\Delta$ transition to be about 5,000 cm^{-1} above the observed (0,0) band and $A^2\Sigma^+$ low-lying state is predicted to be 3,400 cm^{-1} above the $X^2\Delta$ ground state.

A rotationally resolved electronic spectra of Nb_2 Simard *et al.*[24] identifies several bands and assigns as A, B, C, D, and E near 14,650, 14,705, 14,828, 14,833, and 14,844 cm^{-1}, respectively, which originate from the ground state, $X^3\Sigma^-_g(\ldots\sigma_g^2\delta_g^2)$.

Smalley *et al.*[19] have used a resonant two-color photofragmentation experiment to investigate a portion of the electronic spectrum of Nb_2^+. They found an intense, somewhat irregular pattern totally uncharacteristic of a diatomic species. At that time no attempt was made to assign the spectrum. In 1994, a ESR study on Nb_2^+ in argon matrices by Weltner *et al.*[20] suggested that ground state of Nb_2^+as a $^2\Sigma^+_g$, arising from the electronic configuration $\ldots2\sigma_g^1\delta_g^2$. A theoretical work using the density functional method by James *et al.*[25] predicted ground state of Nb_2^+ to be $^4\Sigma^-_g$, arising from the same electronic configuration $\ldots2\sigma_g^1\delta_g^2$. They reported the second-order spin-orbit interaction between the ground state $^4\Sigma^-_{\pm1/2}$ and low lying (T_0 = 3,900 cm^{-1}) state $^2\Sigma^+_{\pm1/2}$ to be 142 cm^{-1}.

Balasubramanian and Zhu[44] have used complete active space multiconfiguration self-consistent field (CASMSCF) followed by the multireference singles + doubles

configuration interaction (MRSDCI) to investigate spectroscopic properties of the Nb_2 and Nb_2^+. The authors report the 45 low-lying states within 26,115 cm^{-1} for the Nb_2 and 18 low-lying states for the Nb_2^+ within 18,000 cm^{-1}. Their calculations predict the lowest ground states of the niobium dimer cation to be a $X^4\Sigma_g^-$ symmetry, arising from the electronic configuration $...1\sigma_g^2 1\pi_u^4 2\sigma_g^1 \delta_g^2$, with the spectroscopic constants R_e = 2.091 Å, ω_e = 430 cm^{-1}, and D_e = 4.58 eV. The authors recommended that the dissociation energy of the Nb_2^+ would be 5.4 ± 0.4 eV on the basis of higher-order correlation effects. They reported four low-lying $^4\Pi_u$ states: $^4\Pi_u$ (61.8 % of $1\sigma_g^2 1\pi_u^3 1\sigma_g^1 \delta_g^3$, 7.6% of $1\sigma_g^2 1\pi_u^3 1\sigma_g^1 \delta_g^1 \delta_u^2$, and 2.5 % of $1\sigma_g^1 1\pi_u^3 1\sigma_g^1 \delta_g^4$) with the T_e = 4,501 cm^{-1}, R_e = 2.264 Å, ω_e = 339 cm^{-1}, $^4\Pi_u$(II) (68.0% of $1\sigma_g^2 1\pi_u^3 1\sigma_g^2 \delta_g^2$, 4.7% of $1\sigma_g^2 1\pi_u^3 1\sigma_g^2 \delta_u^2$, and 3.0% of $1\sigma_g^2 1\pi_u^3 1\sigma_g^1 \delta_g^3$) with the T_e = 5.383 cm^{-1}, R_e = 2.270 Å, ω_e = 419 cm^{-1}, $^4\Pi_u$(III) (21.7 % of $1\sigma_g^1 1\pi_u^3 1\sigma_g^1 \delta_g^4$, 32.2% of $1\sigma_g^2 1\pi_u^3 1\sigma_g^1 \delta_g^3$, 6.2 % of $1\sigma_g^1 1\pi_u^3 1\sigma_g^1 \delta_g^2 \delta_u^2$, etc.) with the T_e = 16,328 cm^{-1}, R_e = 2.322 Å, ω_e = 288 cm^{-1}, and $^4\Pi_u$(IV) (31.0% of $1\sigma_g^1 1\pi_u^3 1\sigma_g^1 \delta_g^4$, 26.4% of $1\sigma_g^2 1\pi_u^3 1\sigma_g^1 \delta_g^3$, 8.0% of $1\sigma_g^1 1\pi_u^3 1\sigma_g^1 \delta_g^2 \delta_u^2$, etc.) with the T_e = 16,882 cm^{-1}, R_e = 2.284 Å, ω_e = 381 cm^{-1}.

In the present study, we carry out a resonant multi-photon fragmentation experiment to obtain the optical spectrum of Nb_2^+. We observe the same features reported by Smalley[19] and extend this investigation from the 15,000 up to 20,000 cm^{-1} regions. We find multiple bands in the 16,000-18,500 cm^{-1} region and threshold energy of the Nb_2^+.[43] We also performed several density functional calculations to predict the lowest ground state and second-order spin-orbit coupling in the ground state.[43] Our calculated ground state symmetry as well as the observed multiple bands suggest that ground state to be $^4\Sigma_g^-$ ($2\sigma_g^1 \delta_g^2$), which is in agreement with the previous theoretical predictions.[25,44] The

predicted ground state symmetry $^4\Sigma^-_g(2\sigma_g{}^1\delta_g{}^2)$ of Nb_2^+ is supported by the experimentally determined ground state electronic configurations of the NbO and Nb_2, $...2\sigma\ {}^1\delta^{\ 2}$ ($^4\Sigma^-$ symmetry) and $...2\sigma_g{}^2\delta_g{}^2$ ($^3\Sigma^-_g$ symmetry), respectively. Further support comes from the observed multiplet structure of the spectrum. Allowed transitions are to states which are of necessity at least quartet in spin multiplicity. With the aid of the previous experimental works and density functional calculations, we present a proposed assignment of this spectrum in terms of transitions from a $X^4\Sigma^-_g$ ($...2\sigma_g{}^1\delta_g{}^2$) ground state to several overlapping excited states of symmetry $^4\Pi_u(\pi_u{}^3 1\sigma_g{}^2 2\sigma_g{}^1\delta_g{}^3)$ and $^4\Pi_u(\pi_u{}^3 1\sigma_g{}^2 2\sigma_g{}^2\delta_g{}^2)$.

X. 2. ONE-COLOR MULTIPHOTON FRAGMENTATION

Fig. 10.1(a-b) shows the resonant three-photon dissociation spectrum of Nb_2^+ obtained by detection of the Nb^+ fragment as a function of incident photon energy, taken at a resolution of 1.3 cm^{-1} in range 16,000-18,450 cm^{-1}. Our results do not provide sufficient resolution to observe rotational lines. The spectrum shows several strong and weak bands, characterized by about 8 strong features centered around 16,127, 17,065, and 17,891cm^{-1} and as many relatively weak features centered around 16,565, 17,525, and 18,378 cm^{-1}. A comparison of the spectrum from Smalley *et al.*[15] to our (Fig. 10.1b), indicates complete agreement over this limited range (the intensities of the peaks at 18,040, 18,065, and 18,085 in our spectra are relatively weaker than corresponding peak intensities in the spectrum from Smalley *et al.*[15]). Their region of observation is from 17,850 cm^{-1} to 18,200 cm^{-1}. A comparison of intensities, however, does indicate that our beam expansion conditions were rotationally hotter than Smalley *et al.* which was ~20K as indicated in Ref. 19. The absorption spectrum of Nb_2^+ from the R2IP experiment is evidence that the absorption spectrum of Nb_2^+ in our experiment is due to a resonance in

the first photon. In any case, we presume the temperature is sufficiently low, and that sufficient collisions take place in our beam that all transitions arise from the lowest state.

Several calculations predict[25,43,44] the ground state of Nb_2^+ to be $X^4\Sigma^-_g$ $(...2\sigma_g^1\delta_g^2)$ symmetry with vibrational frequency 436-474 cm^{-1}. There is no first order spin-orbit splitting in a $^4\Sigma^-_g$ state, but in each case this state may be split into $\Omega = \pm 1/2$ and $\Omega = \pm 3/2$ components by a second-order spin-orbit coupling between the $^4\Sigma^-_{\pm 1/2}$ with a nearby low-lying $^2\Sigma^+_{\pm 1/2}$. Such coupling displaces the $\Omega = \pm 1/2$ components to lower energy, leaving the $\Omega = \pm 3/2$ component unchanged. The second-order spin-obit coupling in the ground state, $X^4\Sigma^-_{1/2}(2\sigma_g\delta_g^2)$, and first order spin-orbit coupling in the $^4\Pi_u(1\pi_u^3 1\sigma_g^2 2\sigma_g^2 \delta_g^2)$ and $^4\Pi_u(1\pi_u^3 1\sigma_g^2 2\sigma_g^1 \delta_g^3)$ excited states are derived in the Sec. X. 4. The spin-orbit splitting between the $\Omega = \pm 1/2$ and $\pm 3/2$ components of $X^4\Sigma^-_\Omega$ ground state is due to the second-order spin-orbit interaction between $X^4\Sigma^-_{1/2}$ and a near by low-lying $^2\Sigma^+_{1/2}$ states is 119 cm^{-1} for the calculated unperturbed energy difference $\Delta E^o = E^o(X^4\Sigma^-_{1/2}) - E^o(^2\Sigma^+_{1/2}) = 4{,}946$ cm^{-1} by the BLYP method. The BVWN DF method gives a value of $\Delta E^o = 3.408$ cm^{-1} and the spin-orbit splitting in Nb_2^+ is estimated to be 166 cm^{-1}. The BVWN5 method gives 109 cm^{-1}, $\Delta E^o = 5402$ cm^{-1}. In any case, the splittings are sufficiently large to allow us to presume that all transitions originate from a $X^4\Sigma^-_{\pm 1/2}$ state.

There are only two types of dipole allowed electronic transitions: either to $^4\Sigma^-_u$ or to $^4\Pi$ states, and we analyze this spectrum with this in mind. It is clear from the irregular nature of the spectrum that it represents a region of several overlapping transitions. For a single electronic state we might expect vibrational spacings of approximately 400-500

cm^{-1}, and several distinct sets of lines can be distinguished with progressions in 486 cm^{-1} and 500 cm^{-1}. These transitions involve clear multiplet structure. In most cases, sets of three lines can be distinguished. Thus, these cannot involve transitions to $^4\Sigma^-_u$. Transitions from the $\Omega = \pm 1/2$ ground state are allowed to only three of the four components of a $^4\Pi$ state (i.e. to $\Omega = \pm 1/2$ and +3/2, the case (c) selection rule is $\Delta\Omega = 0, \pm 1$). Spacings within these triplets are typically 90-235 cm^{-1}, in the range we might expect for spin-orbit coupling. The estimated first-order spin-orbit separation between the Ω and Ω -1 components of $A^4\Pi_u(1\pi_u^3 1\sigma_g^2 2\sigma_g^1 \delta_g^3)$ and $B^4\Pi_u(1\pi_u^3 1\sigma_g^2 2\sigma_g^2 \delta_g^2)$ excited states from the average of the corresponding atomic spin-orbit parameters, $A^4\Pi_\Omega - A^4\Pi_{\Omega-1} = 1/3[2a_\delta - a_\pi]$ should be 88 cm^{-1} and $B^4\Pi_\Omega - B^4\Pi_{\Omega-1} = 1/3[a_\pi]$ should be 231 cm^{-1}, respectively, for the $a_\delta = 478.2$ and $a_\pi = 692.5$, in good agreement with the observed values of 90-235 cm^{-1}), see Sec. X. 4.

The spectrum may be assigned by invoking at least four excited states. These are the $A/C/D^4\Pi_\Omega(1\pi_u^3 1\sigma_g^2 2\sigma_g^1 \delta_g^3)$, $B^4\Pi_\Omega(1\pi_u^3 1\sigma_g^2 2\sigma_g^2 \delta_g^2)$. Only in the case of the B and D states can a clear origin be established, while the intensities for the A and C states require that we utilize a relative quantum number v which remains to be established. The origin of the $B(\Omega = -1/2) \leftarrow X(\Omega = +1/2)$ state is 16,568 cm^{-1} while that of the $D(\Omega = -1/2) \leftarrow X(\Omega = +1/2)$ is presumed to be 17,768 cm^{-1}. Table 10.1 lists our assignments, which must be regarded as tentative in the absence of rotational resolution. States A, B, and C display clear triplet structure from which we can extract experimental values for the spin-orbit splittings. The vibrational progressions lead to values for ω_e and $\omega_e x_e$ for each of the states, which are listed in Table 10.2 along with the other spectral parameters.

The observation of four nearby $^4\Pi_u$ excited states is interesting but not surprising since three $^4\Pi_u(1\pi_u^3 1\sigma_g^2 2\sigma_g^1 \delta_g^3)$ excited states arise from the lowest atomic limit Nb(^{6}D, $4d^4 5s$) + Nb^+(^{5}D, $4d^4$), second lowest atomic limit Nb(^{4}F, $4d^3 5s^2$) + Nb^+(^{5}D, $4d^4$), lying 1,449 cm^{-1} (spin-orbit average) above the lowest energy limit, and third atomic limit Nb(^{6}D, $4d^4 5s$) + Nb^+(^{5}F, $4d^3 5s$), lying 2,639 cm^{-1} (spin-orbit average) above the lowest energy limit. The distances between A, C, and D excited states, $C^4\Pi_{3/2}$ - $A^4\Pi_{3/2}$ =17,117 – 15,708 = 1,409 cm^{-1} and $D^4\Pi_{3/2}$ - $A^4\Pi_{3/2}$ =18,013 – 15,708 =2,305 cm^{-1} are in excellent agreement with the difference between corresponding atomic limits, 1449 and 2639 cm^{-1}. This approach explains almost all observed lines in the spectrum. There are only a few transitions which cannot be assigned using this scheme.

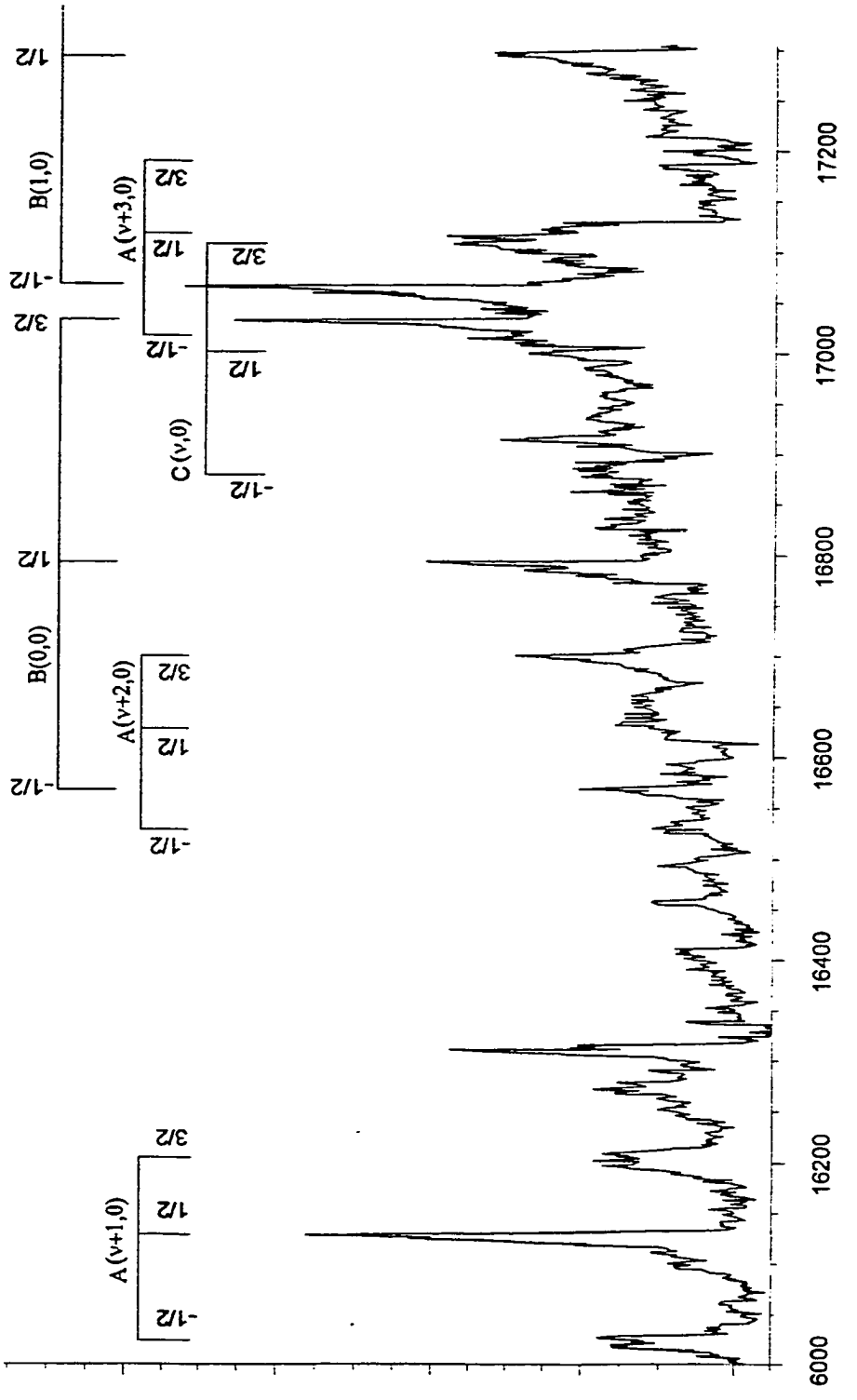

Figure 10.1a. Low resolution one-color multiphoton spectra of Nb_2^+ in the 16,000-17,300 cm^{-1} region.

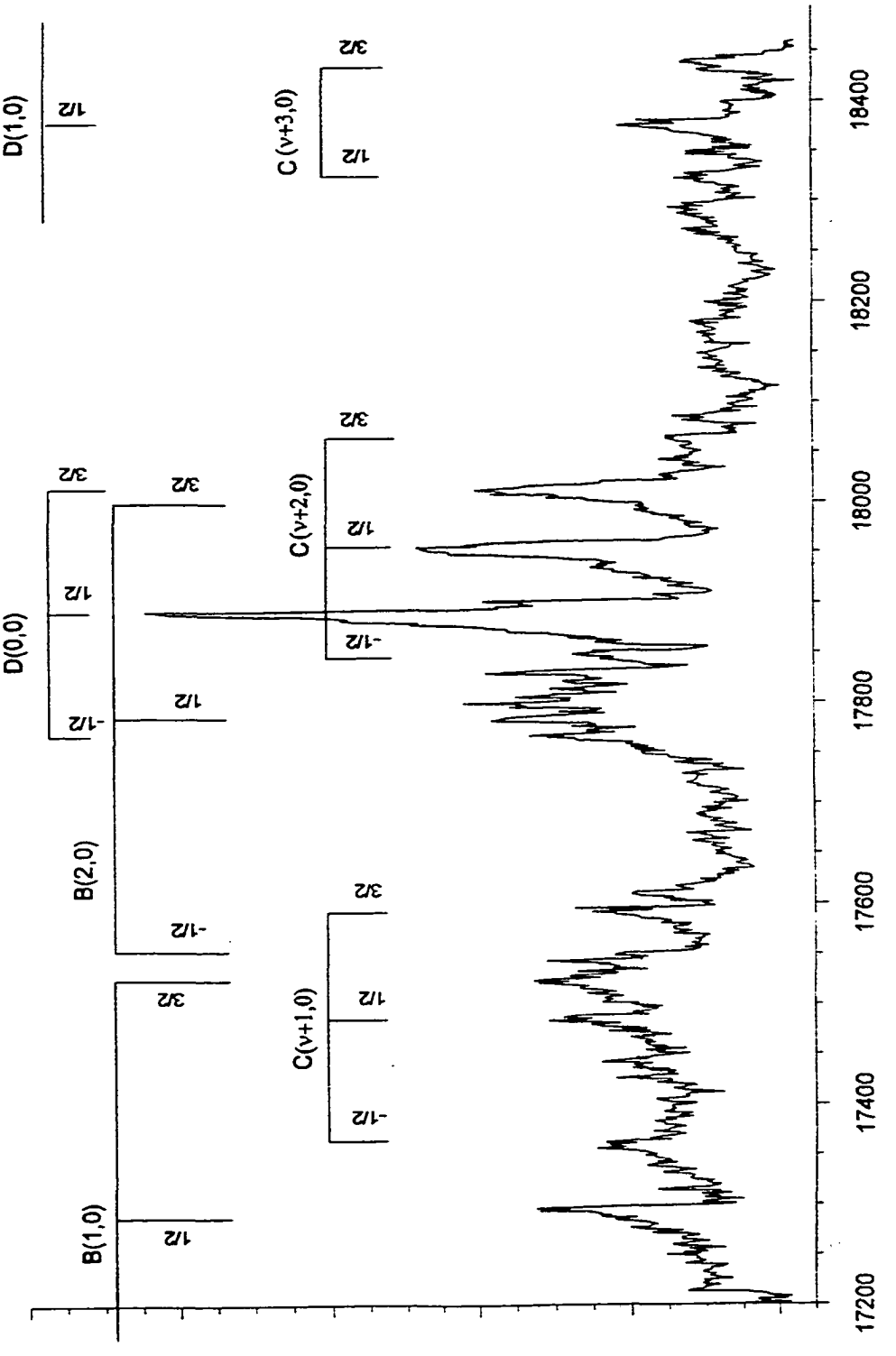

Figure 10.1b. Low resolution one-color multiphoton spectra of Nb_2^+ in the 17,200-18,450 cm^{-1} region.

Table 10.1. The assignments of vibronic bands of Nb_2^+ in the 15,700-18,500 cm^{-1} region. All assigned transitions are originating from the $X^4\Sigma^-_{\pm/2}$ ground state. A/C/D$^4\Pi_u$ and B$^4\Pi_u$ excited states arise from the $1\pi_u^3 1\sigma_g^2 2\sigma_g^1 \delta_g^3$ and $1\pi_u^3 1\sigma_g^2 2\sigma_g^2 \delta_g^2$ configurations, respectively.

Wave number (cm-1)	assignment		
15.708	$A^4\Pi_{3/2}$(v,0)		
16.018			
16,027	$A^4\Pi_{1/2}$(v+1,0)		
16,100	$A^4\Pi_{1/2}$ (v+1,0)		
16,127			
16,198			
16203	$A^4\Pi_{3/2}$ (v+1,0)		
16208			
16,277			
16,310			
16,456			
16,495			
16,530	$A^4\Pi_{1/2}$ (v+2,0)		
16,568		$B^4\Pi_{1/2}$ (0.0)	
16.700	$A^4\Pi_{3/2}$ (v+2,0)		
16.705			
16.793		$B^4\Pi_{1/2}$ (0.0)	
16.883			$C^4\Pi_{1/2}$ (v,0)
16.914			
17,000			$C^4\Pi_{1/2}$ (v,0)
17,017	$A^4\Pi_{1/2}$ (v+3,0)		
17.030		$B^4\Pi_{3/2}$ (0,0)	
17,065		$B^4\Pi_{1/2}$ (1,0)	
17,093			
17,105			$C^4\Pi_{3/2}$ (v,0)
17,117	$A^4\Pi_{1/2}$ (v+3,0)		
17,187	$A^4\Pi_{3/2}$ (v+3,0)		
17,293		$B^4\Pi_{1/2}$ (1,0)	
17,364			$C^4\Pi_{1/2}$ (v+1,0)
17,365			
17,483			$C^4\Pi_{1/2}$ (v+1,0)
17,524		$B^4\Pi_{1/2}$ (1,0)	
17,542			
17,551		$B^4\Pi_{1/2}$ (2,0)	
17,590			$C^4\Pi_{3/2}$ (v+1,0)
17596			

Continuation of Table 10.1.

Wave number (cm-1)	assignment		
17,609	$A^4\Pi_{1/2}$ (v+4,0)		
17,768			$D^4\Pi_{1/2}$ (0,0)
17,785		$B^4\Pi_{1/2}$ (2,0)	
17,800			
17,815			
17,830			
17,848			$C^4\Pi_{1/2}$ (v+2,0)
17,891			$D^4\Pi_{1/2}$ (0,0)
17,901			
17,934			
17,958			$C^4\Pi_{1/2}$ (v+2,0)
17,998	$A^4\Pi_{1/2}$ (v+5,0)		
18,005		$B^4\Pi_{3/2}$ (2,0)	
18,013			$D^4\Pi_{3/2}$ (0,0)
18,042		$B^4\Pi_{1/2}$ (3,0)	
18,066			$C^4\Pi_{3/2}$ (v+2,0)
18,088	$A^4\Pi_{1/2}$ (v+5,0)		
18,268			
18270		$B^4\Pi_{1/2}$ (3,0)	
18,298			
18,325			$C^4\Pi_{1/2}$ (v+3,0)
18,377			$D^4\Pi_{3/2}$ (1,0)
18,437			$C^4\Pi_{1/2}$ (v+3,0)
18,501			$D^4\Pi_{3/2}$ (1,0)

Where the C and $D^4\Pi_{1/2}(1\pi_u^3 1\sigma_g^2 2\sigma_g^1 \delta_g^3)$ associate with the second and third lowest atomic limits since $A^4\Pi_{1/2}(1\pi_u^3 1\sigma_g^2 2\sigma_g^1 \delta_g^3)$ associate with the lowest atomic limit. $B^4\Pi_\Omega(\delta_g^2 2\pi_u)$ is expected to associate with the lowest atomic limit.

Table 10.2. The spectroscopicaly determined parameters of Nb_2^+ in cm^{-1}.

$^4\Pi_\Omega$	A(v,0)	B(0,0)	C(v,0)	D(0,0)
$^4\Pi_{1/2}$	16,027(5)	16,568(3)	16,883(3)	17,768
$^4\Pi_{1/2}$	16,127(2)	16,793(3)	17,000(2)	17,891
$^4\Pi_{3/2}$	16,203(5)	17,030(3)	17,105(2)	18.013
$A_{S.O.}$	89(5)	231(6)	111(5)	122(5)
ω_e	502(3)	496(5)	485(5)	487
$\omega_e\chi_e$	1.7(6)	1.9(5)	1.8	

Where A is the spin-orbit constant and is determined from the average of the first-order spin-orbit width between $\Omega = -1/2$ and $\Omega = 3/2$ components of the $^4\Pi_{1/2}(1\pi_u^3 1\sigma_g^2 2\sigma_g^1\delta_g^3)$ and $^4\Pi_{1/2}(1\pi_u^3 1\sigma_g^2 2\sigma_g^2\delta_g^2)$ excited states, respectively, ($^4\Pi_{3/2} - {}^4\Pi_{1/2} = 2A_{S.O.}$). ω_e and $\omega_e\chi_e$ are a average of the vibrational frequency and unharmonicity for A/B/C/D $^4\Pi_\Omega$, $\Omega = 3/2, 1/2$, and $-1/2$, excited sates, respectively. The uncertainties are due to the broadened band widths.

X. 3. DISCUSSION

Even though the ESR study on the Nb_2^+ in argon matrices suggests that the ground state symmetry of the Nb_2^+ is $^2\Sigma_g^+$, arising from the electronic configuration $...1\sigma_g^2\pi_u^4 2\sigma_g^1\delta_g^2$, according to Hund's rules and the taking exchange energy into account, the electronic configuration $...2\sigma_g^1\delta_g^2$ indicates that a $^4\Sigma_g^-$ state is the more likely ground state and the $^2\Gamma_g$ and $^2\Sigma_g^+$ are the second and third lowest symmetry, respectively. This is in agreement with the theoretical predictions.[25,43] The ground state electronic configuration of the Nb_2^+ may be compared to those of NbO, VNb^+, and V_2^+. The rotational assignment gives the lowest ground state of the NbO to be $^4\Sigma^-$, arising from the electronic configuration $...2\sigma\delta^2$.[22] In resonant two-photon ionization experiments of the V_2, VNb, and Nb_2 by Simard *et al.*,[25] two thresholds were observed from the photo-ionization spectrum of the molecules V_2 and VNb via $\Omega = 0$ and $\Omega = 1$. They assigned the ground state of the V_2^+ and VNb^+ from the threshold via $\Omega = 1$ to be $^4\Sigma_g^-$, arising from the electronic configuration $...2\sigma_g^1\delta_g^2$.,[25] with second-order spin-orbit splitting of 20(3) and 82(3) cm^{-1}. These experimentally determined ground states of the molecules NbO, V_2^+, VNb^+, and the observed multiple bands in the electronic spectra of the Nb_2^+ in the gas phase suggest that the transitions in the 16,000-18,500 cm^{-1} regions provide evidence that the ground state of the Nb_2^+ may be $^4\Sigma_g^-$, arising from the electronic configuration $...2\sigma_g^1\delta_g^2$. We believe that the observed transitions originate in the same ground state under the expectation that the all populated vibrational and low lying electronic states are thermally deactivated to the lowest ground state due to the long delay time about 30 μs between the supersonic expansion and the photofragmentation. Based on the observed band structures in the NbO[21,22,30-32] and NbC [27] it is suggested that

the observed multiple bands are most likely due to the quartet-quartet transitions which are assigned as A/C/D$^4\Pi_\Omega(1\pi_u^3 1\sigma_g^2 2\sigma_g^1 \delta_g^3) \leftarrow X^4\Sigma^-_{\pm 1/2}(1\pi_u^4 1\sigma_g^2 2\sigma_g^1 \delta_g^2)$ and $B^4\Pi_\Omega(1\pi_u^3 1\sigma_g^2 2\sigma_g^2 \delta_g^2) \leftarrow X^4\Sigma^-_{\pm 1/2}(1\pi_u^4 1\sigma_g^2 2\sigma_g^1 \delta_g^2)$ transitions with selection rule $\Delta\Omega = 0, \pm 1$. It is very difficult to determine whether a $^4\Sigma^-_\Omega(1\pi_u^4 1\sigma_g^2 \delta_g^2 2\sigma_u) \leftarrow X^4\Sigma^-_g$ lies in this spectral region. Density functional calculations predict [43] only a vertical orbital transition $2\sigma_u \leftarrow 2\sigma_g$, $^4\Sigma^-_u(1\pi_u^4 1\sigma_g^2 \delta_g^2 1\sigma_u) \leftarrow X^4\Sigma^-_g$, to occur in this region, at about 17,000 cm^{-1}. The calculation predicts six $^4\Pi_u$ low lying states in Nb_2^+. Two of them, resulting from the δ_g^2 and $2\sigma_g^1 \leftarrow 1\pi_u^4$ transitions, are predicted to be 11,369 and 11,496 cm^{-1} above the $X^4\Sigma^-_g$ ground state, respectively. The second two $^4\Pi_u$ excited states (resulting from two-electron excitations. $^4\Pi_u(1\pi_u^3 1\sigma_g^1 2\sigma_g^2 \delta_g^3)$ and $^4\Pi_u(1\pi_u^3 1\sigma_g^1 2\sigma_g^1 \delta_g^4)$ where the ground state configuration is $1\pi_u^4 1\sigma_g^2 2\sigma_g^1 \delta_g^2$) lie around 18.300 cm^{-1} (these two transitions are not accessible in our one-color multiphoton spectral regions because the one photon energy is in the range 16,000-18,500 cm^{-1}). The other two $^4\Pi_u$ excited states ($2\pi_u \leftarrow 2\delta_g$ and $2\pi_u \leftarrow 2\sigma_g$) are predicted to be around 28,000 cm^{-1}.

It is not possible to assign the complex band structure utilizing the $^4\Sigma^-_u \leftarrow X^4\Sigma^-_g$ transition. Therefore, we feel that even though the density functional calculations underestimate the frequency of the $^4\Pi_u \leftarrow X^4\Sigma^-_g$, $\delta_g \leftarrow 1\pi_u$ and $2\sigma_g \leftarrow 1\pi_u$. The separations between the bands around 16,127 cm^{-1}, assigned A band, 17,065 cm^{-1}, assigned as B band, and 17,891 cm^{-1}, assigned as D band are consistent with the estimated first-order spin-orbit splitting between $^4\Pi_\Omega(1\pi_u^3 1\sigma_g^2 2\sigma_g^2 \delta_g^2)$ and $^4\Pi_\Omega(1\pi_u^3 1\sigma_g^2 2\sigma_g^1 \delta_g^3)$ excited states. The reason the density functional methods underestimate the orbital-orbital transitions might be due to the exchange-correlation

energy and multiconfigurational interactions contribution in the $^4\Pi_u$ excited states. For example, as we will discuss in the Sec. X. 4, Langridge-Smith *et al.*[28] determined the $^3\Pi_{0.u} \leftarrow X^4\Sigma^-_{0.g}$ transition in V_2 at 14,306 cm^{-1} by rotationally resolved gas-phase electronic spectrum of the V_2, using the technique of resonant two photon ionization spectroscopy. They did not mention the electronic configuration of the $^3\Pi_u$ state. Our calculations[43] predict the following transitions: $A^3\Pi_u(1\pi_u^3 1\sigma_g^2 2\sigma_g^2\ \delta_g^3) \leftarrow X^3\Sigma^-_g$ $(1\pi_u^4 1\sigma_g^2 2\sigma_g^2 \delta_g^2)$ transition to be 10,000 cm^{-1} and $B^3\Pi_u(1\pi_u^3 1\sigma_g^2 2\sigma_g^1\ \delta_g^4) \leftarrow X^3\Sigma^-_g$ $(1\pi_u^4 1\sigma_g^2 2\sigma_g^1 \delta_g^4)$ transition to be 11,865 cm^{-1}. As discussed in Sec. X.4, the experimentally observed first-order spin-orbit coupling indicate that the observed $^3\Pi_u \leftarrow$ $X^3\Sigma^-_g$ transition must be due to $A^3\Pi_u \leftarrow X^3\Sigma^-_g$ transition and our calculation predicted to be 4,300 cm^{-1} lower than experimental values (14,306 cm^{-1}). In Sec. X. 4, we roughly estimated a value for $T_e(^4\Pi_u)$ of the Nb_2^+ to be 16,446 cm^{-1}, by scaling the calculated T_e value of Nb_2^+ and the calculated and experimental $T_e(^3\Pi_u)$ values of the V_2, in good agreement with our assignment.

Balasubramanian and Zhu[44] calculated 18 low-lying states for the Nb_2^+ within18,000 cm^{-1}, using the CASMSCF followed by MRSDCI methods. Their calculations predict four low-lying $^4\Pi_u$ states: $^4\Pi_u$ with the T_e = 4,501 cm^{-1}, $^4\Pi_u$(II) with the T_e = 5,383 cm^{-1}, $^4\Pi_u$(III) with the T_e = 16,328 cm^{-1}, and $^4\Pi_u$(IV) with the T_e = 16,882 cm^{-1}. The last two $^4\Pi_u$ excited states here lie in the spectral region, but it should be noted that these transitions are most likely two-electron excitations, see introduction for the electronic configurations. As mentioned above, the two-electron excitation is not possible in one-color multiphotofragmentation experiment in this spectral region.

The observed peaks in the present work are red degraded, which indicates that the bond lengths in the excited states are longer than the bond length in the ground state. We have also observed a set of dissociation thresholds for Zr_2^+, Nb_2^+, Nb_3^+, and Nb_4^+ from the fragmentation of the Zr_2^+, Nb_2^+, Nb_3^+, and Nb_4^+ [43] into their fragments, using the present experimental techniques, and will report on these in a subsequent publication.

X. 4. FIRST- and SECOND-ORDER SPIN-ORBIT COUPLING

The second order spin-orbit interaction between the ground state and low-lying state excited state can be treated as a simple two-state perturbation problem. The relevant Slater-type wave functions[25] for the $\Omega = 1/2$ spin-orbit components of the two state are:

$$X^4\Sigma^-_{1/2}\,[\delta_g^2(^3\Sigma_g)\otimes 2\sigma_g] = 3^{-1/2}\,|\,\delta^-\delta^-\sigma\,(\beta\alpha\alpha + \alpha\beta\alpha + \alpha\alpha\beta)> \qquad 1$$

$$^2\Sigma^+_{1/2}\,[\delta_g^2(^1\Sigma_g)\otimes 2\sigma_g] = 2^{-1/2}\,|\,\delta^-\delta^-\sigma\,(\beta\alpha\alpha - \alpha\beta\alpha)> \qquad 2$$

Using these expressions to derive the spin-orbit matrix element, we obtain the result

$$H_{12} = < X^4\Sigma^-_{1/2}\,|\,\Sigma_i a_i L_i S_i\,|\,^2\Sigma^-_{1/2} > = (8/3)^{1/2}[a_\delta] \qquad 3$$

The corresponding non-trivial solution of the eigenvalue equation for this system or second-order spin-orbit splitting, $\Delta = E^o_1(^4\Sigma^-_{1/2}) - E_1(^4\Sigma^-_{1/2})$, can be given:

$$E^o_2(^2\Sigma^+_{1/2}) - E^o_1(^4\Sigma^-_{1/2}) = -\Delta + H^2_{12}/\Delta \qquad 4$$

Based in part on the calculated unperturbed energy difference $\Delta E^o = E^o(X^4\Sigma^-_{1/2}) - E^o(^2\Sigma^+_{1/2})$ between the $X^4\Sigma^-_g$ and a near by low lying $^2\Sigma^+_g$ states, the second-order spin-

orbit splitting in the ground state, $\Delta = E_1(X^4\Sigma^-_{3/2}) - E_1(X^4\Sigma^-_{1/2}) = 119\ cm^{-1}$ for the $\Delta E^0 = E^0(X^4\Sigma^-_{1/2}) - E^0(^2\Sigma^+_{1/2}) = 4{,}946\ cm^{-1}$ by the BLYP, 166 cm^{-1} for the $\Delta E^0 = 3{,}408\ cm^{-1}$ by the BVWN, and 109 cm^{-1} for the $\Delta E^0 = 5{,}402\ cm^{-1}$ by the BVWN5 method.

In the $A^4\Pi_u(1\pi_u^3 1\sigma_g^2 2\sigma_g^2 \delta_g^2)$ and $B^4\Pi_u(1\pi_u^3 1\sigma_g^2 2\sigma_g^1 \delta_g^3)$ excited states, we derived the following relevant Slater-type wave functions[40] and corresponding first-order spin-orbit coupling (see Table 10.3):

$$A^4\Pi_{5/2}(\delta_g^2\pi_u) = |\delta_g^2 2\pi_u\ (\alpha\alpha\alpha)> \qquad 5a$$

$$A^4\Pi_{3/2}(\delta_g^2\pi_u) = 3^{-1/2}\,|\delta_g^2 2\pi_u\ (\alpha\alpha\beta + \beta\alpha\alpha + \alpha\beta\alpha)> \qquad 5b$$

$$H_{so} = < A^4\Pi_{5/2}\,|\,\textstyle\sum_i a_i L_i S_i\,|\,A^4\Pi_{5/2}> = (1/2)[a_\pi] \qquad 6$$

$$A^4\Pi_{5/2} - A^4\Pi_{-3/2} = (1/3)a_\pi \qquad 7$$

and

$$B^4\Pi_{5/2}(\sigma_g\,\delta_g\pi_u) = |\sigma\delta^+\pi_u^-(\alpha\alpha\alpha)> \qquad 8a$$

$$B^4\Pi_{3/2}(\sigma_g\delta_g\pi_u) = 3^{-1/2}\,|\sigma\delta^+\pi^-\ (\alpha\alpha\beta + \beta\alpha\alpha + \alpha\beta\alpha)> \qquad 8b$$

$$H_{so} = < B^4\Pi_{5/2}\,|\,\textstyle\sum_i a_i L_i S_i\,|\,B^4\Pi_{5/2}> = (1/2)[2a_\delta - a_\pi] \qquad 9$$

$$B^4\Pi_{5/2} - B^4\Pi_{-3/2} = (1/3)[2a_\delta - a_\pi] \qquad 10$$

Where $a_\delta(Nb_2^+)$, 478.2 cm^{-1}, can be readily estimated from average of the atomic spin-orbit constant corresponding to $a_\delta(Nb;\ 4d^4 5s,\ ^6D_J) = 454.3$ [cm-1 41] and $a_\delta(Nb^+;\ 4d^4,\ ^6D_J) = 502\ cm^{-1}$.[42] We did not find any value for the spin-orbit constants a_π in Nb_2^+. So. we

roughly estimated a value for the $a_\pi(Nb_2^+; {}^4\Pi_u)$ by scaling the value from the $a_\pi(V_2; A^3\Pi)$.

The total spin-orbit width of the $A^3\Pi$ of V_2 [28] is reported to be 80 cm^{-1}, but the authors did not mention to the electronic configuration. If $A^3\Pi$ arises from the electronic configuration $1\pi_u^3 2\sigma_g^2 2\sigma_g^1 \delta_g^4$ or $1\pi_u^3 2\sigma_g^1 2\sigma_g^2 \delta_g^4$, then the total spin-orbit width would be $a_\pi(V_2; A^3\Pi)$ = 80 cm^{-1}, which is not possible because $a_\pi(VO; B^4\Pi)$ = 193.5 cm^{-1}.[39] Therefore, $A^3\Pi(V_2)$ must arise from the $1\pi_u^3 2\sigma_g^2 2\sigma_g^2 \delta_g^3$ and then the total spin-orbit width is $A^3\Pi_2 - A^3\Pi_0 = [2a_\delta - a_\pi]$ = 80 cm^{-1}. This gives a value for $a_\pi(V_2; A^3\Pi)$ = 210 cm^{-1} by using the known value of $a_\delta(V; {}^6D, 4d^4 5s)$ = 145 cm^{-1}.[25]

In Nb_2^+, $a_\pi(Nb_2^+; A^4\Pi)$ can be obtained by scaling the value from corresponding $a_\pi(V_2; A^3\Pi)$, $a_\delta(Nb_2^+; X^4\Sigma_g^-)$, and $a_\delta(V_2; X^3\Sigma_g^-)$ using the following equation:

$$\begin{aligned} a_\pi(Nb_2^+; A^4\Pi) &= a_\pi(Nb_2; A^3\Pi) \times a_\delta(Nb_2^+; X^4\Sigma_g^-)/a_\delta(Nb_2; X^3\Sigma_g^-) \\ &= a_\pi(V_2; A^3\Pi) \times a_\delta(Nb_2^+; X^4\Sigma_g^-)/a_\delta(V_2; X^3\Sigma_g^-) \qquad 11 \\ &= 210 \times 478.2/145 = 692.5\ cm^{-1} \end{aligned}$$

Now, we can readily calculate the spin-orbit width between the Ω = 3/2 and Ω = 1/2 components of $A^4\Pi(\delta_g^2 2\pi_u)$; $A^4\Pi_{5/2} - A^4\Pi_{3/2} = (1/3)a_\pi = (1/3) \times 692.5 = 231\ cm^{-1}$ and that for $B^4\Pi(2\sigma_g \delta_g 2\pi_u)$, $B^4\Pi_{5/2} - B^4\Pi_{3/2} = (1/3)[2a_\delta - a_\pi] = (1/3)(2 \times 478.2 - 692.5) = 88\ cm^{-1}$.

Our calculations predicted the $\delta_g \leftarrow 1\pi_u$, $^3\Pi\ (1\pi_u^3 1\sigma_g^2 2\sigma_g^1\ \delta_g^2 2\pi_u^1) \leftarrow X^3\Sigma_g^-$ $(1\pi_u^4 1\sigma_g^2 2\sigma_g^2\ \delta_g^2)$ transition to be 10,000 cm^{-1}, T_0(exp.[28])=14,306 cm^{-1} and the predicted $^3\Sigma_u^-\ (1\pi_u^4 1\sigma_g^2 2\sigma_g^1 \delta_g^2 1\sigma_u^1) \leftarrow X^3\Sigma_g^-$ transition is 12,645 cm^{-1}, T_0(exp.[28]) =11,811 cm^{-1} for the V_2. These indicate that while density functional calculations with the effective

core potential (ECP) plus double zeta (DZ) basis set underestimate $\delta_g^3 \leftarrow 1\pi_u^3$ transition and predict the $\sigma_u \leftarrow 1\sigma_g$ transition in agreement with the experimental value within 800 cm^{-1} error.

Therefore, we fell that the DFs underestimate the $\delta_g^3 \leftarrow 1\pi_u^3$ transition (T_e = 11,496 cm^{-1}) in Nb_2^+. A value of the $T_0(^4\Pi_u; \delta_g^3 \leftarrow 1\pi_u^3)$ = 16,446 cm^{-1} for the Nb_2^+ can be roughly estimated by scaling the calculated value of the $T_0(^4\Pi_u; \delta_g^3 \leftarrow 1\pi_u^3)$ transition in Nb_2^+ and the calculated and experimental values of $T_0(^3\Pi_u; \delta_g^3 \leftarrow 1\pi_u^3)$ transition in V_2.

$T_0(Nb_2^+) = T_0(Nb_2^+)_{calc} x T_0(V_2)_{exp} / T_0(V_2)_{calc}$ = (11,496x14,306)/10,000 cm^{-1}

= 16,446 cm^{-1},

in excellent agreement with the observed multiple bands in Nb_2^+, in the 16,000-18,500 cm^{-1} region (this work) .

Table 10.3. The selected first- and second-order spin-orbit coupling for various electronic states of the Nb_2^+.

Electronic state	Slater-Type Wave Function	First-order spin-orbit splitting	Secod-order spin-orbit splitting
$X^4\Sigma^-_{3/2g}$; $\ldots 2\sigma_g\delta_g^2$	$\lvert\sigma\delta^+\delta^-(\alpha\alpha\alpha)\rangle$	0	
$^2\Sigma^-_{1/2}(\delta_g^2(^3\Sigma^-_g)\otimes 2\sigma_g)$	$6^{-1/2}\lvert\sigma\delta^+\delta^-(2\beta\alpha\alpha - \alpha\alpha\beta - \alpha\beta\alpha)\rangle$		0
$^2\Sigma^+_{1/2}(\delta_g^2(^1\Sigma^+_g)\otimes 2\sigma_g)$	$2^{-1/2}\lvert\sigma\delta^+\delta^+(\beta\alpha\beta-\beta\beta\alpha)\rangle$		$(8/3)^{1/2}[a_\delta(\ ^1\Sigma^+_g)]$
$^4\Sigma^-_{3/2u}$; $\ldots 2\sigma_g\delta_g\delta_u$	$\lvert\delta^+\delta^-\sigma(\alpha\alpha\alpha)\rangle$	0	
$^2\Sigma^-_{1/2u}(2\sigma_g\delta_g(^3\Delta_g)\otimes\delta_u)$	$6^{-1/2}\lvert 2\sigma_g\delta_g\delta_u(2\alpha\alpha\beta - \beta\alpha\alpha - \alpha\beta\alpha)\rangle$		0
$^2\Sigma^+_{1/2u}$; $(2\sigma_g\delta_g(^1\Delta_g)\otimes\delta_u)$	$2^{-1/2}\lvert 2\sigma_g\delta_g\delta_u(\beta\alpha\beta-\alpha\beta\beta)\rangle$		$(8/3)^{1/2}[a_\delta(\ ^1\Sigma^+_g)]$
$^4\Sigma^-_{3/2u}$; $\ldots\ \delta_g^2 1\sigma_u$	$\lvert\delta^+\delta^-\sigma(\alpha\alpha\alpha)\rangle$	0	
$^2\Sigma^-_{1/2u}(\delta_g^2(^3\Sigma_g)\otimes 1\sigma_u)$	$6^{-1/2}\lvert\delta^+\delta^-\sigma(2\alpha\alpha\beta - \beta\alpha\alpha\beta\alpha)\rangle$	0	0
$^2\Sigma^+_{1/2u}$; $(\delta_g^2(^1\Sigma_g)\otimes 1\sigma_u)$	$2^{-1/2}\lvert\delta^+\delta^-\sigma(\beta\alpha\beta-\alpha\beta\beta)\rangle$	0	$-(8/3)^{1/2}[a_\delta(\ ^1\Sigma^+_g)]$
$A^4\Pi_{5/2}$; $\ldots 2\sigma_g\delta_g\pi_u$	$\lvert\sigma\delta^+\pi^-(\alpha\alpha\alpha)\rangle$	$3^{-1}[2a_\delta-a_\pi]$	
$a_1{}^2\Pi_{3/2}$;$\ldots 2\sigma_g\delta_g(^3\Delta_g)\otimes\pi_u$	$6^{-1/2}\lvert\sigma\delta^+\pi^-(2\alpha\alpha\beta - \beta\alpha\alpha - \alpha\beta\alpha)\rangle$	$3^{-1}[4a_\delta+a_\pi]$	$-(2/9)^{-1/2}[\ a_\delta+\ a_\pi]$
$a_2{}^2\Pi_{3/2}[2\sigma_g\delta_g(^1\Delta_g)\otimes\pi_u]$	$2^{-1/2}\lvert\sigma\delta^+\pi^-(\alpha\beta\alpha - \beta\alpha\alpha)\rangle$	$-a_\pi$	$(4/6)^{-1/2}[a_\delta]$
$B^4\Pi_{5/2}$; $\ldots\delta_g^2 2\pi_u$	$\lvert\sigma\delta^+\pi(\alpha\alpha\alpha)\rangle$	$3^{-1}[a_\pi]$	
$b_1{}^2\Pi_{3/2}[\delta_g^2(^3\Sigma^-_g)\otimes\pi_u]$	$6^{-1/2}\lvert\delta^+\delta^-\pi(2\alpha\alpha\beta - \beta\alpha\alpha - \alpha\beta\alpha)\rangle$	$-3^{-1}[a_\pi(^3\Sigma^-_g)]$	$-(2/9)^{-1/2}[\ a_\pi(^3\Sigma^-_g)]$
$b_2{}^2\Pi_{3/2}[\delta_g^2(^1\Sigma^+_g)\otimes\pi_u]$	$2^{-1/2}\lvert\delta^+\delta^-\pi(\alpha\beta\alpha - \beta\alpha\alpha)\rangle$	$-2^{-1}[a_\pi(^1\Sigma^+_g)]$	$(8/3)^{-1/2}[a_\delta(^1\Sigma^+_g)]$
$X'{}^2\Gamma_{9/2.g}[\delta_g\delta_g 2\sigma_g]$	$2^{-1/2}\lvert\delta^+\delta^+\sigma(\alpha\beta\alpha -\beta\alpha\alpha)\rangle$	0	
$^2\Gamma_{9/2.u}[\delta_g\delta_g 1\sigma_u]$	$2^{-1/2}\lvert\delta^+\delta^+\sigma(\alpha\beta\alpha -\beta\alpha\alpha)\rangle$	0	
$^4\Gamma_{11/2.u}[\sigma_g\delta_g\delta_u]$	$\lvert\sigma\delta^+\delta^-(\alpha\alpha\alpha)\rangle$	$(4/3)a_\delta$	
$^2\Gamma_{7/2.u}[\delta_g\delta_u\ (^3\Gamma_u)\otimes\sigma_g]$	$6^{-1/2}\lvert\ \delta^+\delta^+\sigma(2\alpha\alpha\beta - \beta\alpha\alpha - \alpha\beta\alpha)\rangle$	$(4/3)\ [a_\delta(^3\Gamma_u)]$	
$^2\Gamma_{7/2.u}[\delta_g\delta_u\ (^1\Gamma_u)\otimes\sigma_g]$	$2^{-1/2}\lvert\sigma\delta^+\delta^+(\alpha\beta\alpha - \beta\alpha\alpha)\rangle$	0	
$^4\Phi_{9/2.u}[2\sigma_g\delta_g\pi_u]$	$\lvert\sigma\delta^+\pi^+(\alpha\alpha\alpha)\rangle$	$(1/3)[2a_\delta+a_\pi]$	
$^2\Phi_{7/2.u}[2\sigma_g\delta_g(^3\Delta_g)\otimes\pi_u]$	$6^{-1/2}\lvert\sigma\delta^+\pi^+(2\alpha\alpha\beta - \beta\alpha\alpha - \alpha\beta\alpha)\rangle$	$(1/3)[4a_\delta-a_\pi]$	

Chapter X References

1 T. G. Dietz, M. A. Duncan, D. E. Powers, and R. E. Smalley, J. Chem. Phys. **74**, 6511 (1981)

2 V. E. Bondybey and J. H. English, J. Chem. Phys. **74**, 6978 (1981).

3 T. G. Dietz, M. A. Duncan, M. G. Liverman, and R. E. Smalley, J. Chem. Phys. **73**, 4816 (1980).

4 D. E. Powers, S. G. Hansen, M. E. Geusic, A. C. Puiu, J. B. Hopkins, T. G. Dietz, M. A. Duncan, P. R. R. L.-Smith, and R. E. Smalley, J. Phys. Chem. **86**, 2556 (1982).

5 B. Simard, S. A. Mitchell, M. R. Humphries, and P. A. Hackett, J. Mol. Spectrosc. **129**, 186 (1988).

6 B. Simard, S. A. Mitchell, M. R. Humphries, and P. A. Hackett, J.Chem. Phys. **89**,1899 (1988).

7 B. Simard, S. A. Mitchell, L. M. Hendel, and P. A. Hackett, Faraday Discuss. Chem. Soc. **86**, 163 (1988).

8 B. Simard, C. Masoni, and P. A. Hackett, J. Mol. Spectrosc. **136**, 44 (1989).

9 V. E. Bondybey and J. H. English, J. Chem. Phys. **73**, 42 (1980).

10 V. E. Bondybey and J. H. English, J. Chem. Phys. **80**, 568 (1984).

11 W. E. Knight, K. Klemenger, and W. A. de Heer, Phys. Rev. B **31**, 2539 (1985).

12 M. E. Geusic, M. D. Morse, S. C. O'Brien, and R. E. Smalley, J. Chem. Phys. **82**, 590 (1985).

13 M. D. Morse, M. E. Geusic, J. R. Heath, and R. E. Smalley, J. Chem. Phys. **83**, 2293 (1985).

14 F. Misaizu, M. Sanekata, K. Tsukamoto, K. Fuke, and S. Iwata, J. Phys. Chem. **96**, 8259 (1992).

15 L. N. Ding, M. A. Young, P. D. Kleiber, and W. C. Stwalley, J. Phys. Chem. **97**, 2181 (1993).

16 R. L. Asher, D. Bellert, T. Buthelezi, and P. J. Brucat, Chem. Phys. Letters. **224**, 525 (1994).

17 C. A. Arrington, T. Blume, M. Morse, M. Doverstal, and U. Sassenberg, J. Phys. Chem. **98**, 1398 (1994).

18 B. Simard, M. A. L. Dorget, A. Marijnissen, and J. J. ter Meulen, J. Chem. Phys. **108**, 9668 (1998).

19 P. J. Brucat, L.-S. Zheng, C. L. Pettiette, S. Yang, and R. E. Smalley, J. Chem. Phys. **84**, 3078 (1986).

20 R. J. V. Zee, S. Li, and W. Weltner Jr, Chem. Phys. Letters. **217**, 381 (1994).

21 A. G. Adam, Y. Azuma, J. A. Barry, A. J. Merer, U. Sassenberg, J. O. Schroder, G. Cheval, and J. L. Femenias, J. Chem. Phys. 100, 6240 (1994).

22 J. L. Femenias, G. Cheval, A. J. Merer, and U. Sassenberg, J. Mol. Spectrosc. **124**, 348 (1987).

23 Z. Hu, B. Shen, Q. Zhou, S. Deosaran, J. R. Lombardi, and M. D. Lindsay, SPIE 1599, 65 (1991).

24 A. M. James, P. Kowalczyk, R. Fournier, and B. Simard, J. Chem. Phys. **99**, 8504 (1993).

25 A. M. James, P. Kowalczyk, E. Langlois M. D. Campbell, A. Ogawa, and B. Simard, J. Chem. Phys. **101**, 4485 (1994).

26 B. Simard, C. Masoni, and P. A. Hackett, J.Chem. Phys. **92**, 7003 (1990).

27 B. Simard, Paul I. Presunka, H. P. Loock, and A. Berces. J. Chem. Phys. **107**, 307 (1997).

28 P. R. R. Langridge-Smith. M. D. Morse, G. P. Hansen, and R. E. Smalley. J. Chem. Phys. **80**, 593 (1984).

29 D. A. Hales. L. Lian, and P. B. Armentrout, Int. J. Mass Spect. And Ion Processes. **102**, 269 (1990).

30 V. R. Rao. Indian J. Phys. **24**, 35 (1950)

31 K. S. Rao, Nature(London) **170**, 670 (1952).

32 V. R. Rao and D. Premaswarup, Indian J. Phys. **27**, 399 (1953)

33 J. M. Brom, C. H. Durham, and W. Weltner, J. Chem. Phys. **61**, 970 (1974).

34 W. A. Saunders, Department of Physics, Swiss Federal Institute of Technology-Lausanne, Switzerland.

35 G. I. Dimov Pribory I Tekhnika Eksperimenta, Nuclear Physics Institute, Academy of Sciences of the USSR, No. 5, pp. 168-171 (1968).

36 J. M. Hayes, Chem. Rev. **87**, 745 (1987).

37 J. M. Pendlebury and K. F. SMITH, Contemp. Phys. **28**, 3 (1987).

38 J. R. Heath, Y. Liu, S. C. O'Brien, Q.-L. Zhang, R. F. Curl, F. K. Tittel, and R. E. Smalley, J. Chem. Phys. **83**, 5520 (1985).

39 A. J. Merer, Annu. Rev. Phys. Chem. **40**, 407 (1989).

40 Can be derived using the ladder operator $\mathbf{S}_- = \mathbf{S}_{1-} + \mathbf{S}_{2-} + \mathbf{S}_{3-}$ to generate all 2S+1 of eigenfunctions for a three electron system having S = 3/2 or see Charles S. Johnson, Jr., Lee G. Pedersen, *Problems and Solutions in Quantum Chemistry and Physics*, Dover Publications, Inc., New York, 1986.

41 C. E. Moore, Atomic Energy Levels, Natl. Bur. Stand. (US) Crit. No. 467, (U.S. GPO, Washington, D.C., 1971), Vols. I and II.

42 See Table 4.7 in Chapter 4 of Helene Lefebvre-Brion and Robert W. Field, *Perturbations in The Spectra of Diatomic Molecules,* Academic Press, New York, 1986.

43 See Chapter VII.

44 K. Balasubramanian and XiaoLei Zhu, submitted.

CHAPTER XI

CONCLUSION

The photofragmentation spectroscopy in a reflectron time-of-flight is a useful tool to determine spectroscopic properties of cluster ions such as: dissociation energy, vibrational frequencies, rotational parameters, first- and second-order spin-orbit coupling, and so on. In this study, we determined the dissociation energies of the $^{90}Zr_2^+$, Nb_2^+, Nb_3^+, Nb_4^+ from the onset of the fairly sharp rise in the background of their photofragmentation spectra and the electronic structure of Nb_2^+ in the 16,000-18,500 cm^{-1} region. In the red region of the A(v',0) band, the niobium dimer cation can be dissociated by a four photon process, using a one-color experiment, with respect to its observed threshold energy at 15,880 cm^{-1}, see Chap. VII. Therefore, it is difficult to observe the electronic transitions by a one-color fragmentation experiment. In the blue region of the D band, we attempted to probe the electronic transitions up to 20,000 cm^{-1}, in this case, because of the lower power of dye laser, the probability of the fragmentation of the parent ions decreases which leading very weak structure and it is hard to distinguish these from the background.

The measured dissociation energies of the Nb_2^+, Nb_3^+, Nb_4^+ are in good agreement with the previous collision-induced dissociation (CID) measurements and with theoretical predictions, see chapter VII, VIII, and IX. The uncertainties on these energies are reduced to the 0.056 – 0.001 eV range from 0.12-0.19 eV (in CID experiments). The dissociation energy of the Zr_2^+ was measured and calculated for the first time and only three peaks, one relatively weak, are found around 18,290 cm^{-1}. Both the experimental

and the calculated dissociation energy of Zr_2^+ are in agreement within a minor uncertainty (see Chapter VI). We also calculated dissociation energies of these neutral and ionic trimer and tetramer niobium clusters for the other possible dissociation pathways, using the thermochemical cycles (see chapters VIII and IX) and the first ionization energy of the Zr_2 (see Chapter VI).

So far we have not found any experimental study on their ground state symmetry, except an electron-spin-resonance (ESR) experiment on Nb_2^+ ion in an argon matrix. The ESR study suggests that the ground state of Nb_2^+ is $^2\Sigma^+_g$, which arises from the electronic configuration $...2\sigma_g\delta_g^2$. The initial mass selected multiphoton fragmentation spectrum of Nb_2^+ in gas phase (present study) show many strong bands with an interval 940 and 830 cm^{-1} as well as many weak transitions. The observed multipleband structure of Nb_2^+ indicates that more than three electronic bands lie in this explored spectral region and are heavily mixed. The separations between the peaks, and their regular progression suggest that these transitions are most likely due to quartet-quartet transitions. This spectroscopic observation may eliminate the $^2\Sigma^+_g(2\sigma_g\delta_g^2)$ to be the lowest ground state as suggested by the ESR experiment. The $^4\Sigma^-_g$ symmetry, arising from the electronic configuration $...2\sigma_g\delta_g^2$, is favorable for the ground state according to Hund's rule and taking the exchange energy into account, which is in agreement with the ab initio predictions (DFT, CASSCF, HF).

The most likely interpretation of these bands is discussed in Chapter-X. A comparison of the estimated first-order spin-orbit coupling, based on the corresponding atomic spin-orbit parameters for the $^4\Pi_u(1\pi_u^3 1\sigma_g^2 2\sigma_g^2 \delta_g^2)$ and $^4\Pi_u(1\pi_u^3 1\sigma_g^2 2\sigma_g^1 \delta_g^3)$ excited states, with the relative distance between the observed peaks suggest that the

observed multiple bands are due to the A/C/D$^4\Pi_u(1\pi_u^3 1\sigma_g^2 2\sigma_g^1 \delta_g^3) \leftarrow X^4\Sigma^-_g(1\pi_u^4 1\sigma g^2 2\sigma_g^1 \delta_g^2)$ and $B^4\Pi_u(1\pi_u^3 1\sigma_g^2 2\sigma_g^2 \delta_g^2) \leftarrow X^4\Sigma^-_g$ transitions, see Table 11.1 in Chap. X. We would like to note that this assignment is not definitive without rotational evidence. We attempted to probe the rotational structure at several bands positions, but it failed due to the broad band width of the fragmentation laser (~ 0.07 cm^{-1}).

The calculations predict only $1\sigma_u \leftarrow 2\sigma_g$ vertical orbital transition $B^4\Sigma^-_u(1\pi_u^4 1\sigma_g^2 \delta_g^2 1\sigma_u^1) \leftarrow X^4\Sigma^-_g$ lies in this spectral region, but it is not possible to assign the multiple bands based on the $^4\Sigma^-_u \leftarrow X^4\Sigma^-_g$ transitions. Even though the $\delta_g \leftarrow 1\pi_u$ and $2\sigma_g \leftarrow 1\pi_u$ vertical orbital transitions, $A^4\Pi_u(1\pi_u^3 1\sigma_g^2 2\sigma_g^1 \delta_g^3) \leftarrow X^4\Sigma^-_g$ and $B\ ^4\Pi_u(1\pi_u^3 1\sigma_g^2 2\sigma_g^2 \delta_g^2) \leftarrow X^4\Sigma^-_g$, are predicted to be approximately 4,500 ± 500 cm^{-1} below the experimental region by the DFs (see Chapter VII), the multiple structures of the spectra suggest that these electronic transitions may be due to the $^4\Pi_u \leftarrow {}^4\Sigma^-_g$ transitions, assigned as mentioned above. We feel that the density functional calculations underestimate $\pi \leftrightarrow \delta$ transitions but predict $\sigma \leftrightarrow \sigma$ transitions within a few hundred wavenumbers. It seems that the reason the density functional methods underestimate the $\pi \leftrightarrow \delta$ orbital-orbital transitions, might be due to the correlation energy contribution in the excited state or due to the densityfunctional methods do not include isoconfigurational effects in the calculations. For example, as we discussed in Chapter X, Langridge-Smith *et al.* determined the $^3\Pi_{0.u} \leftarrow X^4\Sigma^-_{0.g}$ transition in V_2 at 14,306 cm^{-1} by rotationally resolved gas-phase electronic spectrum of the V_2. While the BLYP densityfunctional method predict the $^3\Pi\ (1\pi_u^3 1\sigma_g^2 2\sigma_g^2 \delta_g^3) \leftarrow X^3\Sigma^-_g(1\pi_u^4 1\sigma_g^2 2\sigma_g^2\ \delta_g^2)$ to be about 4,300 cm^{-1} below the experimental value of T_0 = 14,306 cm^{-1}, predicts the $1\sigma_u \leftarrow 2\sigma_g$ transitions or $^3\Sigma^-_u \leftarrow$

$X^3\Sigma^-_g$ transition to be 12,645 cm^{-1}, in agreement with the experimental value of 11,811 cm^{-1} within 830 cm^{-1}.

In this study, the goal of the density functional calculations were to understand and determine whether the DF methods with the ECP plus DZ basis set are successful or fail to predict the spectroscopic properties of the transition metals within an acceptable uncertainty. Researchers have attempted to investigate the spectroscopic properties of transition metals using several different theoretical models, but it is not yet clear which of one predicts true properties of the molecules. For example, the complete active space self-consistent field (CASSCF) method has been used to predict dissociation energy of the niobium dimer by Bauschlicher et al, see Chap. VII. This method underestimates the dissociation energy (2.24 eV); a CID measurement gives a value as 5.22 ± 0.22 while it overestimates the bond distance and vibrational frequency within a minor errors, 0.8% and 5.4%, respectively. However, the density functional methods predicted the dissociation energy within 2-22% error and the bond length and vibrational frequency are predicted within minor errors, see Chap VII. On the other hand, DF methods have had difficulty determining the true ground state for some of the transition metals like Ni (due to many low lying state lie a hundred wavenumber above the ground state) while the CASSCF method predicts that the ground state of nickel dimer is in agreement with the experimental suggestion ($^1\Gamma_u$ or $^3\Gamma_u$). The density functional methods with effective core potential plus DZ (LANL2DZ) and coupled effective core potential like ECP-121G, -31G, etc. basis functions were performed on the first-, second-, and third-row transition metal clusters (ions) to predict their spectroscopic properties such as ground state

symmetry, dissociation energy (D_e), ionization energy (IP), electron affinity (EA), equilibrium bond distance (R_e), and vibrational frequency (ω_e) or force constant (k_e).

Here we would like to present the predicted ground state symmetries with the electronic configurations, ω_e (or k_e), R_e, EA, and IP for the second-row transition metal dimer molecules. The predicted dissociation energies of the neutral and ionic zirconium and niobium clusters are given in Chapter VI-IX. For the first- and second-row transition metal dimers, only calculated the force constants, k_e, are presented. Table 11.1 shows the calculated IP, EA, R_e, ω_e, and k_e of the neutral and ionic second-row transition-metal dimer molecules with their electronic configurations and symmetries. The method overestimates the force constants, most likely with a constant error, for the neutral 3-d transition dimer molecules, but well correlate with their experimental values (see Fig 11.1).

For the 4-d series, the calculated force constants are correlated with their experimental values within minute errors (see Fig. 11.2a). Fig. 11.2b shows the calculated force constants for the anionic and cationic dimer molecules are in the same trend. Unfortunately, we did not find any experimental value for the comparison. The predicted ionization energy of the Zr_2 (5.702 eV), Nb_2 (6.485) and Mo_2(7.079 eV) is in excellent agreement with their experimental values are 5.822 eV, 6.368 eV, and 6.948 eV, respectively. The calculated bond distances for the second row transition metal dimer molecules are consistent with the experimental values within 1-4% errors. In the third-row transition-metal dimer molecules, there is no a regular correlation between calculated and experimental force constants (see Fig. 11.3).

Even though the calculations on the dissociation energies of the transition metal clusters (ions) have not been completed yet, so far our calculations indicate that DF methods overestimate dissociation energies for 3-d series, predict within minute errors for the 4-d series, and underestimates for the 5-d series for the neutral dimer molecules. The ionization energies of the transition metal clusters are consistent with the experimental values within 1-3% errors. This might be evidence that the exchange-correlation energy is not well defined in either atoms or molecular state to predict a accurate dissociation energies of the transition-metal cluster (ions).

Table 11.1. Calculated spectroscopic properties of the second-row transition metal dimer molecules. Where ω_e in cm^{-1}, R_e in Å, k_e in mdyne/Å, IP and AE in eV.

X_2	Symm.	Configuration	ω_e	R_e	k_e	IP	Exptl.	EA
Rb_2	$^1\Sigma^+_g$	$1\sigma_u^2 1\sigma_g^2$	53	4.259	0.067			
Rb_2^+	$^2\Sigma^+_g$	$1\sigma_u^2 1\sigma_g^1$	36	4.987	0.031	4.046		
Rb_2^-	$^2\Sigma^+_u$	$1\sigma_u^2 1\sigma_g^2 1\sigma_u^1$	30	4.997	0.022			0.409
Sr_2	$^1\Sigma^+_g$	$1\sigma_u^2 1\sigma_g^2 1\sigma_u^2$	22	5.467	0.013			
Sr_2^+	$^2\Sigma^+_u$	$1\sigma_u^2 1\sigma_g^2 1\sigma_u^1$	52	4.629	0.070	5.046		
Sr_2^-	$^2\Pi_u$	$1\sigma_g^2 1\sigma_u^2 1\pi_u^1$	32	5.031	0.026			
Y_2	$^1\Sigma^-_g$	$1\sigma_g^2 1\pi_u^2$	221	2.560	1.284	0.313		
Y_2	$^5\Sigma^-_u$	$1\pi_u^2 1\sigma_u^1 1\sigma_g^1$	180	2.960	0.847	4.961		
Y_2^+	$^4\Sigma^-_g$	$1\sigma_g^2 1\pi_u^2 2\sigma_g^1$	200	2.874	1.049			
Y_2^-	$^6\Delta_u$	$1\sigma_g^2 1\sigma_u^1 1\pi_u^2 2\sigma_g^1 \delta_g^1$	171	2.894	0.767			0.386
Zr_2	$^3\Delta_g$	$1\sigma_g^2 1\pi_u^4 2\sigma_g^1 \delta_g^1$	311	2.336	2.511			
Zr_2	$^1\Sigma^+_g$	$1\sigma_g^2 1\pi_u^4 2\sigma_g^2$	366	2.350	3.546	0.299		
Zr_2^+	$^2\Sigma^+_g$	$1\pi_u^4 1\sigma_g^2 2\sigma_g^1$	259	2.377	1.781	5.702	5.822	
Zr_2^-	$^2\Delta_g$	$1\sigma_g^2 1\pi_u^4 2\sigma^2 \delta_g^1$	360	2.304	3.433			0.162
Zr_2^-	$^4\Sigma^-_g$	$1\sigma_g^2 1\pi_u^4 2\sigma_g^1 \delta_g^2$	328	2.303	2.854			
Nb_2	$^3\Sigma^-_g$	$1\pi_u^4 1\sigma_g^2 2\sigma_g^2 \delta_g^2$	444	2.158	5.396			
Nb_2^+	$^4\Sigma^-_g$	$1\pi_u^4 1\sigma_g^2 2\sigma_g^1 \delta_g^2$	436	2.120	5.205	6.485	6.368	
Nb_2^-	$^2\Delta_g$	$1\sigma_g^2 1\pi_u^4 2\sigma_g^2 \delta_g^3$	458	2.109	5.750			
Nb_2^-	$^4\Sigma^-_u$	$1\sigma_g^2 1\pi_u^4 2\sigma_g^1 \delta_g^2 1\sigma_u^1$	416	2.184	4.732			0.563
Mo_2	$^5\Sigma^+_g$	$1\pi_u^4 1\sigma_g^2 2\sigma_g^2 \delta_g^2 \delta_u^2$	419	2.168	5.078			
Mo_2	$^1\Sigma^+_g$	$1\pi_u^4 1\sigma_g^2 \delta_g^4 2\sigma_g^2$	524	2.006	7.918	7.079	6.948	
Mo_2^+	$^2\Sigma^+_g$	$1\pi_u^4 1\sigma_g^2 \delta_g^4 2\sigma_g^1$	500	1.994	7.218			
Mo_2^-	$^2\Sigma^+_u$	$1\pi_u^4 1\sigma_g^2 2\sigma_g^2 \delta_g^4 1\sigma_u^1$	500	2.023	7.208			0.512

Continuation of Table 11.1.

X_2	Symm.	Configuration	ω_e	R_e	k_e	IP	Exptl.	EA
Tc_2	$^1\Gamma_g$	$1\pi_u^4 1\sigma_g^2 2\sigma_g^2 \delta_g^4 \delta_u^2$		2.030	6.973	0.470		
Tc_2	$^3\Sigma^-_g$	$1\pi_u^4 1\sigma_g^2 2\sigma_g^2 \delta_g^4 \delta_u^2$		2.029	7.001			
Tc_2^+	$^4\Sigma^-_g$	$1\pi_u^4 1\sigma_g^2 \delta_g^4 2\sigma_g^1 \delta_u^2$		2.041	6.033	7.352		
Tc_2^-	$^2\Sigma^-_u$	$2\sigma_g^2 \delta_g^4\ \delta_u^{2.\alpha\alpha} 1\sigma_u^{1.\beta}$		2.050	6.361			
Tc_2^-	$^4\Sigma^-_u$	$2\sigma_g^2 \delta_g^4\ \delta_u 1\sigma_u$		2.053	6.221			0.731
Ru_2	$^7\Delta_u$	$\delta_g^3 1\sigma_g^2 \delta_u^2 1\pi_g^2 1\sigma_u^1$	315	2.310	2.971			
Ru_2^+	$^6\Sigma^-_u$	$\delta_g^4 \delta_u^2 1\pi_g^2 1\sigma_u^1$	266	2.378	2.126	7.772		
Ru_2^-	$^6\Gamma_g$	$2\sigma_g^2 \delta_g^3 \delta_u^3 1\sigma_u^1 1\pi_g^2$	299	2.311	2.694			0.886
Rh_2	$^5\Sigma^-_u$		273	2.348	2.264			
Rh_2^+	$^4\Sigma^-_u$	$\delta_u^4 1\pi_g^2 1\sigma_u^1$	245	2.418	1.820	7.512		
Rh_2^-	$^6\Delta_g$	$\delta_u^3 1\pi_g^2 1\sigma_u^1 2\sigma_g^1$	278	2.333	2.348	7.226		
Rh_2^-	$^6\Delta_u$	$2\sigma_g^2 \delta_u^3 1\sigma_u^1 1\pi_g^2 2\sigma_u^1$	278	2.326	2.341			1.269
Pd_2	$^3\Sigma^+_u$	$1\sigma_u^1 \delta_u^4 1\pi_g^4 2\sigma_g^1$	198	2.538	1.225			
Pd_2	$^1\Sigma^\pm_g$	$\delta_u^4 1\sigma_u^2 1\pi_g^4$	144	2.739	0.645	0.360		
Pd_2^+	$^2\Sigma^+_u$	$\delta_u^4 1\sigma_u^1 1\pi_g^4$	253	2.676	0.704	7.505		
Pd_2^-	$^2\Sigma^{+?}_u$	$2\sigma_g^2 1\sigma_u^1 \delta_u^4 1\pi_g^4$	203	2.495	1.289			1.642
Ag_2	$^1\Sigma^+_g$	$1\pi_g^4 1\sigma_u^2 2\sigma_g^2$	174	2.616	0.958			
Ag_2^+	$^2\Sigma^{+?}_g$	$1\pi_g^4 1\sigma_u^2 2\sigma_g^1$	126	2.793	0.503	7.844		
Ag_2^-	$^2\Sigma^{+?}_u$	$1\pi_g^4 1\sigma_u^2 2\sigma_g^2 2\sigma_u^1$	126	2.778	0.503			0.939
Cd_2								
Cd_2^+								
Cd_2^-								

Continuation of Table 11.1.

X_2	Symm.	Configuration	ω_e	R_e	k_e	IP	Exptl.	EA
Sn_2	$^3\Sigma^-_g$	$1\sigma_g^2 1\sigma_u^2 2\sigma_g^2 1\pi_u^2$	163	2.904	0.929			
Sn_2^+	$^4\Sigma^-_g$	$1\sigma_g^2 1\sigma_u^2 2\sigma_g^1 1\pi_u^2$	139	2.932	0.669	6.809		
Sn_2^-	$^2\Pi_u$	$1\sigma_g^2 1\sigma_u^2 2\sigma_g^2 1\pi_u^3$	180	2.796	1.112			1.375
In_2	$^6\Pi_u$	$1\sigma_u^1 2\sigma_g^1 1\pi_u^2 1\pi_g^1$		2.829				
In_2^+								
In_2^-								
Sb_2	$^1\Sigma^+_g$	$1\sigma_u^2 2\sigma_g^2 1\pi_u^4$	249	2.58	2.212			
Sb_2^+	$^2\Pi_u$	$1\sigma_u^2 2\sigma_g^2 1\pi_u^3$	213	2.711	1.610	8.416		
Sb_2^-	$^4\Pi_u$	$1\sigma_u^2 2\sigma_g^2 1\pi_u^3 1\pi_g^2$	156	2.968	0.865			

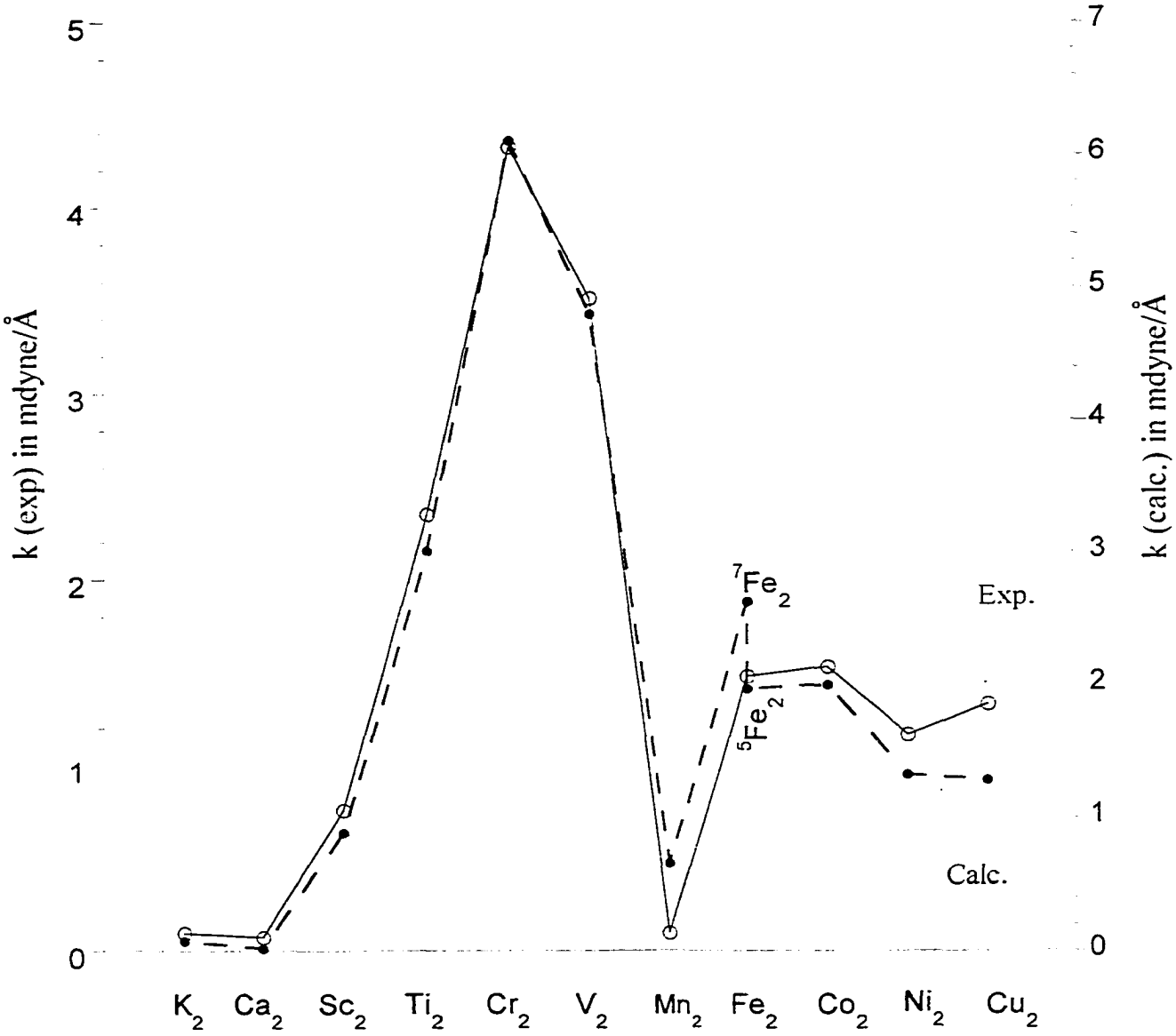

Figure 11. 1. Plot of the calculated force constants with their known experimental values for compression, mdyne/Å, for the first-row transition metal neutral dimer molecules.

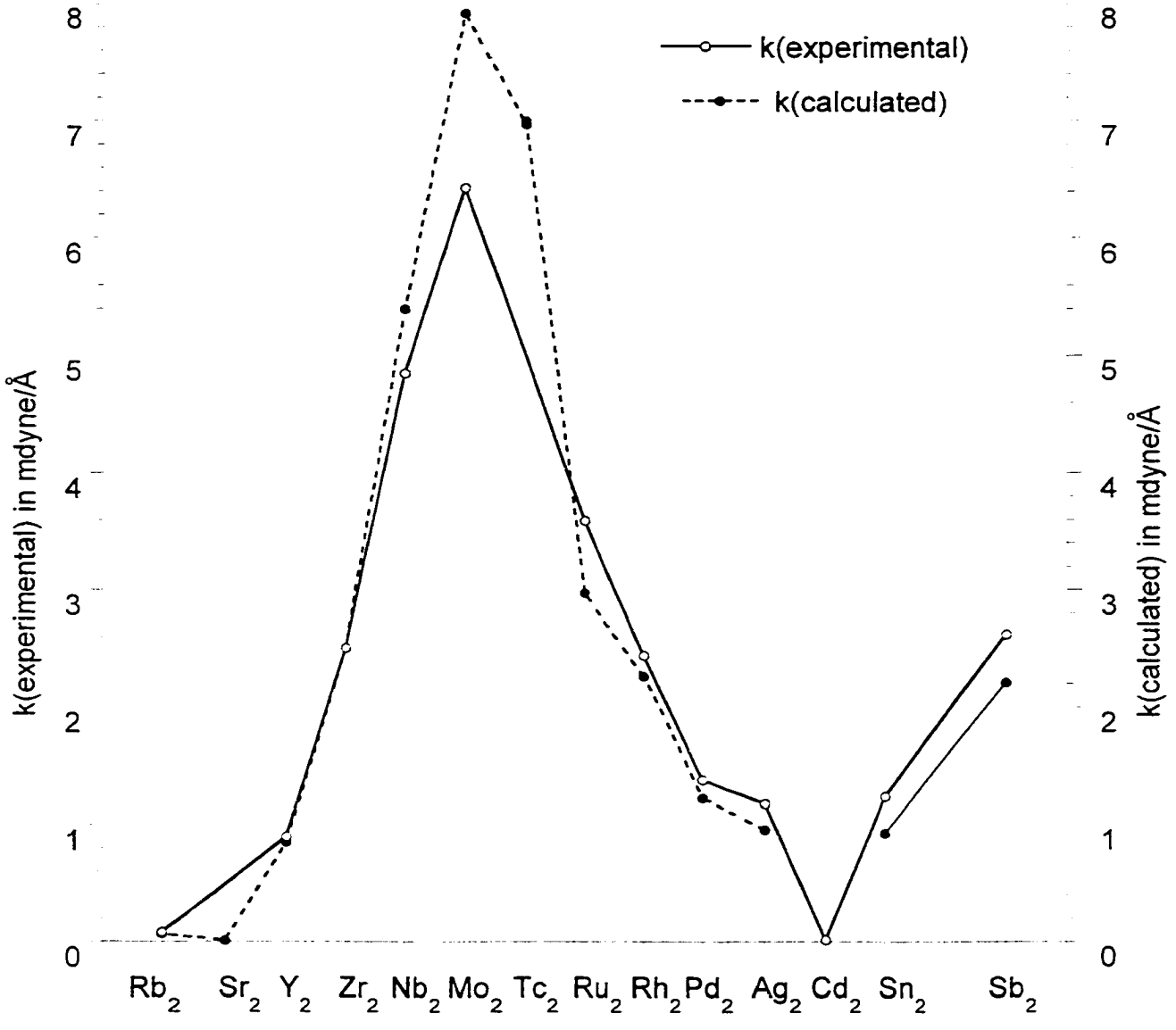

Figure 11. 2(a). Plot of the calculated and experimental force constants, in mdyne/Å, for the second-row transition metal neutral dimer molecules.

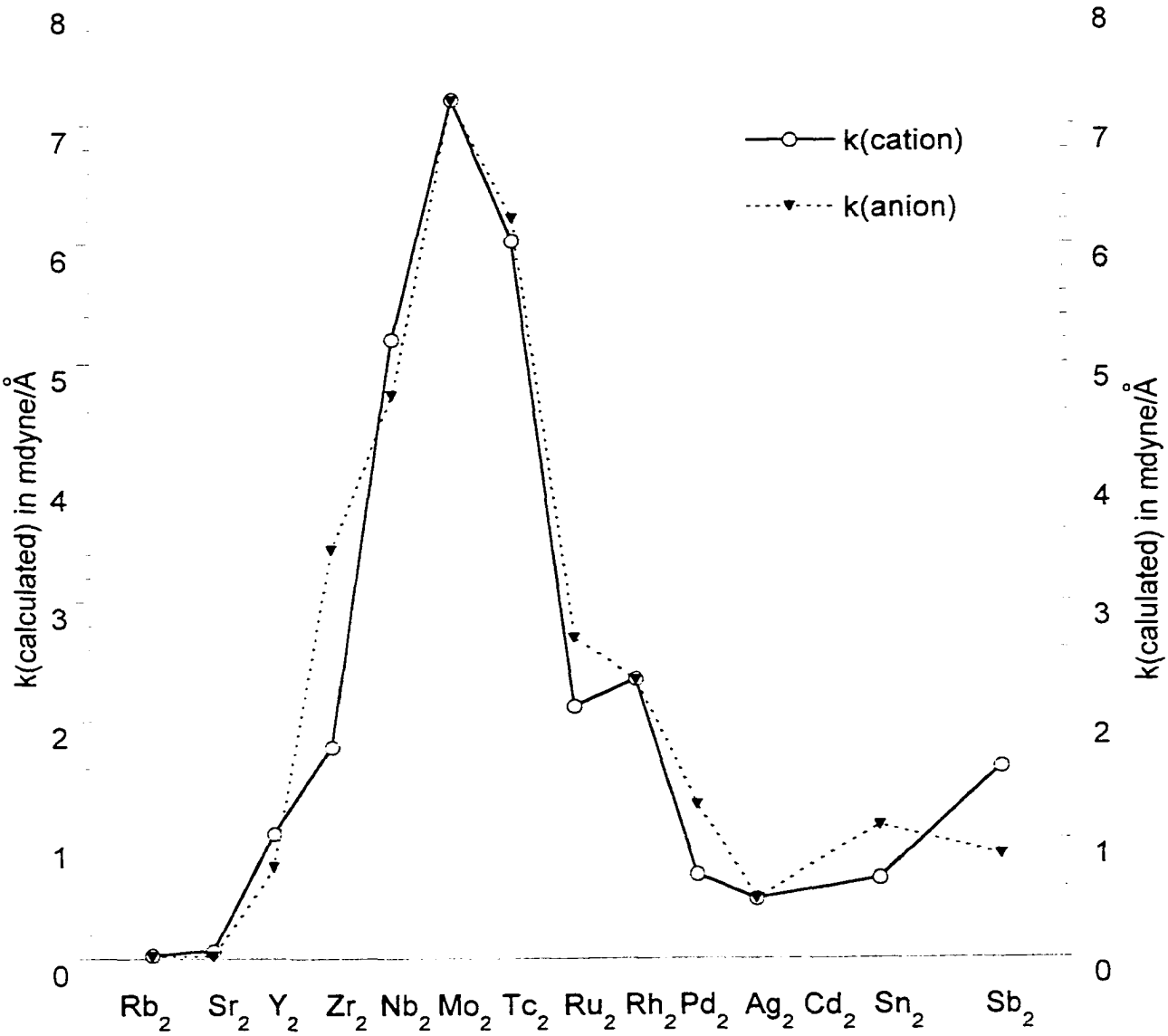

Figure 11. 2(b). Plot of the calculated force constants, in mdyne/Å, for the second-row transition metal cationic and anionic dimer molecules.

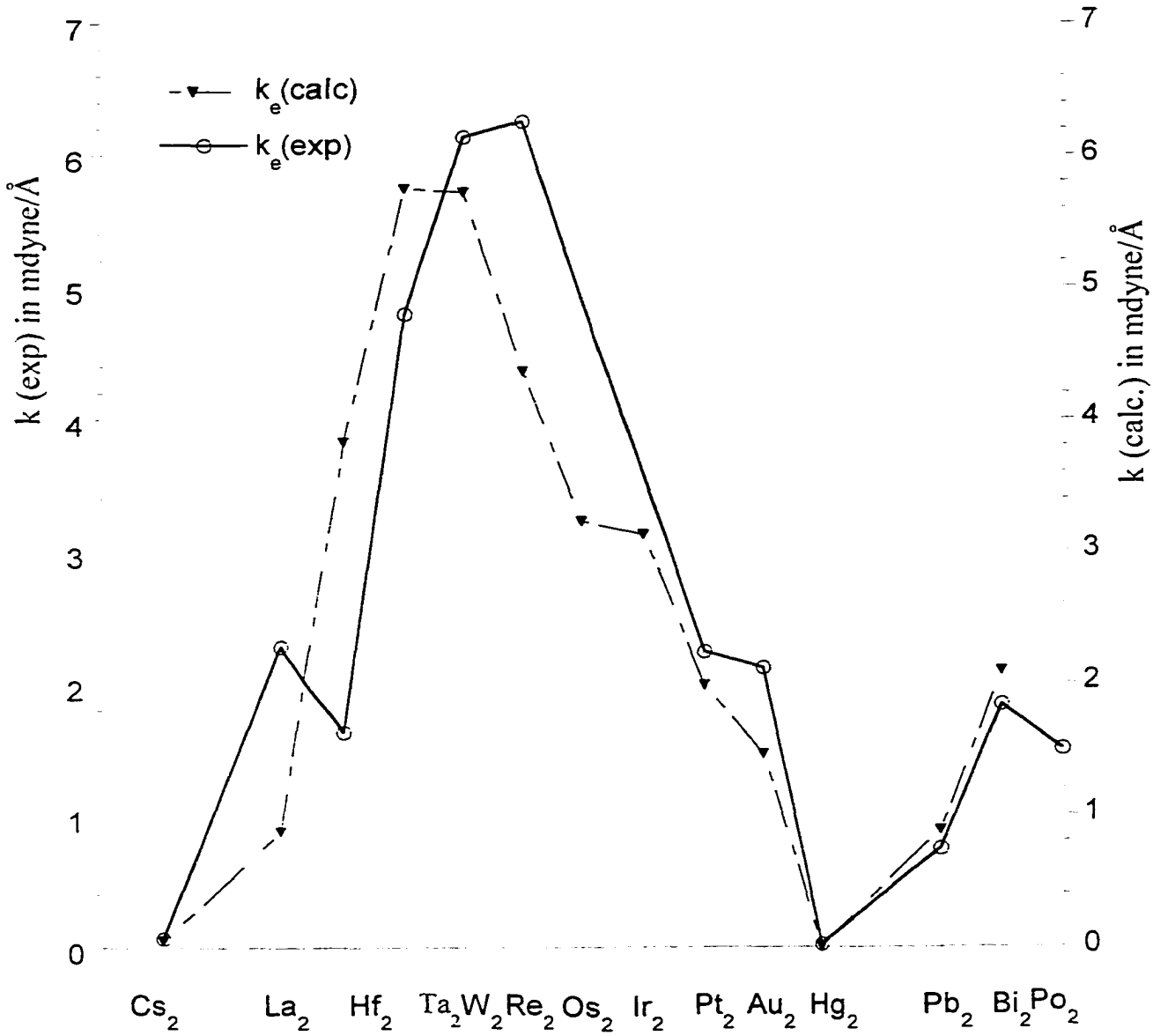

Figure 11. 3. Plot of the calculated force constants with their known experimental values for compression, in mdyne/Å, for the third-row transition metal neutral dimer molecules.

Chapter I References

1 H. Haberland, "*Clusters of Atoms and Molecules I and II*", Springer-Verlag, New York, 1995.

2 C.-Yiu Ng, T. Baer, and I. Powis, "*Cluster Ions*", John Wiley & Sons, New York, 1993.

3 M. Moskovits, "*Metal Clusters*", John Wiley & Sons, New York, 1986.

4 P.-Olov Lowdin, J. R. Sabin, M. C. Zerner, E. Brandas, A. Lami, and V. Barone, "*Advences in Quantum Chemistry*" Vol. 30, Academic Press, New York, 1999.

Chapter II. References

1) Y. Liu, Q. L. Zhang, F. K. Tittel, R. F. Curl and R. E. Smalley, J. Chem. Phys., 85, 7434 (1986).

2) D. E. Powers, S. G. Hansen, M. E. Geusic, D. L. Michalopoulos and R. E. Smalley, J. Chem. Phys., 78, 2286 (1983).

3) P. J. Brucat, L. S. Zheng, C. L. Pettiette, S. Yang and R. E. Smalley, J. Chem. Phys., 84, 3078 (1986).

4) D. E. Powers, S. G. Hansen, M. E. Geusic, A. C. Puiu, J. B. Hopkins, T. G. Dietz, M. A. Duncan, P. R. R. Langridge-Smith and R. E. Smalley, J. Chem. Phys., 86, 2556 (1982).

5) S. Maruyama, L. R. Anderson and Richard E. Smalley, Rev. Sci. Instrum., 61, 3686 (1990).

6) P. Milani and W. A. deheer, Rev. Sci. Instrum., 61, 1835 (1990).

7) P. Gangopadhyay and J. M. Lisy Rev. Sci. Instrum., 62, 502 (1991).

8) W. A. Saunders, Department of Physics, Swiss Federal Institute of Technology - Lausanne, Switzerland.

9) P. K. Carroll and E.T. Kennedy, Contemp. Phys., 22, 61, (1981).

10) P. C. Engelking, Chem. Rev., 91, 399 (1991).

11) O. F. Hagena, Rev. Sci. Instrum., 63, 2374 (1992)

12) G. I. Dimov Pribory I Technika Experimenta, Nuclear Physics Institute, Academy of Sciencea of the USSR, No.5, pp. 168-171, (1968).

13) J. M. Hayes, Chem. Riv., 87, 745 (1987).

14) J. M. Pendlebury and K. F. Smith, Contemp. Phys.,28, 3, (1987).

15) W. C. Wiley and 1. H. McLaren, Rev. Sci. Inst., 26, 1150, (1955).

16) J. A. Syage and J. Steadman, Rev. Sci. Instrum.,61, 1204 (1990).

17) a) H. Haberland, H. Kornmeier, C. Ludewight, A. Risch and M. Schmidt, Rev. Sci. Instrum., 62, 2368 (1991)

b) H. Haberland, H. Kornmeier, C. Ludewight, A. Risch and M. Schmidt, Rev. Sci. Instrum., 62, 2621 (1991)

18) D. S. Cornett, M. Peschke, K. LaiHing, P. Y. Cheng, K. F. Willey and M. A. Duncan, Rev. Sci. Instrum., 63, 2177 (1992)

19) R. T. Laaksonen, D. A. Goetsch, D. W. Owens, D. M. Poirier, F. Stepniak and J. H. Weaver, Rev. Sci. Instrum., 65, 2267 (1994) .

20) W. Begemann, S. Dreihofer, G. Gantefor, H. R. Siekmann, K. H. Meiwes-Broer and H. 0. Lutz, Springer Ser. Mater. Sci., 230 (1988).

21) B. A. Mamyrin, V. I. Karataev, D. V. Shmikk and V. A. Zagulin, Sov. Phys.-JETP., 37, 45 (1973).

22) SIMION PC Version 4.0, courtesy D. A. Dahl, Indaho Natl. Lab. Idaho Falls, ID 83415, USA.

Chapter III References

1. John T. Moseley, Photodissociation and Photoionization, edited by K. P. Lawley (Wiley, 1985).
2. S. P. Goss, J. D. Morrison and D. L. Smith J. Chem. Phys.**75**, 757 and 1820 (1981).
3. R. N. Dixon, Chem. Soc. Rev., (1994).
4. C. R. C. Wang, S. Pollack, D. Cameron and M. Kappes, J. Chem. Phys., **93**, 3787 (1990).
5. P. J. Brucat. L. S. Zheng, C. L. Pettiette, S. Yang and R. E. Smalley, J. Chem. Phys., **84**, 3078 (1986).
6. A. W. Castleman Jr.. and R. G. Keesee, Chem. Rev., **86**, 589 (1986) .
7. K. F. Willey, D. L. Robbins, C.-S. Yeh and M. A. Duncan, Faraday Discuss. **92**, 269 (1991).
8. M. F. Jarrold and K. M. Creegan, I.nt. J. Mass Spec. and Ion Processes, **102**. 161 (1990).
9. M. F. Jarrold and K. M. Creegan, Chem. Phys. Lett., **166**. 116 (1990).
10. P. C. Engelking, Chem. Rev., **91**, 399 (1991).
11. J. M. Hayes, Chem. Rev., **87**, 745 (1987).
12. J. B. Hopkins, P. R. R. Langridge-Smith, M. D. Morse and R. E. Smalley, J. Chem. Phys., **78**, 1627 (1983).
13. Jacqueline C. Pinegar, Jon D. Langenberg, Caleb A. Arrington, Eileen M. Spain and Michael D. Morse, J. Chem. Phys., **102**, 666 (1995).
14. R.J. Van Zee, S. Li and W. Weltner Jr., Chem. Phys. Lett. **217**, 381 (1994) .

15. A. M James, P. Kowalczk, E. Langlois, M. D. Campbell, A. Ogawa and B. Simard, J. Chem. Phys., **101**, 4485 (1994).

16. A. M. James, P. Kowalczk, R. Fournier and B. Simard J. Chem. Phys., **99**, 8504 (1993).

17. Z. Hu, B. Shen, Q. Zhou, S. Deosaran, J. R. Lombardi and D. M. Lindsay, SPIE Proceedings Vol. **1599**, (1992).

18. D. A. Hales, L. Lian, P.B. Armentrout, Int. J. Mass Spec. and Ion Processes, **102**, 269 (1990).

19. S. K. Loh, Li Lian and P.B. Armentrout, J. Chem. Phys., **91**, 6148 (1989.

20. Y. Hamrick, S. Taylor, G. W. Lemire, Z. W. Fu, J, C, Shui and M. D. Morse. J. Chem. Phys., **88**, 4095 (1988).

21. M. Moskovits and W. Limm, Ultramicroscopy **20**, 83 (1986).

22. J. R. Heath, Y. Liu, S. C. O'Brien, Q.-L. Zhang, R. F. Curl, F. K. Tittel, and R. E. Smalley, J. Chem. Phys., **63**, 5520 (1985).

23. R. L.- Asher, D. Bellert, T. Buthelezi and P. J. Brucat, Chem. Phys. Lett., **224**, 525 and 529 (1994).

24. Private communication with P. J. Brucat, University of Florida, Gainesville.

25. Private communication with M. A. Duncan, University of Georgia, Athens.

26. Benoit Simard, Andrew M. James, P. Kowalczyk, R. Fournier and P. A. Hackett, preprint (High Resolution spectroscopy of small transition metal molecules. Recent experimental and theoretical progress on group 5 diatomics.

27. J. C. Weisshaar, J. Chem. Phys., **90**, 1429 (1989).

28. C. W. Bauschlicher Jr., S. R. Langhoff, Chem. Rev., **91**, 701, (1991).

29. S. Taylor, G. W. Lemire, Y. M. Hamrick, Z. Fu and M. D. Morse, J. Chem. Phys., **89**, 5517 (1988).

Chapter III References

30. John T. Moseley, Photodissociation and Photoionization, edited by K. P. Lawley (Wiley, 1985).

31. S. P. Goss, J. D. Morrison and D. L. Smith J. Chem. Phys.**75**, 757 and 1820 (1981).

32. R. N. Dixon, Chem. Soc. Rev., (1994).

33. C. R. C. Wang, S. Pollack, D. Cameron and M. Kappes. J. Chem. Phys., **93**, 3787 (1990).

34. P. J. Brucat, L. S. Zheng, C. L. Pettiette. S. Yang and R. E. Smalley, J. Chem. Phys., **84**, 3078 (1986).

35. A. W. Castleman Jr., and R. G. Keesee, Chem. Rev., **86**, 589 (1986) .

36. K. F. Willey, D. L. Robbins. C.-S. Yeh and M. A. Duncan, Faraday Discuss. **92**, 269 (1991).

37. M. F. Jarrold and K. M. Creegan, I.nt. J. Mass Spec. and Ion Processes. **102**, 161 (1990).

38. M. F. Jarrold and K. M. Creegan. Chem. Phys. Lett., **166**, 116 (1990).

39. P. C. Engelking, Chem. Rev., **91**, 399 (1991).

40. J. M. Hayes, Chem. Rev., **87**, 745 (1987).

41. J. B. Hopkins, P. R. R. Langridge-Smith, M. D. Morse and R. E. Smalley, J. Chem. Phys., **78**, 1627 (1983).

42. Jacqueline C. Pinegar, Jon D. Langenberg, Caleb A. Arrington, Eileen M. Spain and Michael D. Morse, J. Chem. Phys., **102**, 666 (1995).

43. R.J. Van Zee, S. Li and W. Weltner Jr., Chem. Phys. Lett. **217**, 381 (1994) .

44. A. M James, P. Kowalczk, E. Langlois, M. D. Campbell. A. Ogawa and B. Simard, J. Chem. Phys., **101**, 4485 (1994).

45. A. M. James, P. Kowalczk, R. Fournier and B. Simard J. Chem. Phys., **99**, 8504 (1993).

46. Z. Hu, B. Shen, Q. Zhou, S. Deosaran, J. R. Lombardi and D. M. Lindsay, SPIE Proceedings Vol. **1599**, (1992).

47. D. A. Hales, L. Lian, P.B. Armentrout, Int. J. Mass Spec. and Ion Processes, **102**, 269 (1990).

48. S. K. Loh, Li Lian and P.B. Armentrout, J. Chem. Phys., **91**, 6148 (1989.

49. Y. Hamrick, S. Taylor, G. W. Lemire, Z. W. Fu, J, C, Shui and M. D. Morse, J. Chem. Phys., **88**, 4095 (1988).

50. M. Moskovits and W. Limm, Ultramicroscopy **20**, 83 (1986).

51. J. R. Heath, Y. Liu, S. C. O'Brien, Q.-L. Zhang, R. F. Curl, F. K. Tittel, and R. E. Smalley, J. Chem. Phys., **63**, 5520 (1985).

52. R. L.- Asher, D. Bellert, T. Buthelezi and P. J. Brucat, Chem. Phys. Lett., **224**, 525 and 529 (1994).

53. Private communication with P. J. Brucat, University of Florida, Gainesville.

54. Private communication with M. A. Duncan, University of Georgia, Athens.

55. Benoit Simard, Andrew M. James, P. Kowalczyk, R. Fournier and P. A. Hackett, preprint (High Resolution spectroscopy of small transition metal molecules. Recent experimental and theoretical progress on group 5 diatomics.

56. J. C. Weisshaar, J. Chem. Phys., **90**, 1429 (1989).

57. C. W. Bauschlicher Jr., S. R. Langhoff, Chem. Rev., **91**, 701, (1991).

58. S. Taylor, G. W. Lemire, Y. M. Hamrick, Z. Fu and M. D. Morse, J. Chem. Phys., **89**, 5517 (1988).

CHAPTER V REFERENCES

1 F. Hund, Z. Phys. **36**, 657(1926) and **42**, 93(1927).

2 Istvan Kovacs, "*Rotational Structure in the Spectra of Diatomic Molecules*", American Elsevier Publishing Company Inc., New York, 1969.

3 Gerhard Herzberg, "*Molecular Spectra and Molecular Structure, Vol. I-Spectra of Diatomic Molecules*", Krieger Publishing Company, Florida, Reprint Edition 1989

4 H. A. Bethe, E. E. saltpeter, "*Quantum Machanics of One- and Two-Electron Atoms*", Academic Press, Inc., New York, 1957.

5 W. Heisenberg, Z. Phys. **39**, 514(1926).

6 P. R. Fontana, Phys. Rev. **125**, 220(1962).

7 J. H. van Vleck, Phys. Rev. **33**, 467 (1929).

8 J. H. van Vleck, Phys. Rev. **40**, 544(1932).

9 J. H. van Vleck, Rev. Mod. Phys. **23**, 225 (1951).

10 E. L. Hill, J. H. van Vleck, Phys. Rev. **32**, 250 (1928).

11 A. Budo and I. Kovacs, Z. Phys. **109**, 393 (1938).

12 I. Kovacs, Can. J. Phys. **36**, 309 (1958).

13 L. Y. C. Chiu, J. Chem. Phys. **40**, 2276 (1964).

Chapter VI References

1. T. G. Dietz, M. A. Duncan, D. E. Powers, and R. E. Smalley, J. Chem. Phys. **74**, 6511(1981)
2. See, for example, Physics and Chemistry of Finite Systems: From clusters to crystals, edit by P. Jena, S. N. Khanna, and B. K. Rao Kluwer Academic, Boston, (1992). Vols. I and II.
3. I. M. L. Billas, A. Chatelain, and N. A. de Heer, Science **265**, 1682(1994).
4. D. M. Cox, D. J. Trevor, R. L. Whetten, E. A. Rohlfing, and A. Kaldor, Phys. Rev. **B32**, 7290(1985).
5. W. A. de Heer, P. Milani, and A. Chatelain, Phys. Rev. Lett. **65**, 488(1990).
6. J. P. Bucher, D. C. Douglass, and L. A. Bloomfield, Phys. Rev. Lett. **66**, 3052(1991)
7. P. R. R. Langridge-Smith, M. D. Morse, G. P. Hansen, R. E. Smalley, and A. J. Merer, J. Chem. Phys. **80**, 593 (1984).
8. E. M. Spain, J. M. Behm, and M. D. Morse, J. Chem. Phys. **96**, 2512 (1992)
9. E. M. Spain and M. D. Morse, J. Phys. Chem. **96**, 2479 (1992).
10. Z. Hu, Q. Zhou, J. R. Lombardi and D. M. Lindsay, Physics and chemistry of Finite Systems: From Clusters to Crystals, edited by P. Jena et al. (Kluwer, The Netherlands, 1994), Vol. II, p. 969.
11. K. Balasubramanian and Ch. Ravimohan, J. Chem. Phys. **92**, 3659(1990).
12. S. R. Radel and M. H. Navidi, Chemistry, West Publishing Company, New York, (1994).
13. J. Harries and R. O. Jones, J. Chem. Phys. **70**, 830(1979).

14. I. Shim and K. A. Gingerich, J. Chem. Phys. **77**, 2490(1982).

15. D. G. Leopold, J. Almlof, W. C. Lineberger, and P. R. Taylor, J. Chem. Phys. **88**, 3780(1988).

16. T. Noro. C. Ballard, M. H. Palmer, and H. Tatewaki, J. Chem. Phys. **100**, 452(1994).

17. D. R. Salahub. in Ab Initio Methods in Quantum Chemistry-II, edit by K. P. Lawless Wiley, New York, (1987).

18. G. Herzberg. Spectra of Diatomic Molecules. Van Nostrand. New York, (1950).

19. Zhendong Hu, Jian-Guo Dong, John. R. Lombardi, and D. M. Lindsay, J. Chem. Phys. **101**, 95(1994).

20. B. Simard, P. I. Presunka, H. P. Loock. and A. Berces, J. Chem. Phys. **107**. 307(1997).

21. L. -S. Zeng. P. J. Brucat. C. L. Pettiette, S. Yang, and R. E. Smalley. J. Chem. Phys. 83, 4273(1985).

22. P. J. Brucat, L. -S. Zheng, C. L. Pettiette. S. Yang. and R. E. Smalley, J. Chem.Phys. **84**. 3078 (1986)

23. W. E, Klotzbucher, G. A. Ozin, Inorg. Chem. **19**, 3767(1980).

24. A. R. Miedema, K. A. Gingerich, J. Phys. B **12**, 2081 (1979).

25. A. R. Miedema, R. Boom, F. R. de Boer, J. Less-Common Met. **41**. 283 (1975).

26. A. R. Miedema, J. Less-Common Met. **46**, 67 (1976).

27. R. Boom, F. R. de Boor, A. R. Miedema, J. Less-Common Met. **45**. 237(1976).

28. R. Boom, F. R de Boer, A. R Miedema, J. Less-Common. Met. **46**, 271 (1976).

29. A. D. Becke, Phys. Rev. A **38**. 3098 (1988).

30. C. Lee, W. Yang and R. G. Parr, Physical Review B **37**, 785 (1988).

31. B. Miehlich, A. Savin, H. Stoll and H. Preuss, Chem. Phys. Lett. **157**, 200 (1989).

32. S. H. Vosko, L. Wilk and M. Nusair, Canadian J. Phys. **58**, 1200 (1980).

33. K. Burke, J. P. Perdew and Y. Wang, in Electronic Density Functional Theory: Recent Progress and New Directions, Ed. J. F. Dobson, G. Vignale and M. P. Das (Plenum, 1998).

34. J. P. Perdew, in Electronic Structure of Solids '91, Ed. P. Ziesche and H. Eschrig. Akademie Verlag, Berlin. (1991) 11.

35. J. P. Perdew, J. A. Chevary, S. H. Vosko, K. A. Jackson, M. R. Pederson, D. J. Singh and C. Fiolhais, Phys. Rev. B **46** (1992).

36. J. P. Perdew, J. A. Chevary, S. H. Vosko, K. A. Jackson, M. R. Pederson, D. J. Singh and C. Fiolhais, Phys. Rev. B **48** (1993).

37. J. P. Perdew, K. Burke and Y. Wang, Phys. Rev. B **54**, 16533 (1996).

38. J. P. Perdew, Phys. Rev. B **33**, 8822 (1986).

39. J. P. Perdew and A. Zunger, Phys. Rev. B **23**, 5048 (1981).

40. P. J. Hay and W. R. Wadt, J. Chem. Phys. **82**, 270 (1985).

41. W. R. Wadt and P. J. Hay, J. Chem. Phys. **82**, 284 (1985).

42. P. J. Hay and W. R. Wadt, J. Chem. Phys. **82**, 299 (1985).

43. M. Doverstal, B. Lingren, U. Sassenberg, C. A. Arrington, and M. D. Morse, J. Chem. Phys. **97**, 7087 (1992).

44. S. Taylor, E. M. Spain, and M. D. Morse, J. Chem. Phys. **92**, 2698 (1990).

45. S. Taylor, G. Lemire, Y. M. Hamrick, Z. Fu, and M. D. Morse, J. Chem. Phys. **89**, 5517 (1988).

46. S. Taylor, E. M. Spain, and M. D. Morse, J. Chem. Phys. **92**, 2710 (1990).

47. E. M. Spain, J. M. Behm, and M. D. Morse, J. Chem. Phys. **96**, 2511 (1992).

48. E. M. Spain and M. D. Morse, J. Phys. Chem. **96**, 2479 (1992).

49. M. D. Morse, G. P. Hansen, P. R. R. Langridge-Smith. L.-S. Zheng, M. E. Geusic, D. L. Michalopoulos, and R. E. Smalley, J. Chem. Phys. **80**, 5400 (1984).

50. D. E. Lessen, R. L. Asher, and P. J. Brucat, Chem. Phys. Lett. **182**, 412 (1991).

51. L. M. Russon, S. A. Heidecke, M. K. Birke, J. Conceicao, P. B. Armentrout. and M. D. Morse, Chem. Phys. Lett. **204**, 235 11993).

52. K. F. Willey, C. S. Yeh, D. L. Robbins, and M. A. Duncan, Chem. Phys. Lett. **192**, 179 (1992); C. S. Yeh, K. F. Willey, D. L. Robbins, and M. A. Duncan, ibid. **196**, 233 (1992).

53. L. M. Russon, S. A. Heidecke, M. K. Birke, J. Conceicao, M. D. Morse, and P. B. Armentrout, J. Chem. Phys. **100,** 4747 (1994)

54. R. L. Hettich and B. S. Freiser, J. Am. Chem. Soc. **109**, 3537 (1987).

55. C. A. Arrington, T. Blume, and M. D. Morse, M. Doverstal and U. Sassenberg, J. Phys. Chem. **98**, 1398 (1994)

56. J. D. Langenberg and M. D. Morse, J. Chem. Phys. **108**, 2331 (1998).

57. A. Kant and Sin-Shong Lin, J. Chem. Phys. **51**, 1644 (1969)

58. D. R. Salahub and N. A. Baykara, Surf. Sci. **156**, 605 (1985).

59. A. M. James, P. Kowalczyk, R. Fournier, and B. Simard, J. Chem. Phys. **99**, 8504 (1993).

60. M. Doverstal, B. Lindgren, U. Sassenberg, C. A. Arrington, M. D. Morse. J. Chem. Phys. **97**, 7087 (1992).

61. K.M. Ervin and P. B. Armentrout, J. Chem. Phys., **83**, 166 (1985).

62. D. A. Hales, L. Lian, and P. B. Armentrout, Int. J. Mass Spectrometry and Ion Process, **102**, 269 (1990).

Chapter VII References

1. T. G. Dietz, M. A. Duncan, D. E. Powers, and R. E. Smalley, J. Chem. Phys. **74**, 6511(1981)
2. See, for example, "Physics and Chemistry of Finite Systems: From Clusters to Crystals", edited by P. Jena, S. N. Khanna, and B. K. Rao, Kluwer Academic, Boston, (1992). Vols. I and II.
3. B. Simard, Marie-Angle Lebeault-Dorget, A. Marijnissen, and J. J. ter Meulen. J. Chem. Phys. **108**, 9668 (1998).
4. M. Harada and H. Dexpert. J. Phys. Chem. **100**, 565 (1996).
5. W. Kohn and L. J. Sham. J. Phys. Rev. A **140**, 1133, (1965).
6. M. Aydin, D. M. Lindsay, and John R. Lombardi, " Photofragmentation spectroscopy of zirconium dimer cation and ab initio study on Zr_2 and Zr_2^+ ", Submitted to Phys. Rev.
7. S. K. Gupta and K. A. Gingerich. J. Chem. Phys. **70**, 5350 (1979).
8. S. R. Radel and M. H. Navidi, Chemistry, West Publishing Company, New York, (1994).
9. M. D. Morse. Chem. Rev. **86**, 1049 (1986).
10. A. M. James, P. Kowalczyk, R. Fournier, and B. Simard, J. Chem. Phys. **99**, 8505(1993).
11. S. P. Walch and C. W. Bauschlicher, Jr., in "Comparison of Ab Initio Quantum Chemistry with Experiment for Small Molecules", edited by R. J. Bartlett (Reidel, Dondrecht, 1985).
12. K. S. Sohn, S. Lee, D. M. Bylaander, and L. Kleinman, Phys. Rev. B **39**, 9983 (1989).

13. D. R. Salahub, Adv. Chem. Phys. **69**, 447 (1987).

14. L. Goodwin and D.R. Salahub, Phys. Rev. A **47**, R774 (1993).

15. H. Sellers, J. Phys. Chem. **94**, 1338 (1990).

16. I. Shim, Matematisk-fysiske Meddelelser **41** (1985).

17. R. J. Van Zee, S. Li and W. Weltner Jr. Chem. Phys. Letters Vol. **217**, 381 (1994).

18. D. A. Hales, L. Lian, and P. B. Armentrout. Int. J. Mass Spectr. And Ion Proc. **102**, 269 (1990).

19. L. -S. Zeng, P. J. Brucat, C. L. Pettiette, S. Yang, and R. E. Smalley, J. Chem. Phys. **83**, 4273(1985).

20. P. J. Brucat, L. -S. Zheng, C. L. Pettiette, S. Yang, and R. E. Smalley, J. Chem.Phys. **84**, 3078 (1986)

21. A. D. Becke, Phys. Rev. A **38**, 3098 (1988).

22. C. Lee, W. Yang and R. G. Parr, Physical Review B **37**, 785 (1988).

23. B. Miehlich, A. Savin, H. Stoll and H. Preuss, Chem. Phys. Lett. **157**, 200 (1989).

24. J. P. Perdew, Phys. Rev. B **33**, 8822 (1986).

25. A. D. Becke, J. Chem. Phys. **98**, 5648 (1993).

26. A. D. Becke, J. Chem. Phys. **104**, 1040 (1996).

27. C. Adamo and V. Barone, Chem. Phys. Lett. **274**, 242 (1997).

28. P. J. Hay and W. R. Wadt, J. Chem. Phys. **82**, 270 (1985).

29. W. R. Wadt and P. J. Hay, J. Chem. Phys. **82**, 284 (1985).

30. P. J. Hay and W. R. Wadt, J. Chem. Phys. **82**, 299 (1985).

A. M. James, P. Kowalczyk, E. Langlois, and M. D. Campbell, A. Ogawa, and B. Simard. J. Ch

Chapter VIII References

1 L. –S. Zheng, P. J. Brucat, C. L. Pettiette, S. Yang, and R. E. Smalley, J. Chem. Phys. **83**, 4273 (1985).

2 L.N. Ding, M. A. Young, P. D. Kleiber, and W. D. Stwalley, J. Phys. Chem. **97**, 2181 (1993).

3 J. B. Hopkins, P. R. R. Langridge-Smith, M. D. Morse, and R. E. Smalley, J. Chem. Phys. **78**, 1627 (1983).

4 P. R. R. Langridge-Smith, M. D. Morse, G. P. Hansen, R. E. Smalley, and A. J. Merer, J Chem. Phys. **80,** 593 (1984).

5 Taylor, G. W. Lemire, Y. M. Hamrick, Z. Fu, and M. D. Morse, J. Chem. Phys. **89,** 5517 (1988).

6 Taylor, E. M. Spain, and M. D. Morse, J. Chem. Phys. **92,** 2710 (1990).

7 Taylor, E. M. Spain, and M. D. Morse, J. Chem. Phys. **92,** 2698 (1990).

8 E. M. Spain, J. M. Behrn, and M. D. Morse, J. Chem. Phys. **96,** 2511 (1992).

9 M. Doverstal, B. Lindgren, U. Sassenberg, C. A. Arrington, and M. D. Morse, J. Chem. Phys. **97**, 7087 (1992).

10 A. M. James, P. Kowalczyk, R. Fournier, and B. Simard, J. Chem. Phys. **99,** 8504 (1993).

11 A. M. James, P. Kowalczyk, and B. Simard, Chem. Phys. Lett **216**, 512 (1993).

12 A. M. James, P. Kowaiczyic, E. Langlois, M. D. Campbell, A. Ogawa, and B. Simard, J, Chem. Phys. **101**, 4485 (1994).

13 A. M. James, P. Kowalczyk, and B. Simard, J. Mol. Spectrosc. **164,** 260 (1994).

14 L. Song, A. Eychmuller and M. A. El-Sayed, J. Phys. Chem. **92,** 1005 (1988).

15 J. L. Elkind, F. D. Weiss. J. M. Alford, R. T. Laaksonen and R. E. Smalley. J. Chem. Phys. **88,** 5215 (1988).

16 M. R. Sakin, R. O. Brickman, D. M. Cox, and A. Kaldor. J. Chem. Phys. **88,** 3555 (1988).

17 M. R. Sakin. D. M. Cox and A. Kaldor. J. Chem. Phys. **91,** 5224 (1987).

18 S. Li, A. Eychmuller, R. J. St. Pierre, and M. A. El-Sayed J. Phys. Chem. **93,** 2485 (1989).

19 D. J. Trevor and A. Kaldor. J. Chem. Phys. **88,** 111 (1988).

20 S. Li and M. A. El-Sayed. Chem. Phys. Lett. **152,** 281 (1988).

21 S. Li and M. A. El-Sayed, J. Phys. Chem. Phys. **94,** 7907 (1990).

22 J. E. Fowler, A. Garcia, and J. M. Ugalde, J. Phys. Rev. A. **60,** 3058 (1999).

23 K. D. Ball, R. S. Berry, R. E. Kunz, F. Y. Li, and D. J. Wales, Science **271,** 963 (1996).

24 M. D. Morse, M. E. Geusic, J. R. Heath, and R. E. Smalley, J. Chem. Phys. **83,** 2293 (1985)

25 D. J. Trevor, R. L. Whetten, D. M. Cox, and A. Kaldor, 1. Phys. Chem. **107,** 518 (1985).

26 R. J. St. Pierre and M. A. El-Sayed, J. Phys. Chem. **91,** 763 (1987).

27 D. M. Cox, D. J. Trevor, R. L. Whetteri, and A. Kaidor, J. Phys. Chem. **92,** 421 (1988).

28 Y. Hamrick, S. Taylor, G. W. Lemire, Z.-W. Fu, J.-C. Shui, and M. D. Morse. J. Chem. Phys. **88,** 4095 (1988).

29 Y. M. Hamrick and M. D. Morse, J. Phys. Chem. **93**, 6494 (1989).

30 S. Nonose, Y. Sone, K. Onodera, S. Sudo, and K. Kaya, 1. Phys. Chem. **94**, 2744 (1990).

31 X. Ren, P. Hintz, and K. M. Ervin, J. Chem. Phys. **99**, 3575 (1993).

32 S. A. Mitchell, L. Lian, and P. A. Hackett, J. Chem. Phys. **103**, 5539 (1995).

33 S. A. Mitchell, D. Ni. Rayner, and P. A. Hackett, J. Chem. Phys. **104**, 4012 (1996).

34 A. Brces, P. A. Hackett, L. Lian, S. A. Nttchell, and D. M. Rayner. J. Chem. Phys. **108,** 5476 (1998).

35 E. K. Parks, K. P. Kerns, and S. J. Riley, J. Chem. Phys. **112**, 3384 (2000).

36 J. Conceigao, S. K. Loh, L. Lian, and P. B. Armentrout, J. Chem. Phys. **104**, 3976 (1996).

37 J. B. Griffin and P. B. Armentrout, J. Chem. Phys. **106**, 4448 (1997).

38 J. B. Griffin and P. B. Armentrout, 1. Chem. Phys. **107**, 5345 (1997).

39 J. B. Griffin and P. B. Armentrout, J. Chem. Phys. **108**, 8062 (1998).

40 J. B. Griffin and P. B. Armentrout, J. Chem. Phys. **108**, 8075 (1998).

41 S. K. Loh, L. Lian, and P. B. Arrnentrout,1. Am. Chem. Soc. **111**, 3167 (1989).

42 S. K. Loh, D. A. Hales, L. Lian, and P. B. Arinentrout, J. Chem. Phys. **90**, 5466 (1989).

43 D. A. Hales, L. Lian, and P. B. Armentrout, Int. J. Mass Spectrom. Ion Proc. **102**, 269 (1990).

44 L. Lian, C.-X. Su, and P. B. Armentrout, J. Chem. Phys. **97**, 4084 (1992).

45 C.-X. Su and P. B. Armentrout, J. Chem. Phys. **99**, 6506 (1993).

46 C.-X. Su, D. A. Hales, and P. B. Armentrout, J. Chem. Phys. **99,** 6613 (1993).

47 D. A. Hales, C.-X. Su, L. Lian, and P. B. Armentrout, J. Chem. Phys. **100**, 1049 (1994).

48 M. Aydin and John R. Lombardi, "*Photofragmentation spectroscopy of niobium dimer cation molecule and ab initio study on* Nb_2, Nb^-_2", submitted.

49 M. Aydin, D. M. Lindsay and John R. Lombardi, submitted.

50 M. B. Knickelbein and S. Yang, J. Chem. Phys. **93**, 5760 (1990).

51 M. B. Knickelbein, S. Yang, and S. J. Riley, J. Chem. Phys. **93,** 94 (1990).

52 S. Yang and M. B. Knickelbein, Z. Phys. D **31**, 199 (1994).

53 M. Knickelbein, J. Chem. Phys. **102**, 1 (1995).

54 G. M. Koretsky and M. B. Knickelbein, J. Chem. Phys. **106**, 9810 (1997).

55 J. Ho, K. M. Ervin, and W. C. Lineberger, J. Chem. Phys. **93,** 6987 (1990).

56 H. Wu, S. R. Desai, and L. -S. Wang, Phys. Rev. Lett. **76**, 212 (1996).

57 L.-S. Zheng, C. M. Karner, P. J. Brucat, S. H. Yang, C. L. Pettiette, M. J. Craycraft, and R. E. Smalley, J. Chem. Phys. **85**, 1681 (1986).

58 K. J. Taylor, C. L. Pettiette-Hall, 0. Cheshnovsky, and R. E. Smalley, J. Chem. Phys. **96**, 3319 (1992).

59 E. M. Spain and M. D. Morse, J. Phys. Chem. **96,** 2479 (1992).

60 L. M. Russon, S. A. Heidecke, M. K. Birke, J. Conceicao, P. B. Armentrout, and M. D, Morse, Chem. Phys. Lett. **204**, 235 (1993).

61 C. A. Arrington, T. Blume, M. D. Morse, M. Doverstil, and U. Sassenberg, J. Phys. Chem, **98**, 1398 (1994).

62 L. M. Russon, S. A. Heidecke, M. K. Birke, J. Conceicao, M. D. Morse, and P. B Armentrout, J. Chem. Phys. **100**, 4747 (1994).

63 J. D. Langenberg and M. D. Morse, J. Chem. Phys. **108**, 2331 (1998).

64 S. K. Nayak, B. K. Rao, S. N. Khanna, and P. Jena, Chem. Phys. Lett. **259**, 588 (1996).

65 M. B. Knickelbein and S. Yang, J. Chem. Phys. **93**, 1476 (1990).

66 R. L. Whetten, M. R. Zakin, D. M. Cox, D. J. Trevor and A. Kaldor. J. Chem. Phys. **85,** 1697 (1986).

67 M. R. Sakin, R. O. Brickman, D. M. Cox and A. Kaldor. J. Chem. Phys. **88** (1988).

68 J. Zhao, X. Chen, and G. Wang, Phys. Lett. A **214**, 211 (1966).

69 M. Andersson, H. Gronbeck, L. Holmgren, and A. Rosen, Laser Techniques for State-Selected and State-to-State Chemistry III, edited by J. W. Hepburn (SPIE International Society for Optical Engineering, Bellingham, WA, 1995), Vol. **2548**, p 157.]

70 L. Holmgren, M. Andersson, and A. Rosen, Surf. Sci. 331-333 (1995) 231.

71 H. Sellers, J. Phys. Chem. **94,** 1338 (1990).

72 L. Goodwin and D. R. Salahub, Phys. Rev. A. **47**, R774 (1993).

73 C. J. Humphreys and W. F. Meggers, J. Research Nat. Bur. Std. **34**, 515, RP1656 (1945).

74 J. Mack, Rev. Mod. Phys. **22**, 64 (1950).

75 J. M. Chase, C. A. Davies, J.J. R. Downey, D. J. Frurip, R. A. McDonald, and A. N. Syvrud, J. Phys. Chem. Ref. Data Suppl. **14**, 1 (1985).

76 A. D. Becke, Phys. Rev. A **38,** 3098 (1988).

77 C. Lee, W. Yang and R. G. Parr, Phys. Rev. B **37**, 785 (1988).

78 B. Miehlich, A. Savin, H. Stoll and H. Preuss, Chem. Phys. Lett. **157**, 200 (1989).

79 P. J. Hay and W. R. Wadt, J. Chem. Phys. **82**, 270 (1985).

80 W. R. Wadt and P. J. Hay, J. Chem. Phys. **82**, 284 (1985).

81 P. J. Hay and W. R. Wadt, J. Chem. Phys. **82**, 299 (1985).

Chapter IX References

1 (a) L. –S. Zheng, P. J. Brucat, C. L. Pettiette, S. Yang, and R. E. Smalley, J. Chem. Phys. **83** (1985) 4273; (b) P. J. Brucat, L. –S. Zheng, C. L. Pettiette, S. Yang, and R. E. Smalley, J. Chem. Phys. **83** (1985) 4273.

2 L.N. Ding, M. A. Young, P. D. Kleiber, and W. D. Stwalley, J. Phys. Chem. **97** (1993) 2181.

3 J. B. Hopkins, P. R. R. Langridge-Smith, M. D. Morse, and R. E. Smalley, J. Chem. Phys. **78** (1983) 1627.

4 P. R. R. Langridge-Smith, M. D. Morse, G. P. Hansen, R. E. Smalley, and A. J. Merer, J Chem. Phys. **80** (1984) 593.

5 Taylor, G. W. Lemire, Y. M. Hamrick, Z. Fu, and M. D. Morse, J. Chem. Phys. **89** (1988) 5517.

6 Taylor, E. M. Spain, and M. D. Morse, J. Chem. Phys. **92** (1990) 2710.

7 Taylor, E. M. Spain, and M. D. Morse, J. Chem. Phys. **92** (1990) 2698.

8 E. M. Spain, J. M. Behrn, and M. D. Morse, J. Chem. Phys. **96** (1992) 2511.

9 M. Doverstal, B. Lindgren, U. Sassenberg, C. A. Arrington, and M. D. Morse, J. Chem. Phys. **97** (1992) 7087.

10 A. M. James, P. Kowalczyk, R. Fournier, and B. Simard, J. Chem. Phys. **99** (1993) 8504.

11 A. M. James, P. Kowalczyk, and B. Simard, Chem. Phys. Lett. **216** (1993) 512.

12 A. M. James, P. Kowaiczyic, E. Langlois, M. D. Campbell, A. Ogawa, and B. Simard, J, Chem. Phys. **101** (1994) 4485.

13 A. M. James, P. Kowalczyk, and B. Simard, J. Mol. Spectrosc. **164** (1994) 260.

14 M. Aydin, D. M. Lindsay and John R. Lombardi, "Photofragmentation spectroscopy of niobium dimer cation molecule and ab inito study on Nb_2, Nb_2^+", submitted to J. Phys. Chem.

15 D. A. Hales, L. Lian, and P. B. Armentrout, Int. J. Mass Spectrom. Ion Proc. **102** (1990) 269.

16 S. K. Loh, L. Lian, and P. B. Armentrout, J. Am. Chem. Soc. **111** (1989) 3167.

17 M. Andersson, H. Gronbeck, L. Holmgren, and A. Rosen, Laser Techniques for State-Selected and State-to-State Chemistry III, edited by J. W. Hepburn (SPIE International Society for Optical Engineering, Bellingham, WA, 1995), Vol. 2548, p 157.

18 L. Goodwin and D. R. Salahub. Phys. Rev. A. **47** (1993) R774.

19 H. Sellers J. Phys. Chem. **94** (1990) 1338.

20 J. E. Fowler, A. Garcia, and J. M. Ugalde. J. Phys. Rev. A. **60** (1999) 3058.

21 S. K. Gupta and K. A. Gingerich, J. Chem. Phys. **70** (1979) 5350.

22 M. D. Morse, Chem. Rev. **86** (1986) 1049.

23 M. Aydin and John R. Lombardi, submitted.

24 J. M. W. Chase, C. A. Davies, J. J. R. Downey, D. J. Frurip, R. A. McDonald, and A. N. Syvrud. J. Phys. Chem. Ref. Data Suppl., **14** (1985)1.

25 A. D. Becke, Phys. Rev. A. **38** (1988) 3098.

26 (a) C. Lee, W. Yang and R. G. Parr, Phys. Rev. B **37** (1988) 785.

(b) B. Miehlich, A. Savin, H. Stoll and H. Preuss, Chem. Phys. Lett. **157** (1989) 200.

27 P. J. Hay and W. R. Wadt, J. Chem. Phys. **82** (1985) 270.

28 W. R. Wadt and P. J. Hay, J. Chem. Phys. **82** (1985) 284.

29 P. J. Hay and W. R. Wadt, J. Chem. Phys. **82** (1985) 299.

30 C. J. Humphreys and W. F. Meggers, J. Research Nat. Bur. Std. **34**, 515, RP1656 (1945).

31 J. Mack, Rev. Mod. Phys. **22** (1950) 64.

32 R. L. Whetten, M. R. Zakin, D. M. Cox, D. J. Trevor, and A. Kaldor, J. Chem. Phys. **85** (1986) 1697.

33 M. B. Knickelbein and S. Yang, J. Chem. Phys. **93**(1990) 5750.

Chapter X References

1 T. G. Dietz, M. A. Duncan, D. E. Powers, and R. E. Smalley, J. Chem. Phys. **74**, 6511 (1981)

2 V. E. Bondybey and J. H. English, J. Chem. Phys. **74**. 6978 (1981).

3 T. G. Dietz, M. A. Duncan, M. G. Liverman, and R. E. Smalley, J. Chem. Phys. **73**, 4816 (1980).

4 D. E. Powers. S. G. Hansen, M. E. Geusic, A. C. Puiu, J. B. Hopkins, T. G. Dietz, M. A. Duncan, P. R. R. L.-Smith, and R. E. Smalley, J. Phys. Chem. **86**, 2556 (1982).

5 B. Simard, S. A. Mitchell, M. R. Humphries, and P. A. Hackett. J. Mol. Spectrosc. **129**, 186 (1988).

6 B. Simard, S. A. Mitchell, M. R. Humphries, and P. A. Hackett. J.Chem. Phys. **89**,1899 (1988).

7 B. Simard, S. A. Mitchell. L. M. Hendel, and P. A. Hackett. Faraday Discuss. Chem. Soc. **86**, 163 (1988).

8 B. Simard, C. Masoni, and P. A. Hackett, J. Mol. Spectrosc. **136**, 44 (1989).

9 V. E. Bondybey and J. H. English, J. Chem. Phys. **73**, 42 (1980).

10 V. E. Bondybey and J. H. English, J. Chem. Phys. **80**, 568 (1984).

11 W. E. Knight, K. Klemenger, and W. A. de Heer, Phys. Rev. B **31**, 2539 (1985).

12 M. E. Geusic, M. D. Morse, S. C. O'Brien, and R. E. Smalley, J. Chem. Phys. **82**, 590 (1985).

13 M. D. Morse, M. E. Geusic, J. R. Heath, and R. E. Smalley, J. Chem. Phys. **83**, 2293 (1985).

14 F. Misaizu, M. Sanekata, K. Tsukamoto, K. Fuke, and S. Iwata, J. Phys. Chem. **96**, 8259 (1992).

15 L. N. Ding, M. A. Young, P. D. Kleiber, and W. C. Stwalley, J. Phys. Chem. **97**, 2181 (1993).

16 R. L. Asher, D. Bellert, T. Buthelezi, and P. J. Brucat, Chem. Phys. Letters. **224**, 525 (1994).

17 C. A. Arrington, T. Blume, M. Morse, M. Doverstal, and U. Sassenberg, J. Phys. Chem. **98**, 1398 (1994).

18 B. Simard, M. A. L. Dorget, A. Marijnissen, and J. J. ter Meulen, J. Chem. Phys. **108**, 9668 (1998).

19 P. J. Brucat, L.-S. Zheng, C. L. Pettiette, S. Yang, and R. E. Smalley, J. Chem. Phys. **84**, 3078 (1986).

20 R. J. V. Zee, S. Li, and W. Weltner Jr, Chem. Phys. Letters. **217**, 381 (1994).

21 A. G. Adam, Y. Azuma, J. A. Barry, A. J. Merer, U. Sassenberg, J. O. Schroder, G. Cheval, and J. L. Femenias, J. Chem. Phys. 100, 6240 (1994).

22 J. L. Femenias, G. Cheval, A. J. Merer, and U. Sassenberg, J. Mol. Spectrosc. **124**, 348 (1987).

23 Z. Hu, B. Shen, Q. Zhou, S. Deosaran, J. R. Lombardi, and M. D. Lindsay, SPIE 1599, 65 (1991).

24 A. M. James, P. Kowalczyk, R. Fournier, and B. Simard, J. Chem. Phys. **99**, 8504 (1993).

25 A. M. James, P. Kowalczyk, E. Langlois M. D. Campbell, A. Ogawa, and B. Simard, J. Chem. Phys. **101**, 4485 (1994).

26 B. Simard, C. Masoni, and P. A. Hackett, J.Chem. Phys. **92**, 7003 (1990).

27 B. Simard, Paul I. Presunka, H. P. Loock, and A. Berces, J. Chem. Phys. **107**, 307 (1997).

28 P. R. R. Langridge-Smith, M. D. Morse, G. P. Hansen, and R. E. Smalley, J. Chem. Phys. **80**, 593 (1984).

29 D. A. Hales, L. Lian, and P. B. Armentrout, Int. J. Mass Spect. And Ion Processes. **102**, 269 (1990).

30 V. R. Rao. Indian J. Phys. **24**, 35 (1950)

31 K. S. Rao, Nature(London) **170**, 670 (1952).

32 V. R. Rao and D. Premaswarup. Indian J. Phys. **27**, 399 (1953)

33 J. M. Brom, C. H. Durham, and W. Weltner, J. Chem. Phys. **61**, 970 (1974).

34 W. A. Saunders. Department of Physics, Swiss Federal Institute of Technology-Lausanne, Switzerland.

35 G. I. Dimov Pribory I Tekhnika Eksperimenta, Nuclear Physics Institute. Academy of Sciences of the USSR, No. 5, pp. 168-171 (1968).

36 J. M. Hayes, Chem. Rev. **87**, 745 (1987).

37 J. M. Pendlebury and K. F. SMITH, Contemp. Phys. **28**, 3 (1987).

38 J. R. Heath, Y. Liu, S. C. O'Brien, Q.-L. Zhang, R. F. Curl, F. K. Tittel, and R. E. Smalley, J. Chem. Phys. **83**, 5520 (1985).

39 A. J. Merer, Annu. Rev. Phys. Chem. 40, 407 (1989).

40 Can be derived using the ladder operator $S_- = S_{1-} + S_{2-} + S_{3-}$ to generate all 2S+1 of eigenfunctions for a three electron system having S = 3/2 or see Charles S. Johnson, Jr., Lee G. Pedersen, *Problems and Solutions in Quantum Chemistry and Physics*, Dover Publications, Inc., New York, 1986.

41 C. E. Moore, Atomic Energy Levels, Natl. Bur. Stand. (US) Crit. No. 467, (U.S. GPO, Washington, D.C., 1971), Vols. I and II.

42 See Table 4.7 in Chapter 4 of Helene Lefebvre-Brion and Robert W. Field, *Perturbations in The Spectra of Diatomic Molecules*, Academic Press, New York, 1986.

43 See Chapter VII.

44 K. Balasubramanian and XiaoLei Zhu, submitted.